

Planetologie

Temperature-induced effects and phase reddening on near-Earth asteroids

Inaugural-Dissertation
zur Erlangung des Doktorgrades der Naturwissenschaften
im Fachbereich Geowissenschaften
der Mathematisch-Naturwissenschaftlichen Fakultät
der Westfälischen Wilhelms-Universität Münster

vorgelegt von
Juan A. Sánchez
aus Caracas, Venezuela

-2013-

Dekan: Prof. Dr. Hans Kerp

Erster Gutachter: Prof. Dr. Harald Hiesinger

Zweiter Gutachter: Dr. Vishnu Reddy

Tag der mündlichen Prüfung: 4. Juli 2013

Tag der Promotion: 4. Juli 2013

Contents

Summary	5
Preface	7
1 Introduction	11
1.1 Asteroids: origin and evolution	11
1.2 The asteroid-meteorite connection	13
1.3 Spectroscopy as a remote sensing technique	16
1.4 Laboratory spectral calibration	24
1.5 Taxonomic classification of asteroids	31
1.6 The NEA population	36
1.7 Asteroid space weathering	37
1.8 Motivation and goals of the thesis	41
2 VNIR spectra of NEAs	43
2.1 The data set	43
2.2 Data reduction	45
3 Temperature-induced effects on NEAs	55
3.1 Introduction	55
3.2 Temperature-induced spectral effects on NEAs	59
3.2.1 Spectral band analysis of NEAs	59
3.2.2 NEAs surface temperature	59
3.2.3 Temperature correction to band parameters	62
3.3 Results and discussion	70
4 Phase reddening on NEAs	73
4.1 Introduction	73
4.2 Phase reddening from ground-based observations of NEAs	76
4.2.1 Phase reddening effect on the band parameters	76
4.3 Phase reddening from laboratory measurements of ordinary chondrites	82
4.3.1 Data and spectral band analysis	82
4.3.2 Phase reddening effect on the band parameters	83
4.4 Results and discussion	91
4.4.1 Phase reddening and mineralogical analysis	91
4.4.2 Phase reddening and space weathering	92
4.4.3 Phase reddening and taxonomic classification	102

5 Conclusions	107
Publications	109
Bibliography	155
Talks and Posters	165
Acknowledgements	167
Curriculum Vitae	169

Summary

Asteroids are interplanetary bodies that never managed to accumulate into a single planet. Compared to planets, most asteroids have experienced little processing since they formed, and therefore represent the only source of information about the conditions prevailing in the inner portions of the late solar nebula. Among the different tools used to study asteroids, spectroscopy is a powerful remote sensing technique used to derive information about their surface mineralogy. This mineralogical characterization relies primarily on the identification and analysis of diagnostic features present in the spectra of some asteroids. Spectral band parameters (e.g., band centers, band depths, band areas, spectral slope) derived from visible and near-infrared (VNIR) spectra are used to determine the chemistry and abundance of minerals that could be present on the surface of the asteroid. These parameters are also employed for taxonomic classification, and to study the effects of space weathering on asteroids. However, spectral parameters are affected by temperature variations and phase angle effects. Temperature-induced effects on the spectra of mafic minerals are characterized by shifting the band centers and broadening or narrowing the absorption features. Phase angle induced effects, on the other hand, can manifest themselves as phase reddening, which produces an artificial increase of the spectral slope and variations in the strength of the absorption bands with increasing phase angle. In the present work we study the influence of these two effects on the interpretation of asteroid spectral data.

We have analyzed VNIR spectra (0.45-2.5 μm) of 12 near-Earth asteroids (NEAs) observed at different heliocentric distances and phase angles. Due to their highly eccentric orbits NEAs can exhibit a wide range of phase angles and experience significant variations on their average surface temperature. All the asteroids in this study are classified as either S-complex or Q-type asteroids, i.e., all of them exhibit the absorption bands characteristics of olivine-orthopyroxene assemblages. The spectra of these asteroids were obtained with the SpeX instrument on the NASA Infrared Telescope Facility (IRTF). In addition, we analyzed laboratory spectra (0.35 to 2.5 μm) of ordinary chondrite samples acquired at different temperatures (80 to 300 K), and phase angles (13° to 120°).

From the analysis of the meteorite spectra obtained at different temperatures, we found that the spectral band parameters that are more affected by temperature variations are the Band II center, which shows a progressive shift to longer wavelengths as the temperature increases, and the Band II depth and BAR (defined as the ratio of area of Band II to that of Band I), which decrease as the temperature increases. We have developed a new set of calibrations that can be used to correct for temperature variations on olivine-orthopyroxene assemblages.

According to our calculations the average surface temperature for NEAs ranges from ~ 130 to 440 K. We found that the increase in temperature from 130 to 440 K will shift the Band II center $\sim 0.06 \mu\text{m}$, which is larger than the typical uncertainty associated with this parameter measured from asteroid spectra. Our analysis also showed that the change of BAR between 130 and 440 K is ~ 0.23 , which is much larger than the uncertainty measured from asteroid

spectra. This decrease in BAR will produce an overestimation of the olivine abundance in an olivine-orthopyroxene assemblage.

Despite the fact that NEAs can experience a broad range of average surface temperatures, we found that due to observational constraints this range is much narrower ~ 130 to 265 K. The average temperature value for the studied asteroids was found to be about 234 K. These results imply that temperature variations will have a very small impact when comparing the spectral band parameters of the NEAs studied, with those measured for laboratory samples obtained at room temperature (300 k).

For different heliocentric distances of the same asteroid we estimated an average temperature variation of ~ 20 K. This means that, at least for the objects in this study, temperature variations do not have a significant effect when comparing band parameters of the same asteroid observed at different heliocentric distances.

The analysis of the laboratory spectra shows that variations in the band parameters can arise not only by changing the phase angle, but also for the same phase angle using different configurations of the incidence and emission angle. The effects of phase reddening on meteorite and asteroid spectra are seen as variations in the intensity of the absorption bands (band depths) and increase of the spectral slope with increasing phase angle. In the case of asteroid spectra our analysis showed that, on average, Band I and Band II depths will increase 0.66% and 0.93% respectively, for every 10° increase in phase angle. From these data we have derived equations that can be used to correct the effects of phase reddening in the band depths. Small variations in band centers and BAR values with increasing phase angle were also found for both meteorite and asteroid spectra, however these variations are smaller than the error bars. Since band centers and BAR values are used to estimate the mineral chemistry and abundance, these results imply that the effects of phase reddening will have no significant impact on the mineralogical analysis.

Of the three types of ordinary chondrites analyzed, the (olivine-rich) LL6 is the most affected by phase reddening, showing the largest variations in spectral slopes and band depths with increasing phase angles. These results confirm the material-dependence of phase reddening reported by previous studies.

From the analysis of ordinary chondrite spectra obtained at phase angles of 13° to 120° we found that the increase in spectral slope caused by phase reddening can mimic the effect of space weathering, which is characterized by producing reddening of the spectral slopes and suppression of the absorption bands. In particular, an increase in phase angle in the range of 30° to 120° will produce a reddening of the reflectance spectra equivalent to irradiate the sample with high mass ions (Ar^{++} 60 keV) with an ion fluence in the range of $\sim 1.3 \times 10^{15}$ to 1.7×10^{16} ions cm^{-2} . These ion fluences are equivalent to exposure times of $\sim 0.1 \times 10^6$ to 1.3×10^6 years at about 1 AU from the Sun. This increase in spectral slope due to phase reddening is also comparable to the effects caused by the addition of different fractions of submicroscopic metallic iron.

The present work also revealed that the variations in band depths and band areas produced by the phase reddening effect could lead to an ambiguous taxonomic classification of asteroids. These results apply to classifications systems based on Principal Component Analysis and also to classifications systems based on spectral band parameters.

Preface

Among the bodies in our solar system, asteroids represent the remnant debris from the inner solar system formation process (Bottke et al. 2002b). Their physical and dynamical characteristics, composition, and evolution are fundamental to understand how planets formed, and their study could ultimately shed some light about the origin of life on Earth. Because terrestrial planets experienced substantial modification since they formed, asteroids are the only objects that still preserve information about the conditions and processes that took place in the inner portions of the solar nebula and earliest solar system (Bottke et al. 2002b, Gaffey et al. 2002). On the other hand, the carbon-based molecules and volatile materials from which life eventually emerged may have been delivered to the Earth through asteroid impacts (Chyba and Sagan 1992, Botta and Bada 2002, Martins et al. 2008).

The first asteroid discovered was Ceres, which was found by Giuseppe Piazzi in 1801, and was initially considered to be a new planet (Foderà Serio et al. 2002). This was followed by the discovery of other similar bodies over the next few years including (2) Pallas, (3) Juno, and (4) Vesta. In 1891, the German astronomer Max Wolf pioneered the use of astrophotography to detect asteroids. This new technique helped to increase the rate of discoveries compared with earlier visual methods. However, apart from the discovery of new asteroids little work was done to investigate the composition and physical characteristics of these objects. Some early attempts were conducted by e.g., Watson (1941), but it was not until the early 1970s when serious systematic investigations of asteroid composition began (e.g., Gehrels 1970, McCord et al. 1970, Chapman et al. 1971, Chapman and Salisbury 1973). In parallel to these studies spectral data of minerals and meteorites were also obtained (e.g., Adams 1974, 1975, Gaffey 1976).

Of particular interest for study is the population of near-Earth asteroids (NEAs). Due to their proximity NEAs could be the source of some of the meteorites found on Earth. Thus, establishing links between the spectral properties of NEAs and those measured in the laboratory for meteorite samples is fundamental to determine the origin of those meteorites (Burbine et al. 2002). Some NEAs are of high interest due to their low velocities with respect to Earth (ΔV), which make them especially accessible for sample-return and manned missions (e.g., Lewis and Hutson 1993, Reddy et al. 2012a). Furthermore, NEAs could be in the future an important source for elements relatively rare on the Earth's surface (Kargel 1994). In addition, it is now recognized the threat that some NEAs could represent for civilization in the eventuality of collision. For example, Alvarez et al. (1980) showed that the extinction of numerous species at the Cretaceous-Tertiary transition was caused by the impact of a massive asteroid. Hence, having a better understanding of their physical properties could help us to develop mitigation strategies in the future.

In the past decade, spacecraft flyby (951 Gaspra, 243 Ida, 253 Mathilde, 2867 Šteins, 21 Lutetia) and rendezvous (433 Eros and 25143 Itokawa) missions allowed us to observe asteroids

as resolved objects. On July 2011, NASA's Dawn spacecraft entered orbit around asteroid (4) Vesta for a planned one-year exploration. Dawn is the first spacecraft to visit Vesta, and will be the first to visit Ceres, which will be reached in 2015. The main goal of this mission is to investigate how the size and the presence of water and volatiles influence the evolution of the planets. Ceres is geologically very primitive and icy, while Vesta is a differentiated and rocky body. It is thought that these opposite characteristics are due to the fact that these asteroids were formed in different regions of the solar system (McSween et al. 2002).

Two of the instruments on board Dawn are the Framing Cameras (FC) and the Visual and Infrared Spectrometer (VIR). The FC is designed to map the surface of Vesta in seven color filters and one clear filter with up to 20-m spatial resolution in order to examine its geology and cratering history. The VIR instrument, on the other hand, can acquire spectra from 0.3-5 μm covering the near ultraviolet (UV), visible and infrared regions of the spectrum.

Surface temperature and phase angle are two important parameters that affect the photometric and spectral behavior of planetary surfaces in telescopic and spacecraft data (Roush and Singer 1985, Schade and Wäsch 1999, Shestopalov and Golubeva 2000, Luu and Jewitt 1990, Nathues 2010). In order to quantify temperature- and phase angle-induced spectral effects prior to the arrival of Dawn, we conducted a series of laboratory and telescopic studies of Vesta and howardite, eucrite and diogenite (HED) meteorites. The observing campaign conducted in 2010 included photometric observations of Vesta with Dawn's FC filters, visible wavelength spectra (0.4-0.7 μm), and near-IR spectra (0.64-2.5 μm) obtained at a range of phase angles. The laboratory study included the analysis of visible and near-IR spectra of HED meteorites acquired in a broad range of temperatures and phase angles.

The analysis of Vesta spectral data revealed an increase of spectral slope and band depths with increasing phase angle, an effect known as phase reddening. In addition, the laboratory spectra of the HED meteorites showed a shift of the pyroxene absorption bands to longer wavelengths with increasing temperature. These variations caused by changes in viewing geometry and temperature could be misinterpreted as compositional variations if they are not taken into account. The results of this work that includes photometric, spectral phase and temperature effects on 4 Vesta and HED meteorites are presented in Reddy et al. (2012d).

Motivated by our findings in Reddy et al. (2012d) we decided to carry out a similar study with NEAs. Due to their proximity, NEAs can exhibit a wide range of phase angles (Luu and Jewitt 1990). In addition, their highly eccentric orbits can lead these objects to experience significant variations on their average surface temperature (Roush and Singer 1985, Schade and Wäsch 1999, Shestopalov and Golubeva 2000, Moroz et al. 2000). The present thesis investigates how temperature- and phase angle-induced effects can affect the interpretation of NEA spectral data. This work is based on the analysis of VNIR spectra of NEAs observed at different heliocentric distances and phase angles. In addition, and similarly to the work presented in Reddy et al. (2012d), our study also includes laboratory spectra of meteorite samples obtained at different temperatures and phase angles.

Chapter 1 of this thesis gives a general review of asteroids, including origin and evolution, taxonomic classification, laboratory spectral calibrations, asteroid space weathering, etc. This chapter also examines the theoretical aspects of near infrared reflectance spectroscopy, and the mineralogical applications of crystal field theory. Chapter 2 describes the data set, in particular the spectra of NEAs, the telescope and instrument used for the acquisition of the spectra, and the general steps involved in the data reduction procedure.

Our study on temperature-induced spectral effects on NEAs is described in chapter 3. A

description of the temperature series of meteorite spectra used to derive spectral calibrations is also included in this chapter. Chapter 4 focuses on the phase reddening effect and its implications for mineralogical analysis, space weathering and taxonomic classification. The laboratory spectra of meteorite samples obtained at different phase angles used to support this study is presented in this chapter. Both, chapters 3 and 4 include an introduction in the form of a literature review, containing the most important works related to their respective subjects. The results are discussed separately in each chapter. The last chapter summaries the conclusions from the previous chapters.

The main results of this thesis have been published in Sanchez et al. (2012). These results, in particular the temperature corrections derived in chapter 3, were later applied to asteroid spectral data presented in Reddy et al. (2012c) and Sanchez et al. (2013). In Reddy et al. (2012c) we carried out a detailed compositional analysis of NEA (4179) Toutatis and constrained its surface mineralogy. This asteroid is of particular interest because of the possibility of a flyby by the Chinese lunar spacecraft Chang'e 2 on December 13, 2012. In Sanchez et al. (2013) we analyzed visible and near-infrared spectra of a group of NEAs and Mars-crossers asteroids. These data were used to derive the taxonomic classification and surface composition of these asteroids. All these papers, Sanchez et al. (2012), Reddy et al. (2012d), Reddy et al. (2012c) and Sanchez et al. (2013) are presented in the Publications section.

1 Introduction

1.1 Asteroids: origin and evolution

Asteroids are interplanetary bodies, typically rocky, carbonaceous or metallic, formed in the inner planets region. Asteroids differ from comets in that they formed without significant ice content, and thus are incapable of displaying cometary activity (Weissman et al. 2002). Figure 1.1 shows a composite image, to scale, of the asteroids that have been imaged at high resolution by various space missions.

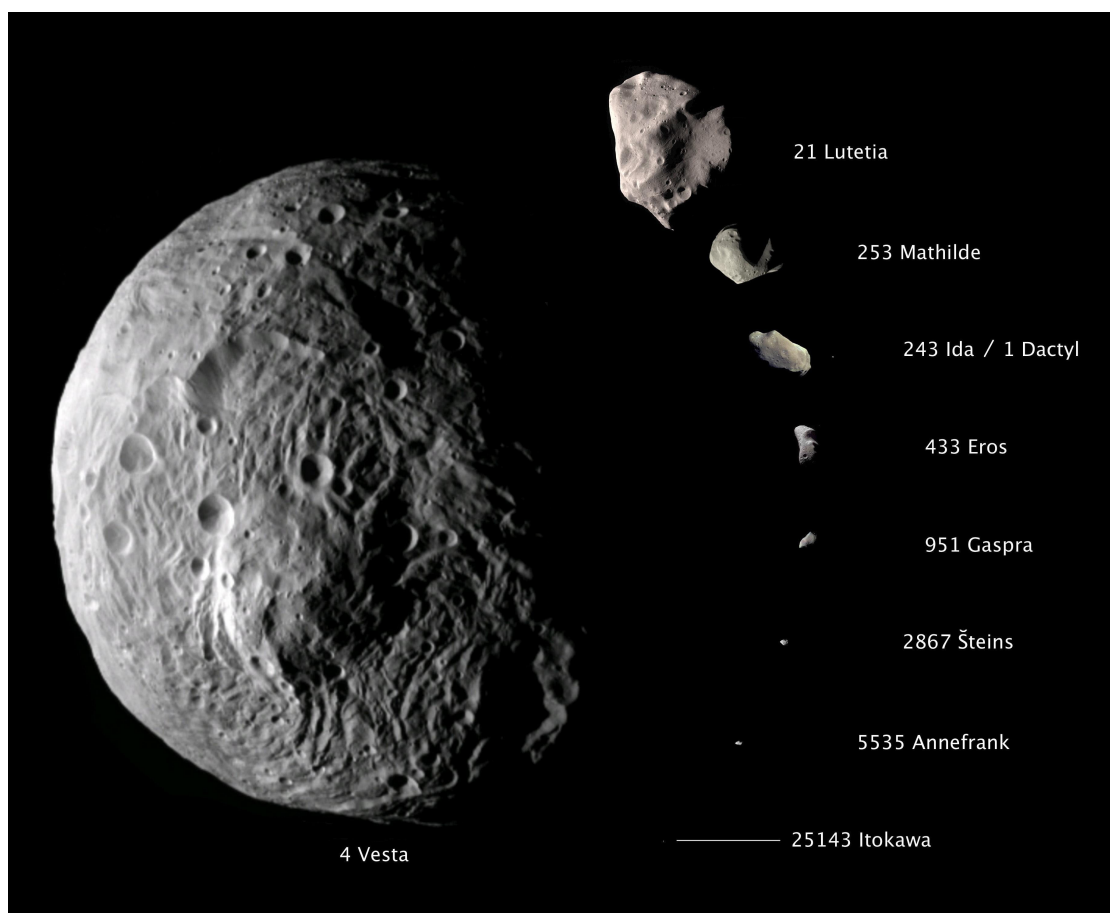


Figure 1.1: Composite image showing the comparative sizes of nine asteroids visited by spacecrafts. Image credit: NASA/JPL-Caltech/JAXA/ESA.

The largest reservoir of asteroids in the inner solar system is the main belt, located between

the orbits of Mars and Jupiter at a distance between 2.1 and 3.3 AU from the Sun.

The processes that led the main belt to its current state are believed to be related to planet formation, particularly the formation of the terrestrial planets and Jupiter (Safronov 1979, Wetherill 1989, Bottke et al. 2002b). The sequence of planet formation in the inner solar system can be divided into four main stages. In the first stage, kilometer-sized planetesimals were formed from the accumulation of dust in the primordial solar nebula. In the second stage, bodies that reached sufficient mass continued growing through gravitational accretion forming numerous protoplanets isolated in their accretion zones. The third stage was characterized by oligarchic growth of protoplanets fed by planetesimals located between their feeding zones. In the last stage mutual perturbations between planetary embryos and Jupiter caused collisions, mergers, and the dynamical excitation of the small bodies that were not accreted by the embryos. As a result those planetesimals within the region which would become the asteroid belt never managed to accumulate into a single planet (Safronov 1979, Wetherill 1989, Bottke et al. 2002b).

During the early stages of the solar system some asteroids in the main belt also experienced different degrees of thermal processing (Shukolyukov and Lugmair 2002). Short-lived radionuclides (e.g., ^{26}Al) are considered the most likely heat source for heating of asteroids (Shukolyukov and Lugmair 2002, McCoy et al. 2006). Depending on the amount of energy available some bodies could have reached temperatures high enough to produce melting and differentiation. In other cases if the body did not accumulate enough energy only some degree of thermal metamorphism occurred. The time of formation as well as the heliocentric distance seem to have played an important role in the degree of thermal processing experienced by asteroids in the main belt. It has been suggested that asteroids in the inner main belt could form much more quickly than those in the outer part, and therefore could accreted more short-lived radionuclides. On the other hand, objects in the outer main belt are thought to have formed in a volatile-rich environment, which would have prevented large scale melting events (McSween et al. 2002). This is a plausible scenario that could explain the current taxonomic distribution of asteroids in the main belt, where the most primitives objects tend to be located in the outer region, while those that experienced thermal metamorphism and melting dominate the inner region of the belt.

Collisions between objects also contributed to shape the present asteroid belt. The fragmentation of an asteroid can lead to the formation of an asteroid family, i.e., a population of asteroids that share similar proper orbital elements as well as similar spectral features (Davis et al. 2002, Zappalà et al. 2002). In most cases, the parent body from which the family originated is shattered, however asteroid families can also originate from a large cratering event that doesn't disrupt the parent body (e.g. the Vesta and Pallas families). There are around 20 reliably recognized families, which represent approximately 35% of the asteroids in the main belt (Zappalà et al. 2002). These families can be found along the entire asteroid belt, in the inner part (e.g. the Vesta family), central part (e.g. the Koronis family) and outer part (e.g. the Themis family).

The strong gravitational influence of Jupiter had a significant impact on the orbital distribution of asteroids in the main belt, due to the creation of mean-motion resonances. Orbital resonances occur when the mean orbital period of the asteroid is an integer fraction of the orbital period of Jupiter. These resonances often destabilize the orbits of asteroids, causing objects to gradually move into different orbits. As a result, there are regions in the main belt, known as Kirkwood gaps, where the density of asteroids is smaller (Nesvorný et al. 2002).

1.2 The asteroid-meteorite connection

Over the last three decades spectroscopic observations of asteroids, as well as laboratory measurements, have established links between many asteroid spectral types and meteorite groups (e.g., McCord et al. 1970, Chapman and Salisbury 1973, Gaffey and McCord 1978, Gaffey et al. 1993, Burbine 1998, Binzel et al. 2002, Vernazza et al. 2008). In total, our meteorite collections could represent between 100 to 150 distinct parent bodies (Burbine et al. 2002). Meteorites can be broadly classified into two types: those that experienced heating but not melting (chondrites) and those that experienced melting and differentiation (achondrites, primitive achondrites, stony-irons, irons) (Burbine et al. 2002). Figure 1.2 shows the classification of major meteorite classes, clans, groups and subgroups from Weisberg et al. (2006).

Chondrites are divided into 15 distinct groups on the basis of their mineralogy, bulk chemical composition, and oxygen isotopic compositions. For some of these meteorites different objects have been postulated as possible parent bodies. For example, ordinary chondrites have been generally linked to either S-complex or Q-type asteroids (e.g., Gaffey et al. 1993, Binzel et al. 2002, Burbine et al. 2002, Nakamura et al. 2011). Ordinary chondrites are the most common type of meteorite to fall on Earth, representing about 80% of all meteorites (Burbine et al. 2002). These meteorites are composed of abundant chondrules containing olivine, pyroxene, plagioclase feldspar, and glass with lesser amounts of an olivine-rich matrix, metal, and sulfides (Weisberg et al. 2006). They are divided into three subgroups (H, L, LL) based on the abundance of Fe and the ratio of metallic Fe (Fe^0) to oxidized Fe (FeO) (Weisberg et al. 2006). Spectrally, ordinary chondrites exhibit the two absorption bands characteristic of olivine-pyroxene mixtures. Vernazza et al. (2008) estimated average $ol/(ol + px)$ ratios of 58.8%, 64.2% and 75.1% for H, L and LL respectively. Ordinary chondrites can also show a wide range in petrologic types (3-6), with 3 being the least altered, and 6 being the most thermally altered (Burbine et al. 2002, Weisberg et al. 2006). Figure 1.3 shows the petrologic types for each chondrite group.

Another group of chondrites that has been linked to specific parent bodies are the enstatite chondrites (also known as E-type chondrites). These meteorites formed under highly reducing nebular conditions. They are dominated by Fe-poor silicates and oldhamite (CaS) (Weisberg et al. 2006). Based on mineralogy and bulk chemistry, they are divided into EH (high Fe) and EL (low Fe) groups. The EH and EL chondrites range in petrologic type from EH3 to EH5 and from EL3 to EL6. Enstatite (MgSiO_3) is the major silicate mineral in the chondrules. Chondrule olivine rarely occurs in low petrologic types (EH3 and EL3) chondrites and is essentially absent in the higher petrologic types. Additionally, they contain a variety of sulfide, metal, and nitride phases that are not found in other chondrite groups (Weisberg et al. 2006). Spectrally, E-type chondrites have relatively featureless spectra because of the absence of Fe^{2+} in their silicates, and exhibit red spectral slopes. E-type chondrites have been proposed as meteoritic analogs to the M asteroids (Gaffey and McCord 1978), which also exhibit relatively featureless spectra, and red spectral slopes. Some of these asteroids are believed to be the remaining cores of differentiated objects that suffered catastrophic disruptions.

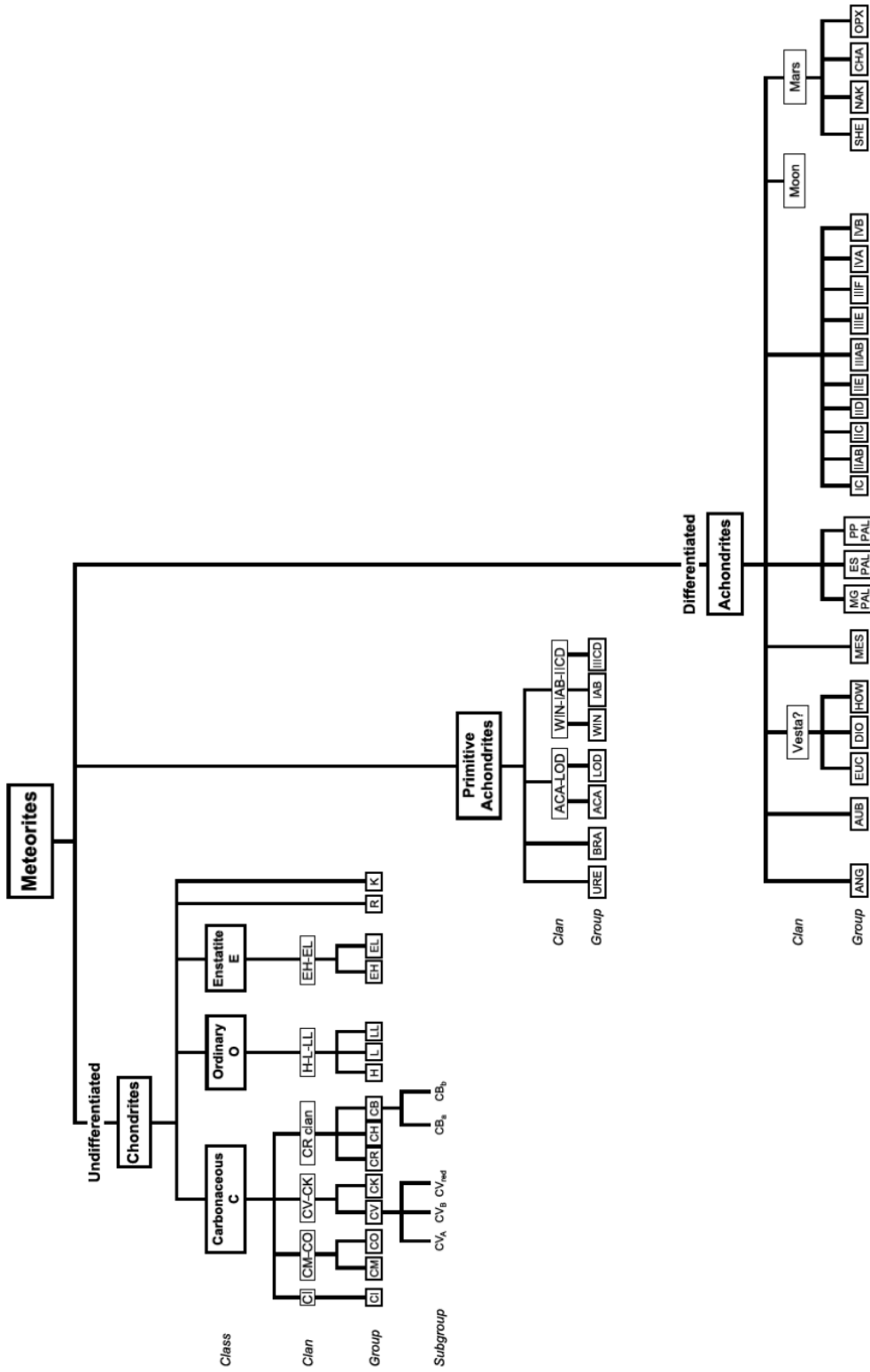
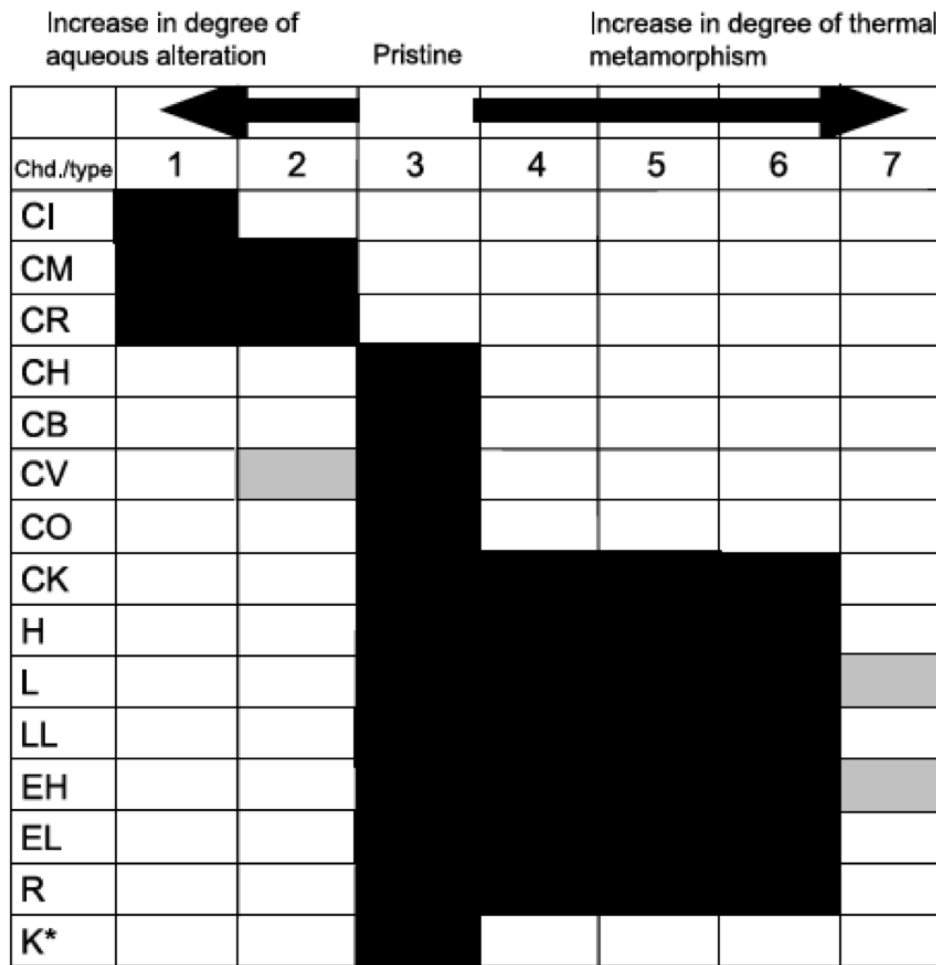


Figure 1.2: Meteorite classification chart. URE (ureilite), ACA (acapulcoite), LOD (lodranite), ANG (angrite), AUB (aubrite), BRA (brachinite), WIN (winonaite), HED (howardite-eucrite-diogenite), MES (mesosiderite), MG PAL (main-group pallasite), ES PAL (Eagle Station pallasite), PP PAL (pyroxene pallasite), SHE (shergottite), NAK (nakhilite), CHA (chassignite), OPX (orthopyroxenite). Figure from Weisberg et al. (2006).



*Grouplet.

Chd. = chondrite group.

Figure 1.3: Diagram showing the petrologic types for each chondrite group. Figure from Weisberg et al. (2006).

Another example are the carbonaceous chondrites, which are among the most pristine materials of the solar system, having bulk compositions close to that of the solar photosphere. They are composed mainly of silicates, oxides and sulfides, while the minerals olivine and serpentine are characteristic (Weisberg et al. 2006). Most of them contain minerals that have undergone some degree of aqueous alteration, as well as large amounts of carbon and organic compounds. The petrologic type of these meteorites can range from 1 to 6, with 1 being the most aqueously altered. Spectrally, carbonaceous chondrites have low visible albedos, relatively strong UV features, a number of weak features between 0.6 and 0.9 μm (in some cases), and relatively featureless spectra from 0.9 to 2.5 μm (Burbine et al. 2002). Some carbonaceous chondrites, in particular CM chondrites have been generally linked to the C-type asteroids because they also have low albedos and relatively featureless spectra (Burbine 1998).

In contrast to chondrites, the differentiated meteorites represent a much larger number of

meteorite parent bodies. The differentiated meteorites range from those that experienced only limited differentiation (primitive achondrites) to those (achondrites, stony-irons, irons) that were produced by extensive melting, melt migration, and fractional crystallization (Burbine et al. 2002). Among the primitive achondrites, the acapulcoites and lodranites share similar mineralogies, largely composed of olivine and pyroxene with minor plagioclase, NiFe metal and troilite (Weisberg et al. 2006). Spectrally, they are dominated by olivine and pyroxene and they have been associated to S-complex asteroids (Gaffey et al. 1993, McCoy et al. 2000).

Among the fully differentiated achondrites, howardites, eucrites and diogenites (known as the HED clan) were the first group of meteorites linked to a specific asteroid (McCord et al. 1970). Eucrites are basalts, which are thought to have formed in shallow magma chambers within the crust of their parent body, where they slowly crystallized. Diogenites are orthopyroxene cumulates, thought to have originated in the lower crust or upper mantle of their parent body (Delaney et al. 1984). Many HED meteorites are impact-produced monomict (same composition) or polymict (different composition) breccias (Weisberg et al. 2006). Howardites are polymict breccias containing eucritic and diogenitic components (Delaney et al. 1984). HEDs have similar Fe/Mn ratios in their pyroxenes, and similar whole-rock oxygen-isotopic compositions, suggesting a close genetic relationship (Consolmagno and Drake 1977, Wiechert et al. 2004). Similarities in the mineralogical compositions of the HEDs and the surface mineralogy of asteroid (4) Vesta, as determined by both ground based and spacecraft VNIR spectroscopy, suggest that the HEDs are impact ejecta of this asteroid (e.g., McCord et al. 1970, Consolmagno and Drake 1977, Binzel and Xu 1993, Gaffey 1997, Keil 2002, Reddy et al. 2012b, De Sanctis et al. 2012). There are also a few eucrites that have oxygen isotopic ratios that differ from the other HEDs, implying that they could have originated in a parent body different from Vesta (Yamaguchi et al. 2002).

Iron meteorites are composed primarily of metallic Fe with usually 5-20 wt% Ni. Spectrally, they have relatively featureless spectra with red spectral slopes and moderate albedos. These meteorites are thought to be the fragments of the cores of differentiated parent bodies that have been shattered by impacts. They have been linked to M-type asteroids since both types of objects share similar spectral characteristics (Cloutis et al. 1990).

To establish a link between meteorites and possible parent bodies can be a difficult task. One of the main reasons is because meteoritic parent bodies could undergo different processes after the meteorites were ejected. Endogenic processes (e.g., heating, metamorphism, partial or complete melting, and aqueous alteration) and exogenic processes (e.g., regolith processes, excavation during cratering events, and space weathering) can alter the spectra of asteroidal surfaces. As a result, the spectral properties of asteroids change causing a mismatch between asteroid and meteorite spectra. In addition, other factors like compositional differences, terrestrial weathering of the meteorites and differences between the asteroidal and laboratory environments (e.g., temperature, grain size, phase angle) also complicate the unambiguous identification of potential parent bodies.

1.3 Spectroscopy as a remote sensing technique

Spectroscopy is the study of the electromagnetic spectrum as emitted, reflected or scattered from a solid, liquid, or gas (Clark 1999). When referring to spectroscopy of airless planetary bodies like the Moon or asteroids, it is common to talk about reflectance spectra, which can

be considered as the ratio of reflected sunlight to incident sunlight as a function of wavelength (e.g., Bus et al. 2002, Gaffey et al. 2002). Reflectance spectra are obtained by ratioing the raw flux measurements at each wavelength for the object to a reference standard. For ground-based observations of solar system objects the reference standard is a solar analog star (i.e., a star with a similar spectral type to the Sun), and thus the resulting ratio corresponds to the relative reflectance spectrum of the object (Gaffey et al. 2002).

Among the different techniques available to study asteroids, visible-near-infrared (VNIR) spectroscopy (~ 0.35 to $3.5 \mu\text{m}$) is a powerful tool to derive information about the minerals that constitute the surface of these objects. There are several reasons for observing asteroids in this spectral region. At VNIR wavelengths the Earth's atmosphere is relatively transparent compared to either the ultraviolet or mid-infrared. Moreover, there are some minerals that exhibit absorption features in this wavelength range, and therefore they are diagnostic of the presence, chemistry and abundance of those minerals on the surface of the asteroid (Gaffey et al. 1989). The origin of absorption features in reflectance spectra involves the presence of transition metal cations in some common rock-forming minerals. An atom consists of a nucleus surrounded by electrons occurring in different atomic orbitals (Fig. 1.4), transition metals are those elements whose atoms have partially filled $3d$ or $4f$ atomic orbitals. These elements comprise scandium, titanium, vanadium, chromium, manganese, iron, cobalt, nickel and copper (Burns 1993).

All transition metals have five $3d$ orbitals having identical energies in an isolated ion, however the energy levels split when the atom is located in a crystal field. The origin of the splitting of the $3d$ orbital energy levels can be described using crystal field theory (CFT) (Burns 1993). It can be explained briefly as follows: When a transition metal cation is in a crystal structure surrounded by ligands, either anions (e.g., O^{2-} , OH^- , SO_4^{2-}) or dipolar molecular species (e.g., H_2O , NH_3), the effect of a non-spherical electrostatic field on the five degenerate d orbitals is to lower the degeneracy by splitting the d orbitals into different energies about the centre of gravity of the unsplit energy levels (Burns 1993, Clark 1999, Geiger 2004). The manner and extent to which the five-fold degeneracy is removed depends on the type, positions and symmetry of ligands surrounding the transition metal. As an example let's consider a transition metal cation in an octahedral field (Fig. 1.5), i.e., surrounded by six identical ligands located at the corners of an octahedron. In structures containing octahedral coordination sites, electrons in all five $3d$ orbitals are repelled by the negatively charged anions or dipolar ligands, and the baricenter of the degenerate levels is raised. Since lobes of the e_g (d_z^2 and $d_{x^2-y^2}$) orbitals (Fig. 1.4) point towards the ligands, electrons in these two orbitals are repelled to a greater extent than those of the three t_{2g} (d_{xz} , d_{yz} and d_{xy}) orbitals that are directed between the ligands. Therefore, the energy levels of the d orbitals are different and they split, whereby those of the e_g orbitals lie at a higher relative energy level than those of the t_{2g} orbitals (Burns 1993, Geiger 2004). This example is represented by an energy level diagram in Fig. 1.6. This splitting of the orbital energy states makes it possible for an electron to move from a lower to a higher level by absorbing a photon with an energy equal to the energy difference between the states. Thus, when light interacts with a mineral containing transition metal cations only photons of specific wavelengths are absorbed, producing the absorption features seen in the spectra (Burns 1993, Clark 1999, Geiger 2004). Since the crystal field varies from mineral to mineral, the amount of splitting will also vary. Hence, the same ion (like Fe^{2+}) will produce different absorptions, allowing the identification of specific minerals from spectroscopy.

Absorption bands can also be the result of charge transfers, or inter-element transitions. In

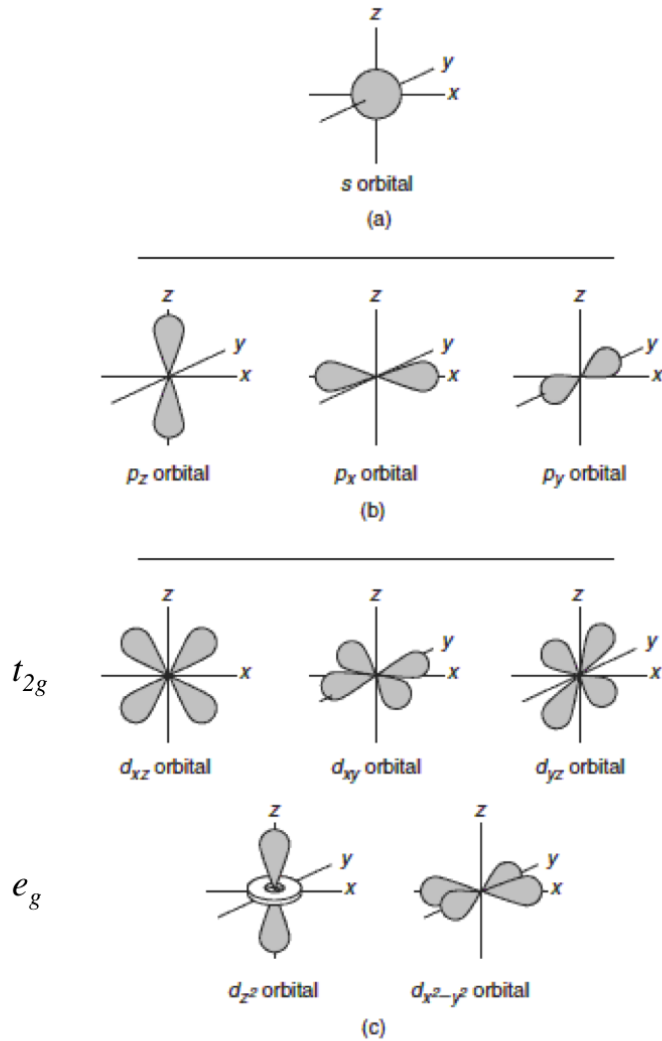


Figure 1.4: Representation of the electron clouds for atomic s (a), p (b) and d (c) orbitals. The d orbitals have been classified into two groups, t_{2g} and e_g , on the basis of spatial configuration with respect to the cartesian axes. Reproduced from <http://www.education.com/study-help/article/atomic-orbitals>.

this case the absorption of a photon will cause an electron to move between ions or between ions and ligands (Clark 1999). These generally occur at shorter wavelengths and are significantly stronger than the crystal-field absorptions. For instance, an overlapping series of such charge-transfer features produces the strong blue-ultraviolet absorption edges in many silicate and oxide minerals (Clark 1999, Burns 1993).

Not all minerals have diagnostic absorption features at VNIR wavelengths. However, a number of the most abundant and important minerals found in asteroids and meteorites do exhibit such diagnostic features. The most important set are crystal field absorptions arising from the presence of bivalent iron (Fe^{2+}) located in specific crystallographic sites in mafic (Mg- and Fe-bearing) silicate minerals (Gaffey et al. 2002). Among these minerals, olivine

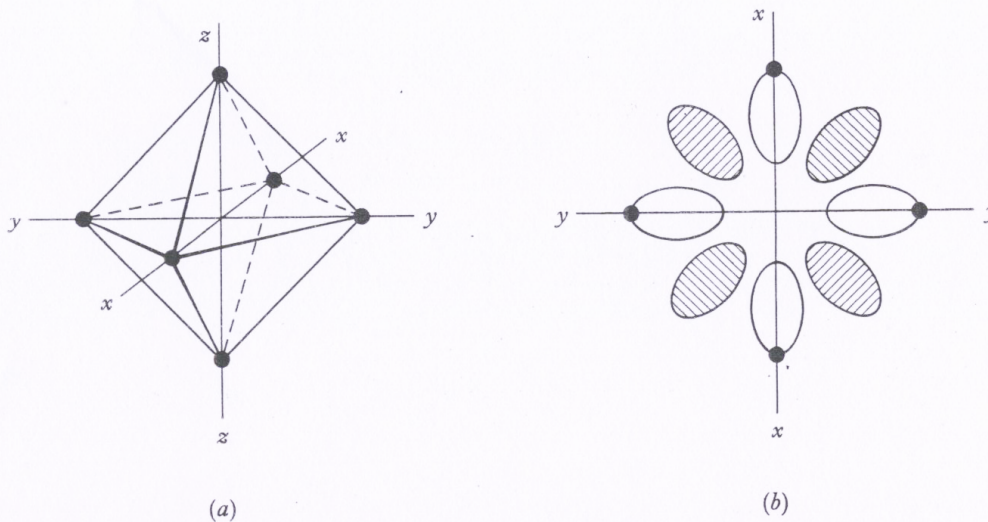


Figure 1.5: Orientation of ligands and d orbitals of a transition metal ion in octahedral coordination. (a) Orientation of ligands with respect to the cartesian axes; (b) the $x - y$ plane of a transition metal ion in an octahedral crystal field. The d_{xy} orbital is crosshatched; the $d_{x^2-y^2}$ orbital is open; ligands are black circles. Reproduced from Burns (1993).

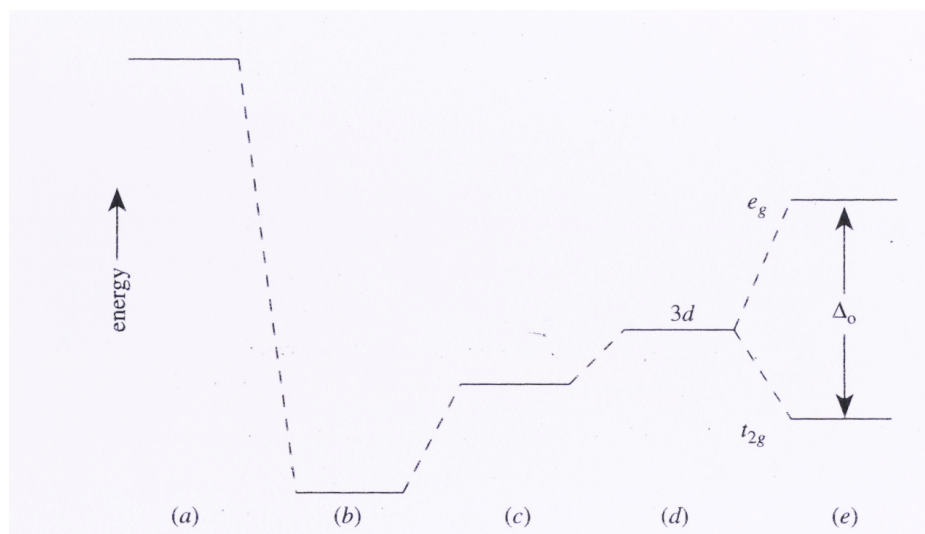


Figure 1.6: Relative energies of a transition metal $3d$ orbitals in octahedral coordination. (a) Energy levels of a free cation; (b) electrostatic attraction between the cation and anions; (c) repulsion between anions and electrons on the cation other than those in $3d$ orbitals; (d) repulsion between anions and the $3d$ electrons; (e) splitting of $3d$ orbital energy levels (Δ_0) in an octahedral field. Reproduced from Burns (1993).

and pyroxene are commonly present as the major silicate phases in asteroids, and their spectral properties dominate the reflectance spectra of some particular taxonomic classes (Gaffey and McCord 1978, Gaffey et al. 1993, 2002).

Olivine is a magnesium iron silicate that exists as a solid solution series, where the ratio of

magnesium and iron varies between the two end members: forsterite (Mg_2SiO_4) and fayalite (Fe_2SiO_4). Compositions of olivine are given as molar percentages of forsterite (Fo) and fayalite (Fa). Minerals of this group crystallize in the orthorhombic system with isolated silicate tetrahedra, meaning that olivine is a nesosilicate. The atomic structure of olivine is hexagonal, consisting of an array of oxygen ions with half of the octahedral sites occupied with magnesium or iron ions and one-eighth of the tetrahedral sites occupied by silicon ions (Burns 1993). The atomic structure of olivine is shown in Figure 1.7. There are three distinct oxygen sites (marked O1, O2 and O3), two distinct metal sites (M1 and M2) and only one distinct silicon site.

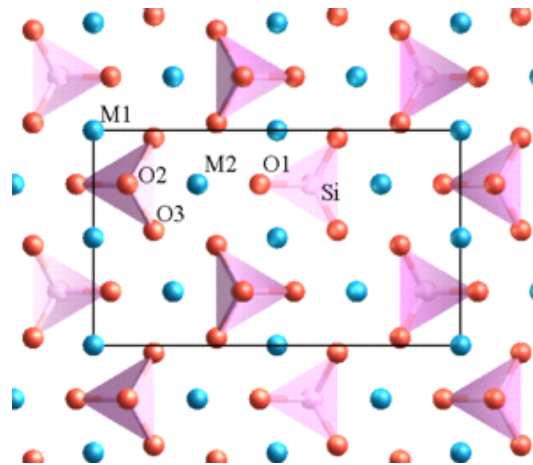


Figure 1.7: The atomic scale structure of olivine. Oxygen is shown in red, silicon in pink, and magnesium/iron in blue. A projection of the unit cell is shown by the black rectangle. Reproduced from <http://en.wikipedia.org/wiki/Olivine>.

The primary diagnostic feature in the spectrum of olivine is composed of three overlapping bands and is centered near $\sim 1 \mu\text{m}$. This composite band is attributed to electronic transitions of Fe^{2+} occupying both the M1 and M2 crystallographic sites (Burns 1993). Figure 1.8 shows an example of the reflectance spectrum of olivine ($\text{Fo}_{70}\text{Fa}_{30}$).

Pyroxenes are a group of inosilicate minerals found among metamorphic and igneous rocks. Their structure consists of single chains of silica tetrahedra and they crystallize in the monoclinic and orthorhombic systems. Monoclinic pyroxenes are referred to as clinopyroxenes, and mostly form a solid solution series between diopside ($(\text{Ca},\text{Mg})\text{Si}_2\text{O}_6$) and hedenbergite ($(\text{Ca},\text{Fe})\text{Si}_2\text{O}_6$). Orthorhombic pyroxenes are called orthopyroxenes and form a solid solution series between ferrosilite $\text{Fe}_2\text{Si}_2\text{O}_6$ and enstatite $\text{Mg}_2\text{Si}_2\text{O}_6$. The four main end members of the pyroxene quadrilateral, along with Ca end member wollastonite ($\text{Ca}_2\text{Si}_2\text{O}_6$) are shown in Figure 1.9.

Pyroxenes can be divided into low-calcium pyroxenes (LCP) and high-calcium pyroxenes (HCP). LCP are conventionally defined as having less than 11 mol% wollastonite (Wo) and make up a solid solution between enstatite (En) and ferrosilite (Fs), including minerals such as bronzite and hypersthene (Adams 1974, McSween and Huss 2010). HCP (≤ 50 mol% Wo) make up a solid solution between diopside and hedenbergite, including augite (Adams 1974, McSween and Huss 2010).

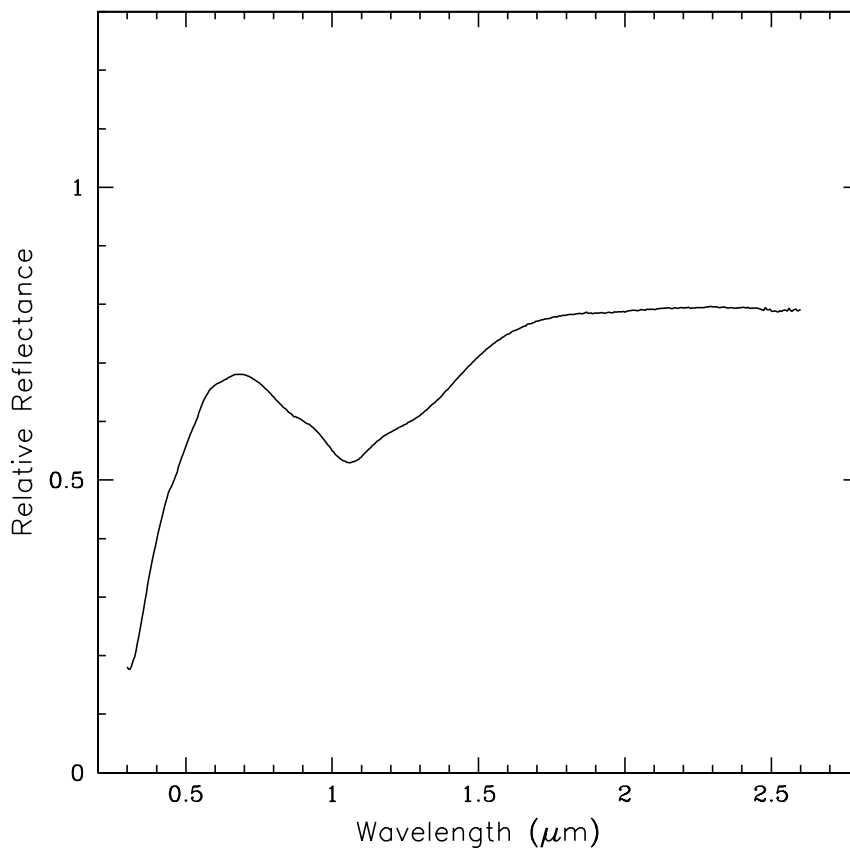


Figure 1.8: Reflectance spectrum of olivine (Fo₇₀Fa₃₀) from Brown University RELAB facility.

Pyroxenes have two absorption bands at $\sim 1 \mu\text{m}$ (Band I) and $\sim 2 \mu\text{m}$ (Band II) that are associated with crystal field transitions in Fe^{2+} , which preferentially occupies the M2 site (Burns 1993). Figure 1.10 shows an example of the reflectance spectrum of orthopyroxene (En₂₅Fs₇₅).

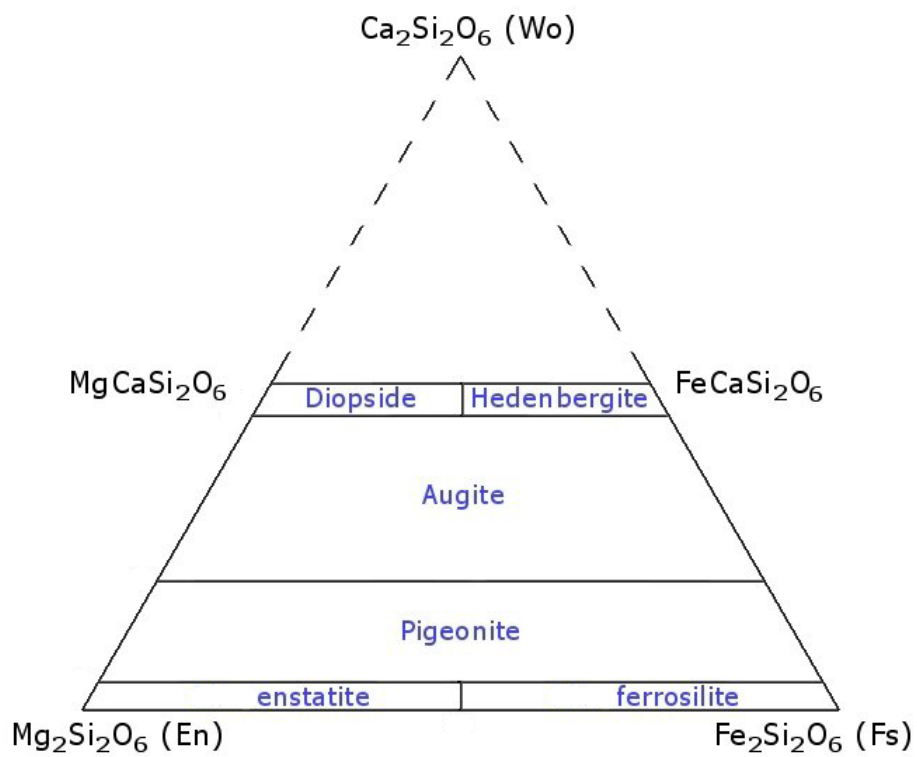


Figure 1.9: The pyroxene quadrilateral, showing the end members of the pyroxene group, along with Ca end member wollastonite (Wo). Reproduced from <http://geology.about.com/od/minerals/ig/pyroxenes/pyxquad.htm>.

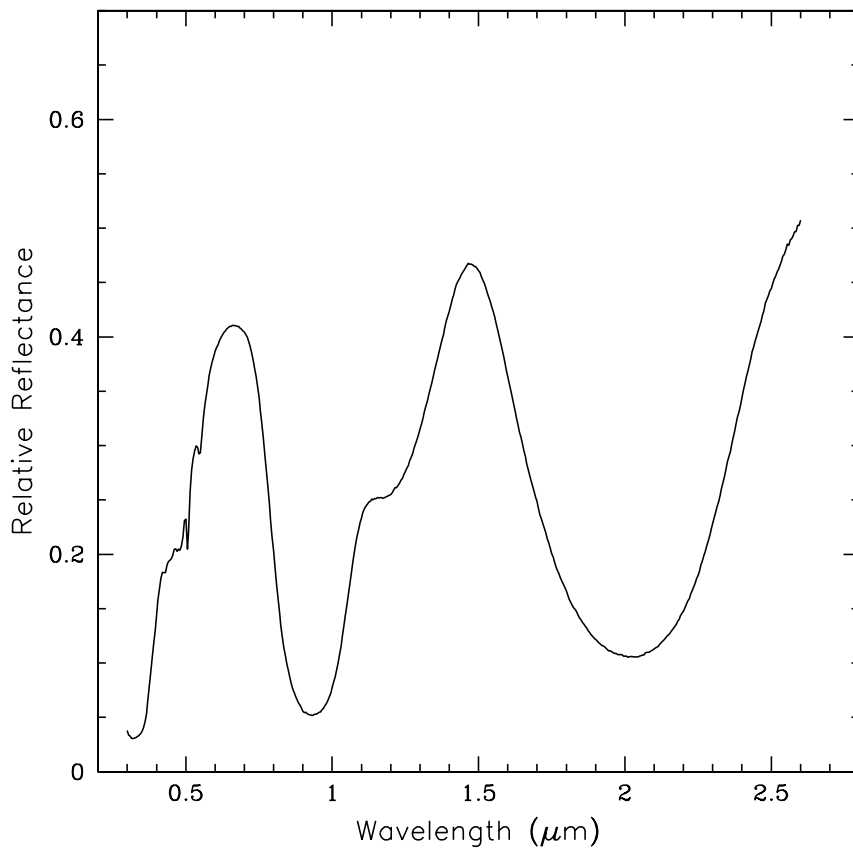


Figure 1.10: Reflectance spectrum of orthopyroxene (En₂₅Fs₇₅) from Brown University RELAB facility.

1.4 Laboratory spectral calibration

The relationship between spectral band parameters measured from reflectance spectra and mafic mineral compositions was first outlined by Adams (1974, 1975) and revisited by King and Ridley (1987) and Cloutis and Gaffey (1991). These spectral band parameters are shown in Figure 1.11 for the NIR spectrum of a S-complex asteroid. This spectrum exhibits two absorption bands characteristics of olivine-orthopyroxene assemblages, one near $1 \mu\text{m}$ (Band I) and the other near $2 \mu\text{m}$ (Band II). The spectral band parameters are: band centers, calculated by dividing out the linear continuum and fitting an n-order polynomial over the bottom third of each band; band areas, which are calculated as the areas between the linear continuum and the data curve; the band area ratio (BAR) given by the ratio of the area of Band II to that of Band I; band depths, which are measured from the continuum to the band center and given as percentage depths, and the spectral slope, which is determined from the fitted continuum across Band I, i.e., a straight line tangent to the reflectance peaks from ~ 0.7 to $\sim 1.55 \mu\text{m}$.

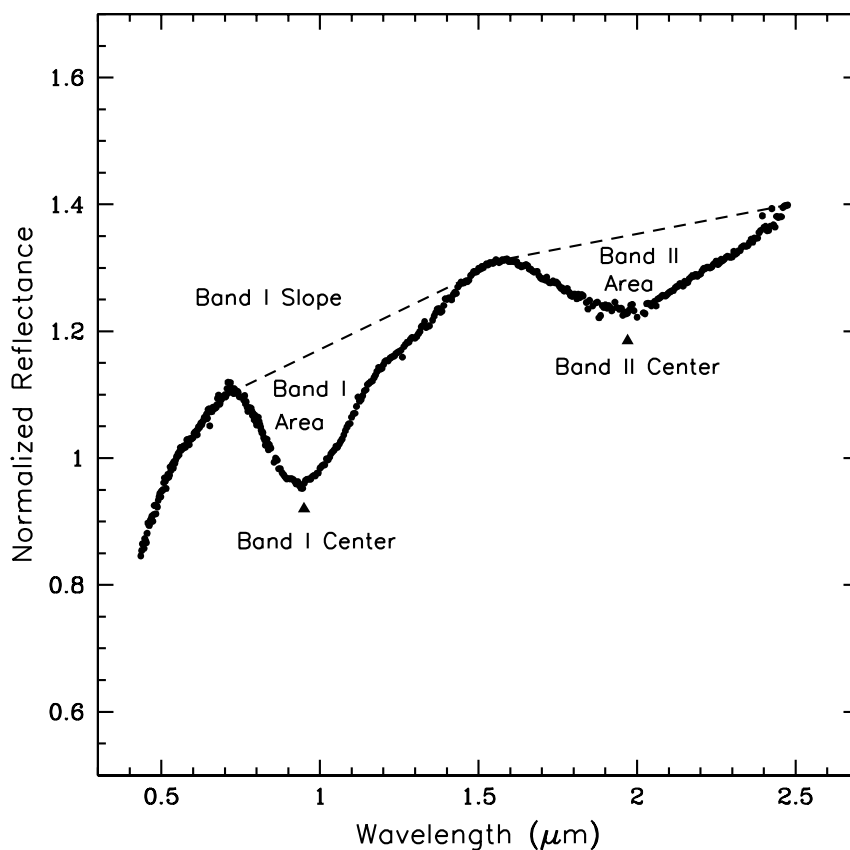


Figure 1.11: Reflectance spectrum of a S-complex asteroid. Spectral band parameters are indicated.

Using NIR diffuse spectral reflectance, King and Ridley (1987) investigated apparent wavelength shifts as a function of mineral chemistry in the Fe/Mg olivine series from Fo₁₁ to Fo₉₁. They found that the composite 1 μm band in olivine moves to longer wavelengths as the Fe²⁺ content increases. Similarly, LCP show a well-defined relationship between absorption band positions and composition, as both Band I and Band II positions move to longer wavelengths with increasing molar iron content (Adams 1974, 1975, Cloutis and Gaffey 1991). This shift in the wavelength position of both bands is explained by CFT, and is due to the effects of substituting the larger Fe²⁺ cation into the crystallographic site of the smaller Mg²⁺ cation, resulting in changes in the crystal structure and thus in the crystal fields and the electronic transitions which produce these absorption features (Burns 1993). For calcic clinopyroxenes, increasing Ca²⁺ content also shifts both band centers to longer wavelengths. In this case this occurs due to the effects of replacing the smaller Fe²⁺ cation by the larger Ca²⁺ cation. The relationship between band center positions and Fe²⁺/Ca²⁺ content for orthopyroxenes and clinopyroxenes is shown in Fig. 1.12. This BandI-BandII plot is useful to determine the type of pyroxene present on the surface of basaltic asteroids. As an example, in Fig. 1.12 we also plotted the measured band centers for three basaltic NEAs (Fig. 1.13) studied by Sanchez et al. (2013).

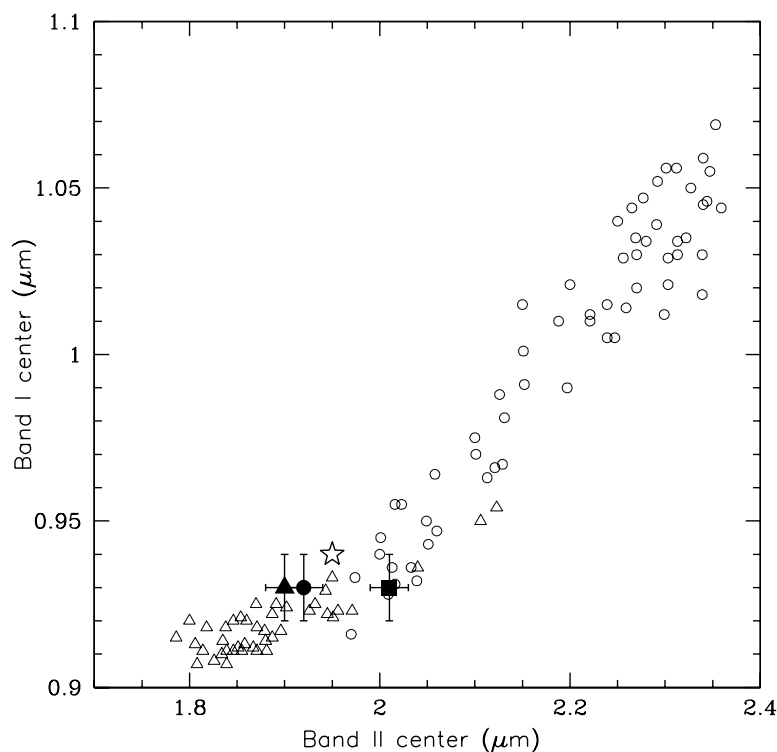


Figure 1.12: Plot of Band I center vs. Band II center for 4055 Magellan (filled circle), 164121 (2003 YT1) (filled triangle), and 5407 (1992 AX) (filled square). Open triangles represent measured band centers for orthopyroxenes from Adams (1974), open circles correspond to measured band centers for clinopyroxenes from Cloutis and Gaffey (1991). For comparison we plotted the band centers of (4) Vesta (star symbol) measured by Reddy et al. (2012d). Figure from Sanchez et al. (2013).

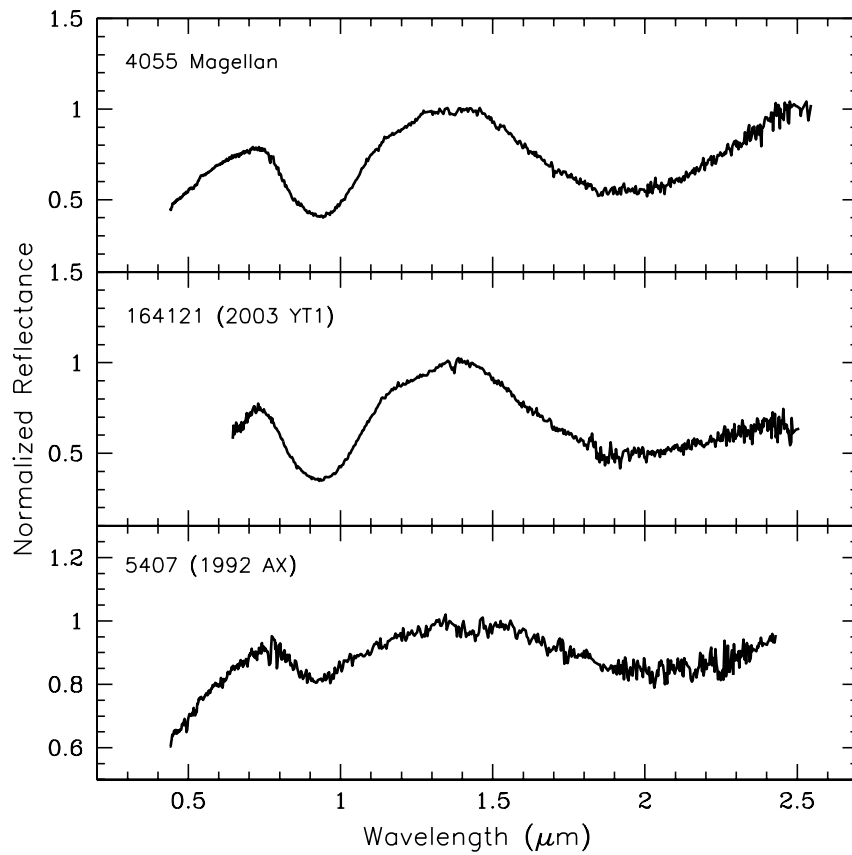


Figure 1.13: VNIR spectra of asteroids 4055 Magellan (top panel) and 5407 (1992 AX) (bottom panel), and NIR spectrum of 164121 (2003 YT1) (middle panel). All spectra are normalized to unity at 1.4 μm . Figure from Sanchez et al. (2013).

Gaffey et al. (2002) developed a set of equations for determining pyroxene chemistries (Fs and Wo contents) from their Band I and Band II centers. These formulas were derived from the spectra of terrestrial minerals. Following a similar procedure, Burbine et al. (2007) analyzed the reflectance spectra of a group of HED meteorites, and derived formulas for determining the average Fs and Wo content from the wavelength position of band centers. These formulas are:

$$Fs = 1023.4 \times (BI) - 913.82 \quad (1.1)$$

$$Fs = 205.86 \times (BII) - 364.3 \quad (1.2)$$

$$Wo = 396.13 \times (BI) - 360.55 \quad (1.3)$$

$$Wo = 79.905 \times (BII) - 148.3 \quad (1.4)$$

where BI and BII are the Band I and Band II center respectively and are given in μm . The resulting values of Fs and Wo are given as the molar contents. Burbine et al. (2007) found that averaging the compositions (Fs and Wo) separately from the Band I and II centers slightly reduces the uncertainty. These equations can be used for determining pyroxene compositions of basaltic asteroids. This is shown in Fig. 1.14 where we plotted the calculated molar contents of Wo vs. Fs for basaltic NEAs (4055) Magellan, 5407 (1992 AX) and 2003 YF1 from Sanchez et al. (2013), along with the measured values for HED meteorites from Mittlefehldt et al. (1998).

From the analysis of visible/near-infrared spectra of 48 ordinary chondrite meteorites, Dunn et al. (2010) found a relationship between measured FeO in mafic minerals and Band I center. They determined that there is a correlation between molar content of Fa in olivine and Band I center, and molar content of Fs in pyroxene and Band I center. These correlations are described by second order polynomial fits given by

$$Fa = -1284.9 \times (BI)^2 + 2656.5 \times (BI) - 1342.3 \quad (1.5)$$

$$Fs = -879.1 \times (BI)^2 + 1824.9 \times (BI) - 921.7 \quad (1.6)$$

where BI is the Band I center given in μm . With these equations it is possible to determine mafic silicate compositions (Fa in olivine, Fs in pyroxene) in olivine-orthopyroxene mixtures. This can be seen in Fig. 1.15 where we plotted the calculated molar contents of Fa vs. Fs for NEAs 241662 (2000 KO44), 19764 (2000 NF5) and 138404 (2000 HA24) (Fig. 1.16) from Sanchez et al. (2013), along with the values for LL, L and H ordinary chondrites from Nakamura et al. (2011).

In spectra of olivine-orthopyroxene mixtures the combined absorption features near 1 and 2 μm are also sensitive to the relative abundance of olivine and pyroxene. The BAR is commonly used to estimate olivine and pyroxene abundances in asteroids and meteorites (Cloutis et al. 1986). The linear relationship between BAR and the ratio of pyroxene to olivine + pyroxene ($px/(ol + px)$) was first recognized by (Cloutis et al. 1986), who expressed this relationship as

$$BAR = 0.024 \times (px/(ol + px)) - 1.25 \quad (1.7)$$

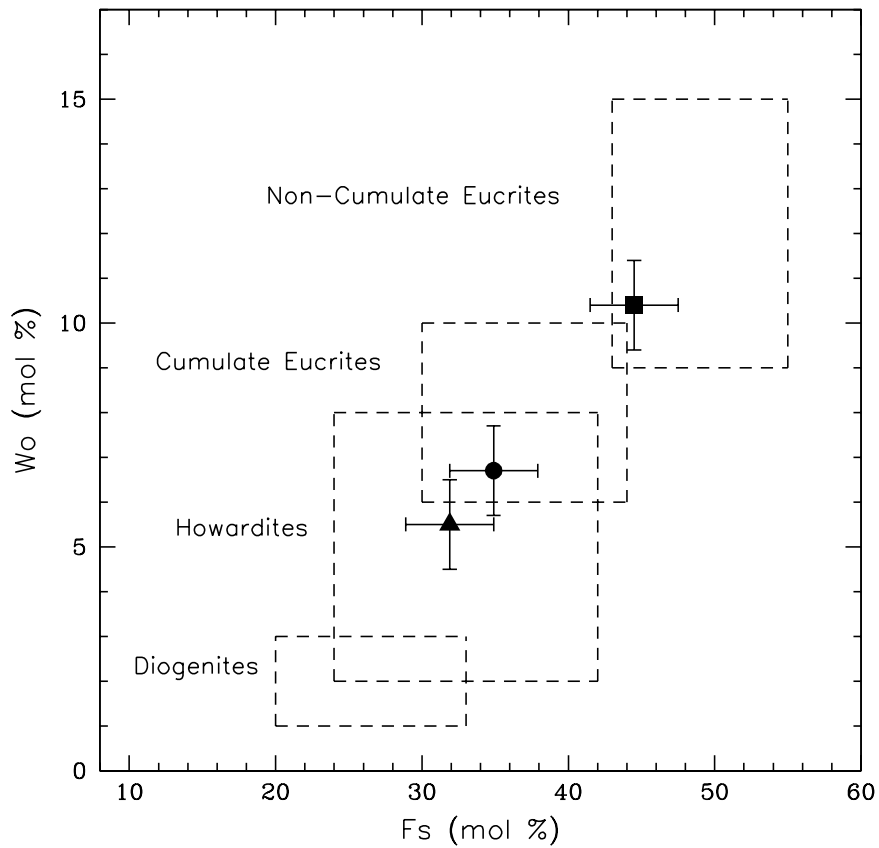


Figure 1.14: Molar contents of Wo vs. Fs for NEAs 4055 Magellan (filled circle), 164121 (2003 YT1) (filled triangle), and 5407 (1992 AX) (filled square). The error bars correspond to the values determined by Burbine et al. (2007), 3 mol % for Fs and 1 mol % for Wo. The approximated range of pyroxene chemistries for howardites, non-cumulate eucrites, cumulate eucrites, and diogenites from Mittlefehldt et al. (1998) are indicated as dashed-line boxes. Figure from Sanchez et al. (2013).

This equation was used by Cloutis et al. (1986) to derive BAR values from mixtures of known mineral proportions, and can be expressed as

$$px/(ol + px) = 0.417 \times BAR + 0.052 \quad (1.8)$$

in order to derive mineral abundances from the calculated BARs of asteroid spectra (Gastineau-Lyons et al. 2002). However, because the Cloutis et al. (1986) regression was based on simple mixtures of olivine and orthopyroxene, the presence of more than one pyroxene can complicate spectral interpretations of asteroids made using this calibration (Gaffey et al. 1993).

Dunn et al. (2010) derived a new calibration for determining mineral abundances ($ol/(ol + px)$) in olivine-orthopyroxene mixtures. This linear regression is expressed as

$$ol/(ol + px) = -0.242 \times BAR + 0.728 \quad (1.9)$$

where the $ol/(ol + px)$ is expressed as a decimal. This relationship was obtained from the analysis of ordinary chondrites and hence can be applied to asteroids with similar mineralogies.

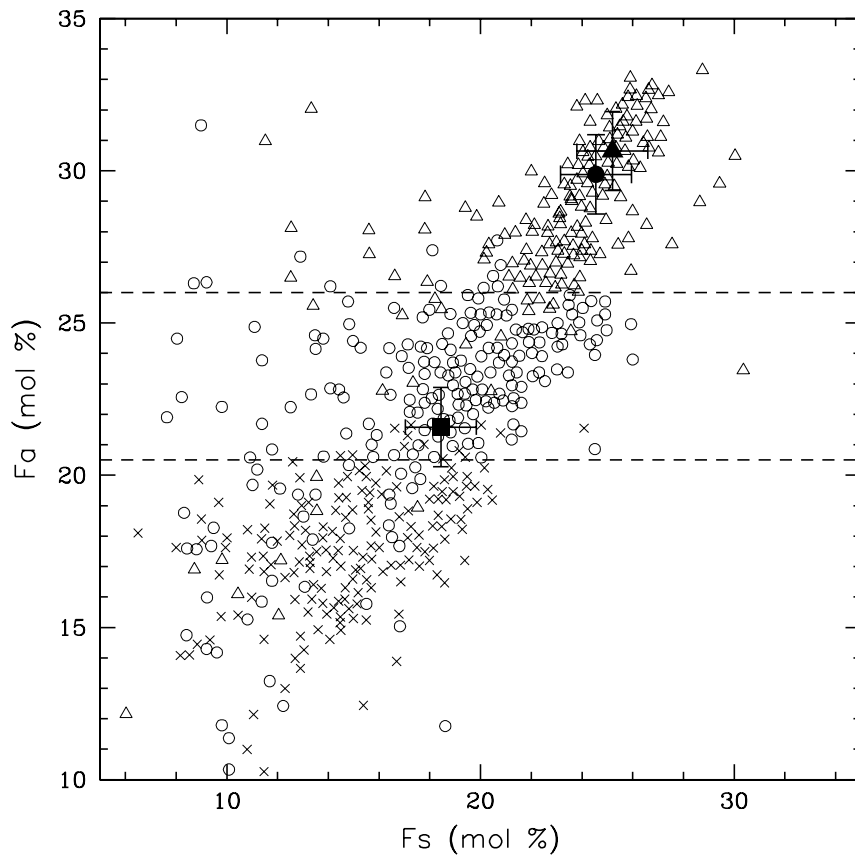


Figure 1.15: Molar contents of Fa vs. Fs for NEAs 241662 (2000 KO44) (filled triangle), 19764 (2000 NF5) (filled circle), 138404 (2000 HA24) (filled square) from Sanchez et al. (2013), along with the values for LL (open triangles), L (open circles) and H (x) ordinary chondrites from Nakamura et al. (2011). The error bars correspond to the values determined by Dunn et al. (2010), 1.4 mol % for Fs and 1.3 mol % for Fa. The horizontal dashed-lines represent the approximate boundaries for LL, L, and H ordinary chondrites. Figure from Sanchez et al. (2013).

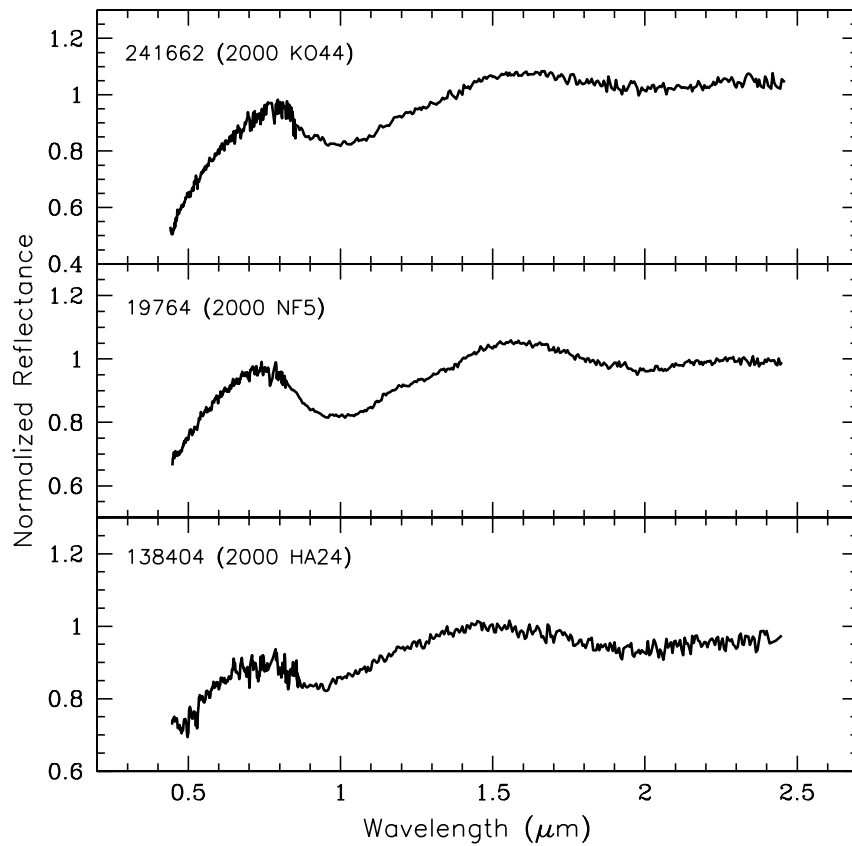


Figure 1.16: VNIR spectra of asteroids 241662 (2000 KO44) (top panel), 19764 (2000 NF5) (middle panel) and 138404 (2000 HA24) (bottom panel) from Sanchez et al. (2013). NIR asteroid spectra were obtained from the NEOSR survey (<http://smass.mit.edu/minus.html>). All spectra are normalized to unity at 1.4 μm . Figure from Sanchez et al. (2013).

1.5 Taxonomic classification of asteroids

The taxonomic classification of asteroids is based on shared observational parameters like spectral slope, color, albedo and band depth (e.g., Chapman et al. 1971, Tholen 1984, Gaffey et al. 1993, Bus and Binzel 2002a,b, DeMeo et al. 2009). Although taxonomic classification does not provide information about the mineralogy and composition of the asteroid, it is a useful tool to identify objects of particular interest that could be later studied using more diagnostic techniques. Currently, the most widely used taxonomic system for asteroids are the Tholen taxonomy (Tholen 1984) and the SMASSII spectral taxonomy (Bus and Binzel 2002a,b). The Tholen system is based on the Eight-Color Asteroid Survey data (ECAS, Zellner et al. 1985) and was developed from the analysis of 978 asteroids, using broad band photometry (0.31 μm to 1.06 μm) in combination with albedo measurements. This scheme includes 14 taxonomic types. The SMASSII classification stands for the Small Main-Belt Asteroid Spectroscopic Survey that includes spectroscopic observation (0.44 μm to 0.92 μm) of 1447 asteroids. This survey produced spectra of a higher resolution than ECAS, and was able to resolve weak spectral features in the spectra (Bus and Binzel 2002a,b). A total of 26 classes are defined, based on the identification of specific spectral features. The SMASSII taxonomic system was used by us in Sanchez et al. (2013) to classify a group of NEAs and Mars crossers (MCs) asteroids using visible spectra obtained with the New Technology Telescope (NTT) at La Silla, Chile, and with the 2.2 m telescope at Calar Alto, Spain. The visible spectra of these asteroids are shown in Figures 1.17 and 1.18. Both the Tholen and SMASSII (some times referred as Bus system) taxonomies were based on Principal Component Analysis (PCA), a multivariate statistical technique that reduces the dimensionality of the data to a small number of factors (components) related to the causes of the variations (Tholen 1984, Smith et al. 1985, Bus and Binzel 2002a,b, DeMeo et al. 2009). These classification systems were based on visible data, in part because only during the last decade sufficient high-quality NIR spectral data became available to extend the classification to the near-infrared wavelengths.

Two of the most common systems used to classify asteroids using VNIR data are those introduced by Gaffey et al. (1993) and more recently by DeMeo et al. (2009). Gaffey et al. (1993) combined data from the survey program of Bell et al. (1988) that covered the wavelength range of 0.8 to 2.5 μm , together with data from the ECAS to provide spectral coverage over the 0.35-2.5 μm interval. In total they analyzed 39 asteroids previously classified as S-type by Tholen (1984). Under Gaffey's system the S-population is divided into seven main compositional subgroups designated S(I)-S(VII). These subgroups range from pure olivine through olivine-pyroxene mixtures to pure pyroxene mixtures, and were derived on the basis of two band parameters, the Band I center and the BAR. Figure 1.19 shows the location of the seven compositional subgroups in a plot of Band I center vs. BAR from Gaffey et al. (1993).

The taxonomic system developed by DeMeo et al. (2009) (Bus-DeMeo taxonomy hereafter), use near-infrared spectral measurements from 0.8 to 2.5 μm obtained with SpeX, the low- to medium-resolution near-IR spectrograph and imager (Rayner et al. 2003), on the 3-meter NASA Infrared Telescope Facility (IRTF) located on Mauna Kea, Hawaii. These spectra were combined with visible wavelength spectra from the SMASS II data set. In total their sample was comprised of 371 objects with both visible and near-IR data covering the wavelength range from 0.44 to 2.5 μm . The Bus-DeMeo taxonomic system is based on PCA and is comprised of 24 classes that include three major complexes (S-, C- and X-complex) and the end members O, Q, R, V, D, K, L, T. The S-complex is subdivided into S, Sa, Sq, Sr and Sv. Figure

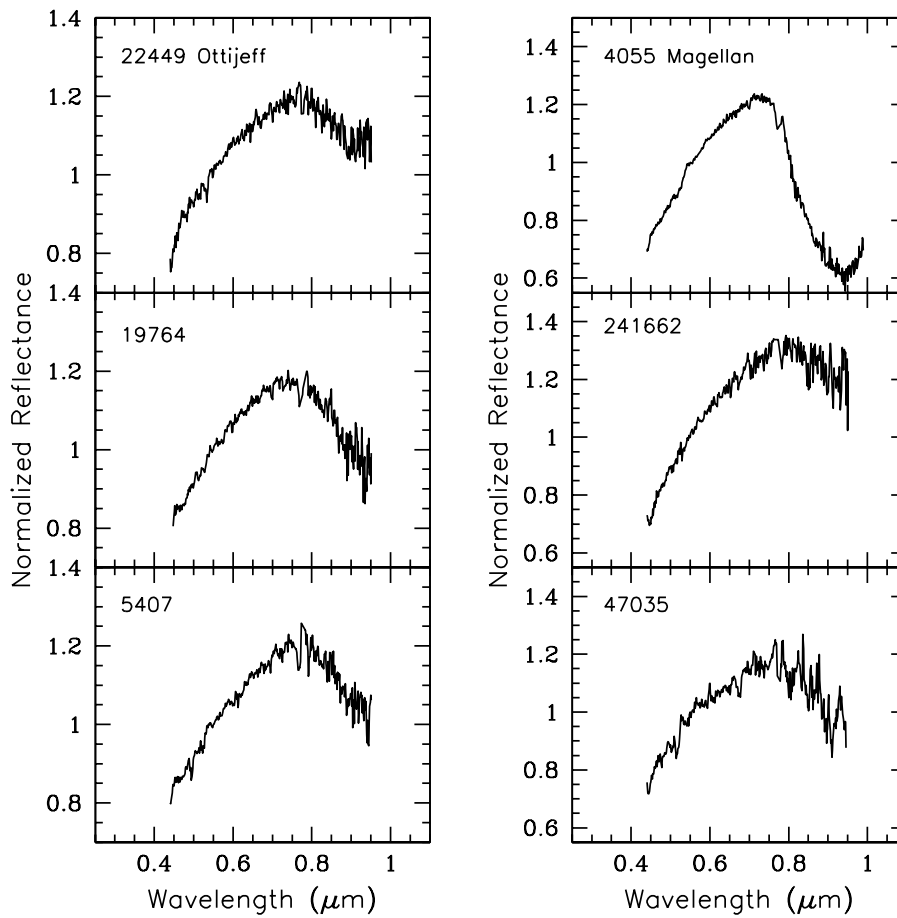


Figure 1.17: Spectra obtained with the NTT. The numerical designation for each asteroid is given. All spectra are normalized to unity at 0.55 μm . Figure from Sanchez et al. (2013).

1.20 shows the Principal Component (PC1') versus the Principal Component (PC2') plotted for the S-complex plus A-, Q-, O-, R-, and V-types of the Bus-DeMeo taxonomy.

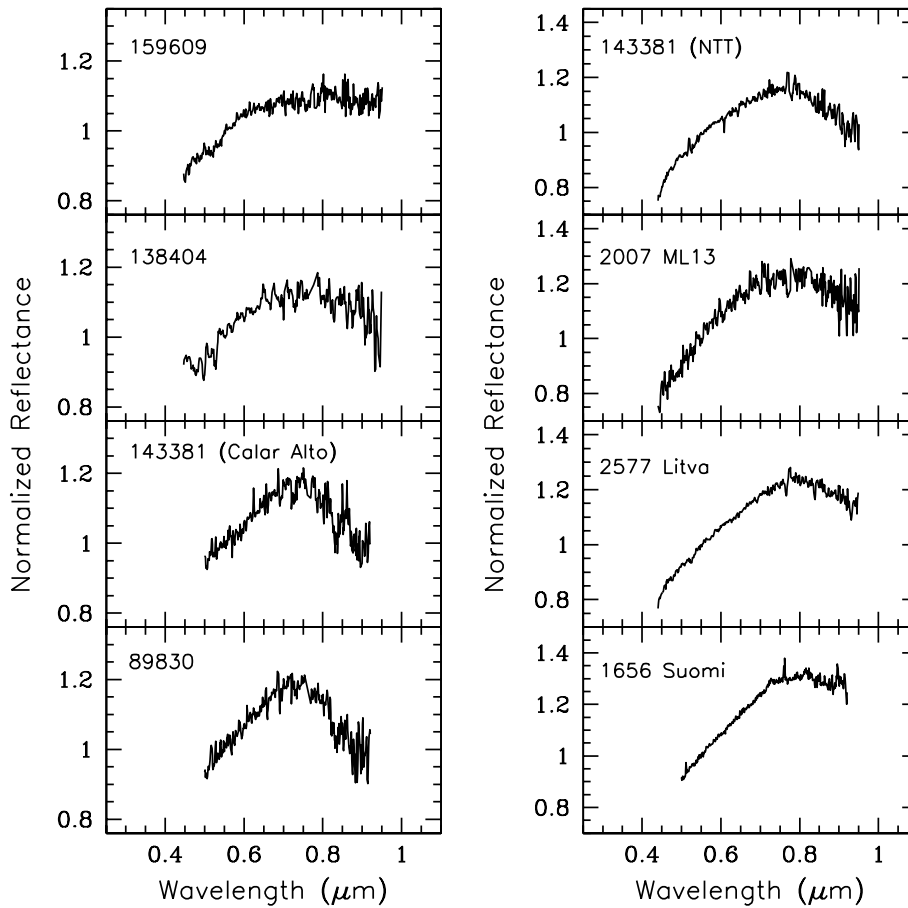


Figure 1.18: Spectra obtained with the NTT and the 2.2 m telescope. The numerical designation for each asteroid is given. All spectra are normalized to unity at $0.55 \mu\text{m}$. Asteroid 143381 (2003 BC21) was observed with both telescopes. Figure from Sanchez et al. (2013).

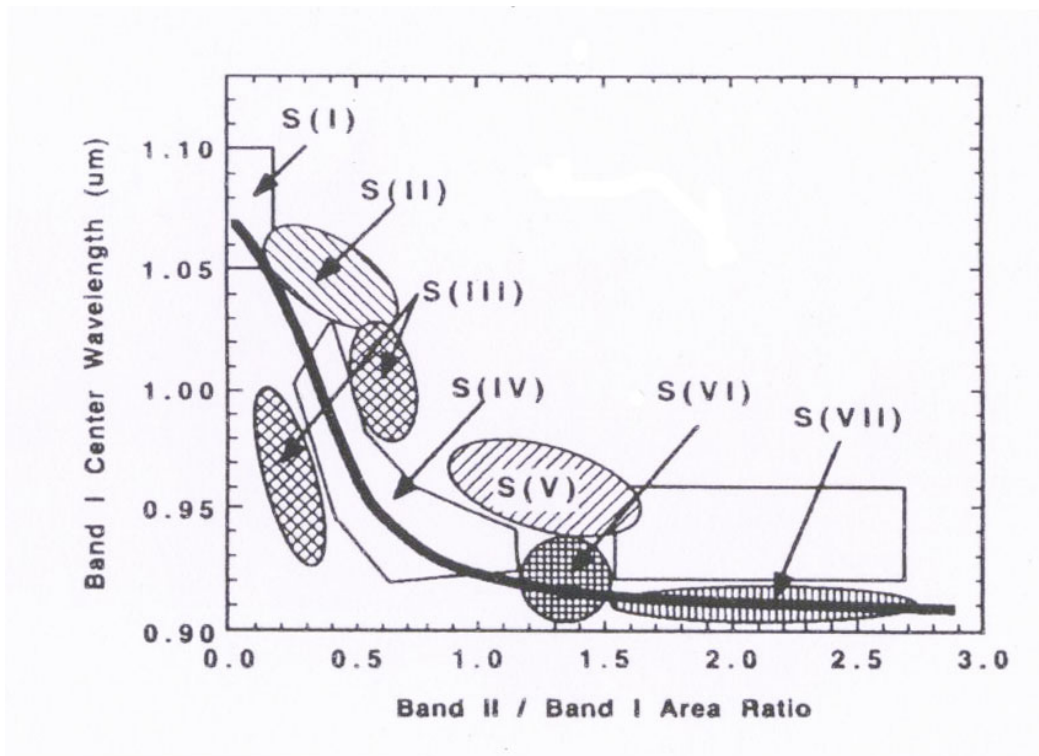


Figure 1.19: Plot of the Band I center vs. BAR from Gaffey et al. (1993). The seven compositional subgroups are indicated. The rectangular region corresponding to the S(I) represents the monomineralic olivine assemblages. The rectangular zone above the S(VII) subgroup includes the pyroxene-dominated basaltic achondrite assemblages. The polygonal region represents the mafic silicate components of ordinary chondrites. The solid line indicates the location of the olivine-orthopyroxene mixing line (Cloutis et al. 1986). Figure from Gaffey et al. (1993).

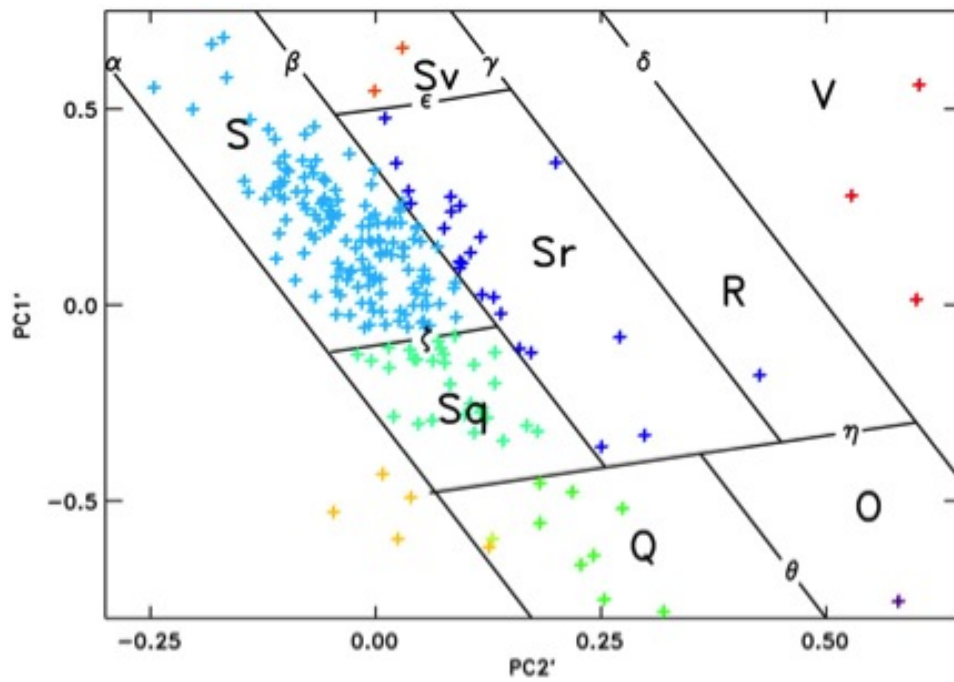


Figure 1.20: PC1' versus PC2' plotted for the S-complex plus A-, Q-, O-, R-, and V-types of the Bus-DeMeo taxonomy. Boundaries chosen for each class are shown and lines are labeled with Greek letters. Figure taken from DeMeo et al. (2009).

1.6 The NEA population

Among the small bodies population, NEAs are defined as asteroids having perihelion distances of ≤ 1.3 AU (Binzel et al. 2002). The accepted origin of these bodies is that asteroids were moved from the main belt through orbital resonances with Jupiter that perturbed the asteroids orbits, moving them into the inner solar system (Michel et al. 1996, Menichella et al. 1996, Rabinowitz 1997, Morbidelli and Nesvorny 1999, Morbidelli et al. 2002).

The NEA population shows a great diversity in terms of taxonomic classification, including almost all classes of asteroids found in the main belt (Binzel et al. 2002). However, this population seems to be dominated by S-complex asteroids (Fig. 1.21). This high proportion of S-complex observed among NEAs is caused in part by a selection effect, due to the fact that S-complex asteroids have higher albedos than C-types (the dominant class among all main-belt asteroids), making them easier to discover. However, even after bias effect corrections are accounted for, S-complex asteroids still remain the dominant taxonomic class among the NEA population, suggesting that some regions in the main belt contribute more than others to the delivery of objects into the inner solar system. This idea is supported by dynamical models (e.g., Morbidelli and Nesvorny 1999, Bottke et al. 2000, 2002a, Morbidelli et al. 2002) that have shown that the 3:1 mean-motion resonance with Jupiter (occurring at ~ 2.5 AU) and the inner asteroid belt (where S-complex are most common) dominate the contributions to the near-Earth population. This region is continuously resupplied with objects that migrate from other parts of the main belt due to the Yarkovsky effect, i.e., anisotropic emission of thermal photons that causes objects to undergo semimajor axis drift, which slowly deliver material to resonances inside the main belt (Bottke et al. 2002c).

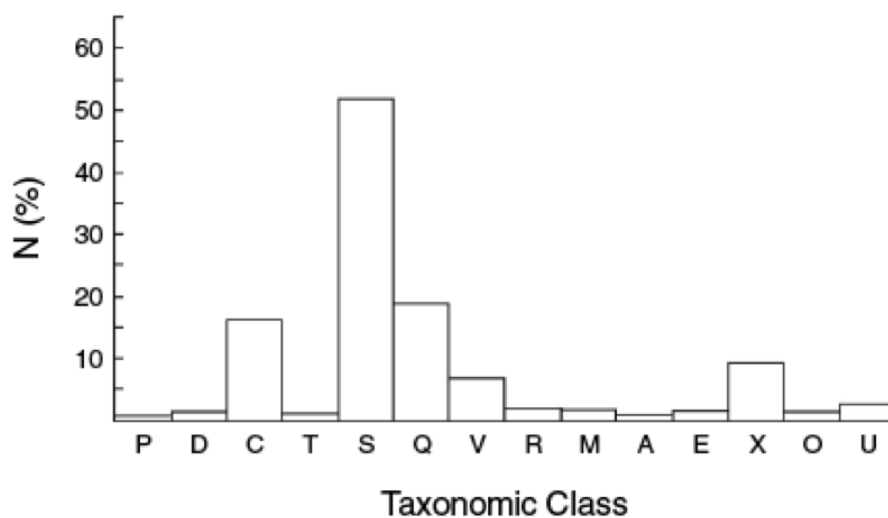


Figure 1.21: Histogram of the relative proportions of measured taxonomic classes for more than 300 NEAs. Figure from Binzel et al. (2002).

Based on their orbital parameters, Shoemaker et al. (1979), divided the NEAs into three subgroups called Amor, Apollo, and Aten asteroids. Amor asteroids are defined as objects

residing outside the orbit of Earth, with a semimajor axis of $a \geq 1$ AU, and a perihelion distance of $1.017 < q \leq 1.3$ AU. Apollo asteroids, are objects having a semimajor axis > 1 AU and $q \leq 1.017$ AU, and Atens asteroids have orbits inside that of Earth ($a < 1$ AU), with an aphelion distance of $Q > 0.983$ AU. Relatively equal numbers of Amor and Apollo asteroids are currently known, and combined they account for $\sim 90\%$ of all known NEAs, while Atens represent only about 8% of the known NEA population (Binzel et al. 2002). In addition to this dynamical classification, some NEAs can be also classified as potentially hazardous asteroids (PHAs), which are defined as objects whose minimal orbital intersection distance (MOID) with Earth is smaller than 0.05 AU, and have a diameter of at least 150 m. Because of the size of these objects, capable of causing significant damage in the event of impact, and due to their close approaches to the Earth, different surveys like the Near-Earth Asteroid Tracking (NEAT) search program are devoted to find them, and to accurately determine their orbital elements.

1.7 Asteroid space weathering

Space weathering is the term commonly used to refer to any process that modifies the optical properties, physical structure, or mineralogical properties of the immediate, remotely sensed surface of an airless body (Clark et al. 2002a). The effects of space weathering on many spectra can be seen as reddening of the spectral slopes, spectral darkening and suppression of the absorption bands (Pieters et al. 2000, Hapke 2001, Gaffey 2010). The analysis of returned samples from the Moon and asteroid (25143) Itokawa have shown that the cause of the spectral changes is the presence of submicroscopic metallic iron (SMFe) incorporated into the soil grains (Pieters et al. 2000, Taylor et al. 2001, Noguchi et al. 2011). This SMFe is produced by condensation of vapors created by micrometeorite impacts and/or deposition of iron atoms sputtered off from iron-bearing silicates by solar wind ions (Taylor et al. 2001, Hapke 2001, Clark et al. 2002a). The effects of the SMFe in the vapor condensates on the optical properties of a regolith can be modeled analytically using the reflectance spectroscopy formalism of Hapke (1993). This model is described in detail in Hapke (2001) and has been used by different authors to accurately describe the reflectance spectra of asteroids (e.g., Hapke 2001, Binzel et al. 2001, Clark et al. 2002a, Rivkin et al. 2004). An example can be seen in Figure 1.22 that shows the effect of adding SMFe to a pulverized ordinary chondrite. The addition of a small amount of SMFe (0.025%) to an ordinary chondrite is sufficient to obtain a spectrum similar to that of a typical S-complex asteroid.

Ion irradiation experiments showed that solar wind irradiation can also redden reflectance spectra by creation of nuclear displacements (the sum of the vacancies and the replacements) caused by elastic collisions between ions and target nuclei (Brunetto and Strazzulla 2005, Brunetto et al. 2006). In this case, the increase of the continuum and decrease of the band areas, as well as the darkening of the samples are interpreted as an effect of changing the optical properties of the upper layers of the target, due to ion irradiation (Brunetto and Strazzulla 2005, Brunetto et al. 2006). These results do not contradict the evidence of sputtering of iron from silicates and the deposition of SMFe, since the two processes take place at very different ion fluence: sputtering of iron is relevant for ion fluence higher than 10^{18} ions cm^{-2} , while the formation of displacements caused by ion irradiation occur for ion fluence below 10^{17} ions cm^{-2} (Brunetto and Strazzulla 2005). Figure 1.23 shows the results of one of these ion irradiation experiments for two samples, the Jackson silicates and the ordinary chondrite Epinal

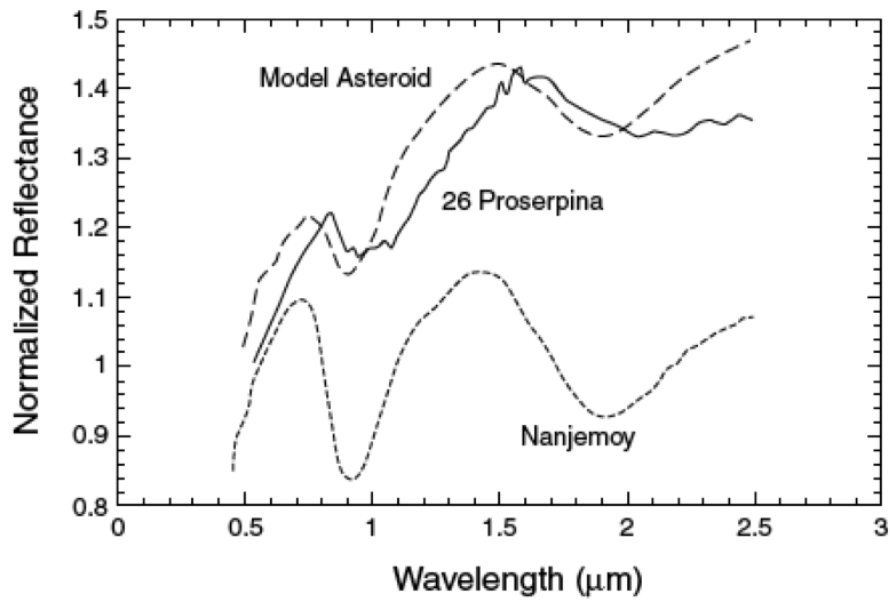


Figure 1.22: Plot showing the effect of adding 0.025% SMFe to a pulverized ordinary chondrite, Nanjemoy. The spectrum depicted with short-dashed lines corresponds to the ordinary chondrite before adding the SMFe. The spectrum represented with long-dashed lines corresponds to the ordinary chondrite after adding the SMFe using the model described by Hapke (2001). The resulting normalized spectrum is compared with that of a typical S-complex asteroid, 26 Proserpina (shown offset for clarity). Figure from Clark et al. (2002a).

before and after ion irradiation. The type of ion, energy and ion fluence used in the experiment are indicated.

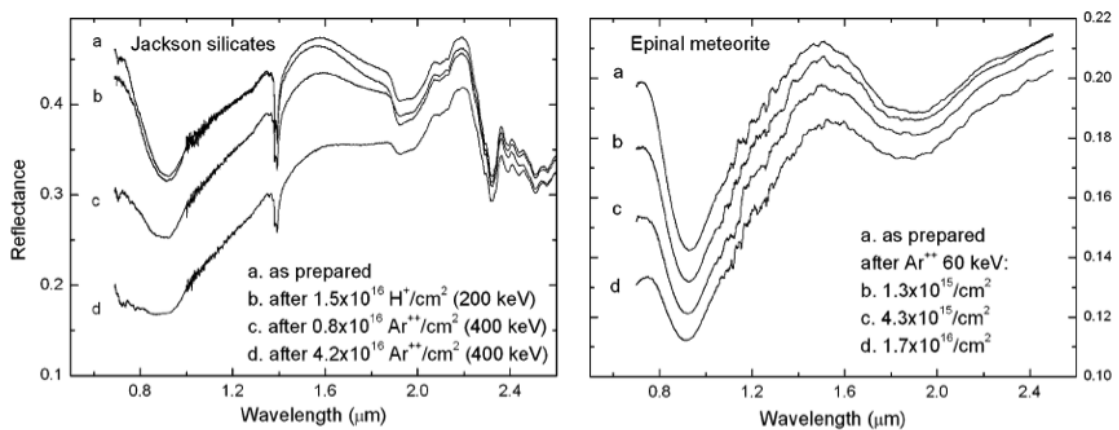


Figure 1.23: Reflectance spectra of Jackson silicates (left) and Epinal chondrite (right) before and after ion irradiation with various ions and fluences, from Brunetto et al. (2006).

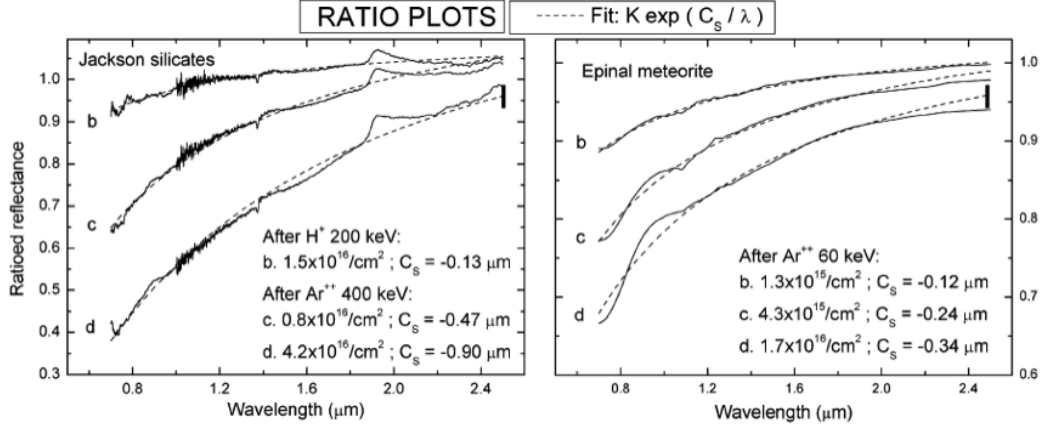


Figure 1.24: Ratio plots of the Jackson silicates and Epinal chondrite spectra; each irradiation step spectrum is divided by the corresponding unirradiated spectrum. Dashed curves are the best fit curves obtained by Eq. (1.10), and the resultant C_S values for each sample are given. Figure from Brunetto et al. (2006).

Brunetto et al. (2006) determined that the effects of space weathering due to ion irradiation can be described by an exponential continuum. They computed the ratio between the reflectance spectra of irradiated and unirradiated samples and then modeled it with an exponential curve given by

$$\text{Ratio} = W(\lambda) = K \exp(C_S / \lambda) \quad (1.10)$$

where λ is the wavelength, K is a scale factor and the parameter C_S is a measure of the effects of space weathering. They called $W(\lambda)$ the weathering function. Figure 1.24 shows the ratio plots of the Jackson silicates and Epinal chondrite spectra, the dashed lines were fitted using Eq. (1.10), the derived C_S values for each sample are included. The weathering function was then incorporated by Brunetto et al. (2006) to the Shkuratov scattering model (Shkuratov et al. 1999) in order to model the spectrum of asteroid (832) Karin. They found that it is impossible to get a good fit of the Karin spectrum without including the space weathering effects.

Brunetto et al. (2006) also found that there is a strong correlation between the C_S parameter and the number of displacements per cm^2 (damage parameter). From their experimental data they were able to create a damage curve that was fitted by

$$C_S = \alpha \ln(\beta d + 1) \quad (1.11)$$

where d is the damage parameter, $\alpha = -0.33 \pm 0.06 \mu\text{m}$ and $\beta = (1.1 \pm 0.5) \times 10^{-19} \text{cm}^2$. The damage curve from Brunetto et al. (2006) is shown in Fig. 1.25.

Since the C_S parameter is strongly related with the d parameter, and each damage value d corresponds to a given exposure time, is possible to estimate an astrophysical timescale for the space weathering process once the ion fluxes and energies of a given astronomical environment are known (Strazzulla et al. 2005, Brunetto et al. 2006). This irradiation timescale is shown in the upper x-axis of Fig. 1.25, and it was calculated at a distance of 2.9 AU from the Sun,

corresponding to the semi-major axis of the orbit of asteroid (832) Karin studied by Brunetto et al. (2006).

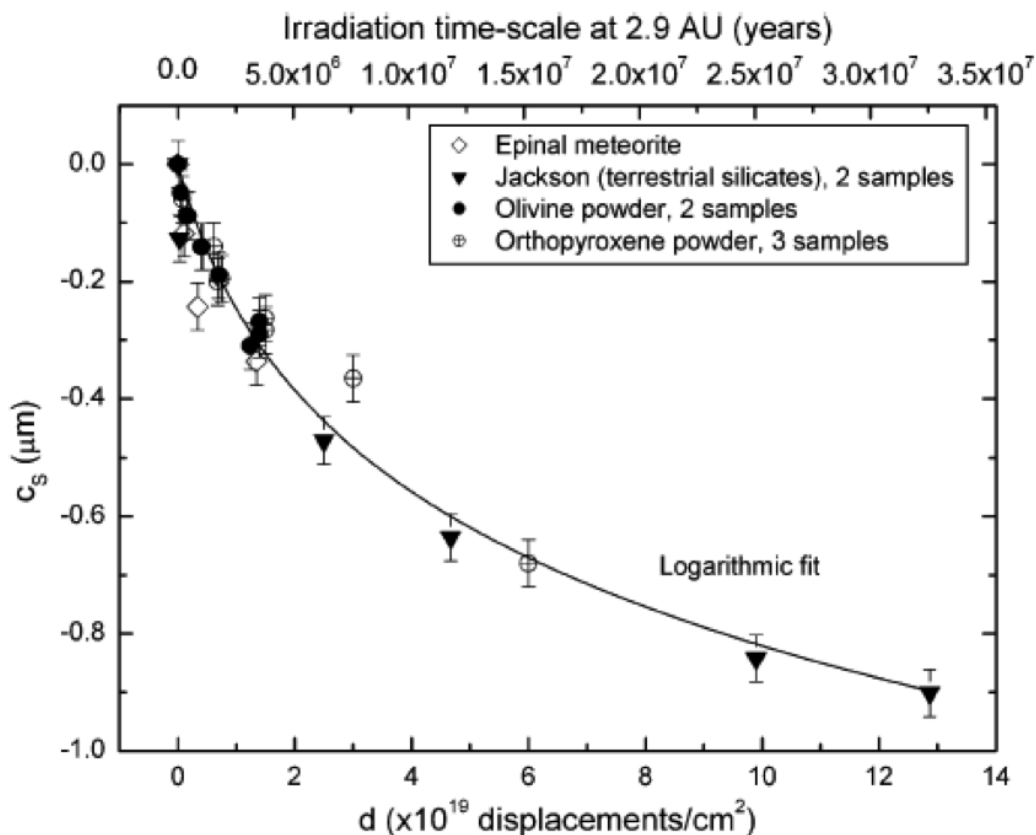


Figure 1.25: The C_s parameter as a function of the damage parameter for the ion irradiation experiments of Brunetto et al. (2006). The upper x-axis gives an estimate of the astrophysical timescale (exposure time) at 2.9 AU. Figure from Brunetto et al. (2006).

For a long time space weathering was invoked to explain the apparent mismatch between ordinary chondrites (the most common type of meteorites on Earth) and S-complex asteroids, which are mineralogically similar to ordinary chondrites and which are one of the most common asteroid type (Pieters et al. 2000, Hapke 2001, Binzel et al. 2001, Clark et al. 2002a, Rivkin et al. 2004). However, it was not until samples from asteroid (25143) Itokawa were brought back to Earth that this hypothesis was finally confirmed (Noguchi et al. 2011). Although these recent studies have shed some light on how space weathering acts on asteroids, there are still open questions about how other factors could modify the space weathering processes on asteroids. For instance, space weathering effects on asteroids seem to depend on the composition of the object (Clark et al. 2002a, Gaffey 2010). Some asteroid types show very little evidence of optical alteration (C-complex), while other types show strong evidence of optical alteration (S-complex). These trends indicate that objects composed of dark, relatively opaque components exhibit minimal space weathering effects while objects composed of bright, relatively transparent components exhibit maximal space weathering effects (Clark et al. 2002a). Only

future sample return missions and in situ explorations of asteroids will help to understand the full range of asteroid space weathering processes.

1.8 Motivation and goals of the thesis

Through out this chapter we have seen how spectral band parameters are useful for different purposes, including mineralogical characterization of asteroids, taxonomic classification, and to derive information about the degree of space weathering experienced by asteroids. However, one must be careful because these spectral band parameters are affected by numerous effects that influence the interpretation of asteroid spectral data. The most significant of these effects are surface temperature and phase angle of the object at the time of observation.

Temperature-induced effects on the spectra of mafic minerals are mainly characterized by shifting the band centers and broadening or narrowing the absorption features (Singer and Roush 1985, Schade and Wäsch 1999, Moroz et al. 2000, Hinrichs and Lucey 2002). While surface temperature variations are considered of minor importance for main-belt asteroids, they may be significant for objects with higher eccentric orbits like NEAs (Roush and Singer 1985, Shestopalov and Golubeva 2000). Furthermore, the spectra of laboratory samples are commonly obtained at room temperature (~ 300 K). Thus, in order to compare the band parameters with those measured for laboratory samples temperature corrections should be applied.

The phase angle (g), is defined as the angular separation between the Sun and the observer as seen from the target. Phase angle induced effects can manifest themselves as phase reddening, which produces an artificial increase (reddening) of the spectral slope and variations in the strength of the absorption bands with increasing phase angle. This effect is explained as the result of the wavelength dependence of the single-scattering albedo (Gradie et al. 1980, Gradie and Veverka 1986, Clark et al. 2002b). Traditionally, the term phase reddening was used to describe only the increase of the spectral slope or continuum, however as will be shown later, as the phase angle increases variations in the absorption bands are also seen. Therefore, in the present work the term phase reddening is extended to refer not only to the increase of the spectral slope, but also to variations in the strength of the absorption bands.

Taken into account the aforementioned, the goal of this investigation is to study temperature-induced effects and phase reddening on NEAs. Due to their proximity, NEAs can exhibit a wide range of phase angles, often much higher than those observed for main belt asteroids. In addition, their highly eccentric orbits can lead to significant variations on the average surface temperature of the body. For these reasons NEAs represent the logical choice for this study. The present work will focus on the analysis of olivine-orthopyroxene assemblages. For that purpose VNIR spectra of S-complex and Q-types asteroids as well as VNIR spectral data of ordinary chondrites are analyzed. Our immediate goals are:

- To study the influence of temperature variations on the spectral band parameters of NEAs observed at different heliocentric distances.
- To quantify the phase reddening effect from VNIR spectra of a group of NEAs and meteorite samples.
- To study the influence of phase reddening on the spectral band parameters and the implications for mineralogical analysis.

- To test the robustness of taxonomic systems when applied to NEAs observed at different phase angles.
- To investigate whether phase reddening could mimic space weathering effect.

2 VNIR spectra of NEAs

2.1 The data set

This kind of study requires obtaining multiple observations of the same asteroids at different heliocentric distances/phase angles, which in terms of allocated observation time can be very difficult to do. For this reason we have decided to combine data from Reddy (2009), DeMeo et al. (2009), Abell et al. (2007), Binzel et al. (2001) and the MIT-UH-IRTF Joint Campaign for NEO Spectral Reconnaissance (NEOSR). All of these observations were conducted with the SpeX instrument (Rayner et al. 2003) on the NASA IRTF.

The IRTF (Figs. 2.1 and 2.2) is a 3.0 m Cassegrain telescope, optimized for infrared observations. This telescope began operations in 1979, and it was first built to support the Voyager missions. Currently the IRTF is the main facility used in the USA for infrared astronomy, and 50% of the observing time is allocated for studies related to solar system objects.

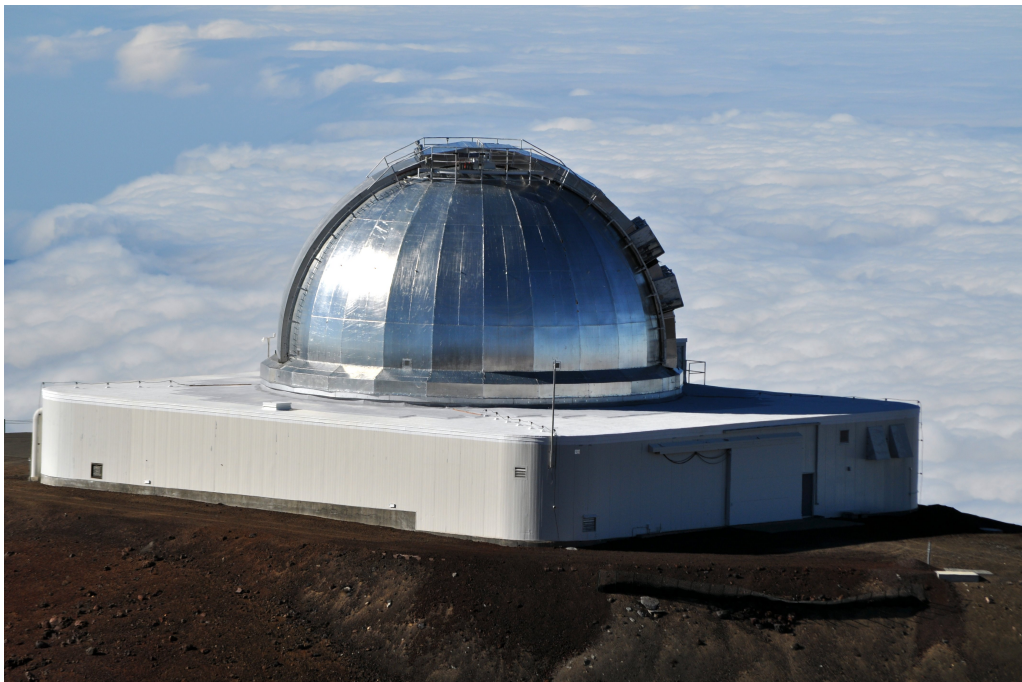


Figure 2.1: NASA Infrared Telescope Facility (IRTF) located at the summit of Mauna Kea, Hawaii, seen from outside. Reproduced from <http://irtfweb.ifa.hawaii.edu/gallery/facility/>.

SpeX (Fig. 2.3) is a medium-resolution 0.7-5.4 μm spectrograph built at the Institute for

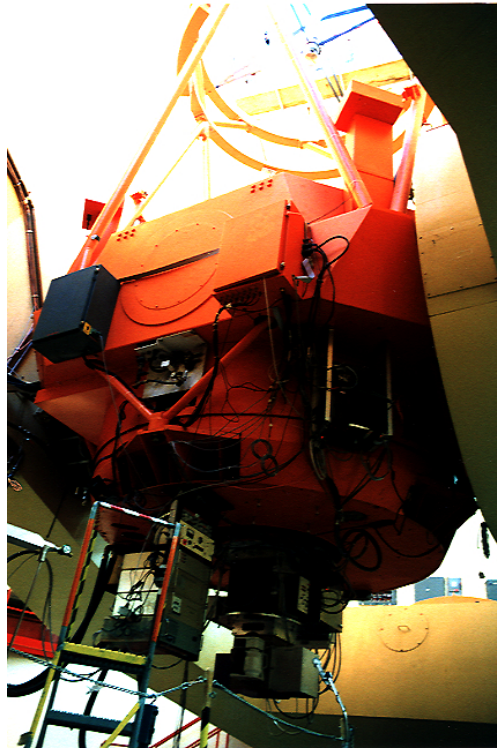


Figure 2.2: NASA Infrared Telescope Facility (IRTF), seen from inside. Reproduced from <http://irtfweb.ifa.hawaii.edu/gallery/facility/>.



Figure 2.3: SpeX instrument. Reproduced from <http://irtfweb.ifa.hawaii.edu/spex/>.

Astronomy, for the NASA IRTF. Among the SpeX science modes, the prism mode, is designed for occultations and faint-object spectroscopy. The $0.7\text{-}2.5\ \mu\text{m}$ region is dispersed by a single prism onto one quadrant of the 1024×1024 Raytheon Aladdin 3 InSb array for fast readout. Since no gratings are required and the spectral resolving power is low (average $R=250$ matched

to a 0".3 slit), spectra can be acquired quickly and efficiently, making it particularly suitable for low-resolution faint-object and time-resolved spectroscopy (Rayner et al. 2003).

The NIR spectra (0.7-2.5 μm) used for this study were obtained using SpeX in its low resolution prism mode with a 0.8" slit width. Typical observations consist of acquiring frames employing a nodding sequence in which the object is alternated between two different slit positions (A and B) following the sequence ABBA. In order to minimize the effects of differential atmospheric refraction the slit is oriented along the parallactic angle during the observations. To correct for telluric water vapor features, and to obtain the relative reflectance, local standard and solar analog stars are observed at airmasses as similar as possible as the asteroids. Flat fields and arc line spectra for each night are also obtained during the observations.

2.2 Data reduction

The data used in the present work were reduced using Spextool (Cushing et al. 2004). Spextool is a spectral extraction and reduction package written in IDL, consisting of a set of semiautomatic routines for reducing SpeX data. This package is driven by a set of graphical user interfaces (GUIs) in which a user specifies various parameters pertinent to the reduction procedures (Cushing et al. 2004). Figure 2.4 shows the main Spextool GUI. Due to its simplicity and because it was specifically designed to reduce data obtained with SpeX, Spextool is often preferred over other packages like IRAF.

As explained by Cushing et al. (2004), the reduction process with Spextool consists of three main steps:

(1) *Preparation of calibration frames.* In this step flat-field exposures are combined and normalized, and an arc image suitable for wavelength calibration is created. The flat-field correction is done in order to remove the variations in the spectra caused by the different sensitivities of the pixels. Multiple flat-field exposures are taken as part of the calibration set and then combined into a master flat to maximize the signal-to-noise ratio. Fig. 2.5 shows a master flat created using Spextool. Before the individual flat-field frames are combined, Spextool computes the median signal level of each frame. It then scales each frame to a common median flux level to compensate for any variations in the flux levels due to changes in the temperature of the lamp filaments. The scaled flat-field exposures are then combined using the statistic chosen by the user (median, mean, or weighted mean). The wavelength calibration of SpeX data is accomplished using argon lines. Similarly to the flat-field exposures, several arc exposures are combined to increase the S/N. Figure 2.6 shows an arc line spectrum acquired with SpeX.

(2) *Spectral extraction.* In this step, target and standard star spectra are extracted and wavelength calibrated. For both cases, target and standard star, the spectral sky background is subtracted. Since the object and the sky are observed simultaneously in each exposure at two different slit positions (Fig. 2.7), it is possible to remove the sky background by subtracting A from B and B from A. The resulting image is then flat-fielded using the normalized flat field created in the first step. The extraction parameters (i.e., extraction apertures and background regions) are defined by the user using the GUI and Spextool extracts the spectra from the sky-subtracted frames. The extracted spectra are wavelength calibrated using the arc frame created in step (1).

(3) *Post-extraction processing.* In this step target spectra are corrected for telluric absorption and then co-added to improve the signal to noise ratio. Observing in the IR is more complex

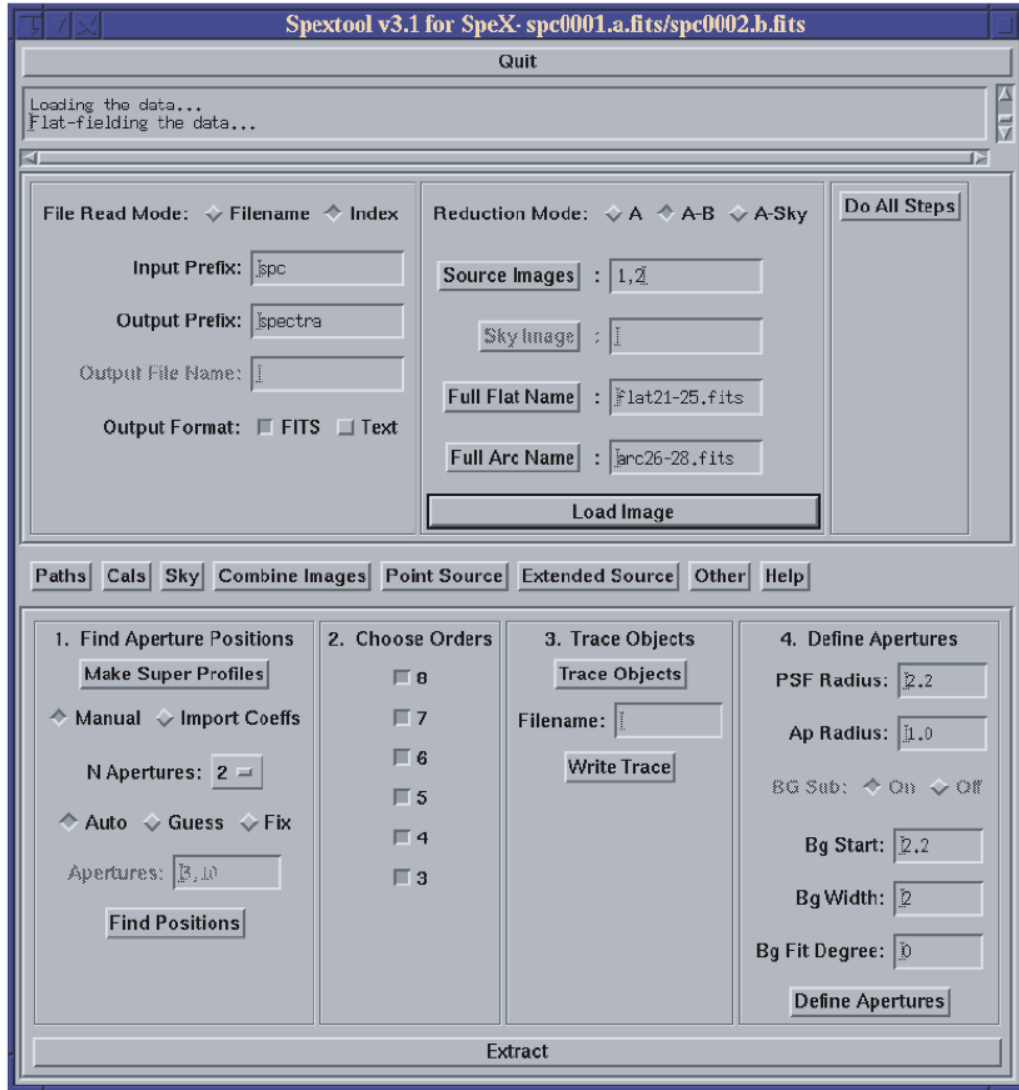


Figure 2.4: Main Spextool GUI. Reproduced from Cushing et al. (2004).

than observing in the optical. The difference arises from a higher and more variable background. Short-ward of $2.3 \mu\text{m}$, the background is dominated by non-thermal emission, mainly by OH and O₂ emission lines. Furthermore, this spectral region contains strong absorption bands due to the presence of H₂O, CO₂ and CH₄ in the atmosphere. Therefore, removing the telluric absorption features in the spectrum of the target is one of the most important steps in the reduction process. This correction is accomplished by dividing the asteroid spectrum by a spectrum of a standard star treated in the same way as the asteroid spectrum. Once the target spectra have been corrected for telluric absorption, the individual spectra can be co-added to improve the S/N. For each input image, Spextool produces an output file containing the wavelength-calibrated flux. Multiple output files (resulting from repeated observations) can be combined with a routine that allows the user to choose the combining procedure (mean, weighted mean, or median). The spectra are resampled onto a common wavelength grid and then combined.

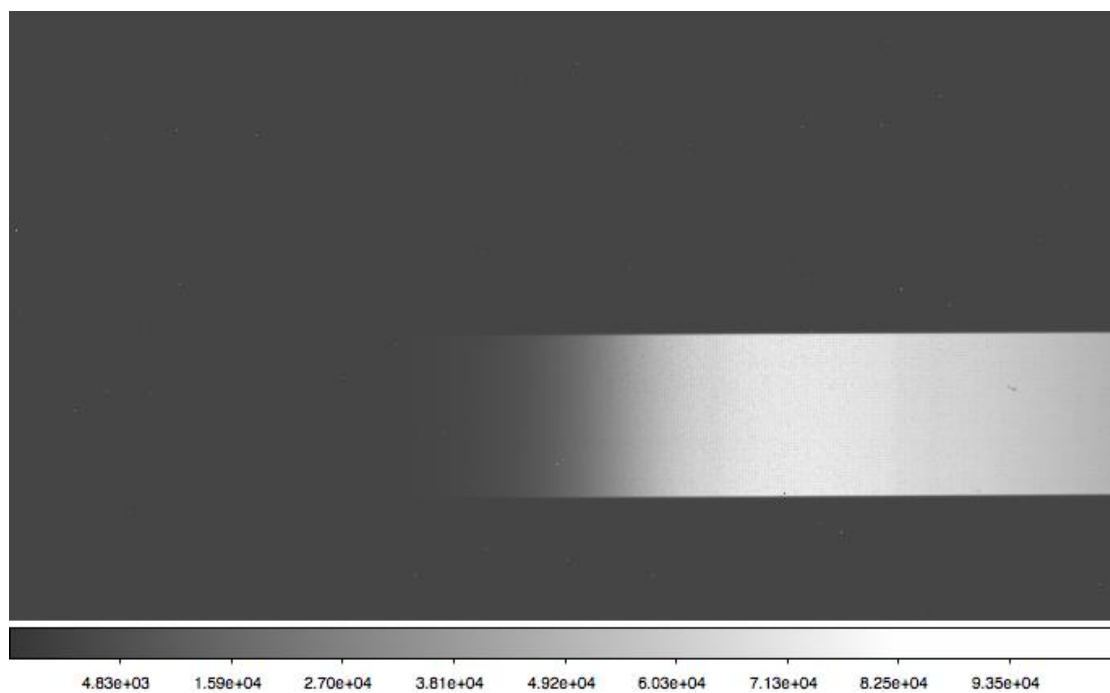


Figure 2.5: Flat-field acquired with SpeX.

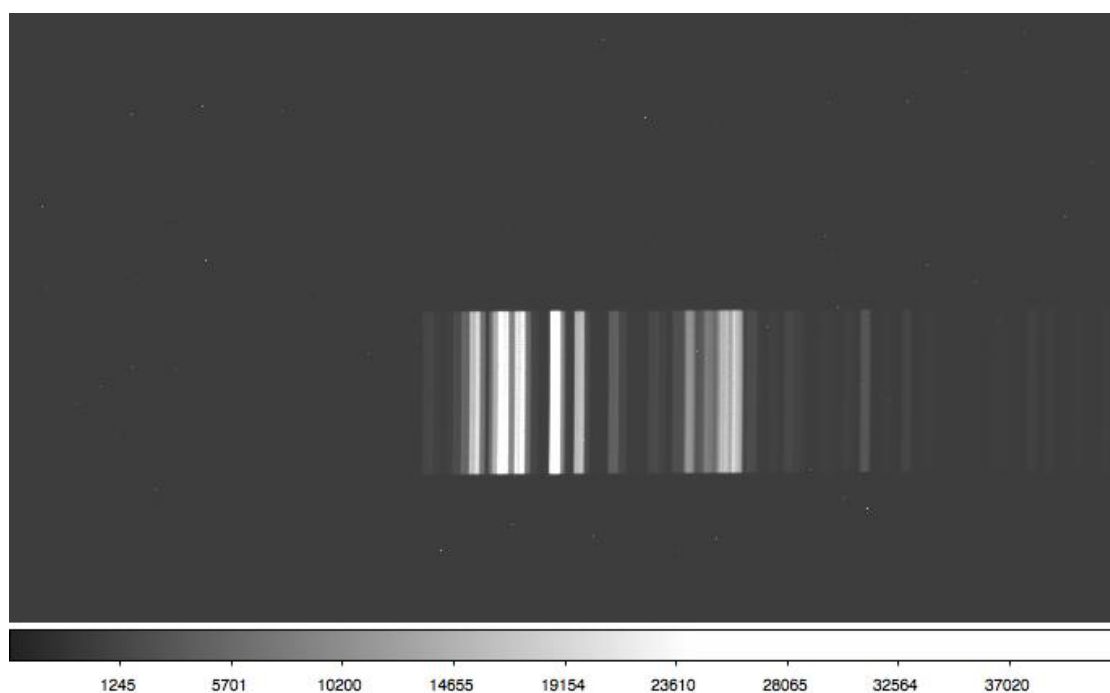


Figure 2.6: Arc line spectrum acquired with SpeX.

A flowchart showing the order of the various reduction steps including the different observing modes for SpeX is shown in Fig. 2.8. For more details about the observing protocols and reduction of these data sets see Cushing et al. (2004), Reddy (2009), DeMeo et al. (2009),

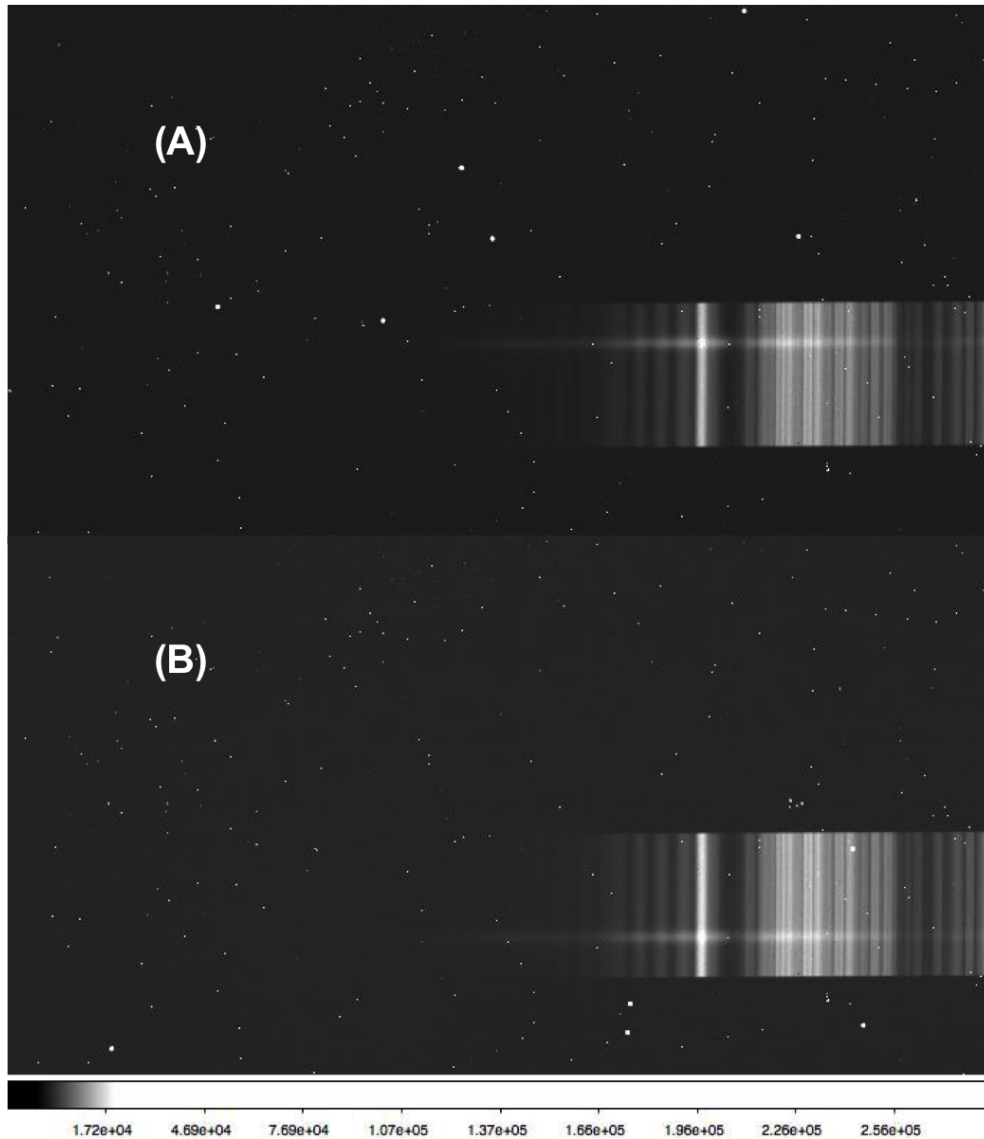


Figure 2.7: Raw spectra of asteroid 4055 Magellan acquired with SpeX at two different slit positions (A and B). Data from Sanchez et al. (2013).

Abell et al. (2007) and Binzel et al. (2001).

In the present work the NIR spectrum of each asteroid has been combined with its visible (VIS) spectrum ($\sim 0.44\text{-}0.9\ \mu\text{m}$) in order to cover the entire wavelength range from 0.44 to $2.5\ \mu\text{m}$. The VIS spectra were taken from Binzel et al. (2001, 2004) and DeMeo et al. (2009). All the spectra are normalized to unity at $0.55\ \mu\text{m}$. In total our sample comprises 27 VNIR spectra of 12 NEAs previously classified as either S-complex or Q-types (Bus-DeMeo). Figures 2.9 to 2.11 show the spectra of all NEAs analyzed in this study. The numerical designation and the date of the observation (YYMMDD) for each asteroid are given. Observational parameters for the studied objects are presented in Table 2.1.

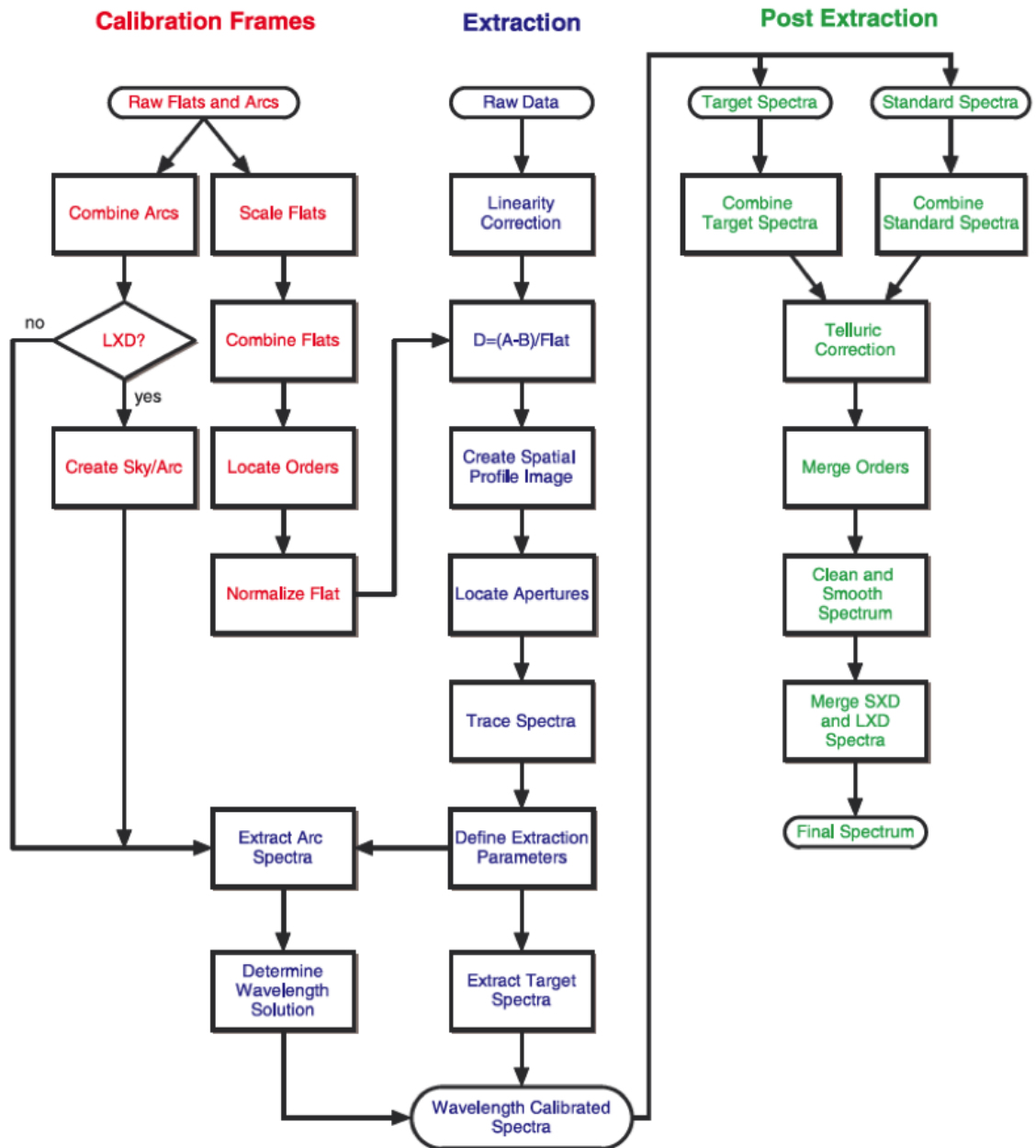


Figure 2.8: Flowchart showing the steps in the reduction process used by Spextool. Reproduced from Cushing et al. (2004).

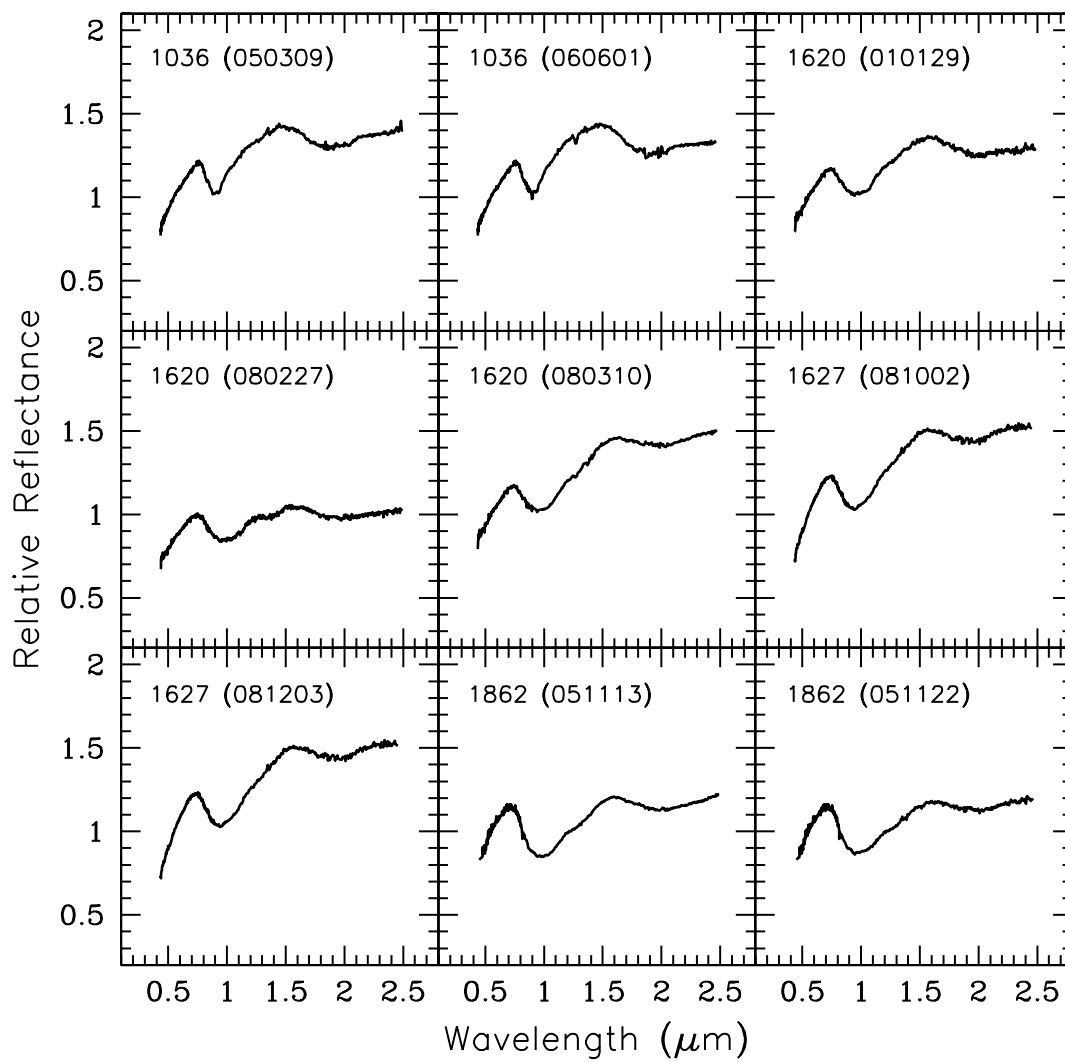


Figure 2.9: Reflectance spectra of NEAs analyzed in this study. Figure from Sanchez et al. (2012).

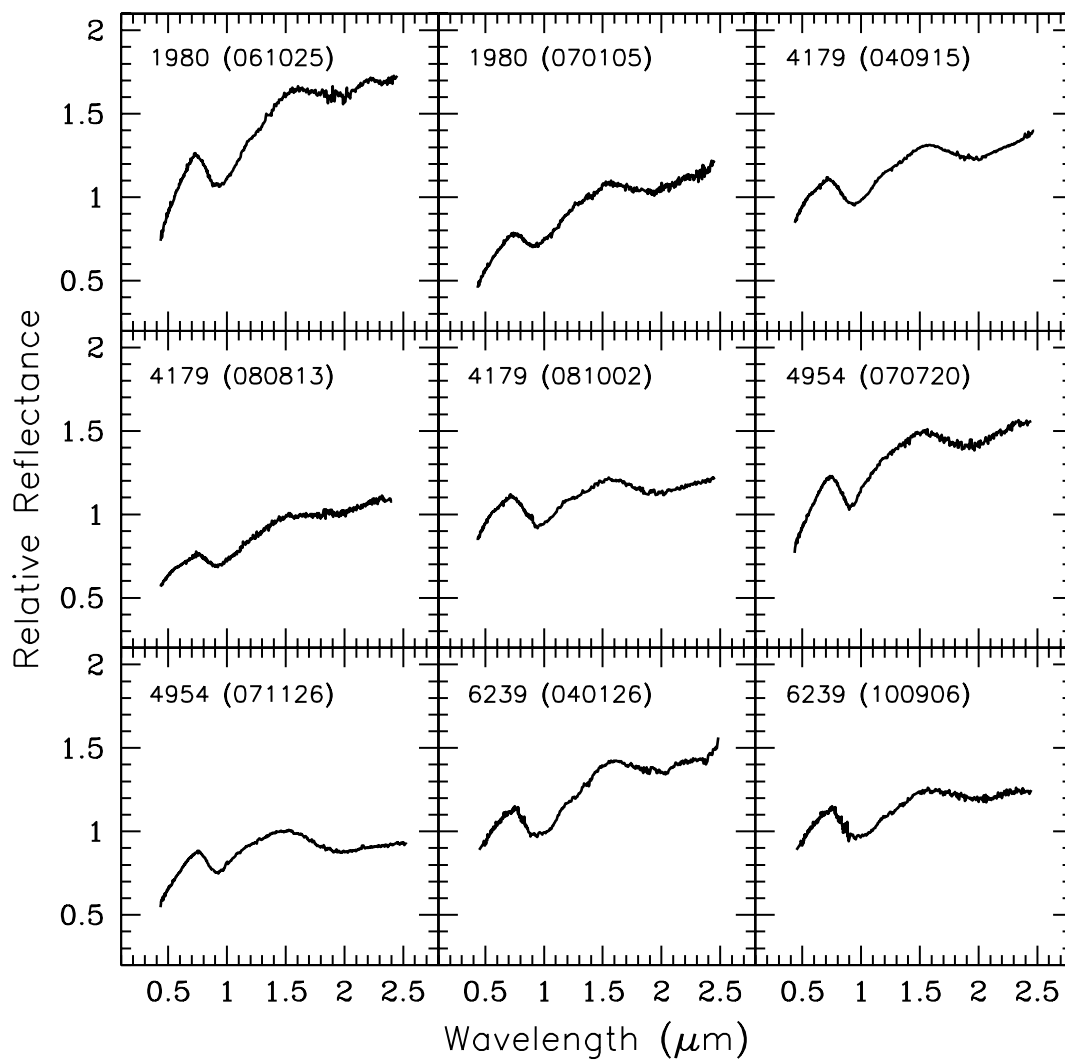


Figure 2.10: Reflectance spectra of NEAs analyzed in this study. Figure from Sanchez et al. (2012).

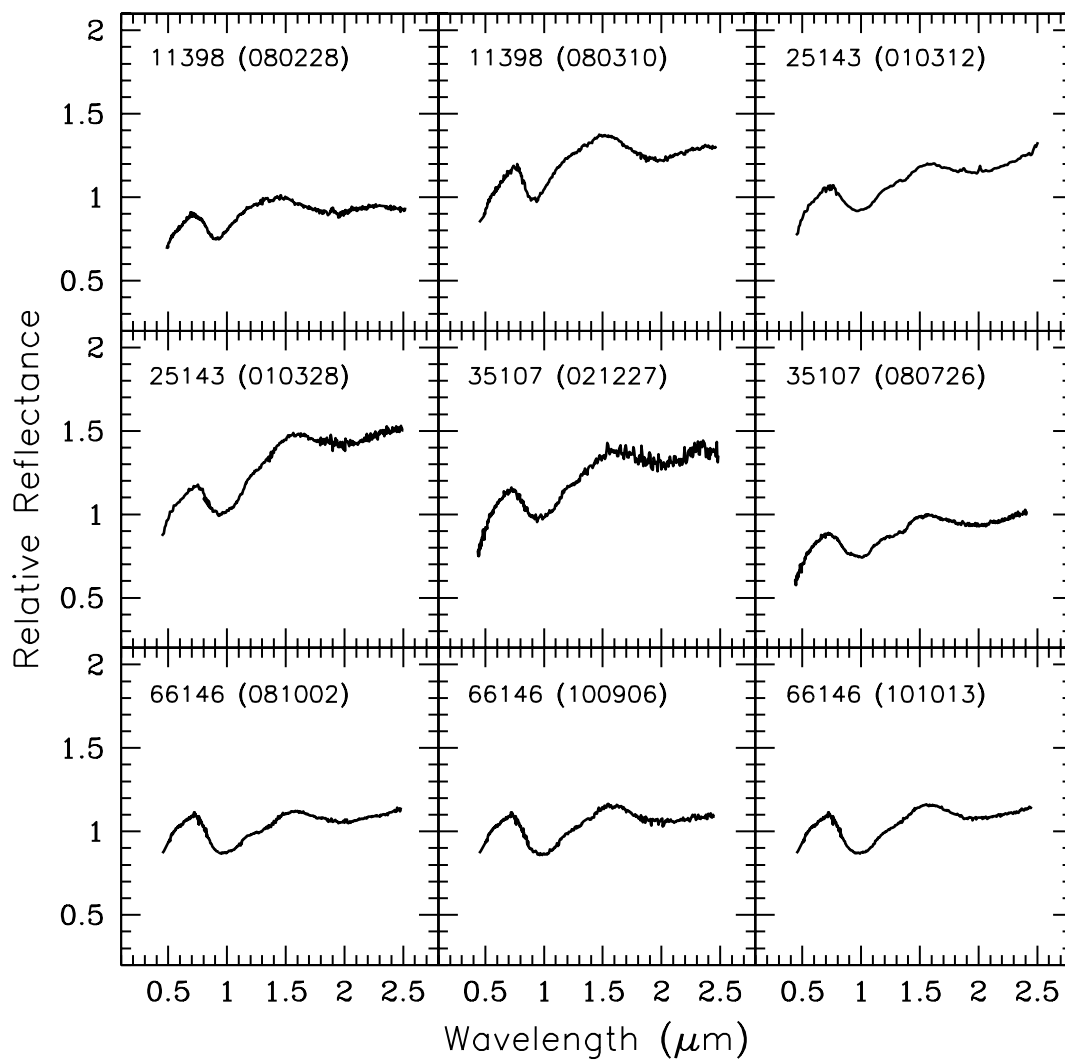


Figure 2.11: Reflectance spectra of NEAs analyzed in this study. Figure from Sanchez et al. (2012).

Table 2.1: NEAs observational parameters. The columns in this table are: object number and designation, UT date of observation, the phase angle (g) and the heliocentric distance at the time of observation.

Object	UT Date	g ($^{\circ}$)	Heliocentric Distance (AU)
1036 Ganymed	09-Mar-05 ^b	5.9	4.09
1036 Ganymed	01-Jun-06 ^c	15.2	3.01
1620 Geographos	10-Mar-08 ^c	38.3	1.09
1620 Geographos	27-Feb-08 ^a	12.0	1.16
1620 Geographos	29-Jan-01 ^b	16.7	1.39
1627 Ivar	02-Oct-08 ^c	31.0	1.58
1627 Ivar	03-Dec-08 ^c	16.0	1.90
1862 Apollo	13-Nov-05 ^c	51.7	1.05
1862 Apollo	22-Nov-05 ^c	15.4	1.20
1980 Tezcatlipoca	25-Oct-06 ^c	54.6	1.17
1980 Tezcatlipoca	05-Jan-07 ^a	25.0	1.48
4179 Toutatis	15-Sep-04 ^c	27.0	1.09
4179 Toutatis	02-Oct-08 ^c	68.0	1.06
4179 Toutatis	13-Aug-08 ^a	6.1	1.45
4954 Eric	20-Jul-07 ^c	28.3	1.67
4954 Eric	26-Nov-07 ^a	62.0	1.10
6239 Minos	26-Jan-04 ^b	47.3	1.03
6239 Minos	06-Sep-10 ^c	2.4	1.20
11398	10-Mar-08 ^c	33.0	1.16
11398	28-Feb-08 ^a	19.0	1.21
25143 Itokawa	12-Mar-01 ^d	25.6	1.07
25143 Itokawa	28-Mar-01 ^e	69.0	1.01
35107	26-Jul-08 ^a	87.0	1.08
35107	27-Dec-02 ^b	45.0	1.20
66146	02-Oct-08 ^c	70.3	1.06
66146	13-Oct-10 ^c	32.1	1.15
66146	06-Sep-10 ^c	55.3	1.16

^a Data from Reddy (2009)

^b Data from DeMeo et al. (2009)

^c Data from NEOSR, <http://smass.mit.edu/minus.html>

^d Data from Abell et al. (2007)

^e Data from Binzel et al. (2001)

3 Temperature-induced effects on NEAs

3.1 Introduction

The effects of temperature on the absorption bands in reflectance spectra of mafic minerals can be explained using CFT (Burns 1993). All cations and ligands in any structure are continuously vibrating about their mean position, such that the sharpness or width of the absorption feature is related to the amplitude of the thermally induced vibrations of the cation about the center of the site. Thus, increasing the temperature will lead to an increase in the amplitude of the thermal vibrations of the cation, producing a broadening of the absorption band. Furthermore, the uniform expansion of the site, due to increased temperature, will produce an increase in the cation-oxygen interatomic distance. As a result, the crystal field splitting energy decreases, producing a shift of the absorption band to longer wavelengths (lower energy). Conversely, a decrease in temperature results in site contraction, i.e., increase in the crystal field splitting energy, and the absorption band shifts to shorter wavelengths (higher energy). If there is differential thermal expansion of the coordination site the situation is more complex, because this could alter the crystallographic symmetry of the cation site and significantly affect the positions of the absorption bands. Band depths can also be affected by temperature variations since the strength of the absorption bands are related to the probability of the occurrence of a certain electronic transition.

Singer and Roush (1985), obtained VNIR spectra (0.4-2.5 μm) of pyroxene and olivine samples over a temperature range of 80 to 448 K. They observed that the absorption bands in all samples become narrower with decreasing temperature as predicted by CFT. Moreover, the three components of the composite olivine band become better resolved with decreased temperature and show changes in relative absorption strength. The Band I center of this composite band, however, did not show any significant wavelength shift. The spectra of their orthopyroxene and clinopyroxene samples show dramatic changes in band symmetry with temperature. However, no significant change was observed in the wavelength position of the Band I. The Band II, in contrast, showed a major shift in the wavelength position. In orthopyroxene spectra the Band II center shifts to longer wavelengths with increased temperature, while for the clinopyroxene spectra it shifts to shorter wavelengths with increased temperature. The higher quality reflectance spectra obtained by Schade and Wäsch (1999) in the temperature range of 80 to 473 K, confirmed the results reported by Singer and Roush (1985) for the Band II of the pyroxene samples, however in the case of the Band I, Schade and Wäsch (1999) found that the Band I center of their HCP shifts to shorter wavelengths with increasing temperature, while the Band I center of their orthopyroxene sample shifts to longer wavelengths as the temperature increases. Moroz et al. (2000) investigated temperature-induced effects on the reflectance spectra of olivine-orthopyroxene-bearing assemblages. They acquired VNIR (0.55-2.8 μm) spectra of

several samples at three different temperatures, 80, 173 and 293 K. They found that the trends with decreasing temperature observed for their olivine and orthopyroxene samples were consistent with those observed previously for orthopyroxenes (Singer and Roush 1985, Schade and Wäsch 1999) and olivine (Singer and Roush 1985).

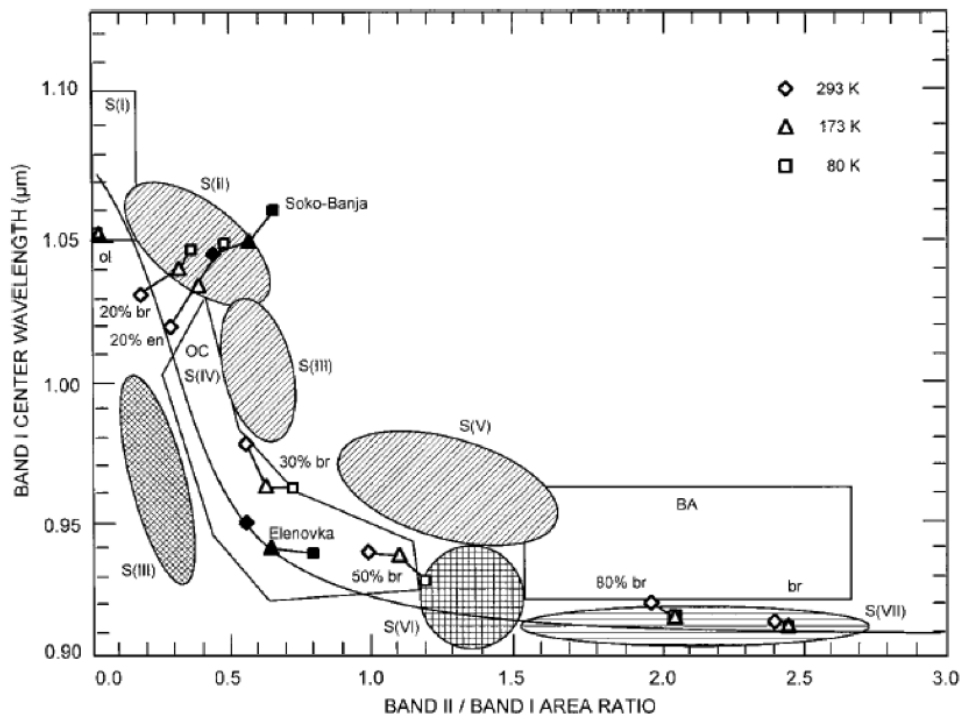


Figure 3.1: Plot of the Band I center vs. BAR for olivine-orthopyroxene mixtures and two ordinary chondrites relative to the S-asteroid subtypes and three types of meteorite assemblages (Gaffey et al. 1993). The rectangular region in the left upper corner encompasses essentially monomineralic olivine assemblages. The "OC" polygonal region represents the mafic silicate components of ordinary chondrites. The "BA" rectangular zone includes the pyroxene-dominated basaltic achondrites. The heavy solid line indicates the location of the olivine-orthopyroxene mixing line (Cloutis et al. 1986). The three different temperatures at which the measurements were acquired are indicated with three symbols, diamonds (293 K), triangles (173 K) and squares (80 K). Figure from Moroz et al. (2000).

The effects of temperature variations have been investigated not only in reflectance spectra of pure mafic minerals, but also in complex mafic assemblages, such as basalt, lunar soil and different meteorite samples. For example, Hinrichs et al. (1999) measured the VNIR spectra of two H5 ordinary chondrites, Allegan and El Hammami, over a wide range of temperatures. These meteorites are composed of olivine, pyroxene, plagioclase and metal, which is a mineral mixture relatively common in the asteroid belt. The analysis of these samples conducted by Hinrichs et al. (1999) showed a progressive shift of the absorption bands to longer wavelengths with increasing temperature. They found that the temperature difference between laboratory conditions and those experienced in the space by main belt asteroids, are large enough to cause detectable spectral variations.

The analysis of the VNIR spectra of the eucrite Millbillillie and the LL4 ordinary chon-

drite Soko-Banja obtained by Schade and Wäsch (1999), showed that additional bands due to calcic clinopyroxene are resolved in the low-temperature spectra. Furthermore, the spectra of Soko-Banja showed a progressive shift of Band I to shorter wavelengths with increasing temperature, while the opposite behavior was found for the eucrite Millbillillie, i.e., the Band I shifts to longer wavelengths with increasing temperature. In the case of the Band II, for both samples this band shifts to longer wavelengths with increasing temperature. Variations of band depths with temperature were also detected. Similar results were obtained by Moroz et al. (2000) from their analysis of another sample of Soko-Banja. For the L5 ordinary chondrite Elenovka, also analyzed by Moroz et al. (2000), both absorption bands shift to longer wavelengths with increasing temperature. A decrease of BAR with increasing temperature for the two ordinary chondrites was also observed. Moroz et al. (2000), pointed out that the influence of temperature on the Band I center positions and BARs is moderate, but not negligible for the olivine-orthopyroxene assemblages relatively rich in olivine. For instance, the upward displacement of the S(II) and S(III) asteroid subgroups from the olivine-orthopyroxene mixing line on the diagram by Gaffey et al. (1993), is interpreted as being due to the presence of high calcium pyroxene on the surfaces of these asteroids (Gaffey et al. 1993). However, Moroz et al. (2000) noticed that a decrease in surface temperature displaces the data points of the Soko-Banja sample and olivine-orthopyroxene mixtures with an $opx/(opx+ol)$ ratio of 0.2 from the olivine-orthopyroxene mixing line to the zone of S(II) asteroids. Therefore, they suggested that the S(II)-type asteroids are not necessarily enriched in calcic clinopyroxene. Instead, the offset of their data points above the olivine-orthopyroxene mixing line can be explained by increased Band I center wavelength position and BAR due to the low surface temperature. This can be seen in Figure 3.1 that shows the Band I center versus BAR diagram of Gaffey et al. (1993) for olivine-orthopyroxene mixtures, Soko-Banja and Elenovka, relative to the S-asteroid subtypes and three types of meteorite assemblages.

Moroz et al. (2000) measured the change in band centers of two pyroxenes (bronzite and enstatite) at different temperatures (293, 173 and 80 K) and based on their results, Burbine et al. (2009) developed a set of equations to correct the band centers for temperature variations. Typically, Band I center corrections are small ($\sim 0.0005 \mu m$), while Band II corrections are slightly larger ($\sim 0.01 \mu m$). However, this may vary depending on the mineral and the temperature differences. The equations developed by Burbine et al. (2009) have been used to correct for temperature variations on V-type asteroids (e.g., Burbine et al. 2009, Moskovitz et al. 2010). However, because they were derived from the analysis of terrestrial samples, they could not provide an accurate description of the effect of temperature variations on this type of asteroids. Acknowledging this problem, we developed a new set of calibrations based on the analysis of HED meteorite spectra, that can be used to correct NIR spectra obtained with the VIR spectrometer on Dawn spacecraft, and color ratios from the Dawn Framing Camera data. The results of this work are presented in Reddy et al. (2012d) and are shown in Figure 3.2.

The wavelength corrections for band centers derived by Reddy et al. (2012d) for howardites and eucrites are

$$\Delta BI(\mu m) = 0.01656 - 0.0000552 \times T(K) \quad (3.1)$$

$$\Delta BII(\mu m) = 0.05067 - 0.00017 \times T(K) \quad (3.2)$$

and for diogenites are give by

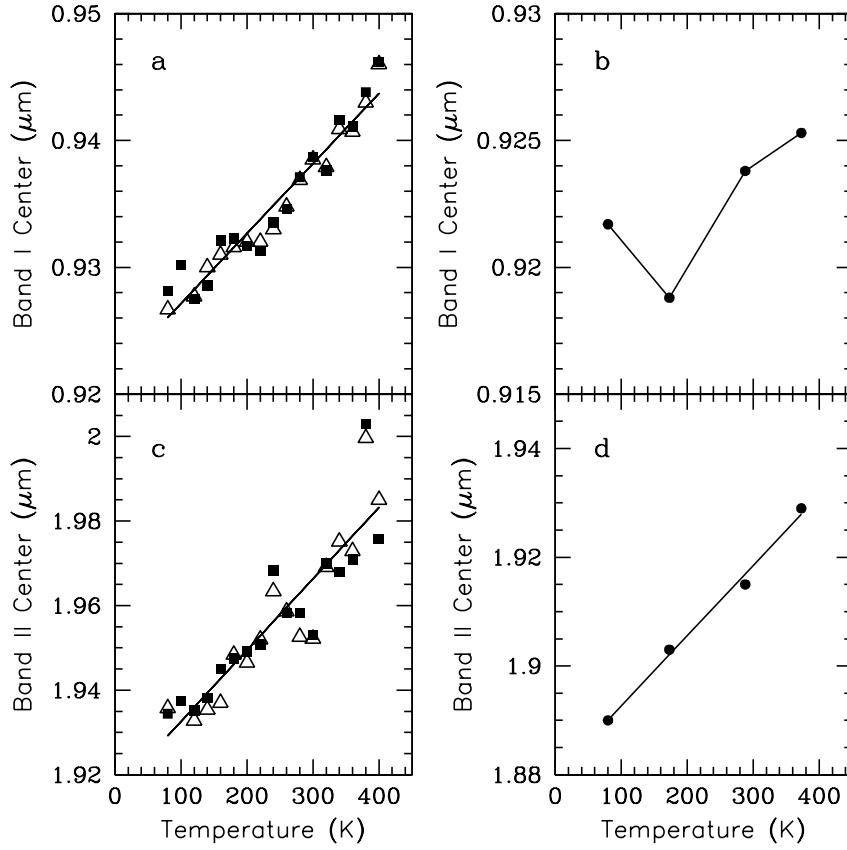


Figure 3.2: Plot of band centers vs. temperature for the HED meteorites analyzed by Reddy et al. (2012d). Panels (a) and (c) show the Band I and Band II center change in eucrite EET83251 (open triangles) and howardite EET87503 (squares) as a function of temperature. Panels (b) and (d) show Band I and Band II center change in diogenite Ellemeet as a function of temperature. Data from Reddy et al. (2012d).

$$\Delta BI(\mu m) = 1.7 \times 10^{-9} \times T^3(K) - 1.26 \times 10^{-6} \times T^2(K) + 2.66 \times 10^{-4} \times T(K) - 0.0124 \quad (3.3)$$

$$\Delta BII(\mu m) = 0.038544 - 0.000128 \times T(K) \quad (3.4)$$

where BI and BII are the Band I and Band II centers, respectively. These wavelength corrections need to be added to the Band I and II centers to obtain values at 300 K.

The equations derived by Burbine et al. (2009) and Reddy et al. (2012d) can be applied to pyroxene assemblages like V-type asteroids, however for olivine-orthopyroxene mixtures, like S-complex and Q-type asteroids, they may not be suitable.

3.2 Temperature-induced spectral effects on NEAs

3.2.1 Spectral band analysis of NEAs

The spectral band parameters for each VNIR spectrum were measured using the Spectral Processing Routine (SpecPR) program based on the protocols discussed by Cloutis et al. (1986), Gaffey et al. (2002), and Gaffey (2003). Band centers are calculated by dividing out the linear continuum and fitting an n -order polynomial over the bottom third of each band. In the case of Band II, we defined the unresolved red edge as $2.44 \mu\text{m}$. After ratioing the absorption features to the straight-line continuum, a subroutine in SpecPR was used to calculate the band areas and band depths. The band areas were then used to calculate the BAR values. Each band parameter was measured ten times using different order polynomial fits (typically third and fourth order) and sampling different ranges of points within the corresponding intervals. Averages of these measurements were taken as the final values. The uncertainties are given by the average $1-\sigma$ (standard deviation of the mean) calculated from the multiple measurements of each band parameter. The olivine-pyroxene abundance ratio of the asteroids was estimated using the relationship between $ol/(ol + px)$ and BAR derived by Dunn et al. (2010) from the analysis of 48 ordinary chondrite samples (see Eq. 1.9). The band parameters and $ol/(ol + px)$ ratios with their corresponding errors obtained for each asteroid are presented in Table 3.1.

3.2.2 NEAs surface temperature

The simplest method to calculate the average surface temperature of an asteroid, is to assume that the thermal emission from any point on the asteroid's surface is in instantaneous equilibrium with the solar radiation absorbed at that point. This is the basis of the standard thermal model (STM) (Lebofsky and Spencer 1989, Delbó and Harris 2002, Harris and Lagerros 2002), which allows to estimate the average surface temperature by equating the amount of energy absorbed and emitted by the object. In the case of a spherical asteroid the total incoming energy incident on the surface is:

$$U_i = \frac{S_{\odot}}{r^2} \pi R^2 \quad (3.5)$$

where S_{\odot} is the solar constant, r is the asteroid's heliocentric distance, and R is the radius of the asteroid. Energy that is not reflected is absorbed by the asteroid surface:

$$U_a = U_i(1 - A) \quad (3.6)$$

where A is the bolometric Bond albedo. If we assume that an asteroid behaves like a gray body, i.e., a body that does not absorb all incident radiation and is characterized by an emissivity, $\varepsilon < 1$, then according to the Stefan-Boltzmann law, the energy emitted from the entire spherical surface of the asteroid is:

$$U_e = 4\pi R^2 \sigma \varepsilon T^4 \quad (3.7)$$

where σ is the Stefan-Boltzmann constant and T is the temperature in K. Assuming instantaneous thermal equilibrium, conservation of energy implies that $U_a = U_e$, which can be expressed as

$$\frac{S_{\odot}}{r^2}\pi R^2(1 - A) = 4\pi R^2\sigma\epsilon T^4 \quad (3.8)$$

so the temperature is given by

$$T = \left[\frac{(1 - A)S_{\odot}}{4\epsilon\sigma r^2} \right]^{1/4} \quad (3.9)$$

The equation above can be written as a function of the solar luminosity L_0 (3.827×10^{26} W), so the final expression for the average surface temperature of an asteroid is given by

$$T = \left[\frac{(1 - A)L_0}{16\eta\epsilon\sigma\pi r^2} \right]^{1/4} \quad (3.10)$$

where η is an empirical term called the beaming parameter, which is a normalization constant that is introduced to take into account the observed enhancement of thermal emission at small solar phase angles due to surface roughness, known as the beaming effect (Harris and Lagerros 2002). In practice, η acts as a proxy of both surface roughness and thermal inertia, and has the value 1.0 for a smooth, nonrotating body. The Bond albedo can be linked to the geometric albedo p_v through

$$A = qp_v \quad (3.11)$$

where q is the phase integral and is given by

$$q = 0.290 + 0.684G \quad (3.12)$$

where G is the slope parameter. We have used Eq. (3.10) to calculate the average surface temperatures of the NEAs. The infrared emissivity, ϵ is assumed to be 0.9, which is the typical value measured for silicate minerals that are dominant on asteroid surfaces (Christensen et al. 2000, Lim et al. 2005). The beaming parameter, η is assumed to be unity (Cohen et al. 1998). If the albedo of the asteroid is unknown a value is assumed based on its taxonomic class. Changes in those assumed parameters will typically produce variations of approximately +/- 10 K in the calculated temperatures. The average surface temperatures of the NEAs are given in Table 3.1.

Table 3.1: NEAs spectral band parameters and their errors. The columns in this table correspond to: object number and designation, phase angle (g), average surface temperature (T), Band I center (BI \pm 0.01), Band I depth (BI $_{\text{dep}}\pm$ 0.3), Band II center (BII \pm 0.03), Band II depth (BII $_{\text{dep}}\pm$ 0.5), temperature corrected Band II center (ABII \pm 0.03), Band II depth (BII $_{\text{dep}}\pm$ 0.5), temperature corrected Band II depth (Δ BII $_{\text{dep}}\pm$ 0.5), band area ratio (BAR \pm 0.04), temperature corrected band area ratio (Δ BAR \pm 0.04), olivine-pyroxene abundance ratio (ol/(ol+px) \pm 0.03) and temperature corrected olivine-pyroxene ratio (Δ ol/(ol+px) \pm 0.03).

Object	g ($^{\circ}$)	T (K)	BI (μm)	BI $_{\text{dep}}$ (%)	BII (μm)	Δ BII (μm)	BII $_{\text{dep}}$ (%)	Δ BII $_{\text{dep}}$ (%)	BAR	Δ BAR	ol/(ol+px)	Δ ol/(ol+px)
1036 Ganymed	5.9	129.6	0.909	18.79	1.867	1.901	8.05	5.49	0.901	0.768	0.51	0.54
1036 Ganymed	15.2	150.9	0.917	18.22	1.883	1.913	9.29	7.05	1.101	0.984	0.46	0.49
1620 Geographos	12.0	240.4	0.995	16.34	1.970	1.982	5.68	4.79	0.497	0.447	0.61	0.62
1620 Geographos	16.7	219.6	0.997	16.77	1.967	1.984	6.56	5.35	0.490	0.425	0.61	0.63
1620 Geographos	38.3	247.7	1.001	18.03	2.013	2.023	4.19	3.40	0.278	0.234	0.66	0.67
1627 Ivar	16.0	198.9	0.948	19.14	1.955	1.975	6.26	4.74	0.407	0.326	0.63	0.65
1627 Ivar	31.0	218.4	0.959	20.28	1.964	1.980	5.04	3.82	0.253	0.186	0.67	0.68
1862 Apollo	15.4	243.3	0.986	25.00	1.997	2.008	4.81	3.96	0.188	0.141	0.68	0.69
1862 Apollo	51.7	260.0	0.988	27.54	1.989	1.997	6.53	5.93	0.260	0.225	0.66	0.67
1980 Tezcatlipoca	25.0	218.6	0.947	16.05	1.932	1.949	6.62	5.40	0.526	0.460	0.60	0.62
1980 Tezcatlipoca	54.6	246.2	0.950	20.45	1.946	1.956	4.37	3.56	0.228	0.183	0.67	0.68
4179 Toutatis	6.1	222.3	0.943	14.91	1.971	1.987	4.89	3.72	0.551	0.487	0.59	0.61
4179 Toutatis	27.0	256.9	0.951	17.44	1.973	1.981	7.29	6.64	0.524	0.487	0.60	0.61
4179 Toutatis	68.0	260.5	0.952	18.04	1.962	1.970	6.90	6.31	0.487	0.452	0.61	0.62
4954 Eric	28.3	207.1	0.929	18.74	1.925	1.944	9.78	8.39	1.073	0.998	0.47	0.49
4954 Eric	62.0	255.2	0.923	16.69	1.946	1.955	8.81	8.14	0.917	0.878	0.51	0.52
6239 Minos	2.4	244.1	0.994	16.56	2.030	2.041	4.03	3.19	0.239	0.192	0.67	0.68
6239 Minos	47.3	263.2	0.993	19.02	2.010	2.017	6.10	5.55	0.348	0.315	0.64	0.65
11398	19.0	243.3	0.913	19.04	1.935	1.946	6.89	6.04	0.622	0.575	0.58	0.59
11398	33.0	248.3	0.925	19.81	1.945	1.955	8.33	7.55	0.653	0.610	0.57	0.58
25143 Itokawa	25.6	229.2	0.988	17.02	2.017	2.030	6.07	5.01	0.448	0.390	0.62	0.63
25143 Itokawa	69.0	235.2	0.982	19.85	2.017	2.030	5.45	4.48	0.395	0.341	0.63	0.65
35107	45.0	244.1	0.984	19.57	2.019	2.030	7.40	6.56	0.452	0.405	0.62	0.63
35107	87.0	257.6	0.997	18.90	1.996	2.004	6.92	6.28	0.444	0.407	0.62	0.63
66146	32.1	250.1	0.992	22.17	1.983	1.993	6.20	5.45	0.339	0.296	0.65	0.66
66146	55.3	249.1	0.987	22.99	1.984	1.994	6.35	5.59	0.290	0.246	0.66	0.67
66146	70.3	260.2	0.986	22.57	1.992	2.000	5.75	5.15	0.306	0.272	0.65	0.66

3.2.3 Temperature correction to band parameters

All the objects in our study have been classified as either S-complex or Q-types (Bus-DeMeo), therefore in order to obtain calibrations that can be used to correct for temperature-induced effects on olivine-orthopyroxene assemblages, we have to derive a new set of equations based on the analysis of ordinary chondrites. For this reason we have reanalyzed spectra of two H5 ordinary chondrites from Hinrichs and Lucey (2002) acquired in the temperature range between 80 and 300 K, with a temperature resolution of 20 K. The VNIR spectra of the H5 ordinary chondrite Allegan and the H5 El Hammammi were obtained at the Hawaii Institute of Geophysics and Planetology, using an Analytical Spectral Devices FR field reflectance spectrometer. The instrument covers the wavelength range from 0.35 to 2.5 μm at 3-nm resolution shortward of 1 μm and 10-nm resolution longward of 1 μm . The data are referenced to a Spectralon reflectance standard and a broadband collimated light source (Hinrichs and Lucey 2002). Spectral band parameters (band centers, band depths and BAR) and their uncertainties were measured using the same methods applied to the asteroid spectra. These data were combined with the results obtained by Moroz et al. (2000) for a L5 and a LL4 ordinary chondrite acquired at temperatures between 293 and 80 K. The band parameters with their corresponding errors obtained for each sample are presented in Table 3.2. Figures 3.3 and 3.4 show the temperature series for Allegan and El Hammammi, respectively. Figures 3.5 and 3.6 show the reflectance spectra of Soko-Banja and Elenovka acquired at three different temperatures.

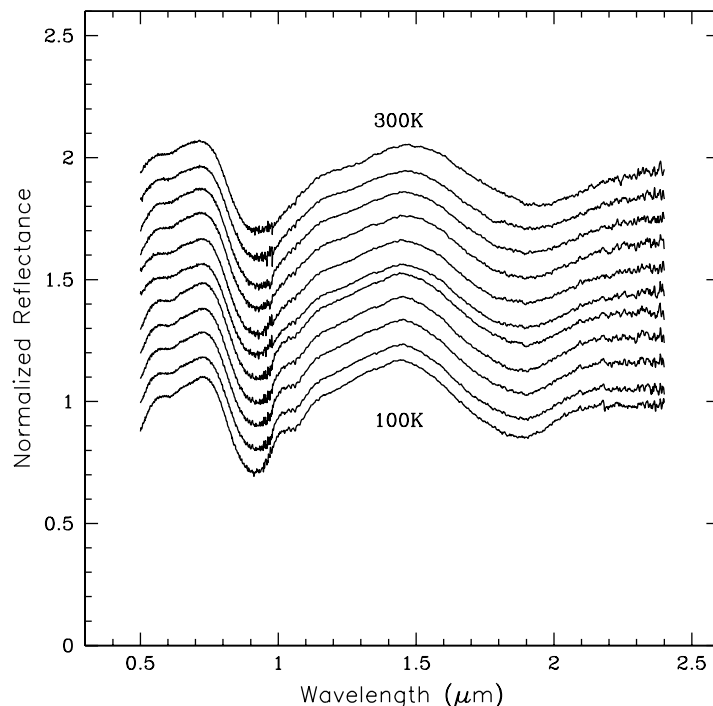


Figure 3.3: Temperature series for H5 ordinary chondrite Allegan. The top spectrum was collected with the sample at 300 K. Spectra below are for sample temperatures decreasing at 20 K intervals. Spectra have been offset for clarity. Data from Hinrichs and Lucey (2002).

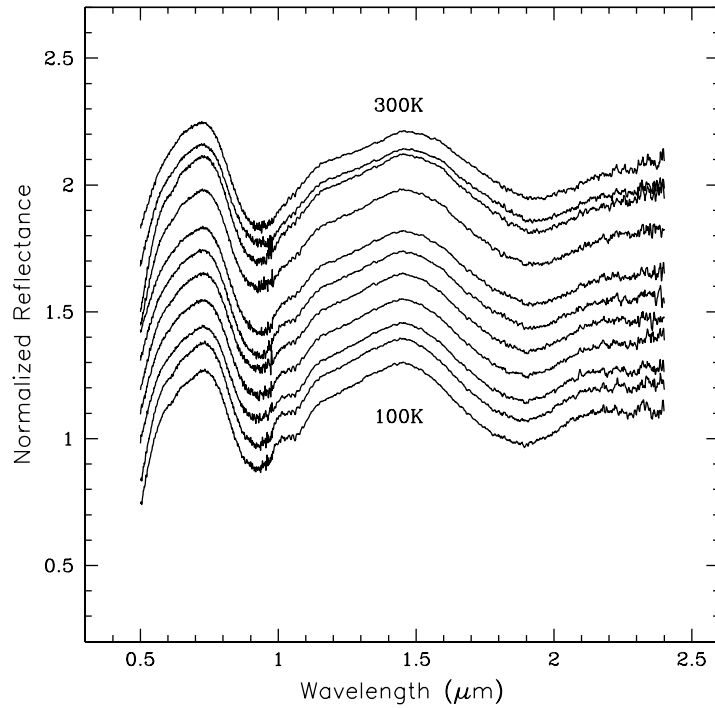


Figure 3.4: Temperature series for H5 ordinary chondrite El Hammammi. The top spectrum was collected with the sample at 300 K. Spectra below are for sample temperatures decreasing at 20 K intervals. Spectra have been offset for clarity. Data from Hinrichs and Lucey (2002).

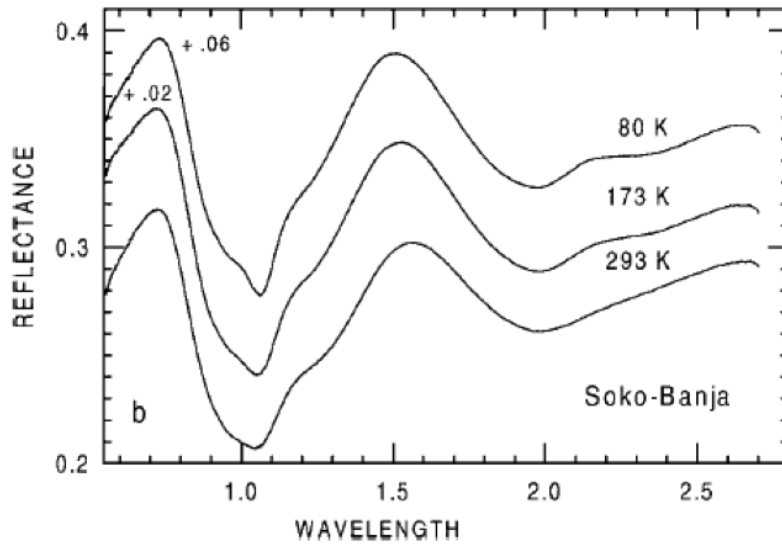


Figure 3.5: Reflectance spectra of LL4 chondrite Soko-Banja acquired at three different temperatures. Spectra are offset for clarity. For each spectrum the degree of the shift is provided in the figure. Wavelengths are in micrometers. Figure from Moroz et al. (2000).

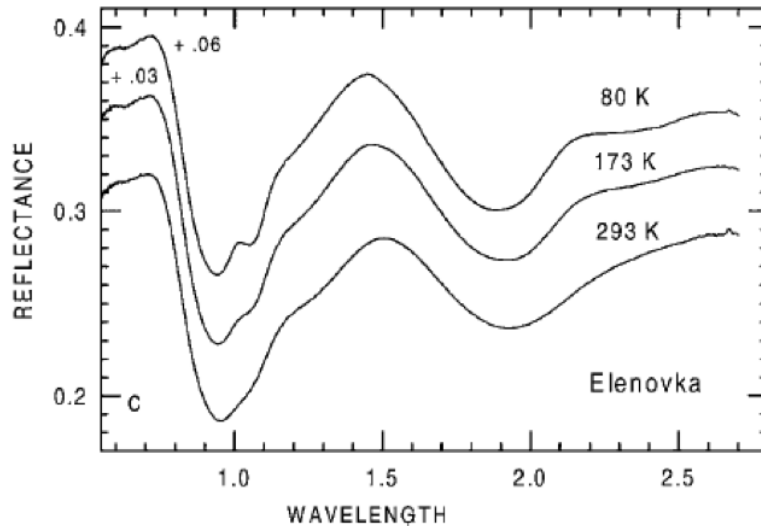


Figure 3.6: Reflectance spectra of L5 chondrite Elenovka acquired at three different temperatures. Spectra are offset for clarity. For each spectrum the degree of the shift is provided in the figure. Wavelengths are in micrometers. Figure from Moroz et al. (2000).

Figure 3.7 shows the Band I center as a function of temperature for the LL4 ordinary chondrite Soko-Banja (circles), the L5 ordinary chondrite Elenovka (triangles) and the H5 El Hammami (squares). The dashed lines are least-squares fits to the data. Although the uncertainties associated with the band parameters of Soko-Banja and Elenovka are not indicated in the work of Moroz et al. (2000), due to the high S/N ratio of the laboratory spectra these values are usually much smaller than the uncertainties associated with asteroid spectra. From the data of Hinrichs and Lucey (2002) we estimated a $1-\sigma$ error of $0.001 \mu\text{m}$ for the Band I center. A weak trend of Band I center moving to longer wavelengths with increasing temperature is observed for Elenovka and El Hammami. However, the opposite trend was found for Soko-Banja. This anomalous behavior was observed by Roush and Singer (1986) after analyzing laboratory spectra of an olivine sample obtained over a temperature range of 80 to 448 K. They interpreted this trend as the result of differential expansion of the coordination site, resulting in greater splitting of the upper energy levels, which causes a shift of the absorption band center to shorter wavelengths. Because the Band I is a composite absorption feature, the direction of the wavelength shift will depend on the olivine abundance. Moroz et al. (2000) noted that their Soko-Banja sample was enriched in olivine compared to the average LL-chondrites. Therefore, in an olivine-rich assemblage this mineral will contribute more to the position of the Band I than the pyroxene, causing the Band I to move in the opposite direction with increasing temperature.

Taking into account that the Band I center of olivine-orthopyroxene mixtures can shift either to longer or to shorter wavelengths as the temperature increases, and considering that this wavelength shift is very small, we did not derive a temperature correction for Band I center.

Figure 3.8 shows the Band II center as a function of temperature for Soko-Banja (circles), Elenovka (triangles) and the H5 ordinary chondrite Allegan (squares). The $1-\sigma$ error of the Band II centers estimated from the data of Hinrichs and Lucey (2002) give us a value of $0.005 \mu\text{m}$. As expected for the pyroxene absorption band, the Band II center shifts to longer wave-

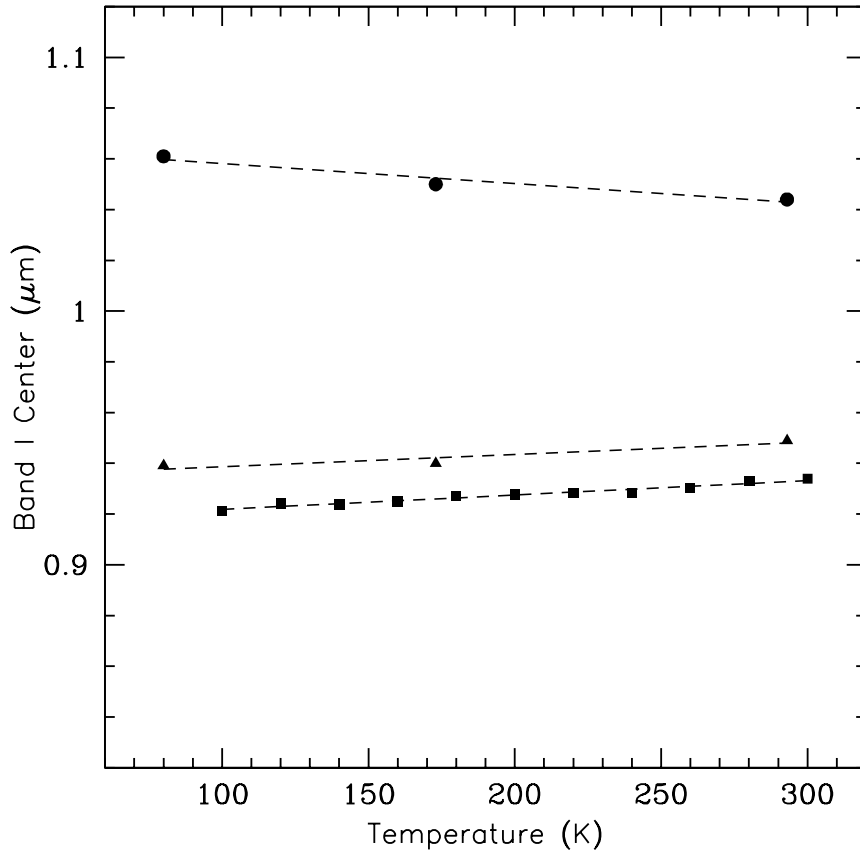


Figure 3.7: Band I center as a function of temperature for three ordinary chondrites, LL4 Soko-Banja (circles), L5 Elenovka (triangles) and H5 El Hammammi (squares). The dashed lines were fitted by least-squares. The R^2 values determined from the linear fits for Soko-Banja, Elenovka and El Hammammi are: 0.94, 0.88 and 0.95 respectively. The $1-\sigma$ error bars ($0.001 \mu\text{m}$) of Band I centers are smaller than the data points.

lengths as the temperature increases for all samples. This effect seems to be more significant for the L5 and H5 ordinary chondrites. To each data set a linear fit was made (dashed lines), and as a measure of the goodness of fit, the coefficient of determination (R^2) was calculated. We found that for all the samples under study $R^2 > 0.97$, meaning that a strong correlation between the Band II center and temperature exists. From these data we averaged the equations that represent each linear fit (including the H5 ordinary chondrite El Hammammi not shown in Fig.3.8 for clarity) and obtained the following expression

$$BII(T) = 0.0002 \times T(K) + 1.87 \quad (3.13)$$

where the Band II center (BII) is given in μm . This expression can be used to estimate the approximate shift of the Band II center of an olivine-orthopyroxene mixture for a given range of temperatures. From this equation we derived a wavelength correction for the Band II center

$$\Delta BII(\mu\text{m}) = 0.06 - 0.0002 \times T(K) \quad (3.14)$$

This correction is derived with respect to room temperature (300 K) and must be added to the calculated Band II center of each asteroid before comparing with those calculated for laboratory samples obtained at room temperature. The temperature corrected Band II centers are presented in Table 3.1.

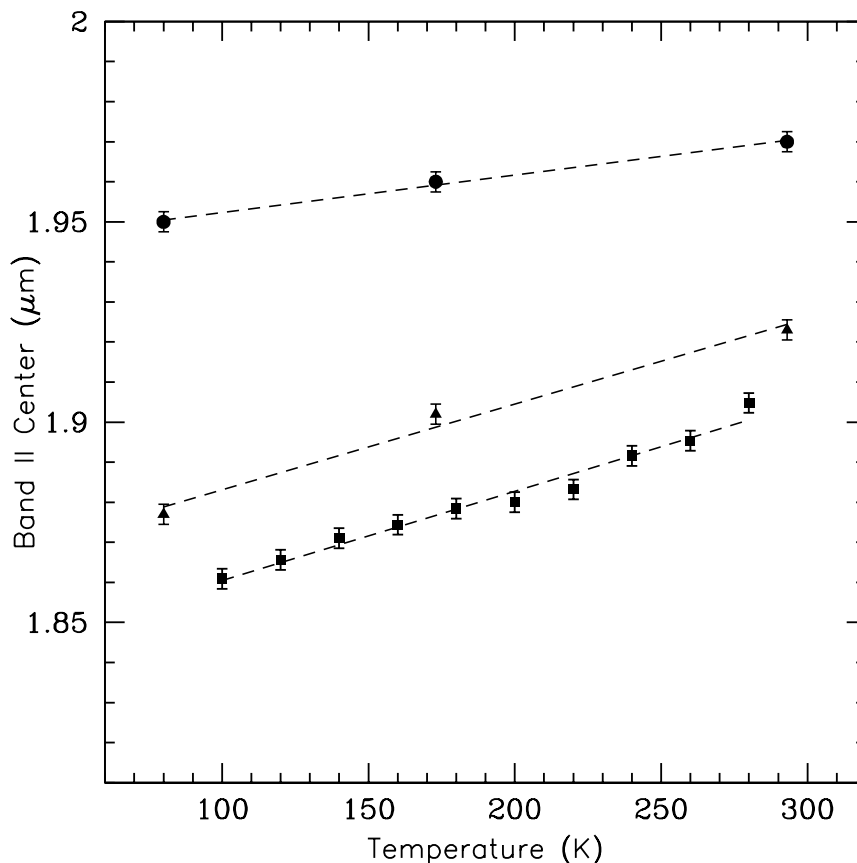


Figure 3.8: Band II center as a function of temperature for three ordinary chondrites, LL4 Soko-Banja (circles), L5 Elenovka (triangles) and H5 Allegan (squares). The dashed lines were fitted by least-squares. The R^2 values determined from the linear fits for Soko-Banja, Elenovka and Allegan are: 0.99, 0.98 and 0.97 respectively.

In addition to the band centers we also investigated possible temperature-induced effects on the band depths and BAR. A decrease in Band II depth with increasing temperature was found for the three groups of ordinary chondrites (Fig. 3.9). The $1-\sigma$ error of the Band II depth from the data of Hinrichs and Lucey (2002) is 0.15%. The linear fits to the data gave values of $R^2 > 0.8$ for all the samples studied. No obvious trend was observed for the Band I depth.

Following the same procedure as for the Band II center, we derived an equation that can be used to estimate the approximate change of the Band II depth for a range of temperatures

$$BII_{dep}(T) = 20.89 - 0.015 \times T(K) \quad (3.15)$$

where the Band II depth (BII_{dep}) is given in %. From this equation we derived a temperature correction for the Band II depth

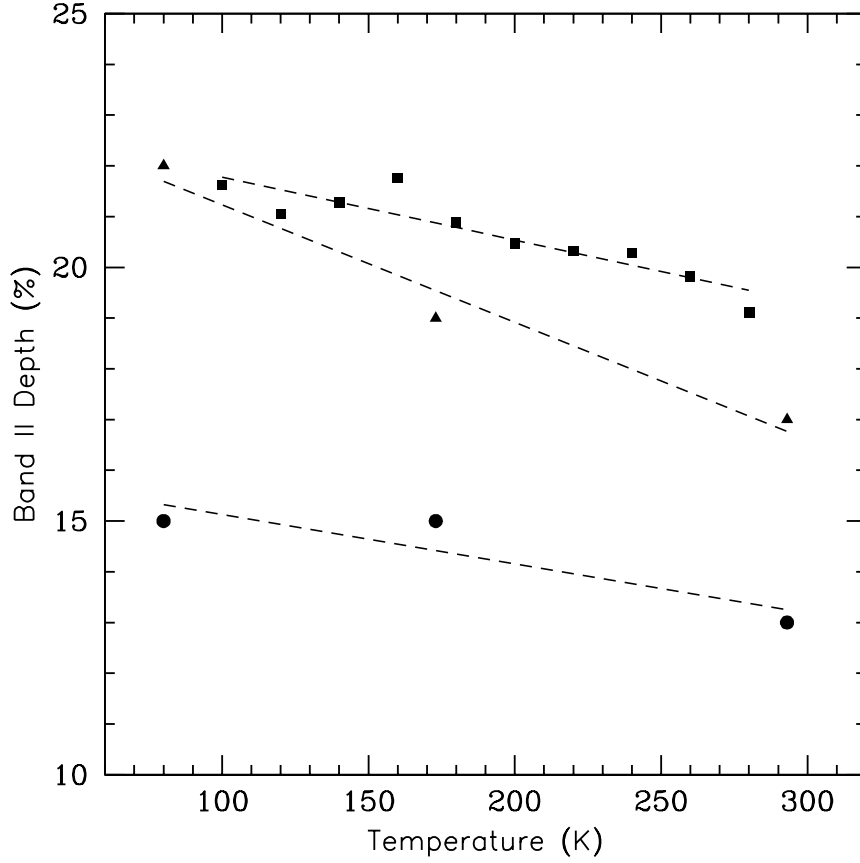


Figure 3.9: Band II depth as a function of temperature for the LL4 ordinary chondrite Soko-Banja (circles), L5 ordinary chondrite Elenovka (triangles) and H5 Allegan (squares). The dashed lines were fitted by least-squares. The R^2 values determined from the linear fits for Soko-Banja, Elenovka and Allegan are: 0.81, 0.96 and 0.83 respectively. The $1-\sigma$ error bars (0.15%) of Band II depths are on the order of the size of the data points.

$$\Delta BII_{dep}(\%) = 0.015 \times T(K) - 4.5 \quad (3.16)$$

This correction is derived with respect to room temperature and must be added to the calculated Band II depth of each asteroid.

An inverse correlation between BAR and temperature was also found for the ordinary chondrites samples (Fig. 3.10). The average error associated with BAR obtained from the data of Hinrichs and Lucey (2002) is 0.01. In this case, the linear fits to the data gave values of $R^2 > 0.67$ for the samples studied. As in the previous cases we obtained an average equation to calculate the change of BAR for a range of temperatures

$$BAR(T) = 0.83 - 0.00075 \times T(K) \quad (3.17)$$

from where a temperature correction with respect to room temperature was derived

$$\Delta BAR = 0.00075 \times T(K) - 0.23 \quad (3.18)$$

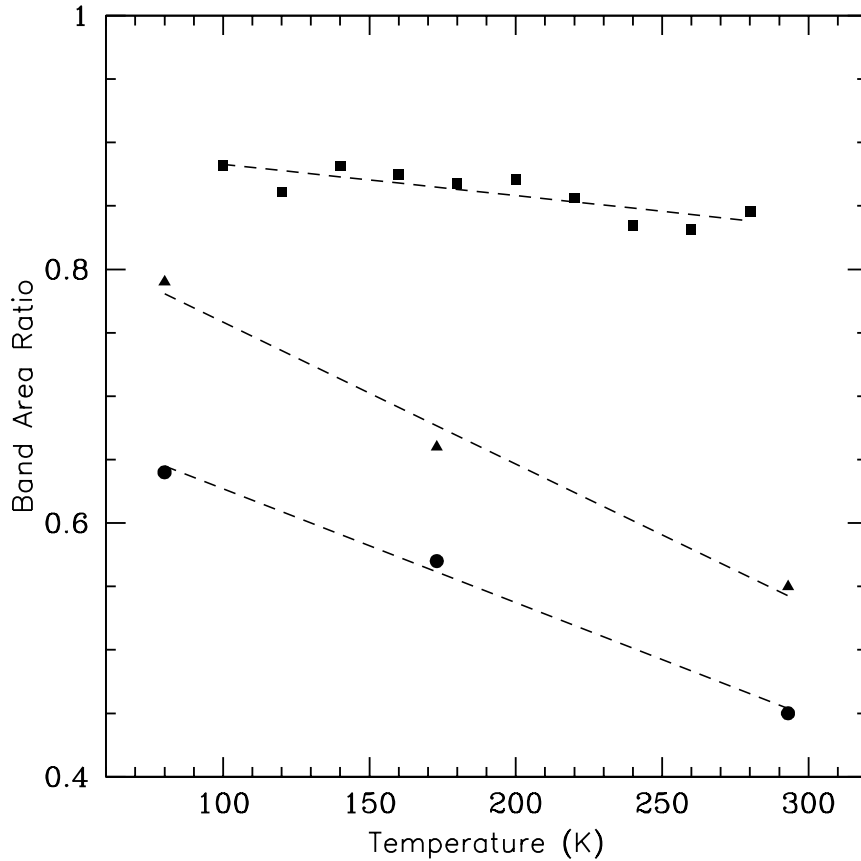


Figure 3.10: Band area ratio (BAR) as a function of temperature for the LL4 ordinary chondrite Soko-Banja (circles), L5 ordinary chondrite Elenovka (triangles) and H5 Allegan (squares). The dashed lines were fitted by least-squares. The R^2 values determined from the linear fits for Soko-Banja, Elenovka and Allegan are: 0.99, 0.99 and 0.67 respectively. The $1-\sigma$ error bars (0.01) of BAR values are smaller than the data points.

This correction must be added to the calculated BAR values of each asteroid before comparing with those calculated for laboratory samples obtained at room temperature. The temperature corrected Band II depths and BARs are presented in Table 3.1. Based on the corrected BAR values, the olivine abundance of each asteroid was recalculated using Eq. (1.9). These values are included in Table 3.1.

Table 3.2: Spectral band parameters of the ordinary chondrites. The columns in this table correspond to: sample type, temperature, Band I center ($BI \pm 0.001$), Band I depth ($BI_{dep} \pm 0.1$), Band II center ($BII \pm 0.005$), Band II depth ($BII_{dep} \pm 0.15$), and band area ratio ($BAR \pm 0.01$). Spectral band parameters of Allegan and El Hammammi were measured from data obtained by Hinrichs and Lucey (2002). Spectral band parameters of Elenovka and Soko-Banja were taken from Moroz et al. (2000).

Sample	Temperature (K)	BI (μm)	BI_{dep} (%)	BII (μm)	BII_{dep} (%)	BAR
Allegan	100	0.9179	36.71	1.8609	21.62	0.8817
Allegan	120	0.9223	35.78	1.8656	21.05	0.8612
Allegan	140	0.9237	35.98	1.8710	21.28	0.8816
Allegan	160	0.9249	36.44	1.8744	21.77	0.8748
Allegan	180	0.9245	36.74	1.8784	20.89	0.8673
Allegan	200	0.9250	34.71	1.8800	20.48	0.8709
Allegan	220	0.9253	36.30	1.8832	20.32	0.8561
Allegan	240	0.9268	36.26	1.8916	20.28	0.8347
Allegan	260	0.9288	37.26	1.8954	19.82	0.8317
Allegan	280	0.9290	35.09	1.9048	19.11	0.8457
Allegan	300	0.9296	34.24	1.9335	20.15	0.8517
El Hammammi	100	0.9212	30.91	1.8703	19.14	0.8545
El Hammammi	120	0.9243	31.87	1.8739	19.94	0.9202
El Hammammi	140	0.9237	29.32	1.8785	19.15	0.8767
El Hammammi	160	0.9249	29.97	1.8835	19.85	0.9659
El Hammammi	180	0.9272	30.02	1.8921	18.84	0.8371
El Hammammi	200	0.9277	33.44	1.8976	19.14	0.8530
El Hammammi	220	0.9281	33.18	1.9029	18.17	0.8043
El Hammammi	240	0.9284	29.96	1.9068	17.92	0.8402
El Hammammi	260	0.9302	31.67	1.9175	19.00	0.9036
El Hammammi	280	0.9329	30.65	1.9199	18.55	0.8507
El Hammammi	300	0.9339	32.53	1.9262	18.77	0.8731
Elenovka	80	0.939	37.00	1.877	22.00	0.79
Elenovka	173	0.94	39.00	1.902	19.00	0.66
Elenovka	293	0.949	40.00	1.923	17.00	0.55
Soko-Banja	80	1.061	35.00	1.950	15.00	0.64
Soko-Banja	173	1.050	35.00	1.960	15.00	0.57
Soko-Banja	293	1.044	34.00	1.970	13.00	0.45

3.3 Results and discussion

Table 3.3 shows the orbital elements of the NEAs studied. The eccentric orbits of some of these objects can bring them as close as 0.41 AU from the Sun (66146) and as far as 4.12 AU (4179 Toutatis) from it. This broad range of heliocentric distances results in objects that experience an equally broad range of average surface temperatures. This can be seen in Figure 3.11 where we have constructed a theoretical temperature curve using Eq. (3.10). The approximate orbital range of NEAs is given by the two extreme values found among the NEAs studied, i.e., the perihelion of asteroid (66146) and the aphelion of asteroid (4179 Toutatis), which correspond to a temperature range of ~ 130 to 440 K.

As described earlier, we found that the shift of the Band I center with increasing temperature is very small, and no temperature correction was derived. This decision seems to be validated after considering the two extreme temperature values (130 and 440 K), which produce a maximum shift of the Band I center of $\sim 0.012 \mu\text{m}$, which is on the order of the uncertainty associated with this parameter measured for asteroid spectra. In the case of the Band II center, we found that the increase in temperature from 130 to 440 K will shift the Band II center $\sim 0.06 \mu\text{m}$. This variation is larger than the typical uncertainty associated with the Band II center measured from asteroid spectra. Dunn et al. (2010), found that there is no significant correlation between Band II position and relative pyroxene abundance, and therefore they concluded that Band II should not be used to derive relative abundances of high-calcium pyroxene to total pyroxene from reflectance spectra. In addition, as we saw in chapter 1 in the case of olivine-orthopyroxene mixtures only the Band I center is used to derive mafic silicate compositions (see Eqs. 1.5 and 1.6), this means that the effects of temperature variations on the Band II center will do not have any influence on the mineralogical analysis. It is important to point out however, that the derived temperature correction for the Band II center is still useful and should be applied when studying the influence of other effects (e.g., phase reddening) on spectral band parameters, in order to disentangle the effects of temperature variations from these effects.

Table 3.3: NEAs orbital elements. The columns in this table correspond to: object number and designation, perihelion distance (q), aphelion distance (Q) and semimajor axis (a).

Object	q (AU)	Q (AU)	a (AU)
1036 Ganymed	1.24	4.09	2.66
1620 Geographos	0.83	1.66	1.25
1627 Ivar	1.12	2.6	1.86
1862 Apollo	0.65	2.29	1.47
1980 Tezcatlipoca	1.09	2.33	1.71
4179 Toutatis	0.94	4.12	2.53
4954 Eric	1.10	2.9	2.00
6239 Minos	0.68	1.63	1.15
11398	1.05	2.39	1.72
25143 tokawa	0.95	1.70	1.31
35107	0.97	1.30	1.14
66146	0.41	1.17	0.79

Using Eq. (3.17) we calculated the change of BAR between 130 and 440 K. We found that the increase in temperature will decrease the BAR by ~ 0.23 , which is a value much larger than the uncertainty associated with this parameter measured from asteroid spectra. This decrease in BAR will produce a slight overestimation (~ 0.06) of the olivine abundance when applying Eq. (1.9) to an olivine-orthopyroxene assemblage. Furthermore, the decrease in BAR with increasing temperature implies that objects observed at different heliocentric distances could be ambiguously classified when using the taxonomic system developed by Gaffey et al. (1993).

The variation in Band II depth with increasing temperature from 130 to 440 K using Eq. (3.15) was estimated to be 4.65 %. Although the Band II depth alone provides little quantitative information about surface mineralogy, our results suggest that a temperature correction to the Band II depth should be applied before studying the influence of other effects, like grain size and phase reddening, on this band parameter.

The results found before show how spectral band parameters are affected by a significant temperature variation corresponding to extreme heliocentric distances along the orbit of a NEA. In practice, due to observational constraints, it is unlikely that NEAs will be observed at the most extreme heliocentric distances, i.e., when the object is closest or farthest from the Sun. If the object is too close to the Sun we can not see it, on the other hand, because NEAs are in general small objects it is uncommon to observe them at far distances from the Sun, since they are too faint. If we look at the calculated average surface temperatures for the NEAs studied (Table 3.1), we found that the temperature range is much narrower ~ 130 to 265 K, with an average value of about 234 K. After applying the temperature corrections to the band parameters we found that relative to laboratory measurements obtained at room temperature (300 K), the average wavelength shift of the Band II center is $\sim 0.013 \mu\text{m}$. Overall there is a decrease of 1% in the Band II depth, and the BAR value decreases in ~ 0.055 with respect to room temperature. On average, a slight increase of ~ 0.01 in the $ol/(ol + px)$ ratio is observed after applying the temperature correction, however this value is smaller than the uncertainty associated with this quantity. These results suggest that temperature variations will have a very small impact when comparing the spectral band parameters of the NEAs studied, with those measured for laboratory samples obtained at room temperature.

For different heliocentric distances of the same asteroid in our sample, we estimated an average temperature variation of ~ 20 K. This means that, at least for the objects in this study, temperature variations do not have a significant effect when comparing band parameters of the same asteroid observed at different heliocentric distances. This can be explained by the fact that NEAs, in general, are observed when they are high in magnitude, and therefore it is likely that multiple observations of the same object have been obtained when the object was at similar distances from the Sun.

Several studies about temperature-induced effects on mafic minerals have been conducted in the laboratory, however there are not too many references in the literature regarding the effects of temperature variations on spectra of NEAs. Our results, however, seem to be in agreement with those obtained by Burbine et al. (2009) from the analysis of a group of near-Earth vestoids, which indicate an average surface temperature for NEAs of ~ 230 K, and only a very small wavelength shift of band centers relative to laboratory measurements obtained at room temperature. Although temperature variations (on average) seem to have no major effects on spectra of NEAs, each case should be evaluated separately, and temperature corrections should be applied to better quantify the influence of other effects on spectral band parameters. Therefore, in the following chapter, where we study phase reddening effect, we will work with

the temperature corrected parameters to account for any temperature contribution even if small.

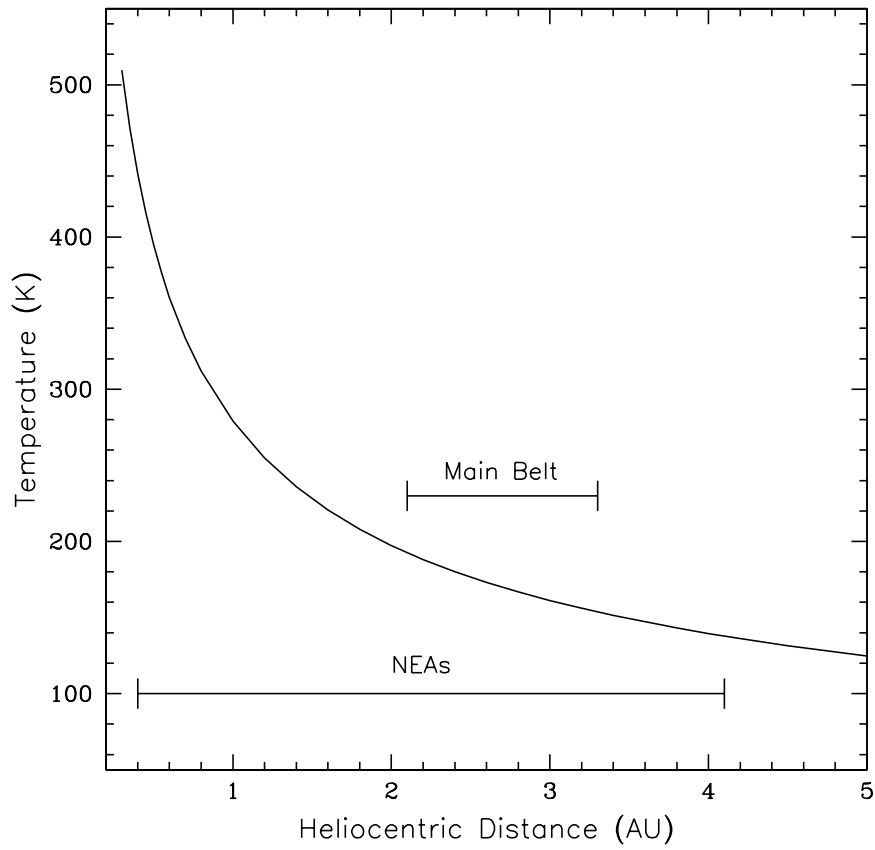


Figure 3.11: Plot of temperature vs. heliocentric distance for the entire spherical surface of an asteroid assuming instantaneous thermal equilibrium. The average surface temperature has been calculated using Eq. (2.10). The following parameters have been assumed: $A = 0.09$ (corresponding to $p_v = 0.23$; $G = 0.15$), $\varepsilon = 0.9$, and $\eta = 1$. The Main belt region and the approximate orbital range of NEAs are shown.

4 Phase reddening on NEAs

4.1 Introduction

The phase reddening effect among Solar System objects was first noticed in asteroid broad band colors. For example, Gehrels (1970) reported a phase reddening in the B-V and U-B colors of (4) Vesta to be 0.0018 and 0.0027 mag/degree, respectively. Similarly, Millis et al. (1976) obtained UBV observations of asteroid (433) Eros finding a phase reddening of 0.0009 mag/degree for B-V and 0.0004 mag/degree for the U-B color. A more extensive study carried out by Lumme and Bowell (1981) from observations of 20 C-, 21 S- and 6 M-type asteroids also found evidence of phase reddening for the three taxonomic types. The effects of phase reddening have also been observed among NEAs. Luu and Jewitt (1990) found that the spectral slopes of NEAs in general are higher than those measured for 3:1 resonance asteroids. Since NEAs are often observed at high phase angles this increase in the spectral slopes was interpreted as phase reddening.

Nathues (2000, 2010) carried out a spectroscopic and spectrophotometric survey of the Eunomia asteroid family, obtaining spectra at VIS and NIR wavelengths of 97 of its members. The analysis of the spectral slopes of these asteroids revealed an average increase of 0.067%/100 nm per degree with increasing phase angle in the range of $2^\circ < g < 24^\circ$. Apart from the increase of the spectral slope he also observed an increase of the $1 \mu\text{m}$ absorption band (depth) with increasing phase angle.

Reddy et al. (2012d), conducted an extensive study of asteroid (4) Vesta in order to quantify phase angle-induced spectral effects on this asteroid prior to the arrival of the Dawn spacecraft. Rotationally resolved NIR spectral observations ($0.7\text{-}2.5 \mu\text{m}$) at different phase angles were obtained for this purpose. Figure 4.1 shows the NIR spectra of Vesta obtained at two different phase angles. The analysis of these data revealed an increase in Band I and Band II depths of 2.35% and 1.5% respectively, for every 10° increase in phase angle in the range of $0^\circ < g \leq 25^\circ$. This can be seen in Figure 4.2 where we have plotted the measured Band I and Band II depths as a function of phase angle for asteroid (4) Vesta. From these results we were able to derive equations to correct for the effects of phase reddening on band depths. These equations are presented in Reddy et al. (2012d) and are given by:

$$BI_{depc} = BI_{dep} - 0.2402 \times g \quad (4.1)$$

$$BII_{depc} = BII_{dep} - 0.1525 \times g \quad (4.2)$$

where BI_{dep} and BII_{dep} are the measured band depths and BI_{depc} and BII_{depc} are the corrected band depths. An increase of 0.3 in BAR for every 10° increase in phase angle was also

found. Similarly to the band depths, an equation to correct for the effects of phase reddening was derived. This equation is presented in Reddy et al. (2012d) and is given by:

$$BAR_c = BAR - 0.0292 \times g \quad (4.3)$$

where BAR and BAR_c are the measured and corrected band area ratios respectively.

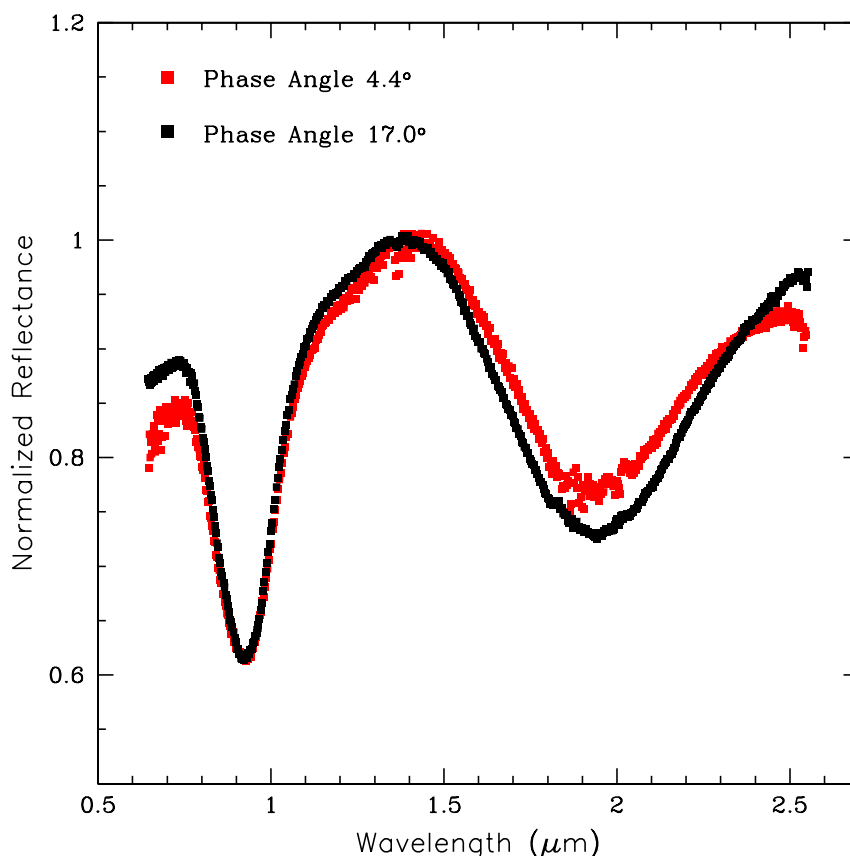


Figure 4.1: Full rotation average NIR spectra of Vesta taken at 4.4° (red) and 17.0° (black) phase angle. The data is normalized to unity at $1.4 \mu\text{m}$. Figure from Reddy et al. (2012d).

The phase reddening effect has also been detected and quantified from spacecraft observations of asteroids. The NEAR Shoemaker spacecraft obtained NIR spectroscopic observations ($0.8\text{-}2.4 \mu\text{m}$) of asteroid (433) Eros at phase angles ranging from 0° to 100° . These observations showed the most intense phase reddening for wavelengths inside of the $1.0 \mu\text{m}$ band, occurring at the level of 10% across this phase angle range (Clark et al. 2002b, Bell et al. 2002). Similar results were observed from NIR reflectance spectra ($0.76\text{-}2.25 \mu\text{m}$) of asteroid (25143) Itokawa acquired by the NIRS instrument of the Hayabusa spacecraft, which revealed an increase of 3% and 1% in Band I and Band II depths respectively, with increasing phase angle between 10° and 40° (Kitazato et al. 2008).

Ground-based observations of the Moon have also found evidence for phase reddening. Lane and Irvine (1973) obtained photometric observations of the entire lunar disk over phase angles $6^\circ \leq g \leq 120^\circ$ in nine narrow bands ($0.35\text{-}1.0 \mu\text{m}$) and in UVB. The phase curves obtained

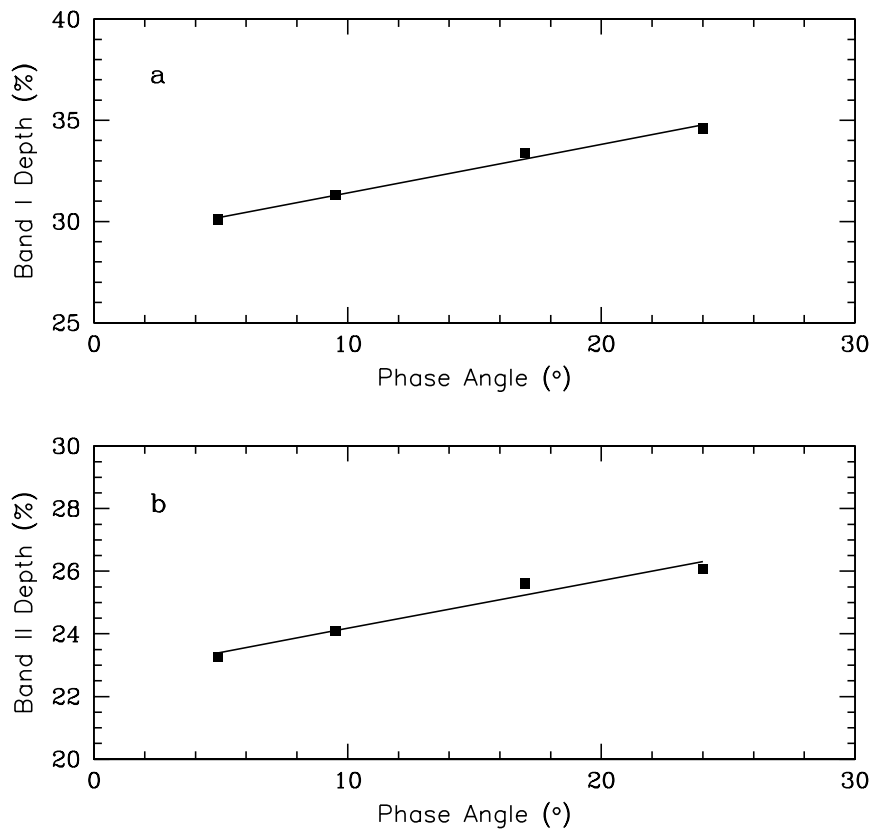


Figure 4.2: Change in Vesta's Band I (panel a) and Band II (panel b) depths as a function of phase angle. The 1- σ error of Band I and Band II depths (0.1%) is smaller than the data points. The black lines are linear fits through the measured values. Data from Reddy et al. (2012d).

for each pass band showed a trend where the light drops gradually more slowly with phase angle as wavelength increases. These results confirmed the phase reddening observed for particular areas of the Moon reported by previous studies (e.g., Gehrels et al. 1964, Hayakawa et al. 1968).

Laboratory measurements of different materials have confirmed the existence of the phase reddening effect. Adams and Filice (1967) studied different particulate rocks and minerals, finding changes in the R/B color (ratio of the reflectance at $0.7 \mu\text{m}$ to that at $0.4 \mu\text{m}$) with increasing phase angle. They noted a general increase of the R/B color from 15° to 30° - 50° (depending on the sample) and then a decrease at higher phase angles. Gradie et al. (1980) investigated phase angle induced effects on the spectrophotometric properties of powdered materials. Among the materials studied, they analyzed the C3 carbonaceous chondrite Allende, a terrestrial basalt sample, the pyroxene hedenbergite and the L6 chondrite Bruderheim. The reflectance spectra of these materials were obtained at phase angles of $4^\circ \leq g \leq 120^\circ$, in the wavelength range $0.4 \leq \lambda \leq 1.2 \mu\text{m}$. All the samples studied showed a significant reddening as the phase angle increases from 4 to 120° . Furthermore, the hedenbergite and the L6 sample showed variations in the spectral contrast of the absorption bands with increasing phase angle.

More recently, Mann et al. (2011) obtained laboratory spectra (0.35 to $2.5 \mu\text{m}$) of the

Moama eucrite and a Fe-rich orthopyroxene at phase angles ranging from 13° to 120° . Their analysis of these spectra showed variations on band centers, band depths, band areas, absolute reflectance and spectral slope. The effect of phase reddening on band depths was also noticed by Shepard and Cloutis (2011) who acquired laboratory spectra (0.4 to $1.0 \mu\text{m}$) of a particulate sample of lazurite, finding variations of up to 20% in the band depth of the $0.6 \mu\text{m}$ feature over the phase angle range of 3° to 140° .

Despite the fact that phase reddening has been known for a long time, its effect on the analysis of asteroid spectra has not been fully assessed. In this chapter we investigate the phase reddening on NEAs and its implications for mineralogical analysis, space weathering and taxonomic classification. This study focuses on the analysis of 27 VNIR spectra corresponding to 12 NEAs already described in chapter 2. In addition to the ground-based observations, laboratory spectra of ordinary chondrites are also analyzed and the results compared to those obtained from the asteroid spectral data. The following discussion describes the work published in Sanchez et al. (2012).

4.2 Phase reddening from ground-based observations of NEAs

4.2.1 Phase reddening effect on the band parameters

An inspection of the measured Band I depths presented in Table 3.1 indicates a change of this parameter with phase angle. These values are plotted as a function of phase angle in Figure 4.3. The black circles represent the measured Band I depths. Values derived from multiple observations of individual asteroids are connected by lines and have been displayed into two panels for clarity. A tendency of increasing spectral contrast as the phase angle increases is observed for most of the objects in the range of $\sim 2^\circ < g < 70^\circ$. When higher phase angles are included (up to $\sim 90^\circ$) a slight decrease in Band I depth is observed. However, as we do not have sufficient data at such high phase angles, it remains unclear whether this is the actual tendency for $g > 70^\circ$. A similar situation is observed with the temperature corrected Band II depths (Fig. 4.4). In this case the depth of the absorption band seems to increase in the range of $\sim 2^\circ < g < 55^\circ$ and then it remains more or less constant for higher phase angles. In some cases we notice a deviation from these trends among the measured band depths, i.e., a decrease of band depths with increasing phase angle. Although compositional variations cannot be completely ruled out, this is more likely due to the fact that some spectra show more scattering than others, especially in the Band II. This is probably caused by an incomplete correction of the telluric water bands, and due to the decreased response of the detector for wavelengths beyond $2.4 \mu\text{m}$. This was seen in the Band I of asteroids 1036 Ganymed ($g = 15.2^\circ$) and 4954 Eric ($g = 62^\circ$) and in the Band II of asteroids 1620 Geographos ($g = 38.3^\circ$), 1627 Ivar ($g = 31.0^\circ$) and 1980 Tezcatlipoca ($g = 54.6^\circ$).

In an effort to quantify the phase reddening effect on band depths we performed a linear fit to the data of each asteroid. Only the data in the phase angle ranges where the correlations are observed were fitted. Those values that deviate from the general tendency were not considered. The equations derived from the linear fits were then averaged to obtain a general expression for each band depth. Previous works have derived correlations between band parameters and phase angle (e.g., Luu and Jewitt 1990, Moskovitz et al. 2010). However, these correlations were obtained from mixed observations of different objects, making it very difficult to disentangle the phase reddening from other effects. Our approach, on the other hand, attempts to overcome

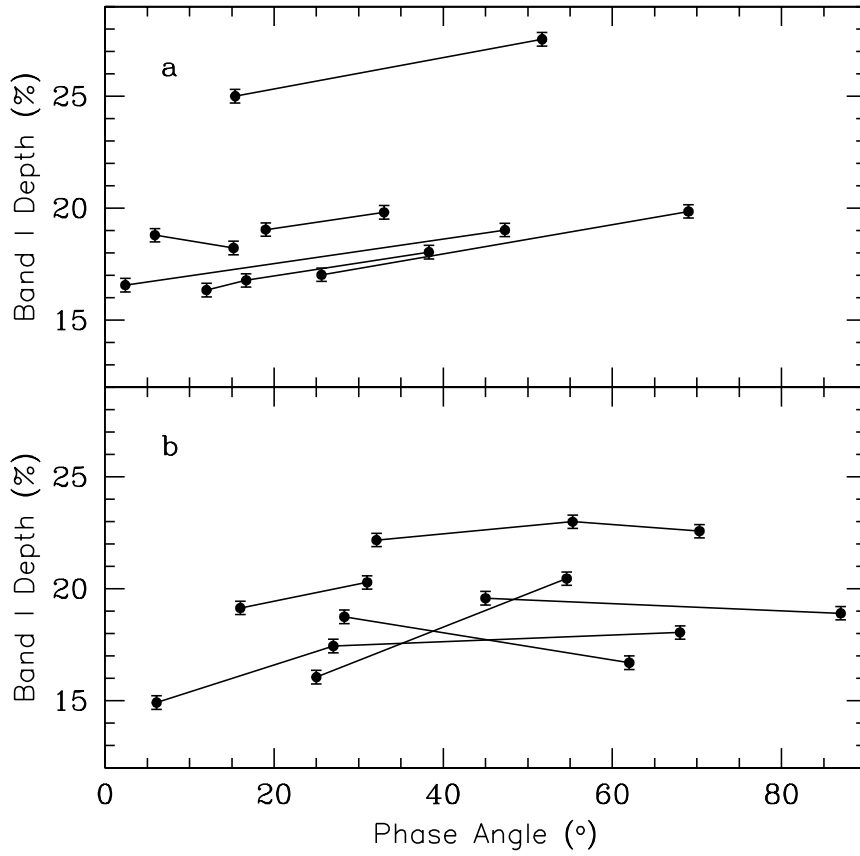


Figure 4.3: Band I depth as a function of phase angle for the NEAs. Values derived from multiple observations of individual asteroids are connected by lines and have been displayed into two panels for clarity. Figure from Sanchez et al. (2012).

this problem by evaluating the phase reddening on individual objects from which an average expression is then derived. We caution that this procedure only provides a rough estimation of the effects of phase reddening on band depths, since for each asteroid we have a limited phase angle range. The general equations for the band depths are given by

$$BI_{dep}(g) = 0.066 \times (g) + 17.42 \quad (4.4)$$

$$BII_{dep}(g) = 0.093 \times (g) + 3.73 \quad (4.5)$$

where the band depths are measured in %. Thus, according to these equations, on average, Band I and Band II depths will increase 0.66% and 0.93% respectively, for every 10° increase in phase angle in the range of $2^\circ < g < 70^\circ$ for Band I and $2^\circ < g < 55^\circ$ for Band II.

From equations (4.4) and (4.5) we can obtain expressions for band depth corrections that are a function of the phase angle,

$$BI_{dep_c} = BI_{dep} - 0.066 \times (g) \quad (4.6)$$

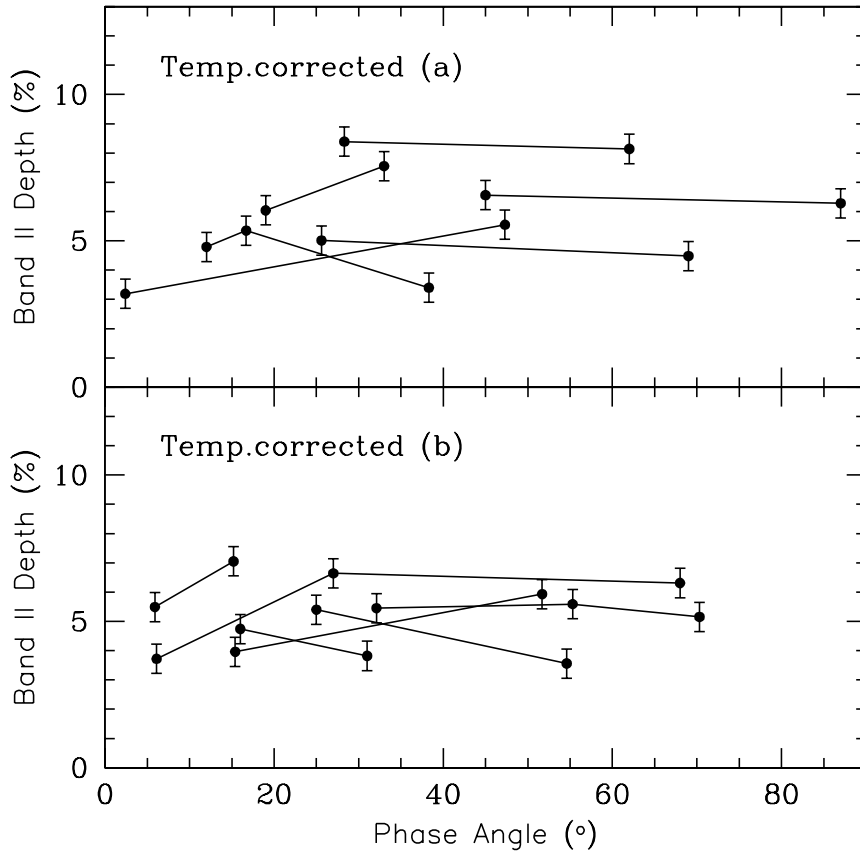


Figure 4.4: Temperature corrected Band II depth as a function of phase angle for the NEAs. Values derived from multiple observations of individual asteroids are connected by lines and have been displayed into two panels for clarity. Figure from Sanchez et al. (2012).

$$BII_{depc} = BII_{dep} - 0.093 \times (g) \quad (4.7)$$

where BI_{depc} and BII_{depc} are the corrected band depths. With these equations we can roughly correct the effect of phase reddening in the band depths in the phase angle ranges of $2^\circ < g < 70^\circ$ for Band I and $2^\circ < g < 55^\circ$ for Band II.

The temperature corrected BAR values presented in Table 3.1 and plotted in Figure 4.5 indicate variations with increasing phase angle, however no obvious trend can be seen. The most significant change in BAR is observed for the same objects whose absorption bands show more scattering.

Small variations on band centers with increasing phase angle were found, however they are within the uncertainties associated with these band parameters. This can be seen in Figures 4.6 and 4.7 where we plotted Band I and Band II centers respectively, as a function of phase angle for the NEAs. The black circles represent the measured band centers. Values derived from multiple observations of the same asteroids are connected by lines.

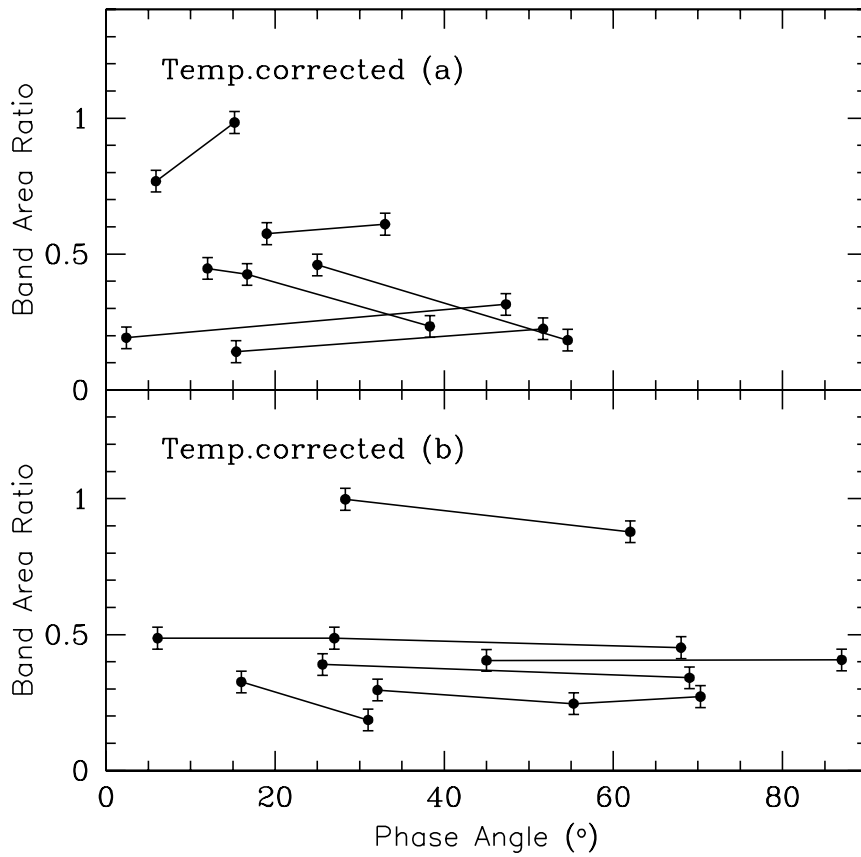


Figure 4.5: Temperature corrected BAR values as a function of phase angle for the NEAs. Values derived from multiple observations of individual asteroids are connected by lines and have been displayed into two panels for clarity. Figure from Sanchez et al. (2012).

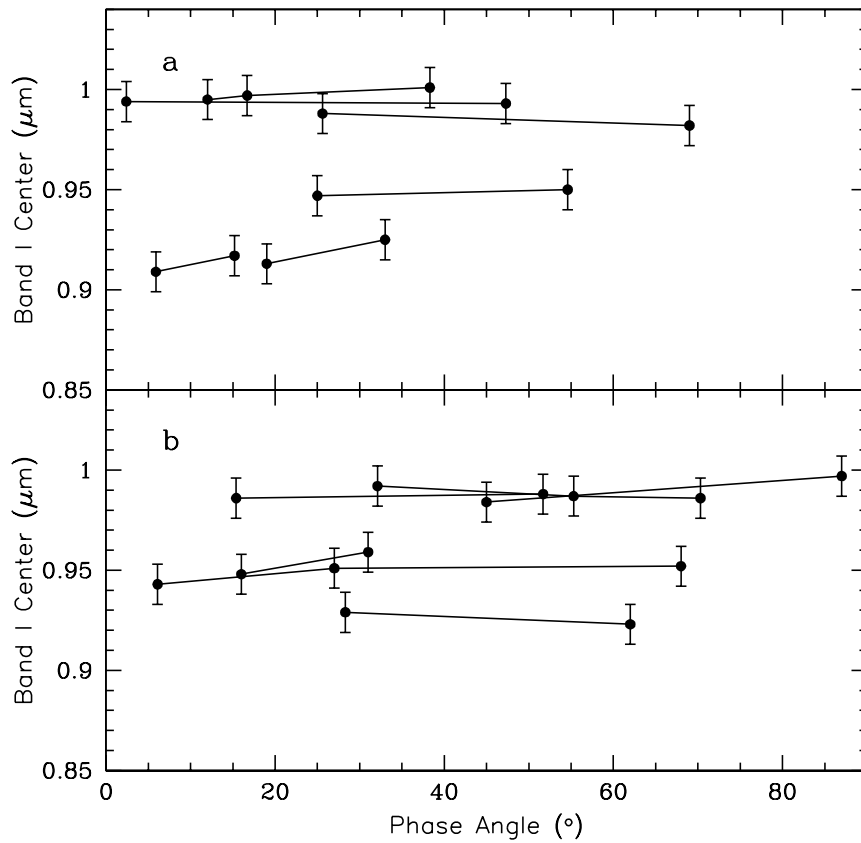


Figure 4.6: Band I center as a function of phase angle for the NEAs. Values derived from multiple observations of individual asteroids are connected by lines and have been displayed into two panels for clarity. Figure from Sanchez et al. (2012).

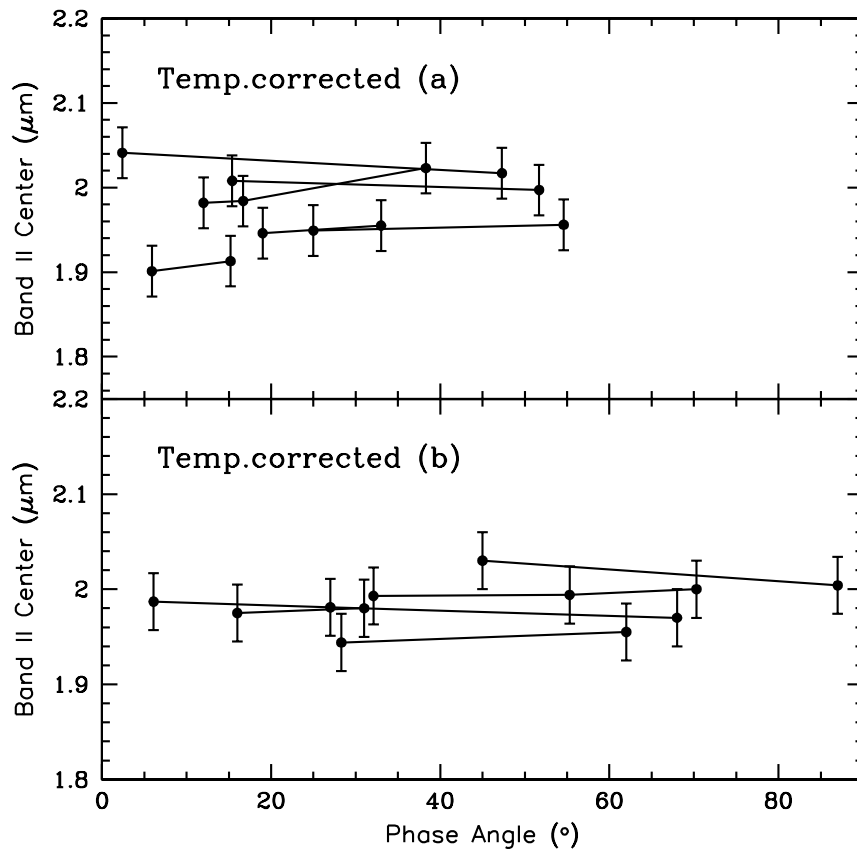


Figure 4.7: Band II center as a function of phase angle for the NEAs. Values derived from multiple observations of individual asteroids are connected by lines and have been displayed into two panels for clarity. Figure from Sanchez et al. (2012).

4.3 Phase reddening from laboratory measurements of ordinary chondrites

4.3.1 Data and spectral band analysis

As it was stated before, ordinary chondrites are considered to be the meteorite analogs of S-complex and Q-type asteroids. Therefore, in order to complement our study we have analyzed the spectra of a group of ordinary chondrites obtained at a wide range of phase angles.

Diffuse reflectance spectra were collected at the University of Winnipeg Planetary Spectrophotometer Facility (UWPSF) using an ASD FieldSpec Pro HR spectrometer covering the wavelength range of 0.35 to 2.5 μm . The three samples that have been analyzed are Dhurmsala (LL6, fell 1860), Pavlograd (L6, fell 1826), and Lancon (H6, fell 1897). They were all crushed and sieved to a grain size of $< 150 \mu\text{m}$. The samples were gently poured into aluminum sample cups and the edge of a glass slide was drawn across the sample to provide a flat surface for the spectral measurements. Reflectance spectra were acquired relative to a 100% Labsphere Spectralon disk measured at an incident angle $i=13^\circ$ and emission angle $e=0^\circ$ (13° phase angle). Ten sets of measurements were acquired for each sample resulting in three emission angles ($e=0^\circ, 30^\circ, 60^\circ$), five incidence angles ($i=0^\circ, 13^\circ, 30^\circ, -30^\circ, 60^\circ$) and five different phase angles ranging from 13° to 120° . Positive angles (i and e) are measured when the light source and the detector are on either side of the normal, while negative incidence angles are measured when both light source and detector are on the same side of the normal. Figure 4.8 shows the goniometer used to acquire the spectra. For each measurement, a total of 250 scans were collected and averaged to improve the signal to noise ratio.

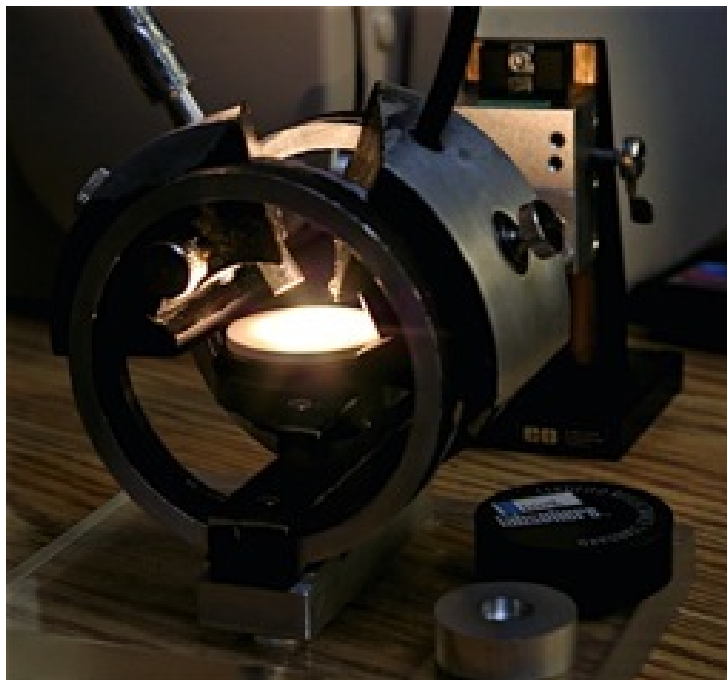


Figure 4.8: Goniometer used to acquire laboratory spectra at the University of Winnipeg Planetary Spectrophotometer Facility. Reproduced from <http://psf.uwinnipeg.ca/Facilities.html>.

Spectral band parameters and their uncertainties were measured for each VNIR spectrum using the same methods applied to the asteroid spectra. In addition to the band parameters we have also measured the spectral slope. This parameter was not measured from the asteroid spectra since it is known to be very sensitive to various factors. Apart from the viewing geometry, atmospheric differential refraction (Filippenko 1982), airmass differences between the standard star and the asteroid at the time of the observations (DeMeo et al. 2011), incorrect centering of the object in the slit (Cushing et al. 2004), poor weather conditions (Bus et al. 2002) and the use of different solar analogs (Sunshine et al. 2004) are often the cause of fluctuations in the asteroid's spectral slope. In some cases, the origin of these error sources is difficult to determine since they are seen as nonsystematic variations in the final asteroid reflectance spectrum (Hardersen et al. 2006). Therefore, in order to better quantify the effect of phase reddening on the spectral slope we only measured it from the laboratory spectra. The spectral slope was determined from the fitted continuum across Band I, i.e., a straight line tangent to the reflectance peaks from ~ 0.7 to $\sim 1.55 \mu\text{m}$. The uncertainty is given by the average $1-\sigma$, estimated from sampling different ranges of points near the reflectance peaks on either side of the absorption band. In addition, the olivine-pyroxene abundance ratio of the samples was estimated using Eq.(1.9). The band parameters, spectral slopes and $ol/(ol + px)$ ratios with their corresponding errors obtained for each sample are presented in Table 4.1.

4.3.2 Phase reddening effect on the band parameters

The analysis of the laboratory spectra shows that variations in the band parameters can arise not only by changing the phase angle, but also for the same phase angle using different configurations of the incidence and emission angle. As can be seen in Table 4.1, phase angles of 30° , 60° and 90° were obtained using different combinations of i and e , and these different combinations produced, in some cases, very different band parameter values. Since we want to quantify the effects of phase reddening on the spectral band parameters, for those phase angles where more than one combination of i and e was used the average value for each band parameter was taken. These average values are presented in Table 4.1.

Figures 4.9 to 4.11 show the reflectance spectra of the LL6, L6 and H6 ordinary chondrites respectively, at five different phase angles. From the bottom to the top the phase angles are 13° , 30° , 60° , 90° and 120° . The spectra corresponding to $g = 30^\circ$, 60° and 90° are average spectra obtained from different combinations of incidence and emission angles. All the spectra are normalized to unity at $0.55 \mu\text{m}$. An increase in the spectral slope with increasing phase angle is evident for the three samples, being more significant for phase angles higher than 30° . For phase angles between 13° and 30° a slight reddening is observed in the LL6 spectra, while a slight blueing (i.e., decreasing of the spectral slope with increasing phase angle) is seen in the L6 and H6 spectra. Variations on the strength of the absorption bands are also seen for the three samples.

In Figures 4.12, 4.13 and 4.14 we plotted the spectral slopes (panel a), the BAR values (panel b), the Band I depths (panel c), the Band II depths (panel d) and the band centers (panels e and f) as a function of the phase angle for the LL6, L6 and H6 respectively. The dashed lines are polynomial fits.

From the "a" panels we can see that the measured spectral slopes in the three samples remain more or less constant for phase angles between 13° and 30° , and then they increase as the phase angle increases up to 120° . The largest difference in spectral slope between the lowest (13°)

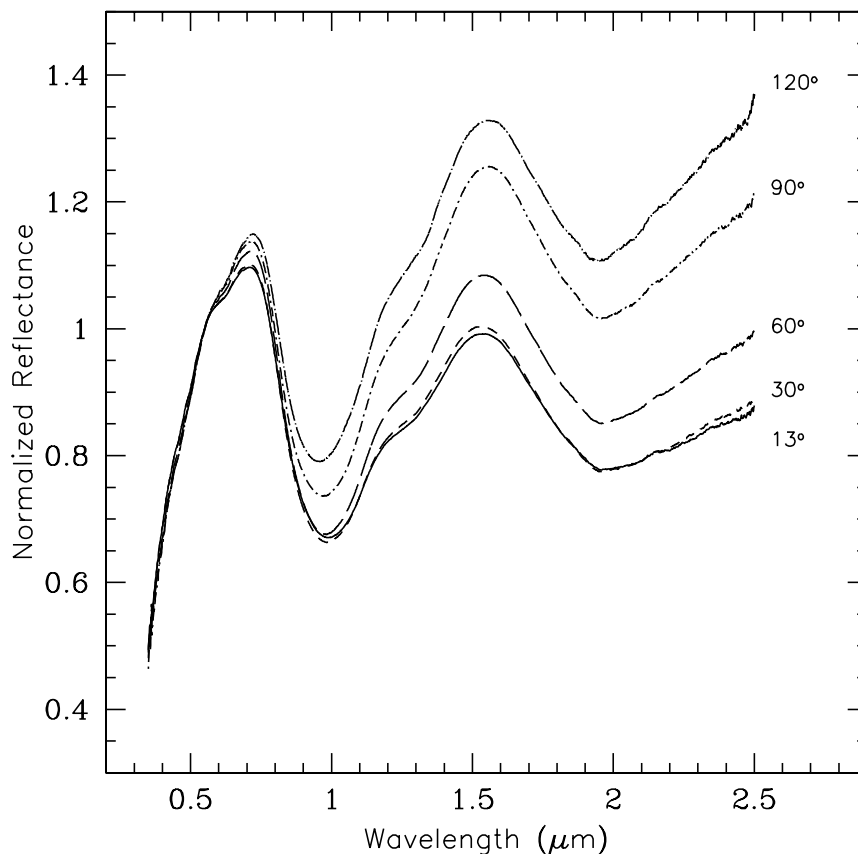


Figure 4.9: Reflectance spectra of the LL6 chondrite Dhurmsala obtained at five different phase angles. From the bottom to the top $g=13^\circ$ (solid line), $g=30^\circ$ (short dashed line), $g=60^\circ$ (long dashed line), $g=90^\circ$ (dot-short dashed line) and $g=120^\circ$ (dot-long dashed line). All the spectra are normalized to unity at $0.55 \mu\text{m}$. Figure from Sanchez et al. (2012).

and the highest (120°) phase angle was found for the LL6 ordinary chondrite, which increased $0.34 \mu\text{m}^{-1}$, followed by the L6 ordinary chondrite with an increase of $0.29 \mu\text{m}^{-1}$ and the H6 ordinary chondrite with an increase of $0.16 \mu\text{m}^{-1}$.

The Band I depth of the three samples has its maximum spectral contrast near $g = 60^\circ$. The LL6 spectra show a progressive increase of Band I depth from $g = 13^\circ$ to 60° (Fig. 4.12 panel c), however the L6 and H6 spectra show almost no change in Band I depth for phase angles between 13° and 30° , and then an increase in Band I depth from $g = 30^\circ$ to 60° (Figs. 4.13 and 4.14 panel c). The spectra of the three samples show a decrease in Band I depth between 60° and 120° phase angle. The largest increase in Band I depth between the lowest phase angle (13°) and the phase angle at which the Band I reaches its maximum spectral contrast ($\sim 60^\circ$) corresponds to the LL6 sample, with an increase of 2.25%, followed by the L6 and H6 with an increase of 1.36 and 0.53% respectively. Of the three samples, the LL6 also shows the most significant decrease of Band I depth between the phase angle corresponding to the maximum spectral contrast and the highest phase angle (120°), with a decrease of 4.88%, followed by the H6 with a decrease of 4.21% and the L6 with a decrease of 3.89%

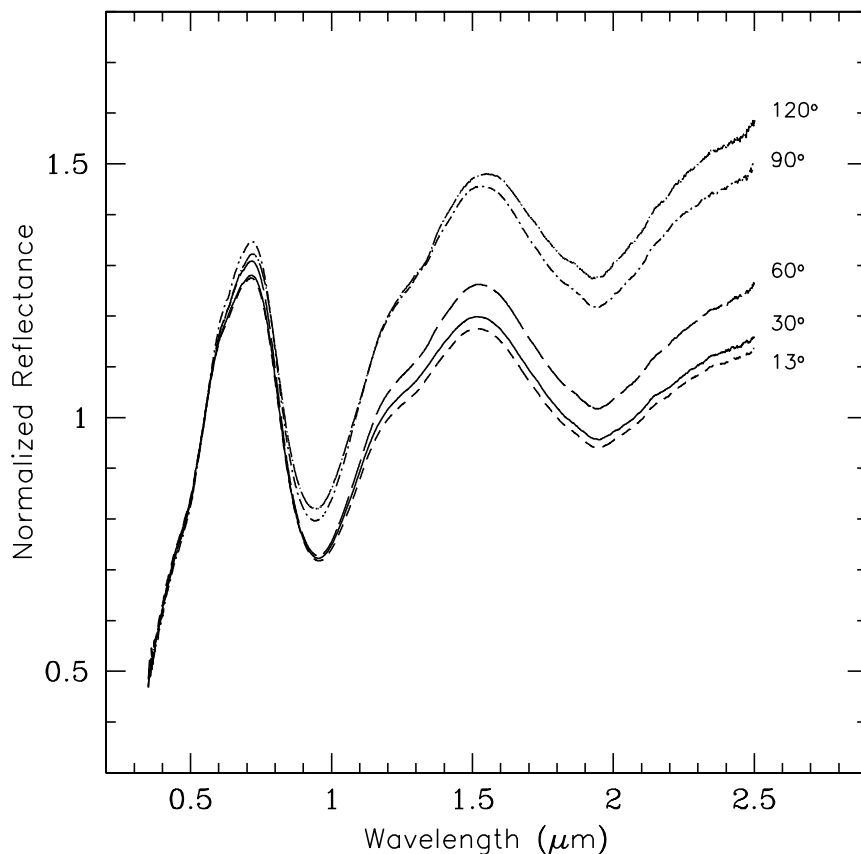


Figure 4.10: Reflectance spectra of the L6 chondrite Pavlograd obtained at five different phase angles. From the bottom to the top $g=13^\circ$ (solid line), $g=30^\circ$ (short dashed line), $g=60^\circ$ (long dashed line), $g=90^\circ$ (dot-short dashed line) and $g=120^\circ$ (dot-long dashed line). All the spectra are normalized to unity at $0.55 \mu\text{m}$. Figure from Sanchez et al. (2012).

The behavior of the Band II depths seems to be more complex. The LL6 spectra show a progressive increase of Band II depths from $g = 13^\circ$ to $\sim 45^\circ$ (where the band reaches its maximum spectral contrast) and then it drops between 45° and 90° , becoming more or less constant from 90° to 120° phase angle (Fig. 4.12 panel d). The Band II depths of the L6 spectra show almost no change between 13° and 30° . From 30° to 60° Band II depths increase and beyond 60° gradually decrease with phase angle increasing to 120° (Fig. 4.13 panel d). The Band II depths of the H6 spectra show a slight increase from 13° to 30° and then drop from 30° to 120° (Fig. 4.14 panel d). The most significant increase in Band II depths between the lowest phase angle and the phase angle at which the Band II reaches its maximum spectral contrast was observed for the LL6 sample, which shows an increase of 1.56%, followed by the L6 with an increase in Band II depth of 0.56% and the H6 with the lowest increase of 0.16%. The largest difference in Band II depth between the phase angle corresponding to the maximum spectral contrast and the largest phase angle (120°) was observed for the L6 sample that shows a decrease of 3.11%, followed by the H6 with a decrease of 3.02% and the L6 with a decrease of 1.33%.

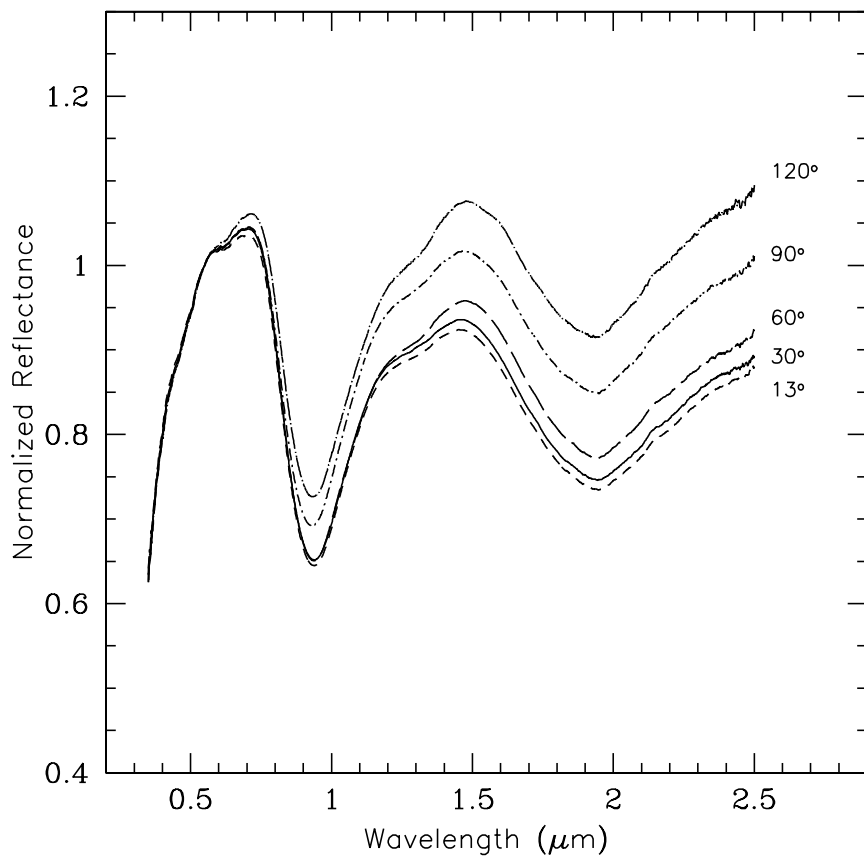


Figure 4.11: Reflectance spectra of the H6 chondrite Lancon obtained at five different phase angles. From the bottom to the top $g=13^\circ$ (solid line), $g=30^\circ$ (short dashed line), $g=60^\circ$ (long dashed line), $g=90^\circ$ (dot-short dashed line) and $g=120^\circ$ (dot-long dashed line). All the spectra are normalized to unity at $0.55 \mu\text{m}$. Figure from Sanchez et al. (2012).

Variations in the BAR values are observed among the three samples, being the maximum difference between the lowest and highest phase angle ~ 0.1 , however no systematic trends were found (Figs. 4.12-4.14 panel b). A similar situation occurs with the band centers, where the maximum shift (to shorter wavelengths) between the lowest and highest phase angle is $\sim 0.01 \mu\text{m}$ for the Band I center of the LL6 sample (Fig. 4.12 panel e).

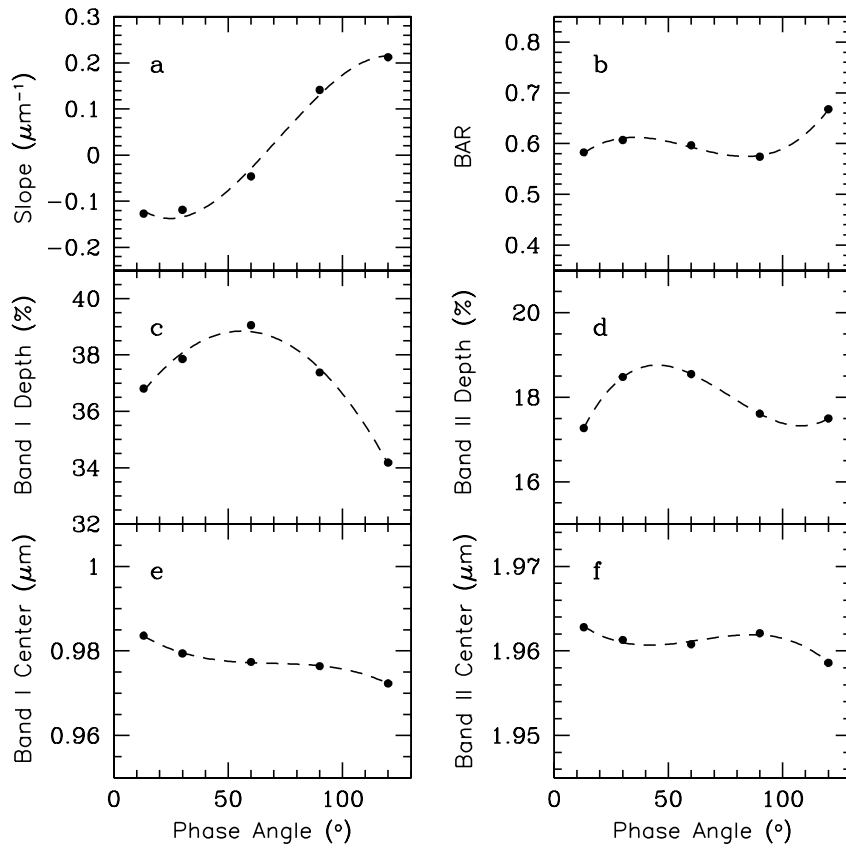


Figure 4.12: LL6 ordinary chondrite: Measured spectral slopes (a), BAR values (b), Band I depths (c), Band II depths (d) Band I centers (e) and Band II centers (f) as functions of the phase angle. The error bars are smaller than the symbols. The dashed lines represent polynomial fits. Figure from Sanchez et al. (2012).

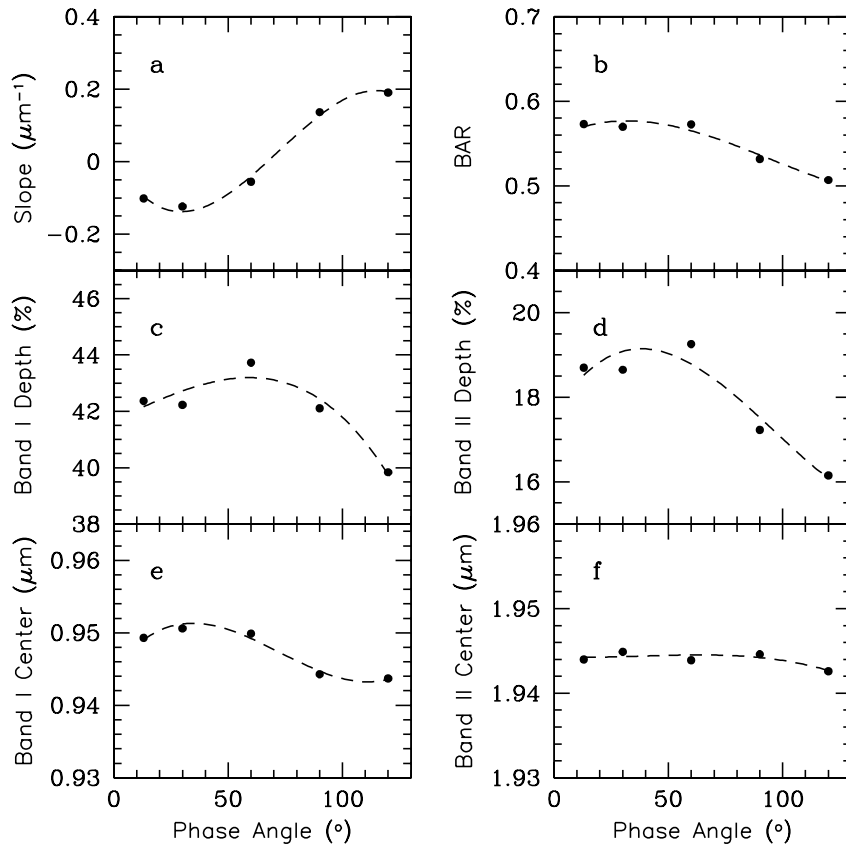


Figure 4.13: L6 ordinary chondrite: Measured spectral slopes (a), BAR values (b), Band I depths (c), Band II depths (d) Band I centers (e) and Band II centers (f) as functions of the phase angle. The error bars are smaller than the symbols. The dashed lines represent polynomial fits. Figure from Sanchez et al. (2012).

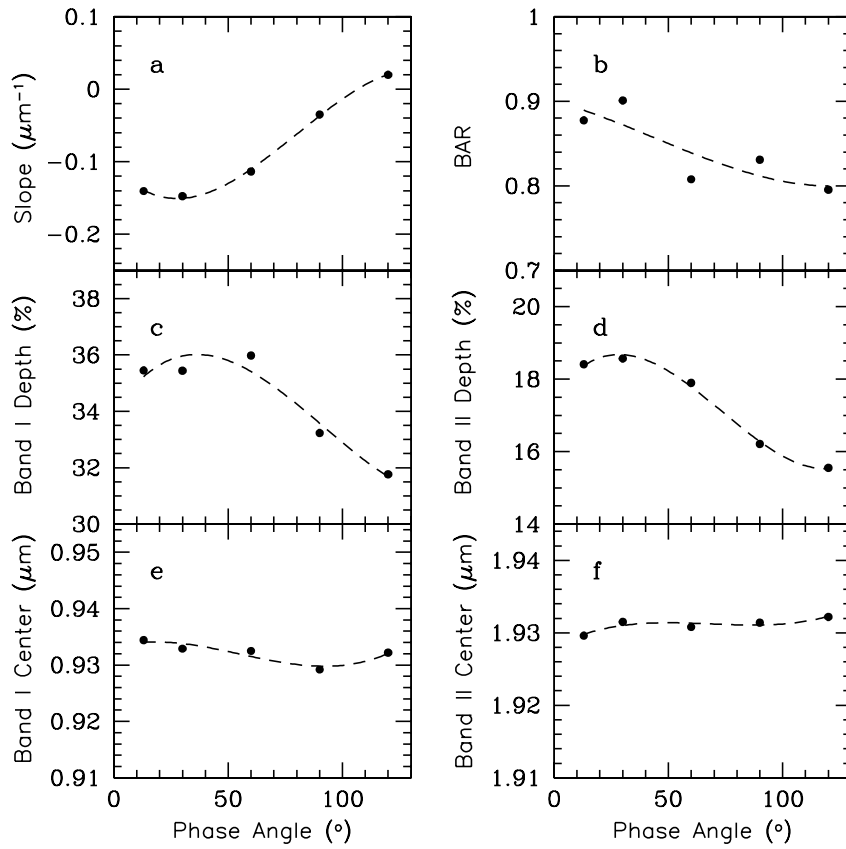


Figure 4.14: H6 ordinary chondrite: Measured spectral slopes (a), BAR values (b), Band I depths (c), Band II depths (d) Band I centers (e) and Band II centers (f) as functions of the phase angle. The error bars are smaller than the symbols. The dashed lines represent polynomial fits. Figure from Sanchez et al. (2012).

Table 4.1: Spectral band parameters of the ordinary chondrites. The columns in this table correspond to: sample type, incidence angle (i), emission angle (e), phase angle (g), spectral slope ± 0.004 , Band I center ($BI \pm 0.003$), Band I depth ($BI_{dep} \pm 0.1$), Band II center ($BII \pm 0.005$), Band II depth ($BII_{dep} \pm 0.2$), band area ratio ($BAR \pm 0.01$) and olivine-pyroxene abundance ratio ($ol/(ol+px) \pm 0.03$).

Sample	i (°)	e (°)	g (°)	Slope (μm^{-1})	BI (μm)	BI_{dep} (%)	BII (μm)	BII_{dep} (%)	BAR	ol/(ol+px)
LL6	13	0	13	-0.127	0.984	36.81	1.963	17.27	0.58	0.59
LL6	30	0	30	-0.094	0.982	38.41	1.959	18.35	0.58	0.59
LL6	0	30	30	-0.083	0.978	38.47	1.961	18.73	0.61	0.58
LL6	-30	60	30	-0.179	0.978	36.69	1.964	18.36	0.63	0.58
LL6	30,0,-30	0,30,60	30	-0.119	0.979	37.86	1.961	18.48	0.61	0.58
LL6	60	0	60	0.002	0.981	40.28	1.957	18.55	0.55	0.59
LL6	0	60	60	-0.097	0.969	37.30	1.965	18.89	0.68	0.56
LL6	30	30	60	-0.043	0.982	39.61	1.960	18.22	0.56	0.59
LL6	60,0,30	0,60,30	60	-0.046	0.977	39.06	1.961	18.55	0.60	0.58
LL6	60	30	90	0.099	0.973	37.91	1.963	18.75	0.62	0.58
LL6	30	60	90	0.184	0.980	36.84	1.961	16.46	0.53	0.60
LL6	60,30	30,60	90	0.141	0.976	37.38	1.962	17.61	0.57	0.59
LL6	60	60	120	0.212	0.972	34.18	1.959	17.50	0.67	0.57
L6	13	0	13	-0.102	0.949	42.37	1.944	18.70	0.57	0.59
L6	30	0	30	-0.090	0.951	42.71	1.943	18.92	0.56	0.59
L6	0	30	30	-0.089	0.950	42.39	1.945	19.03	0.58	0.59
L6	-30	60	30	-0.192	0.950	41.58	1.947	18.00	0.57	0.59
L6	30,0,-30	0,30,60	30	-0.124	0.951	42.23	1.945	18.65	0.57	0.59
L6	60	0	60	-0.084	0.954	43.16	1.945	18.21	0.51	0.60
L6	0	60	60	-0.085	0.949	43.36	1.948	18.73	0.59	0.59
L6	30	30	60	0.004	0.947	44.68	1.939	20.86	0.62	0.58
L6	60,0,30	0,60,30	60	-0.055	0.950	43.73	1.944	19.26	0.57	0.59
L6	60	30	90	0.097	0.945	42.53	1.941	17.21	0.51	0.61
L6	30	60	90	0.177	0.944	41.69	1.948	17.24	0.56	0.59
L6	60,30	30,60	90	0.137	0.944	42.11	1.945	17.23	0.54	0.60
L6	60	60	120	0.191	0.944	39.84	1.943	16.15	0.51	0.61
H6	13	0	13	-0.141	0.934	35.45	1.930	18.41	0.88	0.52
H6	30	0	30	-0.151	0.935	36.20	1.929	19.12	0.89	0.51
H6	0	30	30	-0.115	0.933	35.33	1.934	18.33	0.88	0.52
H6	-30	60	30	-0.177	0.931	34.80	1.931	18.26	0.93	0.50
H6	30,0,-30	0,30,60	30	-0.148	0.933	35.44	1.932	18.57	0.90	0.51
H6	60	0	60	-0.149	0.935	36.48	1.926	18.91	0.83	0.53
H6	0	60	60	-0.096	0.929	34.54	1.935	16.93	0.84	0.52
H6	30	30	60	-0.096	0.933	36.93	1.931	17.85	0.76	0.55
H6	60,0,30	0,60,30	60	-0.114	0.933	35.98	1.931	17.90	0.81	0.53
H6	60	30	90	-0.058	0.932	34.77	1.928	17.65	0.83	0.53
H6	30	60	90	-0.012	0.926	31.69	1.934	14.77	0.84	0.53
H6	60,30	30,60	90	-0.035	0.929	33.23	1.931	16.21	0.83	0.53
H6	60	60	120	0.020	0.932	31.77	1.932	15.55	0.80	0.54

4.4 Results and discussion

4.4.1 Phase reddening and mineralogical analysis

The analysis of the laboratory samples indicate that the (olivine-rich) LL6 ordinary chondrite is the most affected by phase reddening. This sample shows the largest variation in spectral slopes and band depths with increasing phase angles. This material-dependence of the phase reddening confirms the results reported by previous studies (e.g., Adams and Filice 1967, Gradie et al. 1980). A comparison between the measurements obtained from the laboratory samples with those from the NEAs spectra, reveal that the changes in band depths for the ordinary chondrites are lower than those found for the asteroids. Differences in grain size, composition and packing between the NEAs studied and the meteorite samples could explain this discrepancy. Of the three samples, the spectral behavior of the LL6 is the closest to the NEAs. This resemblance could be attributed to the fact that half of the asteroids studied are located in the same region as the LL ordinary chondrites in the Band I center versus BAR diagram (see Figs. 4.22 and 4.23).

Because band centers and composition of mafic minerals are related, this band parameter is used to derive information about the pyroxene and olivine composition of asteroid surfaces. For that purpose, and from the analysis of laboratory samples, different empirical equations have been derived (e.g., Gaffey et al. 2002, Burbine et al. 2007, Dunn et al. 2010). Our results show that there is no significant change in band centers with increasing phase angle for both asteroid and meteorite spectra. The largest observed shift is $\sim 0.01 \mu\text{m}$ (for the meteorite spectra), which is on the order of the uncertainty associated with this parameter for the asteroid spectra. Based on this, it seems unlikely that phase reddening could lead to a misinterpretation of mineral compositions in asteroids. This can be seen in Figure 4.15 where we have plotted the molar contents of Fs versus Fa for the LL6 (black circles), L6 (red squares) and H6 (blue triangles) ordinary chondrites, calculated using Eqs. (1.5) and (1.6) from the measured Band I centers obtained at five different phase angles. The variations in molar contents of Fs and Fa for the three samples are within the error bars.

In addition to the band centers, we used the BAR values and Eq. (1.9) to estimate olivine and pyroxene abundances for both NEAs and the laboratory samples. The results obtained (Tables 3.1 and 4.1) show that the largest variation in the $ol/(ol + px)$ ratio with increasing phase angles for NEAs is ~ 0.02 (not taken into account the values obtained from the noisy spectra), and for the ordinary chondrites between 0.03 and 0.05. Since these variations are on the order of the errors, effects of phase reddening on the estimation of the olivine-pyroxene abundance ratio seems to be negligible.

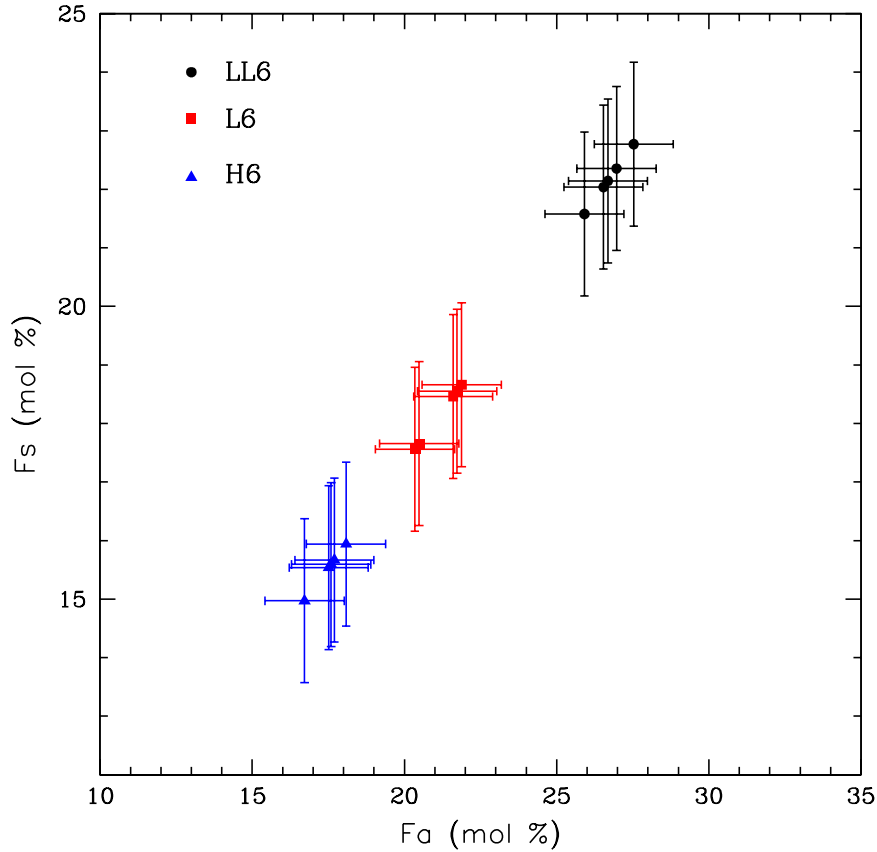


Figure 4.15: Molar contents of Fs vs. Fa for the LL6 (black circles), L6 (red squares) and H6 (blue triangles) ordinary chondrites, calculated using Eqs. (1.5) and (1.6) from the measured Band I centers obtained at five different phase angles.

4.4.2 Phase reddening and space weathering

In chapter 1 we discussed space weathering effect on asteroids, and we reviewed some of the experiments that were conducted in the laboratory in order to understand the physical mechanism responsible for the weathering of silicates. In addition, we showed the theoretical approaches that have been developed in order to model space weathering on asteroids. Since both effects, phase reddening and space weathering, are manifested in a similar way, i.e., increasing of the spectral slope and variations in the strength of the absorption bands, we investigated whether the red slopes exhibited by spectra obtained at high phase angles could be misinterpreted as space weathering. For this purpose we carried out two different experiments.

For the first experiment we followed the same procedure used by Brunetto et al. (2006) (see chapter 1), with the difference that instead of dividing the reflectance spectra of an irradiated sample by an unirradiated sample, we computed the ratio between the spectra obtained in the lab at high phase angles and those obtained at low phase angles. Since there is no significant change in spectral slope between $g=13^\circ$ and 30° we used the spectrum obtained at a phase angle of 30° as reference point. Figure 4.16 shows the ratio plots (solid lines) between the spectra of the LL6 obtained at $g=60^\circ$ and $g=30^\circ$ (bottom), at $g=90^\circ$ and $g=30^\circ$ (middle) and at $g=120^\circ$ and

$g=30^\circ$ (top panel). The ratio plots were modeled by fitting the same exponential curve used by Brunetto et al. (2006)

$$\text{Ratio} = P_R(\lambda) = A \exp(C_P/\lambda) \quad (4.8)$$

where we have just changed the name of the function, we call it the phase reddening function (P_R) and the parameters A and C_P are equivalents to the parameters K and C_S respectively, with the difference that C_P would be a measure of the effect of the phase reddening. The best fit curves obtained using Eq. (4.8) are represented with dashed lines in Fig. 4.16. Here we have used the LL6 spectra as an example, but the same procedure can be used with the other samples. In Fig. 4.16 we have also included the resultant A and C_P values and the coefficient of determination (R^2) of the fitted curves for each ratio plot. Similarly to the results obtained by Brunetto et al. (2006) the ratio of the spectra show some traces of Bands I and II, which can affect the fitting in those spectral regions. Nevertheless, the R^2 for the fitted curves ranges between 0.88 and 0.96 and, in general, the results are comparable to those of Brunetto et al. (2006). After comparing the C_P values with the C_S obtained by Brunetto et al. (2006) for different samples, we found that the C_P values are similar to the C_S obtained for the H5 ordinary chondrite Epinal, which was irradiated with Ar^{++} (60 keV) at three different ion fluences.

As was mentioned in chapter 1, Brunetto et al. (2006) found that there is a correlation between the C_S parameter and the number of displacements per cm^2 (d). Using this correlation (Eq. 1.11) we calculated the number of displacements per cm^2 that would correspond to our C_P values. It is important to point out that in this case the d values calculated using the C_P have no real physical meaning, since the C_P parameter quantifies the effect of the phase reddening and not the space weathering, however their calculation is useful to illustrate how the phase reddening can resemble different degrees of space weathering. This can be seen in Figure 4.17 where we have plotted the C_P (LL6 ordinary chondrite) and C_S (Epinal ordinary chondrite) values versus the calculated damage parameter for each sample. The LL6 data are represented with filled symbols while the Epinal values are plotted as open symbols. These results indicate that an increase in phase angle in the range of 30° to 120° would be equivalent to irradiate the sample with high mass ions (Ar^{++} 60 keV) with an ion fluence in the range of $\sim 1.3 \times 10^{15}$ to 1.7×10^{16} ions cm^{-2} . These ion fluences are equivalent to exposure times of $\sim 0.1 \times 10^6$ to 1.3×10^6 years at about 1 AU from the Sun (calculated as in Strazzulla et al. 2005). Laboratory experiments (e.g., Strazzulla et al. 2005) have shown that the timescale for the weathering of NEAs surfaces due to ion irradiation is on the order of 10^4 - 10^6 years. Thus, observing NEAs at high phase angles could produce spectral slopes that resemble those exhibited by weathered surfaces.

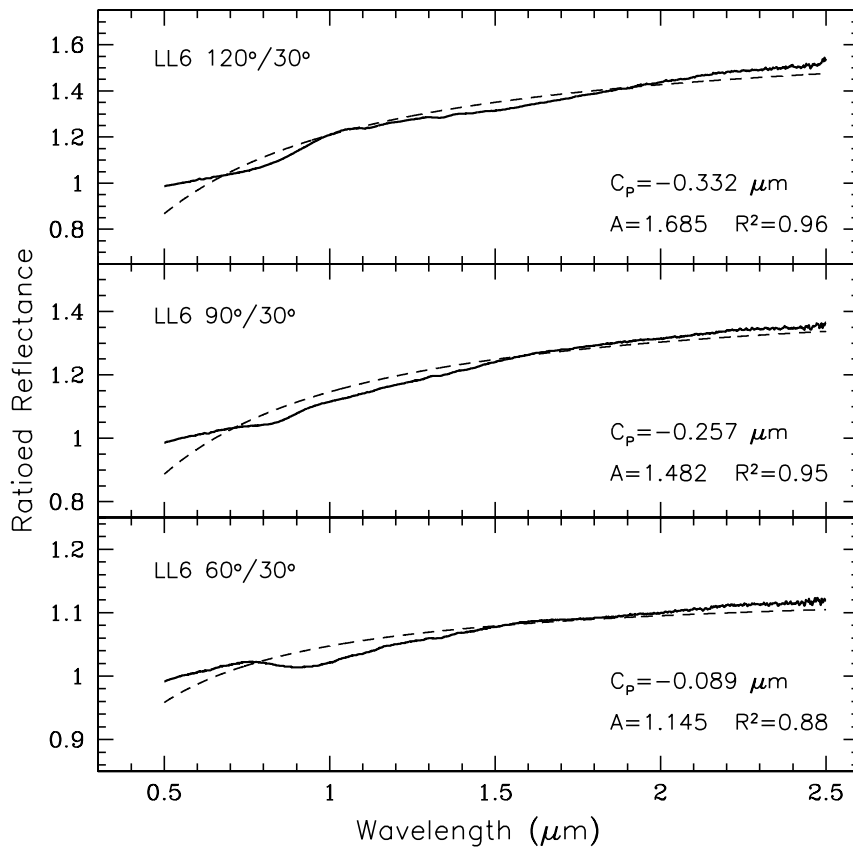


Figure 4.16: Ratio plots (solid lines) between the spectra of the LL6 obtained at $g=60^\circ$ and $g=30^\circ$ (bottom), at $g=90^\circ$ and $g=30^\circ$ (middle) and at $g=120^\circ$ and $g=30^\circ$ (top panel). Dashed curves are the best fit curves obtained using Eq. (4.8). For each ratio plot the resultant A , C_p and R^2 values are given. Figure from Sanchez et al. (2012).

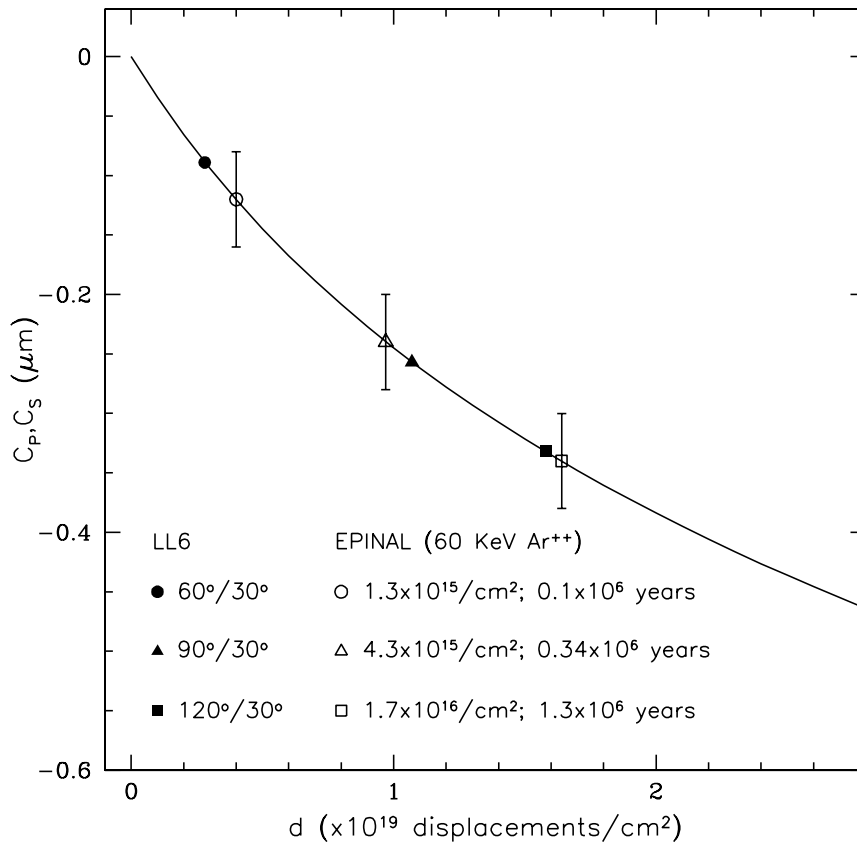


Figure 4.17: The C_P (LL6 ordinary chondrite) and C_S (Epinal ordinary chondrite) parameters as a function of the number of displacements per cm^2 (damage parameter). The data corresponding to the Epinal meteorite were obtained from Brunetto et al. (2006). The LL6 and the Epinal data are plotted as filled and open symbols respectively. For the LL6 each symbol represents the value obtained from the ratioed spectra of different phase angles. The symbols corresponding to the Epinal meteorite represent different ions fluences. Approximate exposure times (at 1 AU) corresponding to each ion fluence are also shown. The solid line represents the experimental damage curve from Brunetto et al. (2006). The error bars of the LL6 data are on the order of the size of symbols. Figure from Sanchez et al. (2012).

For the second experiment we modeled the optical effects of the SMFe on the laboratory spectra by using Hapke's radiative transfer model (Hapke 1981, 1993, 2001), and then we compared these spectra with those obtained at different phase angles.

From Hapke (2001) the bidirectional reflectance of a medium of isotropic scatterers ignoring the opposition effect is given by

$$r(i, e, g) = \frac{w}{4\pi} \frac{\mu_0}{\mu_0 + \mu} H(\gamma, \mu_0) H(\gamma, \mu) \quad (4.9)$$

where i , e and g are the incidence, emission and phase angle respectively, $\mu_0 = \cos(i)$, $\mu = \cos(e)$, w is the single scattering albedo, $\gamma = (1 - w)^{1/2}$, and $H(\gamma, \mu)$ is an analytic approximation to the Ambartsumian-Chandrasekhar H functions. Since most reflectances are relative to a standard, Hapke (2001) represented this relative reflectance as

$$\Gamma(\gamma) = \frac{1 - \gamma^2}{(1 + 2\gamma\mu_0)(1 + 2\gamma\mu)} \quad (4.10)$$

from which γ can be determined, and the single scattering albedo of the sample can be calculated as

$$w = 1 - \gamma^2 \quad (4.11)$$

The single scattering albedo can be also written as a function of the properties of the particles of the medium by

$$w = S_e + (1 - S_e) \frac{1 - S_i}{1 - S_i \Theta} \Theta \quad (4.12)$$

where S_e is the Fresnel reflection coefficient for externally incident light, S_i is the Fresnel reflection coefficient for internally scattered light, and Θ is the single-pass transmission of the particle. For nonmetallic particles with imaginary refractive index $\ll 1$, S_e and S_i can be approximated by

$$S_e = \frac{(n - 1)^2}{(n + 1)^2} + 0.05 \quad (4.13)$$

$$S_i = 1 - \frac{4}{n(n + 1)^2} \quad (4.14)$$

where n is the real part of the refractive index. If there is no internal scattering, then

$$\Theta = e^{-\alpha \langle D \rangle} \quad (4.15)$$

where $\langle D \rangle$ is the mean ray path length, which can be calculated from Hapke (1993) as

$$\langle D \rangle = \frac{2}{3} \left[n^2 - \frac{1}{n} (n^2 - 1)^{3/2} \right] D \quad (4.16)$$

where D is the grain size. The parameter α in equation (4.15) is the absorption coefficient, which is given by

$$\alpha = \frac{4\pi nk}{\lambda} \quad (4.17)$$

where k is the imaginary part of the refractive index and λ is the wavelength. From Eqs. (4.12) and (4.15) the absorption coefficient can be also calculated as

$$\alpha = \frac{1}{\langle D \rangle} \ln \left[S_i + \frac{(1 - S_e)(1 - S_i)}{w - S_e} \right] \quad (4.18)$$

To model the effects of the SMFe, the absorption coefficient of the host material (α_h) is increased by adding to it the absorption coefficient of the SMFe (α_{Fe}). Using the Maxwell-Garnett effective medium theory, Hapke (2001) derived an expression to calculate α_{Fe} ,

$$\alpha_{Fe} = \frac{36\pi z f \rho_h}{\lambda \rho_{Fe}} \quad (4.19)$$

where f is the mass fraction of the Fe particles, ρ_h is the density of the host material, ρ_{Fe} is the density of iron and z is given by

$$z = \frac{n_h^3 n_{Fe} k_{Fe}}{(n_{Fe}^2 - k_{Fe}^2 + 2n_h^2)^2 + (2n_{Fe} k_{Fe})^2} \quad (4.20)$$

where n_h and n_{Fe} are the real part of the refractive indices of the host material and iron respectively, and k_{Fe} is the imaginary part of the refractive index of iron. Thus, if we use Eq. (4.18) to calculate the absorption coefficient of the host material (α_h), then the absorption coefficient of the material containing SMFe is given by

$$\alpha_w = \alpha_h + \alpha_{Fe} \quad (4.21)$$

Looking at Eqs. (4.9), (4.12), (4.15) and (4.17), we can understand why phase reddening and space weathering are manifested in similar ways. Reflectance spectra are controlled by the single scattering albedo (w), which is a function of the absorption coefficient (α). The absorption coefficient is a parameter that characterizes how deep into a material light of a particular wavelength can penetrate before being absorbed. As the phase angle increases, light is less able to escape from the medium, meaning that photons are more absorbed, resulting in a decrease of reflectance throughout the entire spectrum. However, because the absorption coefficient is inversely proportional to the wavelength (the shorter the wavelength the higher the absorption coefficient) the reflectance in the blue part of the spectrum will decrease faster than in the red part, producing the increase in spectral slope (reddening). This can be seen in Figure 4.18 that shows the reflectance spectra of the LL6 chondrite Dhurmsala obtained at five different phase angles. In this case spectra are shown as they were measured in the lab. Similarly, the addition of the SMFe (Eq. 4.21) will decrease the blue part of the spectrum more than the red part due to the stronger absorption at short wavelengths, increasing the spectral slope (Hapke 2001).

For our experiment we used the spectrum of the LL6 ordinary chondrite obtained at a phase angle of 13° as reference point. Using these data we first calculated α_h with Eqs. (4.10) to (4.18), where we have assumed $n_h = 1.7$, which is a typical value for mafic minerals (Hapke 2001). Then using Eqs. (4.19) and (4.20) we estimated α_{Fe} . For this calculation we have assumed $\rho_h = 3.48$, which is the average grain density for LL chondrites (Britt and Consolmagno 2003) and $\rho_{Fe} = 7.87$. The optical constants of iron, n_{Fe} and k_{Fe} , were taken from Johnson and Christy (1974). Since these values were measured only for $\lambda \sim 1.9 \mu\text{m}$, we did a polynomial fit to the data in order to extrapolate them to $2.5 \mu\text{m}$ (Fig. 4.19). The α_{Fe} was calculated for different mass fractions of Fe; the resulting values were then added to the calculated α_h in order

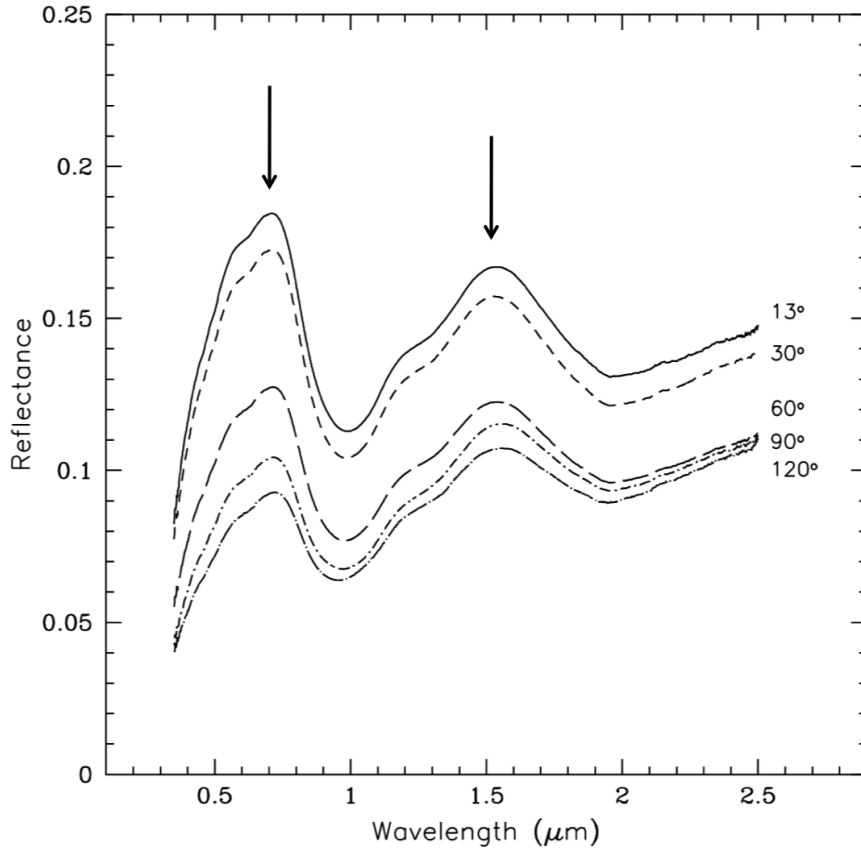


Figure 4.18: Reflectance spectra of the LL6 chondrite Dhurmsala obtained at five different phase angles. From the top to the bottom $g=13^\circ$ (solid line), $g=30^\circ$ (short dashed line), $g=60^\circ$ (long dashed line), $g=90^\circ$ (dot-short dashed line) and $g=120^\circ$ (dot-long dashed line). The spectra in this figure are not normalized, and they have not been offset. The reflectance decreases throughout the entire spectrum with increasing phase angle. The arrows indicate the two reflectance peaks of the spectra, and show how the blue part of the spectrum decreases faster than the red part as the phase angle increases, producing the increase in spectral slope.

to obtain α_w . Figure 4.20 shows the absorption coefficient α_{Fe} per mass fraction of Fe^0 . The α_w values were then inserted into equation (4.15), which combined with equation (4.12) allowed us to determine the new single scattering albedos. Finally, we calculated γ from Eq. (4.11) and using Eq. (4.10) we obtained the "weathered spectra" for the different % of SMFe. In Figure 4.21 we plot the reflectance spectra of the LL6 after adding different amounts of SMFe. We found that the spectrum obtained at $g = 60^\circ$ shows a spectral slope comparable to the spectrum obtained at $g = 13^\circ$ after adding 0.0015 % SMFe. For phase angles of 90° and 120° the spectral slopes are equivalent to adding 0.0048 and 0.0062 % SMFe respectively, to the spectrum obtained at $g = 13^\circ$. If we consider that an amount of $\sim 0.02\%$ of SMFe is required to explain the red slopes of some S-complex asteroids (e.g., Hapke 2001, Rivkin et al. 2004), this means that the spectral slope for the highest phase angle ($g = 120^\circ$) would be equivalent to $\sim 30\%$ of that SMFe.

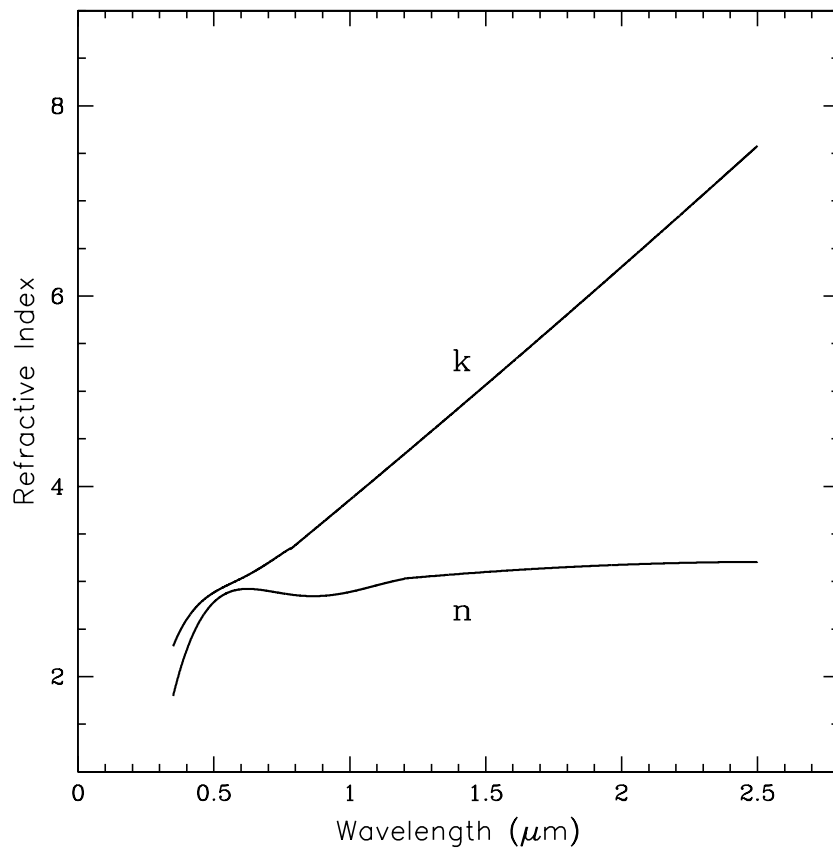


Figure 4.19: Real (n) and imaginary (k) parts of the refractive index of Fe^0 as measured by Johnson and Christy (1974). The original data have been extrapolated to $2.5 \mu\text{m}$.

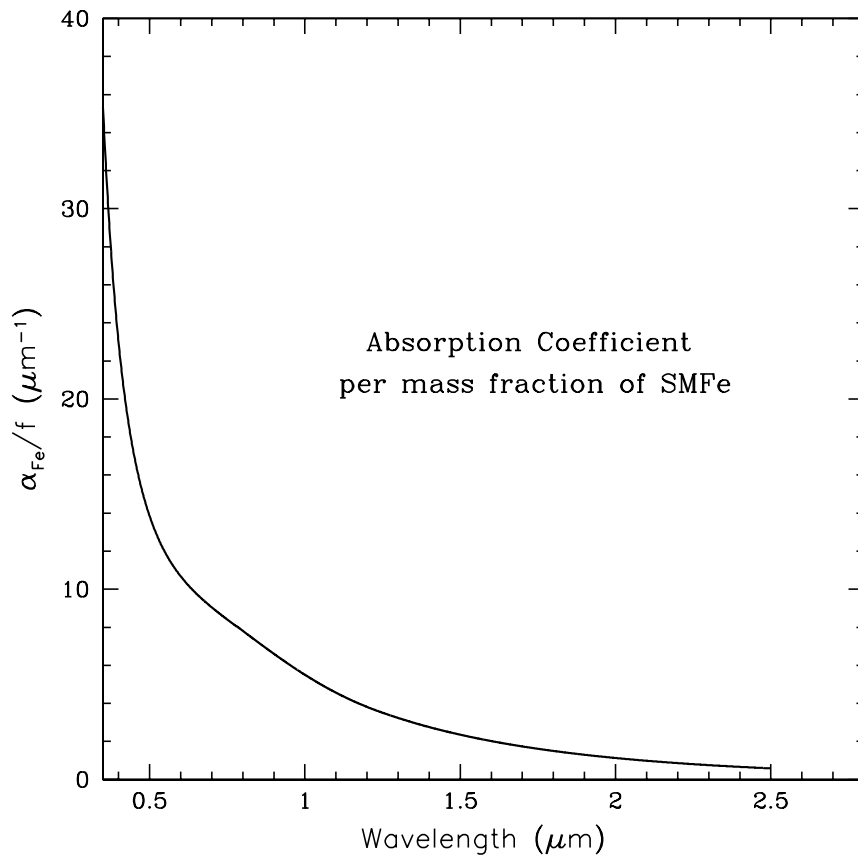


Figure 4.20: Absorption coefficient α_{Fe} divided by mass fraction f of Fe^0 . The matrix of material is assumed to have $n = 1.7$. The absorption coefficient was calculated from the data of Johnson and Christy (1974) using effective medium theory.

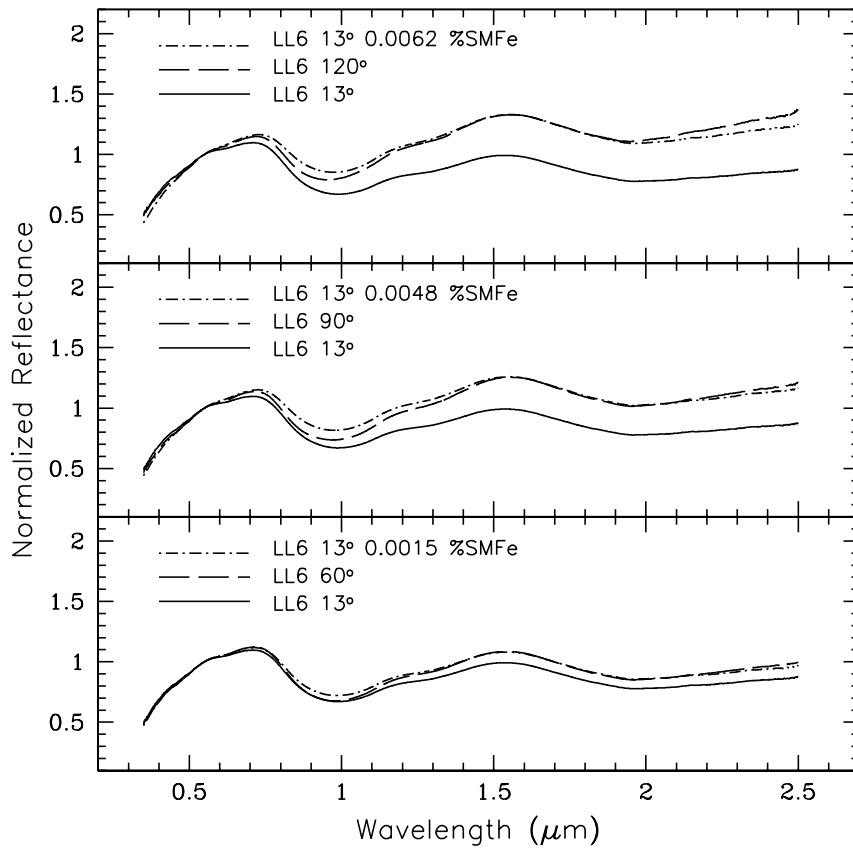


Figure 4.21: Reflectance spectra of the LL6 chondrite Dhurmsala after adding different amounts of SMFe (dot-short dashed lines) to the spectrum obtained at $g=13^\circ$. For comparison the spectra of the LL6 obtained at $g=13^\circ$ (solid lines) and $g=60^\circ$, 90° and 120° (long dashed lines from the bottom to the top) have been included. All the spectra are normalized to unity at $0.55 \mu\text{m}$. Figure from Sanchez et al. (2012).

4.4.3 Phase reddening and taxonomic classification

As mentioned in chapter 1, VNIR spectra of asteroids can be classified under two different system, one developed by Gaffey et al. (1993), which uses band parameters (Band I center and BAR), and the other called the Bus-DeMeo system, which is based on Principal Component Analysis. Since both systems use band depths as one of the primary criteria to classify the objects, multiple observations of the same asteroid obtained at different phase angles could lead to ambiguous classifications. In order to test the influence of phase reddening on the taxonomic classification, we have applied these two classification systems to each of the asteroids in our sample.

Figure 4.22 shows the measured Band I center versus BAR for the NEAs. Within the uncertainties all the NEAs studied are classified either as S(III) or S(IV). There are four cases (1620 Geographos, 1627 Ivar, 1980 Tezcatlipoca and 1036 Ganymed) that show large variations of the BAR from one phase angle to another, but this is likely attributed to noisy spectra rather than phase reddening. The rest of the asteroids show variations in Band I centers and BAR that are on the order of the error bars. The results obtained from the laboratory samples (Fig. 4.23) indicate that the largest variation in the BAR (~ 0.1) is larger than the typical uncertainty associated with the BAR values measured from asteroids (represented by the $1-\sigma$ error bars in the upper corner of this figure). This means that in certain cases phase reddening could contribute to an ambiguous classification, particularly if the measured band parameters of the object are located close to the boundaries that define each class.

The classification into the Bus-DeMeo system was done using the online taxonomy calculator (<http://smass.mit.edu/busdemeoclass.html>). The class assigned to each spectrum and the calculated principal components PC1' and PC2' are given in Table 4.2. Only in three cases asteroids were ambiguously classified. asteroid (1036) Ganymed was classified as S and Sr, (1620) Geographos was classified as S and Sq and (4954) Eric was classified as Sw and Sr. The letter "w" was introduced by DeMeo et al. (2009) to indicate an object exhibiting a high slope, but does not represent a different class, thus an object designated as "Sw" is an asteroid classified as S-type that exhibit a higher slope than the typical S-types. This distinction is based on an arbitrary cutoff at slope = 0.25 (DeMeo et al. 2009). Table 4.2 shows that the notation of "w" was added to many asteroids from one phase angle to another. Certainly the phase reddening plays a role on this variation in spectral slope, however as it was stated earlier this is a very sensitive parameter that can be affected by other factors. What is important to point out is that in the Bus-DeMeo system the spectral slope is removed prior to the classification. For those objects which were given two classifications it is likely that the phase reddening was not the only contribution, since some of the spectra show more scatter than others. However, from our analysis we estimate an average variation of about 0.04 and 0.03 for the PC1' and PC2' respectively, that could be attributed to phase reddening. These results suggest that phase reddening could lead to an ambiguous classification but only if the calculated PC values are close to the lines that separate each class. This can be seen in Figure 4.24 where we have plotted the PC values in a PC1' versus PC2' diagram from DeMeo et al. (2009). For clarity only the calculated PC values for some of the asteroids have been plotted. These values are represented by different symbols, which are connected by lines to indicate multiple values for individual asteroids.

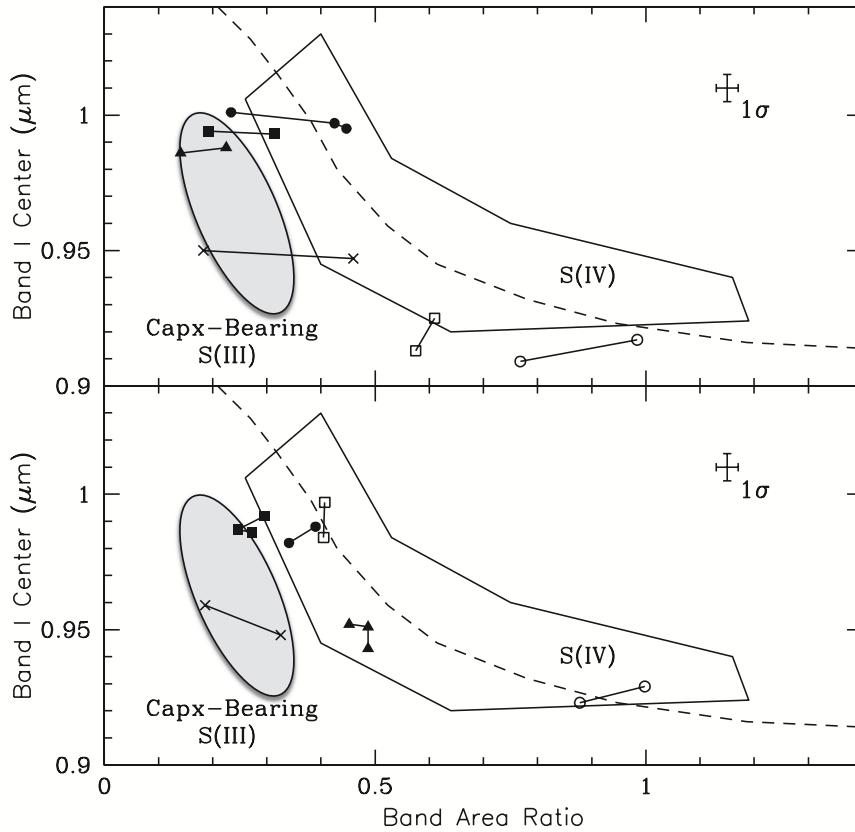


Figure 4.22: Plot of the Band I center versus BAR for the NEAs. The polygonal region represents the mafic silicate components of ordinary chondrites and S(IV) asteroids (Gaffey et al. 1993). The grey oval region represents the mineralogical zone corresponding to the calcic pyroxene-bearing where the S(III) subtypes are located (Gaffey et al. 1993). The dashed curve indicates the location of the olivine-orthopyroxene mixing line (Cloutis et al. 1986). The top panel shows the measured values for asteroids 1620 Geographos (filled circles), 1036 Ganymed (open circles), 1862 Apollo (filled triangles), 1980 Tezcatiploca (crosses), 11398 (open squares) and 6239 Minos (filled squares). The bottom panel shows the measured values for asteroids 4954 Eric (open circles), 66146 (filled squares), 1627 Ivar (crosses), 35107 (open squares), 25143 Itokawa (filled circles) and 4179 Toutatis (filled triangles). Measured values from multiple observations of individual asteroids are connected by lines. The average $1\text{-}\sigma$ error bars are shown in the upper right corner. Figure from Sanchez et al. (2012).

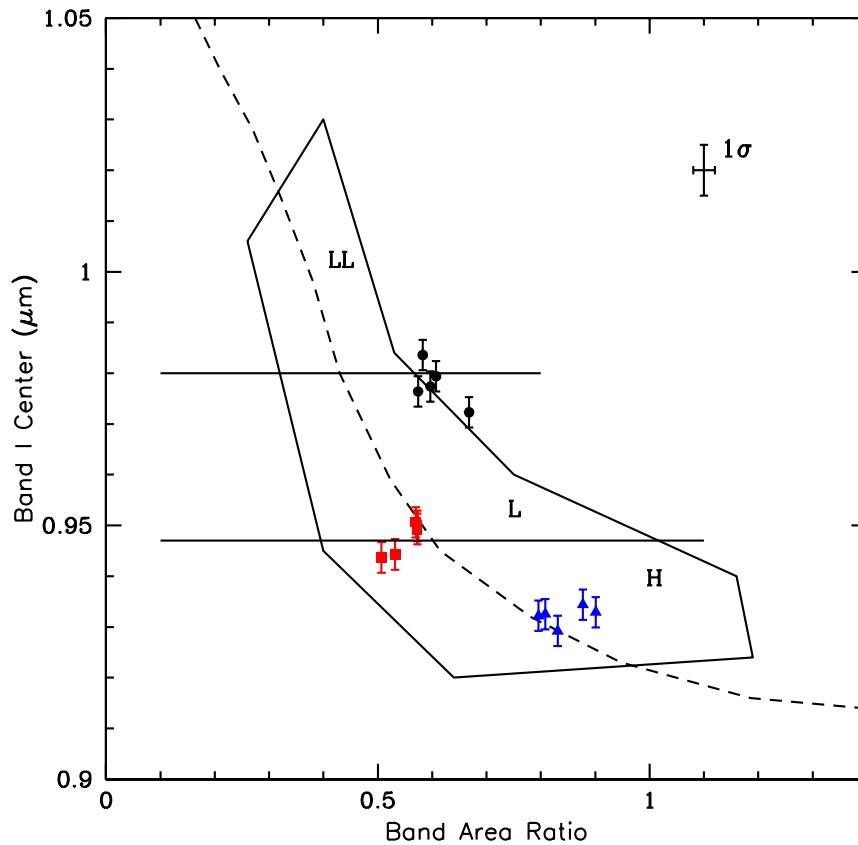


Figure 4.23: Plot of the Band I center versus BAR for the LL6 (black circles), L6 (red squares) and H6 (blue triangles) ordinary chondrites. The polygonal region represents the mafic silicate components of ordinary chondrites and S(IV) asteroids (Gaffey et al. 1993). The dashed curve indicates the location of the olivine-orthopyroxene mixing line (Cloutis et al. 1986). The horizontal lines represent the approximate boundaries that separate the three types of ordinary chondrites found by Dunn et al. (2010). The error bar in the x-axis is of the order of the size of symbols. For comparison we have included the average $1\text{-}\sigma$ error bars (upper right corner) associated with the Band I center and BAR value measured for asteroids. Figure from Sanchez et al. (2012).

Table 4.2: Taxonomic classification for the NEAs. The columns in this table are: object number and designation, the phase angle (g), taxonomic classification (Bus-DeMeo) and principal components PC1' and PC2' for each asteroid.

Object	g ($^{\circ}$)	Taxonomy	PC1'	PC2'
1036 Ganymed	5.9	S	0.2400	0.0416
1036 Ganymed	15.2	Sr	0.3957	0.0381
1620 Geographos	12.0	Sq	-0.1096	0.0038
1620 Geographos	16.7	S	-0.0169	0.0206
1620 Geographos	38.3	Sqw	-0.2337	0.0503
1627 Ivar	16.0	S	-0.0151	0.0517
1627 Ivar	31.0	Sw	-0.0591	0.0689
1862 Apollo	15.4	Q	-0.5926	0.1996
1862 Apollo	51.7	Q	-0.6011	0.2387
1980 Tezcatlipoca	25.0	Sw	0.1132	0.0508
1980 Tezcatlipoca	54.6	Sw	-0.0238	0.0588
4179 Toutatis	6.1	Sqw	-0.2825	0.0972
4179 Toutatis	27.0	Sq	-0.3115	0.1622
4179 Toutatis	68.0	Sq	-0.3278	0.1282
4954 Eric	28.3	Sw	0.1552	0.0433
4954 Eric	62.0	Sr	0.4719	-0.0369
6239 Minos	2.4	Sq	-0.2907	0.0557
6239 Minos	47.3	Sqw	-0.3090	0.1231
11398	19.0	Sr	0.0631	0.0978
11398	33.0	Sr	0.1312	0.0912
25143 Itokawa	25.6	Sq	-0.3425	0.0946
25143 Itokawa	69.0	Sqw	-0.3283	0.1579
35107	45.0	Sq	-0.2848	0.1281
35107	87.0	Sq	-0.3077	0.1182
66146	32.1	Q	-0.5262	0.1994
66146	55.3	Q	-0.5737	0.1824
66146	70.3	Q	-0.4978	0.1938

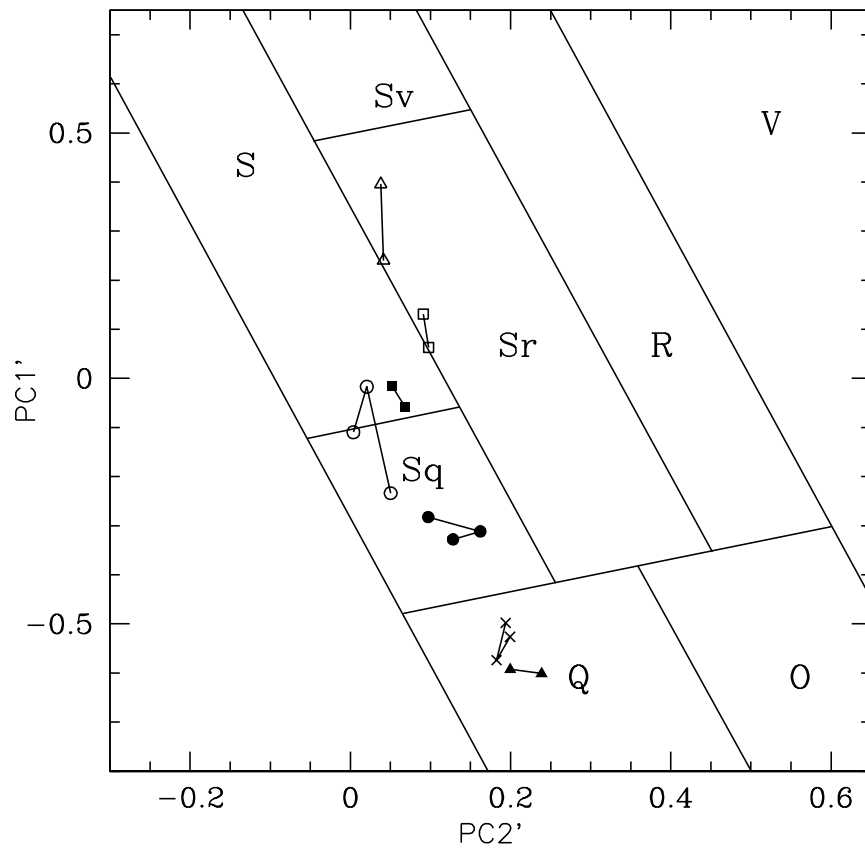


Figure 4.24: Calculated PC values for some of the NEAs studied represented in a PC1' versus PC2' diagram from DeMeo et al. (2009). The letters indicate the different classes within the S-complex plus Q-, O-, R- and V-types. The asteroids whose calculated PC values have been plotted are: (1036) Ganymed (open triangles), (1620) Geographos (open circles), (1627) Ivar (filled squares), (4179) Toutatis (filled circles), (1862) Apollo (filled triangles), 11398 (open squares) and 66146 (crosses). Figure from Sanchez et al. (2012).

5 Conclusions

In this thesis we investigated temperature-induced effects and phase reddening on NEAs. Our research was based on the analysis VNIR spectra of NEAs observed at different heliocentric distances and phase angles. All the asteroids studied are classified as either S-complex or Q-types, meaning that they are essentially olivine-orthopyroxene assemblages. Apart from the asteroid spectra our study was complemented by laboratory spectra of ordinary chondrites obtained at different temperatures and phase angles.

Regarding the study of temperature-induced effects the main results are the following:

- The analysis of VNIR spectra of a group of ordinary chondrites acquired over a wide range of temperatures showed that the spectral band parameters that are more affected by temperature variations are the Band II center, which shows a progressive shift to longer wavelengths as the temperature increases, the Band II depth, which decreases with increasing temperature, and the BAR, which also decreases as the temperature increases. In the case of the Band I center, we found that the shift with increasing temperature is very small. Using this information we developed a new set of calibrations that can be used to correct for the effect of temperature variations on the spectral band parameters of olivine-orthopyroxene assemblages.
- On the basis of the orbital elements of the NEAs studied, we estimated an average surface temperature for NEAs in the range of ~ 130 to 440 K. We noticed, however, that in practice due to observational constraints the temperature range for NEAs is much narrower ~ 130 to 265 K, with an average value of about 234 K. After applying the temperature corrections to the band parameters measured from the asteroid spectra we found that, on average, temperature variations will have a very small impact when comparing the spectral band parameters of NEAs with those measured for laboratory samples obtained at room temperature. Furthermore, from our analysis we determined that for different heliocentric distances of the same asteroid the average temperature variation (~ 20 K), will not have a significant effect when comparing band parameters of the same asteroid observed at different heliocentric distances. The results found for NEAs can be extended to main-belt asteroids since the range of surface temperatures among these objects is smaller than for NEAs.

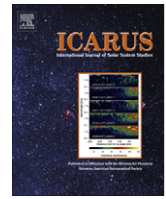
The study of phase reddening on spectra of NEAs and ordinary chondrite meteorites revealed a wealth of new information. The main results are the following:

- The analysis of VNIR spectra of NEAs observed at different phase angles revealed an increase of band depths with increasing phase angles in the range of $2^\circ < g < 70^\circ$ for Band I and $2^\circ < g < 55^\circ$ for Band II. Our analysis showed that, on average, Band I

and Band II depths will increase 0.66% and 0.93% respectively, for every 10° increase in phase angle. From the available data we have derived equations that can be used to correct the effects of phase reddening in the band depths. Small variations in band centers and BAR values with increasing phase angle were also found.

- Of the three types of ordinary chondrites, the (olivine-rich) LL6 is the most affected by phase reddening, showing the largest variations in spectral slopes and band depths with increasing phase angles. These results confirm the material-dependence of phase reddening reported by previous studies. The studied ordinary chondrites have their maximum spectral contrast of Band I depths at a phase angle of $\sim 60^\circ$, followed by a decrease between 60° and 120° phase angle. The Band II depths of these samples have their maximum spectral contrast at phase angles of $30^\circ - 60^\circ$, which then gradually decreases to 120° phase angle. The spectral slope of the ordinary chondrite spectra shows a significant increase with increasing phase angle for $g > 30^\circ$. The results obtained from the lab spectra support the idea that the increase of the spectral slope caused by phase reddening is due to a wavelength dependence of the single-scattering albedo.
- The results obtained from both meteorite and asteroid spectra indicate that the variations in spectral band parameters caused by phase reddening have no significant impact on the mineralogical analysis. However, these variations could lead to an ambiguous taxonomic classification of asteroids, but only if the measured spectral band parameters and/or principal components (depending on the taxonomic system) are located close to the boundaries that define each class.
- We found that the increase in spectral slope caused by phase reddening can mimic the effect of space weathering. In particular, an increase in phase angle in the range of 30° to 120° will produce a reddening of the reflectance spectra equivalent to exposure times of $\sim 0.1 \times 10^6$ to 1.3×10^6 years at about 1 AU from the Sun. Furthermore, the increase in spectral slope due to phase reddening is comparable to the effects caused by the addition of various amounts of SMFe. These results imply that phase reddening should be considered when studying space weathering effects on spectral data.
- Our results suggest that because of the limited phase angle range exhibited by main-belt asteroids, typically $< 30^\circ$, the effects of phase reddening on these objects will be less significant than on NEAs.

Publications



Phase reddening on near-Earth asteroids: Implications for mineralogical analysis, space weathering and taxonomic classification

Juan A. Sanchez^{a,b,*}, Vishnu Reddy^{a,c,1}, Andreas Nathues^{a,1}, Edward A. Cloutis^d, Paul Mann^d, Harald Hiesinger^b

^a Max Planck Institut für Sonnensystemforschung, Max Planck Str. 2, 37191 Katlenburg-Lindau, Germany

^b Institut für Planetologie, 48149 Münster, Germany

^c Department of Space Studies, University of North Dakota, Grand Forks, ND 58202, USA

^d Department of Geography, University of Winnipeg, Winnipeg, Manitoba, Canada

ARTICLE INFO

Article history:

Received 22 February 2012

Revised 2 April 2012

Accepted 2 April 2012

Available online 25 April 2012

Keywords:

Asteroids

Near-Earth objects

Spectroscopy

Infrared observations

Meteorites

ABSTRACT

Phase reddening is an effect that produces an increase of the spectral slope and variations in the strength of the absorption bands as the phase angle increases. In order to understand its effect on spectroscopic observations of asteroids, we have analyzed the visible and near-infrared spectra (0.45–2.5 μm) of 12 near-Earth asteroids observed at different phase angles. All these asteroids are classified as either S-complex or Q-type asteroids. In addition, we have acquired laboratory spectra of three different types of ordinary chondrites at phase angles ranging from 13° to 120°. We have found that both, asteroid and meteorite spectra show an increase in band depths with increasing phase angle. In the case of the asteroids the Band I depth increases in the range of $\sim 2^\circ < g < 70^\circ$ and the Band II depth increases in the range of $\sim 2^\circ < g < 55^\circ$. Using this information we have derived equations that can be used to correct the effect of phase reddening in the band depths. Of the three meteorite samples, the (olivine-rich) LL6 ordinary chondrite is the most affected by phase reddening. The studied ordinary chondrites have their maximum spectral contrast of Band I depths at a phase angle of $\sim 60^\circ$, followed by a decrease between 60° and 120° phase angle. The Band II depths of these samples have their maximum spectral contrast at phase angles of 30–60° which then gradually decreases to 120° phase angle. The spectral slope of the ordinary chondrites spectra shows a significant increase with increasing phase angle for $g > 30^\circ$. Variations in band centers and band area ratio (BAR) values were also found, however they seem to have no significant impact on the mineralogical analysis. Our study showed that the increase in spectral slope caused by phase reddening is comparable to certain degree of space weathering. In particular, an increase in phase angle in the range of 30–120° will produce a reddening of the reflectance spectra equivalent to exposure times of $\sim 0.1 \times 10^6$ – 1.3×10^6 years at about 1 AU from the Sun. This increase in spectral slope due to phase reddening is also comparable to the effects caused by the addition of different fractions of SMFe. Furthermore, we found that under some circumstances phase reddening could lead to an ambiguous taxonomic classification of asteroids.

© 2012 Elsevier Inc. All rights reserved.

1. Introduction

Near-infrared (NIR) spectroscopy is a powerful technique to derive information about the surface mineralogy of asteroids. This mineralogical characterization relies primarily on the identification and analysis of diagnostic features present in the spectra of

some asteroids. Olivine and pyroxene are two common mafic minerals found on asteroids (Gaffey et al., 2002), and their spectral properties dominate the reflectance spectra of some particular classes. Asteroids belonging to the S-complex and Q-types (DeMeo et al., 2009, Bus–DeMeo taxonomy hereafter) are examples of these objects. In the case of olivine, the absorption feature is composed of three overlapping bands and is centered near 1.04–1.1 μm , while pyroxenes show major absorption bands, centered near 0.9–1 μm and 1.9–2 μm , all of them caused by the presence of Fe^{2+} cations (e.g., Adams, 1974, 1975; Burns, 1993). In the spectra of olivine–pyroxene mixtures the wavelength position (band centers) of the combined absorption features near 1 μm (Band I) is a function of relative abundance and composition of olivine and pyroxene, while the position of the feature near 2 μm (Band

* Corresponding author at: Max Planck Institut für Sonnensystemforschung, Max Planck Str. 2, 37191 Katlenburg-Lindau, Germany.

E-mail address: sanchez@mps.mpg.de (J.A. Sanchez).

¹ Visiting Astronomer at the Infrared Telescope Facility, which is operated by the University of Hawaii under Cooperative Agreement No. NNX-08AE38A with the National Aeronautics and Space Administration, Science Mission Directorate, Planetary Astronomy Program.

II) is a function of the pyroxene composition (Cloutis et al., 1986; Gaffey et al., 1993). In addition to the absorption band centers, the ratio of the area of Band II to that of Band I, known as band area ratio (BAR), is used to estimate olivine and pyroxene abundances in asteroids and meteorites (Cloutis et al., 1986; Burbine et al., 2003; Dunn et al., 2010). Together, these spectral band parameters constitute a useful tool to obtain information about the surface mineralogy and composition of asteroids. However, band parameters can also be affected by other factors not related to compositional variations. One of these factors is the phase angle at the moment of the observation. The phase angle (g), is defined as the angular separation between the Sun and the observer as seen from the target. Phase angle induced effects can manifest themselves as phase reddening, which produces an artificial increase (reddening) of the spectral slope and variations in the strength of the absorption bands with increasing phase angle. This effect is explained as the result of the wavelength dependence of the single-scattering albedo (Gradie et al., 1980; Gradie and Veverka, 1986; Clark et al., 2002b). Traditionally, the term phase reddening was used to describe only the increase of the spectral slope or continuum, however as will be shown later, as the phase angle increases variations in the absorption bands are also seen. Therefore, in the present work the term phase reddening is extended to refer not only to the increase of the spectral slope, but also to the variations in the strength of the absorption bands.

Phase reddening effect among Solar System objects was first noticed in asteroid broad band colors. Gehrels (1970) reported a phase reddening in the B-V and U-B colors of 4 Vesta to be 0.0018 and 0.0027 mag/degree, respectively. Additional studies using photometric observations include the works of Millis et al. (1976) and Lumme and Bowell (1981). The effects of phase reddening have been also observed among NEAs. Luu and Jewitt (1990) found that the spectral slopes of NEAs in general are higher than those measured for 3:1 resonance asteroids. Since NEAs are often observed at high phase angles this increase in the spectral slopes was interpreted as phase reddening.

Nathues (2000, 2010) carried out a spectroscopic and spectrophotometric survey of the Eunomia asteroid family, obtaining spectra in visible (VIS) and NIR wavelengths of 97 of its members. The analysis of the spectral slopes of these asteroids revealed an average increase of 0.067%/100 nm per degree with increasing phase angle in the range of $2^\circ < g < 24^\circ$. Apart from the increase of the spectral slope he also observed an increase of the 1 μm absorption band (depth) with increasing phase angle.

Reddy et al. (2012) conducted an extensive study of Asteroid (4) Vesta in order to quantify phase angle-induced spectral effects on this asteroid prior to the arrival of the Dawn spacecraft. Rotationally resolved NIR spectral observations (0.7–2.5 μm) were obtained for this purpose. They found that in the phase angle range of $0^\circ < g \leq 25^\circ$ for every 10° increase in phase angle, Vesta's Band I and Band II depths increase 2.35% and 1.5%, respectively, and the BAR value increases by 0.30.

Phase reddening effect has been also detected and quantified from spacecraft observations of asteroids. The NEAR Shoemaker spacecraft obtained NIR spectroscopic observations (0.8–2.4 μm) of Asteroid (433) Eros at phase angles ranging from 0° to 100° . These observations showed the most intense phase reddening for wavelengths inside of the 1.0 μm band, occurring at the level of 10% across this phase angle range (Clark et al., 2002b; Bell et al., 2002). Similar results were observed from NIR reflectance spectra of Asteroid (25143) Itokawa acquired by the Hayabusa spacecraft (Kitazato et al., 2008).

Laboratory measurements of different materials have confirmed the existence of the phase reddening effect. Gradie et al. (1980) investigated phase angle induced effects on the spectrophotometric properties of powdered materials. They obtained

reflectance spectra at phase angles of $4^\circ \leq g \leq 120^\circ$, in the wavelength range $0.4 \leq \lambda \leq 1.2 \mu\text{m}$. All the samples studied by them showed a significant reddening as the phase angle increases from 4° to 120° . Furthermore, some of the spectra showed variations in the spectral contrast of the absorption bands with increasing phase angle. More recent laboratory studies related to phase reddening include the works of Mann et al. (2011) and Shepard and Cloutis (2011).

Despite the fact that phase reddening has been known for a long time, its effect on the analysis of asteroid spectra has not been fully assessed. In the present work we study the phase reddening on NEAs and its implications for mineralogical analysis, space weathering and taxonomic classification. Due to their proximity, NEAs can exhibit a wide range of phase angles, often much higher than those observed for main belt asteroids, which make them the logical choice for this study. Our investigation focuses on the analysis of 27 VIS–NIR spectra of 12 NEAs previously classified as either S-complex or Q-types (Bus–DeMeo), which have been observed at different phase angles. In addition to the ground-based observations, laboratory spectra of ordinary chondrites are also analyzed and the results compared to those obtained from the asteroid spectral data.

2. Phase reddening from ground-based observations of NEAs

2.1. The data

One of the drawbacks of this kind of study is the necessity to obtain multiple observations of the same asteroids at different phase angles, which in terms of allocated observation time can be very difficult to do. For this reason we have decided to combine data from Reddy (2009), DeMeo et al. (2009), Abell et al. (2007), Binzel et al. (2001) and the MIT-UH-IRTF Joint Campaign for NEO Spectral Reconnaissance (NEOSR). All of these observations were conducted with the SpeX instrument (Rayner et al., 2003) on the NASA Infrared Telescope Facility (IRTF). The NIR spectra (0.7–2.5 μm) were obtained using SpeX in its low resolution ($R \sim 150$) prism mode with a 0.8" slit width. Typical observations consist of acquiring frames employing a nodding sequence in which the object is alternated between two different slit positions (A and B) following the sequence ABBA. Since the object and the sky are observed simultaneously in each exposure, by subtracting A from B and B from A, it is possible to remove the sky background during the data reduction process. In order to minimize the effects of differential atmospheric refraction the slit is oriented along the parallactic angle during the observations. To correct for telluric water vapor features, and to obtain the relative reflectance, local standard and solar analog stars are observed at airmasses as similar as possible as the asteroids. Flat fields and arc line spectra for each night are also obtained during the observations. The data reduction is performed using different packages, including IRAF and Spextool (Cushing et al., 2004). For more details about the observing protocols and reduction of these data sets see Reddy (2009), DeMeo et al. (2009), Abell et al. (2007) and Binzel et al. (2001). The spectra of the NEAs at visible wavelengths used in the present work were taken from Binzel et al. (2001, 2004) and DeMeo et al. (2009). All the spectra were normalized to unity at 0.55 μm . Observational circumstances for the studied objects are presented in Table 1.

2.2. Spectral band analysis of NEAs

As mentioned earlier, increasing the phase angle will produce an increase in the spectral slope and changes in the strength of the absorption bands. Spectral slope variations can be interpreted as surface heterogeneities caused by different factors such as metal

Table 1

NEAs observational circumstances. The columns in this table are: object number and designation, UT date of observation, the phase angle (g) and the heliocentric distance at the time of observation.

Object	UT date	g ($^{\circ}$)	Heliocentric distance (AU)
1036 Ganymed ^a	09–March–2005	5.9	4.09
1036 Ganymed ^b	01–June–2006	15.2	3.01
1620 Geographos ^b	10–March–2008	38.3	1.09
1620 Geographos ^c	27–February–2008	12.0	1.16
1620 Geographos ^a	29–January–2001	16.7	1.39
1627 Ivar ^b	02–October–2008	31.0	1.58
1627 Ivar ^b	03–December–2008	16.0	1.90
1862 Apollo ^b	13–November–2005	51.7	1.05
1862 Apollo ^b	22–November–2005	15.4	1.20
1980 Tezcatlipoca ^b	25–October–2006	54.6	1.17
1980 Tezcatlipoca ^c	05–January–2007	25.0	1.48
4179 Toutatis ^b	15–September–2004	27.0	1.09
4179 Toutatis ^b	02–October–2008	68.0	1.06
4179 Toutatis ^c	13–August–2008	6.1	1.45
4954 Eric ^b	20–July–2007	28.3	1.67
4954 Eric ^c	26–November–2007	62.0	1.10
6239 Minos ^a	26–January–2004	47.3	1.03
6239 Minos ^b	06–September–2010	2.4	1.20
11398 ^b	10–March–2008	33.0	1.16
11398 ^c	28–February–2008	19.0	1.21
25143 Itokawa ^d	12–March–2001	25.6	1.07
25143 Itokawa ^e	28–March–2001	69.0	1.01
35107 ^c	26–July–2008	87.0	1.08
35107 ^a	27–December–2002	45.0	1.20
66146 ^b	02–October–2008	70.3	1.06
66146 ^b	13–October–2010	32.1	1.15
66146 ^b	06–September–2010	55.3	1.16

^a Data from DeMeo et al. (2009).

^b Data from NEOSR, <http://smass.mit.edu/minus.html>.

^c Data from Reddy (2009).

^d Data from Abell et al. (2007).

^e Data from Binzel et al. (2001).

content, particle size and space weathering (Gaffey et al., 1993; Clark et al., 2002a; Gaffey, 2010). However, this parameter is also known to be very sensitive to other factors. Apart from the viewing

geometry, atmospheric differential refraction (Filippenko, 1982), airmass differences between the standard star and the asteroid at the time of the observations (DeMeo et al., 2011), incorrect centering of the object in the slit (Cushing et al., 2004), poor weather conditions (Bus et al., 2002) and the use of different solar analogs (Sunshine et al., 2004) are often the cause of fluctuations in the asteroid's spectral slope. In some cases the origin of these error sources is difficult to determine since they are seen as nonsystematic variations in the final asteroid reflectance spectrum (Hardersen et al., 2006). Therefore, in order to better quantify the effect of phase reddening on the spectral slope we will leave that part of the study to the laboratory spectra (see Section 3), and will focus our attention on the analysis of the absorption bands of the asteroid spectra.

The spectral band parameters for each VIS–NIR spectrum were measured using the Spectral Processing Routine (SpecPR) program based on the protocols discussed by Cloutis et al. (1986), Gaffey et al. (2002), and Gaffey (2003). Band centers are calculated by dividing out the linear continuum and fitting an n -order polynomial over the bottom third of each band. In the case of Band II, we defined the unresolved red edge as 2.44 μm . After ratioing the absorption features to the straight-line continuum, a subroutine in SpecPR was used to calculate the band areas (areas between the linear continuum and the data curve) and band depths (measured from the continuum to the band center and given as percentage depths). The band areas were then used to calculate the BAR values. Each band parameter was measured 10 times using different order polynomial fits (typically third and fourth order) and sampling different ranges of points within the corresponding intervals. Averages of these measurements were taken as the final values. The uncertainties are given by the average $1 - \sigma$ (standard deviation of the mean) calculated from the multiple measurements of each band parameter. The olivine–pyroxene abundance ratio of the asteroids was estimated using the relationship between $ol/(ol + px)$ and BAR derived by Dunn et al. (2010) from the analysis of 48 ordinary chondrite samples. This linear regression is expressed as

Table 2

NEAs spectral band parameters and their errors. The columns in this table correspond to: object number and designation, the phase angle (g), the average surface temperature (T), the Band I center ($BI \pm 0.01$), the Band I depth ($BI_{\text{dep}} \pm 0.3$), the Band II center ($BII \pm 0.03$), the temperature corrected Band II center ($\Delta BII \pm 0.03$), the Band II depth ($BII_{\text{dep}} \pm 0.5$), the temperature corrected Band II depth ($\Delta BII_{\text{dep}} \pm 0.5$), the band area ratio ($BAR \pm 0.04$) and the temperature corrected band area ratio ($\Delta BAR \pm 0.04$).

Object	g ($^{\circ}$)	T (K)	BI (μm)	BI_{dep} (%)	BII (μm)	ΔBII (μm)	BII_{dep} (%)	ΔBII_{dep} (%)	BAR	ΔBAR
1036 Ganymed	5.9	129.6	0.909	18.79	1.867	1.901	8.05	5.49	0.901	0.768
1036 Ganymed	15.2	150.9	0.917	18.22	1.883	1.913	9.29	7.05	1.101	0.984
1620 Geographos	12.0	240.4	0.995	16.34	1.970	1.982	5.68	4.79	0.497	0.447
1620 Geographos	16.7	219.6	0.997	16.77	1.967	1.984	6.56	5.35	0.490	0.425
1620 Geographos	38.3	247.7	1.001	18.03	2.013	2.023	4.19	3.40	0.278	0.234
1627 Ivar	16.0	198.9	0.948	19.14	1.955	1.975	6.26	4.74	0.407	0.326
1627 Ivar	31.0	218.4	0.959	20.28	1.964	1.980	5.04	3.82	0.253	0.186
1862 Apollo	15.4	243.3	0.986	25.00	1.997	2.008	4.81	3.96	0.188	0.141
1862 Apollo	51.7	260.0	0.988	27.54	1.989	1.997	6.53	5.93	0.260	0.225
1980 Tezcatlipoca	25.0	218.6	0.947	16.05	1.932	1.949	6.62	5.40	0.526	0.460
1980 Tezcatlipoca	54.6	246.2	0.950	20.45	1.946	1.956	4.37	3.56	0.228	0.183
4179 Toutatis	6.1	222.3	0.943	14.91	1.971	1.987	4.89	3.72	0.551	0.487
4179 Toutatis	27.0	256.9	0.951	17.44	1.973	1.981	7.29	6.64	0.524	0.487
4179 Toutatis	68.0	260.5	0.952	18.04	1.962	1.970	6.90	6.31	0.487	0.452
4954 Eric	28.3	207.1	0.929	18.74	1.925	1.944	9.78	8.39	1.073	0.998
4954 Eric	62.0	255.2	0.923	16.69	1.946	1.955	8.81	8.14	0.917	0.878
6239 Minos	2.4	244.1	0.994	16.56	2.030	2.041	4.03	3.19	0.239	0.192
6239 Minos	47.3	263.2	0.993	19.02	2.010	2.017	6.10	5.55	0.348	0.315
11398	19.0	243.3	0.913	19.04	1.935	1.946	6.89	6.04	0.622	0.575
11398	33.0	248.3	0.925	19.81	1.945	1.955	8.33	7.55	0.653	0.610
25143 Itokawa	25.6	229.2	0.988	17.02	2.017	2.030	6.07	5.01	0.448	0.390
25143 Itokawa	69.0	235.2	0.982	19.85	2.017	2.030	5.45	4.48	0.395	0.341
35107	45.0	244.1	0.984	19.57	2.019	2.030	7.40	6.56	0.452	0.405
35107	87.0	257.6	0.997	18.90	1.996	2.004	6.92	6.28	0.444	0.407
66146	32.1	250.1	0.992	22.17	1.983	1.993	6.20	5.45	0.339	0.296
66146	55.3	249.1	0.987	22.99	1.984	1.994	6.35	5.59	0.290	0.246
66146	70.3	260.2	0.986	22.57	1.992	2.000	5.75	5.15	0.306	0.272

Table 3

Olivine abundance with its error and taxonomy for the NEAs. The columns in this table are: object number and designation, the phase angle (g), the olivine–pyroxene abundance ratio ($ol/(ol + px) \pm 0.03$), the temperature corrected olivine–pyroxene ratio ($\Delta ol/(ol + px) \pm 0.03$), taxonomic classification (Bus–DeMeo) and principal components PC1' and PC2' for each asteroid.

Object	g (°)	$ol/(ol + px)$	$\Delta ol/(ol + px)$	Taxonomy	PC1'	PC2'
1036 Ganymed	5.9	0.51	0.54	S	0.2400	0.0416
1036 Ganymed	15.2	0.46	0.49	Sr	0.3957	0.0381
1620 Geographos	12.0	0.61	0.62	Sq	−0.1096	0.0038
1620 Geographos	16.7	0.61	0.63	S	−0.0169	0.0206
1620 Geographos	38.3	0.66	0.67	Sqw	−0.2337	0.0503
1627 Ivar	16.0	0.63	0.65	S	−0.0151	0.0517
1627 Ivar	31.0	0.67	0.68	Sw	−0.0591	0.0689
1862 Apollo	15.4	0.68	0.69	Q	−0.5926	0.1996
1862 Apollo	51.7	0.66	0.67	Q	−0.6011	0.2387
1980 Tezcatlipoca	25.0	0.60	0.62	Sw	0.1132	0.0508
1980 Tezcatlipoca	54.6	0.67	0.68	Sw	−0.0238	0.0588
4179 Toutatis	6.1	0.59	0.61	Sqw	−0.2825	0.0972
4179 Toutatis	27.0	0.60	0.61	Sq	−0.3115	0.1622
4179 Toutatis	68.0	0.61	0.62	Sq	−0.3278	0.1282
4954 Eric	28.3	0.47	0.49	Sw	0.1552	0.0433
4954 Eric	62.0	0.51	0.52	Sr	0.4719	−0.0369
6239 Minos	2.4	0.67	0.68	Sq	−0.2907	0.0557
6239 Minos	47.3	0.64	0.65	Sqw	−0.3090	0.1231
11398	19.0	0.58	0.59	Sr	0.0631	0.0978
11398	33.0	0.57	0.58	Sr	0.1312	0.0912
25143 Itokawa	25.6	0.62	0.63	Sq	−0.3425	0.0946
25143 Itokawa	69.0	0.63	0.65	Sqw	−0.3283	0.1579
35107	45.0	0.62	0.63	Sq	−0.2848	0.1281
35107	87.0	0.62	0.63	Sq	−0.3077	0.1182
66146	32.1	0.65	0.66	Q	−0.5262	0.1994
66146	55.3	0.66	0.67	Q	−0.5737	0.1824
66146	70.3	0.65	0.66	Q	−0.4978	0.1938

$$ol/(ol + px) = -0.242 \times \text{BAR} + 0.728 \quad (1)$$

where the $ol/(ol + px)$ is expressed as a decimal. The band parameters and $ol/(ol + px)$ ratios with their corresponding errors obtained for each asteroid at different phase angles are presented in Tables 2 and 3 respectively.

2.3. Temperature correction to band parameters

Temperature-induced effects on the spectra of mafic minerals are characterized by shifting the band centers and broadening or narrowing the absorption features (Singer and Roush, 1985; Schade and Wäsch, 1999; Moroz et al., 2000; Hinrichs and Lucey, 2002). While surface temperature variations are considered of minor importance for main-belt asteroids, they may be significant for objects with higher eccentric orbits like NEAs (Moroz et al., 2000; Shestopalov and Golubeva, 2000). Furthermore, the spectra of laboratory samples are commonly obtained at room temperature (~300 K). Thus, in order to compare the band parameters with those measured for laboratory samples temperature corrections should be applied.

For each asteroid we have determined the average surface temperature (T) in the same way as (e.g., Burbine et al., 2009), where the temperature of the asteroid is approximated by the equation for energy conservation. The calculated temperatures of the NEAs are given in Table 2.

Since all the asteroids studied in this work are S-complex or Q-types, i.e., olivine–orthopyroxene assemblages, we have derived temperature corrections based on the analysis of ordinary chondrites. These meteorites are the most common type of meteorite to fall on Earth (~85% of all), and they have been generally linked to either S-complex or Q-type asteroids (e.g., Gaffey et al., 1993; Vernazza et al., 2008; Nakamura et al., 2011).

We have reanalyzed spectra of two H5 ordinary chondrites from Hinrichs and Lucey (2002) acquired in the temperature range between 80 and 400 K. Spectral band parameters (band centers, band depths and BAR) and their uncertainties were measured using the

same methods applied to the asteroid spectra. These data were combined with the results obtained by Moroz et al. (2000) for a L5 and a LL4 ordinary chondrite acquired at temperatures between 293 and 80 K.

We found that Band II is the most affected by temperature variations. A correlation between Band II centers and temperature is observed for all samples, i.e., Band II centers shift to longer wavelengths as the temperature increases. Therefore, to each data set a linear fit was performed and the equations that represent those linear fits were averaged, obtaining the following expression:

$$\text{BII}(T) = 0.0002 \times T \text{ (K)} + 1.87 \quad (2)$$

where the Band II center (BII) is given in μm . From this equation we derived a wavelength correction for the Band II center

$$\Delta \text{BII} (\mu\text{m}) = 0.06 - 0.0002 \times T \text{ (K)} \quad (3)$$

This correction is derived with respect to room temperature (300 K) and must be added to the calculated Band II center of each asteroid. The temperature corrected Band II centers are presented in Table 2. For the Band I center we found that the wavelength shift is in general very small (~0.003 μm), so no temperature correction was derived.

A decrease in Band II depth with increasing temperature was found for the three groups of ordinary chondrites. No obvious trend was observed for the Band I depth. Applying a similar procedure to the Band II center, we can estimate the approximate rate of change of the Band II depth for a range of temperatures

$$\text{BII}_{\text{dep}}(T) = 20.89 - 0.015 \times T \text{ (K)} \quad (4)$$

where the Band II depth (BII_{dep}) is given in %. From this equation we derived a temperature correction for the Band II depth

$$\Delta \text{BII}_{\text{dep}} (\%) = 0.015 \times T \text{ (K)} - 4.5 \quad (5)$$

This correction is derived with respect to the room temperature and must be added to the calculated Band II depth of each asteroid.

An inverse correlation between BAR and temperature was also found for the ordinary chondrites samples. As in the previous cases we obtained an average expression to calculate the rate of change of BAR for a range of temperatures

$$\text{BAR}(T) = 0.83 - 0.00075 \times T \text{ (K)} \quad (6)$$

from which a temperature correction with respect to room temperature was derived

$$\Delta\text{BAR} = 0.00075 \times T \text{ (K)} - 0.23 \quad (7)$$

This correction must be added to the calculated BAR values of each asteroid before comparing with those calculated for laboratory samples obtained at room temperature. The temperature corrected Band II depths and BARs are presented in Table 2. Based on the corrected BAR values, the olivine abundance of each asteroid was recalculated using Eq. (1). These values are included in Table 3.

2.4. Phase reddening effect on the band parameters

An inspection of the measured Band I depths presented in Table 2 indicates a change of this parameter with phase angle. These values are plotted as a function of phase angle in Fig. 1. The black circles represent the measured Band I depths. Values derived from multiple observations of individual asteroids are connected by lines and have been displayed into two panels for clarity. A tendency of increasing spectral contrast as the phase angle increases is observed for most of the objects in the range of $\sim 2^\circ < g < 70^\circ$. When higher phase angles are included (up to $\sim 90^\circ$) a slight decrease in Band I depth is observed. However, as we do not have sufficient data at such high phase angles, it remains unclear whether this is the actual tendency for $g > 70^\circ$. A similar situation is observed with the temperature corrected Band II depths (Fig. 2). In this case the absorption band seems to increase in the range of $\sim 2^\circ < g < 55^\circ$ and then it remains more or less constant for higher phase angles. In some cases we notice a deviation from these trends among the measured band depths, i.e., a decrease of band depths with increasing phase angle. Although compositional variations cannot be completely ruled out, this is more likely due to the fact that some spectra show more scattering than others, especially in the Band II. This is probably caused by an incomplete correction

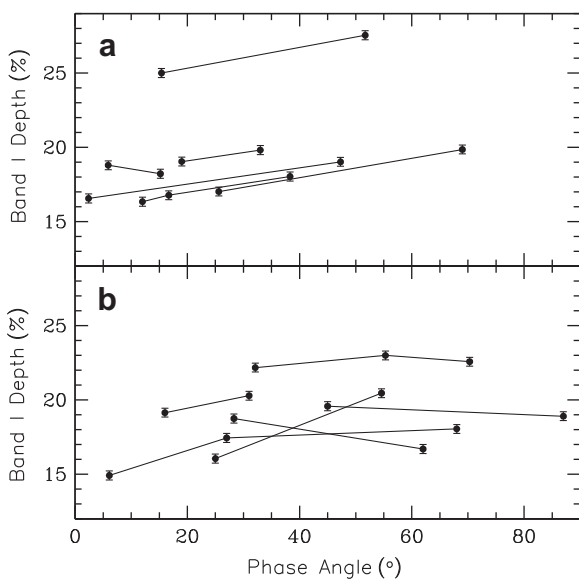


Fig. 1. Band I depth as a function of phase angle for the NEAs. Values derived from multiple observations of individual asteroids are connected by lines and have been displayed into two panels for clarity.

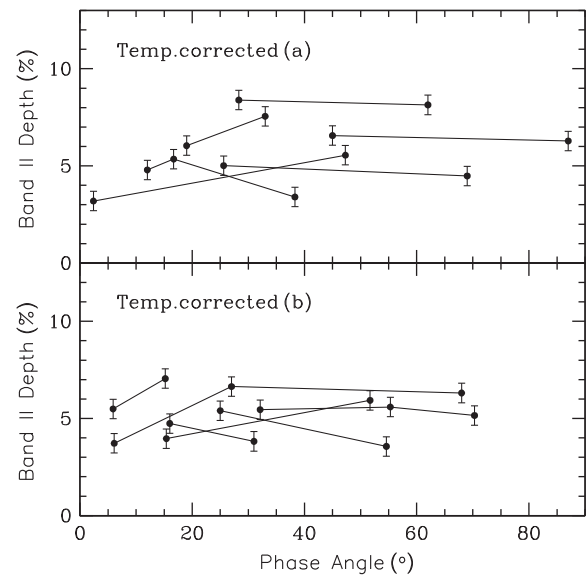


Fig. 2. Temperature corrected Band II depth as a function of phase angle for the NEAs. Values derived from multiple observations of individual asteroids are connected by lines and have been displayed into two panels for clarity.

of the telluric water bands, and due to the decreased response of the detector for wavelengths beyond $2.4 \mu\text{m}$. This was seen in the Band I of Asteroids 1036 Ganymed ($g = 15.2^\circ$) and 4954 Eric ($g = 62^\circ$) and in the Band II of Asteroids 1620 Geographos ($g = 38.3^\circ$), 1627 Ivar ($g = 31.0^\circ$) and 1980 Tezcatlipoca ($g = 54.6^\circ$).

In an effort to quantify the phase reddening effect on band depths we performed a linear fit to the data of each asteroid. Only the data in the phase angle ranges where the correlations are observed were fitted. Those values that deviate from the general tendency were not considered. The equations derived from the linear fits were then averaged to obtain a general expression for each band depth. Previous works have derived correlations between band parameters and phase angle (e.g., Luu and Jewitt, 1990; Moskovitz et al., 2010). However, these correlations were obtained from mixed observations of different objects, making it very difficult to disentangle the phase reddening from other effects. Our approach, on the other hand, attempts to overcome this problem by evaluating the phase reddening on individual objects from which an average expression is then derived. We caution that this procedure only provides a rough estimation of the effects of phase reddening on band depths, since for each asteroid we have a limited phase angle range. The general equations for the band depths are given by

$$\text{BI}_{dep}(g) = 0.066 \times (g) + 17.42 \quad (8)$$

$$\text{BII}_{dep}(g) = 0.093 \times (g) + 3.73 \quad (9)$$

where the band depths are measured in %. Thus, according to these equations, on average, Band I and Band II depths will increase 0.66% and 0.93% respectively, for every 10° increase in phase angle in the range of $2^\circ < g < 70^\circ$ for Band I and $2^\circ < g < 55^\circ$ for Band II.

From Eqs. (8) and (9) we can obtain expressions for band depth corrections that are a function of the phase angle,

$$\text{BI}_{depc} = \text{BI}_{dep} - 0.066 \times (g) \quad (10)$$

$$\text{BII}_{depc} = \text{BII}_{dep} - 0.093 \times (g) \quad (11)$$

where BI_{depc} and BII_{depc} are the corrected band depths. With these equations we can roughly correct the effect of phase reddening in the band depths in the phase angle ranges of $2^\circ < g < 70^\circ$ for Band I and $2^\circ < g < 55^\circ$ for Band II.

The temperature corrected BAR values presented in Table 2 and plotted in Fig. 3 indicate variations with increasing phase angle, however no obvious trend can be seen. The most significant change in BAR is observed for the same objects whose absorption bands show more scattering.

Small variations on band centers with increasing phase angle were found, however they are within the uncertainties associated to these band parameters. This can be seen in Fig. 4 where we plotted Band I center as a function of phase angle for the NEAs. The black circles represent the measured Band I centers. Values derived from multiple observations of the same asteroids are connected by lines.

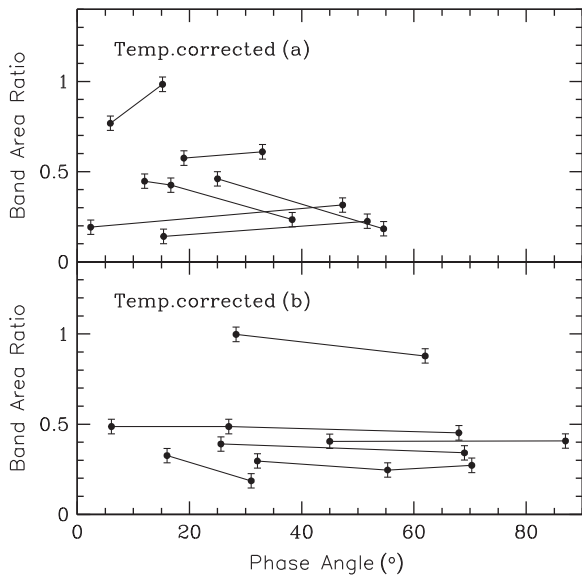


Fig. 3. Temperature corrected BAR values as a function of phase angle for the NEAs. Values derived from multiple observations of individual asteroids are connected by lines and have been displayed into two panels for clarity.

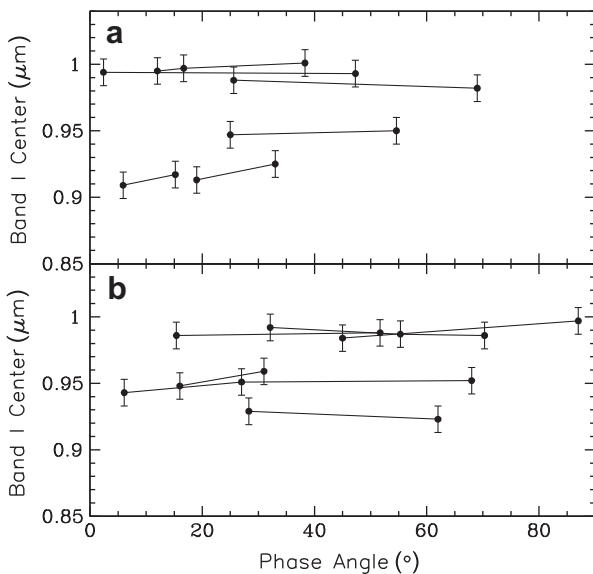


Fig. 4. Band I center as a function of phase angle for the NEAs. Values derived from multiple observations of individual asteroids are connected by lines and have been displayed into two panels for clarity.

3. Phase reddening from laboratory measurements of ordinary chondrites

3.1. Data and spectral band analysis

As it was stated before, ordinary chondrites are considered to be the meteorite analogs of S-complex and Q-type asteroids. Therefore, in order to complement our study we have analyzed the spectra of a group of ordinary chondrites obtained at a wide range of phase angles.

Diffuse reflectance spectra were collected at the University of Winnipeg Planetary Spectrophotometer Facility (UWPSF) using an ASD FieldSpec Pro HR spectrometer over the wavelength range of 0.35–2.5 μm . The three samples that have been analyzed are Dhurmsala (LL6, fell 1860), Pavlograd (L6, fell 1826), and Lancon (H6, fell 1897). They were all crushed and sieved to a grain size of <150 μm . The samples were gently poured into aluminum sample cups and the edge of a glass slide was drawn across the sample to provide a flat surface for the spectral measurements. Reflectance spectra were acquired relative to a 100% Labsphere Spectralon disk measured at an incident angle $i = 13^\circ$ and emission angle $e = 0^\circ$ (13° phase angle). Ten sets of measurements were acquired for each sample resulting in three emission angles ($e = 0^\circ, 30^\circ, 60^\circ$), five incidence angles ($i = 0^\circ, 13^\circ, 30^\circ, -30^\circ, 60^\circ$) and five different phase angles ranging from 13° to 120° . Positive angles (i and e) are measured when the light source and the detector are on either side of the normal, while negative incidence angles are measured when both light source and detector are on the same side of the normal. For each measurement, a total of 250 scans were collected and averaged to improve the signal to noise ratio.

Spectral band parameters and their uncertainties were measured for each VIS–NIR spectrum using the same methods applied to the asteroid spectra. In addition to the band parameters we have also measured the spectral slope, which was determined from the fitted continuum across Band I, i.e., a straight line tangent to the reflectance peaks from ~ 0.7 to $\sim 1.55 \mu\text{m}$. The uncertainty of the spectral slope is given by the average $1 - \sigma$, estimated from sampling different ranges of points near to the reflectance peaks on either side of the absorption band. The olivine–pyroxene abundance ratio of the samples was estimated using Eq. (1). The band parameters, spectral slopes and $ol/(ol + px)$ ratios with their corresponding errors obtained for each sample are presented in Table 4.

3.2. Phase reddening effect on the band parameters

The analysis of the laboratory spectra shows that variations in the band parameters can arise not only by changing the phase angle, but also for the same phase angle using different configurations of the incidence and emission angle. As can be seen in Table 4 phase angles of $30^\circ, 60^\circ$ and 90° were obtained using different combinations of i and e , and these different combinations produced, in some cases, very different band parameter values. Since we want to quantify the effects of phase reddening on the spectral band parameters, for those phase angles where more than one combination of i and e was used the average value for each band parameter was taken. These average values are presented in Table 4.

Fig. 5 shows the reflectance spectra of the LL6 ordinary chondrite at five different phase angles. From the bottom to the top the phase angles are $13^\circ, 30^\circ, 60^\circ, 90^\circ$ and 120° . The spectra corresponding to $g = 30^\circ, 60^\circ$ and 90° are the average spectra obtained from different combinations of the incidence and emission angles. All the spectra are normalized to unity at $0.55 \mu\text{m}$. An increase in the spectral slope with increasing phase angle is evident, being more significant for phase angles higher than 30° . A similar

Table 4
Spectral band parameters of the ordinary chondrites. The columns in this table correspond to: sample type, the incidence angle (i), the emission angle (e), the phase angle (g), the spectral slope ± 0.004 , the Band I center (BI ± 0.003), the Band I depth ($BI_{dep} \pm 0.1$), the Band II center (BII ± 0.005), the Band II depth ($BII_{dep} \pm 0.2$), the band area ratio (BAR ± 0.01) and the olivine–pyroxene abundance ratio ($ol/(ol + px) \pm 0.03$).

Sample	i (°)	e (°)	g (°)	Slope ($\% \mu^{-1}$)	BI (μm)	BI_{dep} (%)	BII (μm)	BII_{dep} (%)	BAR	$ol/(ol + px)$
LL6	13	0	13	-0.127	0.984	36.81	1.963	17.27	0.58	0.59
LL6	30	0	30	-0.094	0.982	38.41	1.959	18.35	0.58	0.59
LL6	0	30	30	-0.083	0.978	38.47	1.961	18.73	0.61	0.58
LL6	-30	60	30	-0.179	0.978	36.69	1.964	18.36	0.63	0.58
LL6	30,0,-30	0,30,60	30	-0.119	0.979	37.86	1.961	18.48	0.61	0.58
LL6	60	0	60	0.002	0.981	40.28	1.957	18.55	0.55	0.59
LL6	0	60	60	-0.097	0.969	37.30	1.965	18.89	0.68	0.56
LL6	30	30	60	-0.043	0.982	39.61	1.960	18.22	0.56	0.59
LL6	60,0,30	0,60,30	60	-0.046	0.977	39.06	1.961	18.55	0.60	0.58
LL6	60	30	90	0.099	0.973	37.91	1.963	18.75	0.62	0.58
LL6	30	60	90	0.184	0.980	36.84	1.961	16.46	0.53	0.60
LL6	60,30	30,60	90	0.141	0.976	37.38	1.962	17.61	0.57	0.59
LL6	60	60	120	0.212	0.972	34.18	1.959	17.50	0.67	0.57
L6	13	0	13	-0.102	0.949	42.37	1.944	18.70	0.57	0.59
L6	30	0	30	-0.090	0.951	42.71	1.943	18.92	0.56	0.59
L6	0	30	30	-0.089	0.950	42.39	1.945	19.03	0.58	0.59
L6	-30	60	30	-0.192	0.950	41.58	1.947	18.00	0.57	0.59
L6	30,0,-30	0,30,60	30	-0.124	0.951	42.23	1.945	18.65	0.57	0.59
L6	60	0	60	-0.084	0.954	43.16	1.945	18.21	0.51	0.60
L6	0	60	60	-0.085	0.949	43.36	1.948	18.73	0.59	0.59
L6	30	30	60	0.004	0.947	44.68	1.939	20.86	0.62	0.58
L6	60,0,30	0,60,30	60	-0.055	0.950	43.73	1.944	19.26	0.57	0.59
L6	60	30	90	0.097	0.945	42.53	1.941	17.21	0.51	0.61
L6	30	60	90	0.177	0.944	41.69	1.948	17.24	0.56	0.59
L6	60,30	30,60	90	0.137	0.944	42.11	1.945	17.23	0.54	0.60
L6	60	60	120	0.191	0.944	39.84	1.943	16.15	0.51	0.61
H6	13	0	13	-0.141	0.934	35.45	1.930	18.41	0.88	0.52
H6	30	0	30	-0.151	0.935	36.20	1.929	19.12	0.89	0.51
H6	0	30	30	-0.115	0.933	35.33	1.934	18.33	0.88	0.52
H6	-30	60	30	-0.177	0.931	34.80	1.931	18.26	0.93	0.50
H6	30,0,-30	0,30,60	30	-0.148	0.933	35.44	1.932	18.57	0.90	0.51
H6	60	0	60	-0.149	0.935	36.48	1.926	18.91	0.83	0.53
H6	0	60	60	-0.096	0.929	34.54	1.935	16.93	0.84	0.52
H6	30	30	60	-0.096	0.933	36.93	1.931	17.85	0.76	0.55
H6	60,0,30	0,60,30	60	-0.114	0.933	35.98	1.931	17.90	0.81	0.53
H6	60	30	90	-0.058	0.932	34.77	1.928	17.65	0.83	0.53
H6	30	60	90	-0.012	0.926	31.69	1.934	14.77	0.84	0.53
H6	60,30	30,60	90	-0.035	0.929	33.23	1.931	16.21	0.83	0.53
H6	60	60	120	0.020	0.932	31.77	1.932	15.55	0.80	0.54

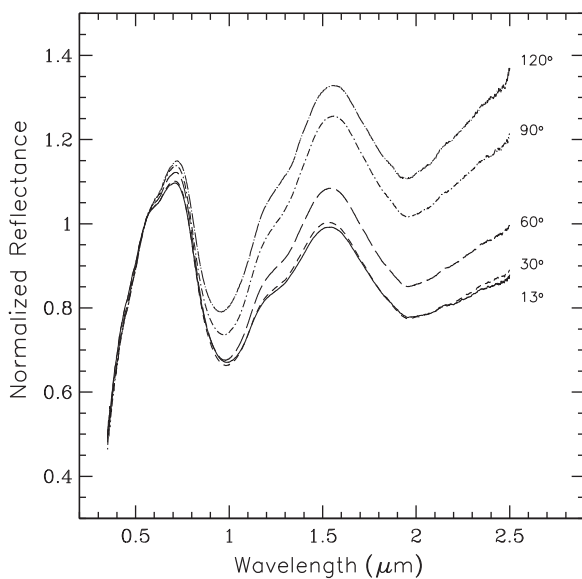


Fig. 5. Reflectance spectra of the LL6 chondrite Dhurmsala obtained at five different phase angles. From the bottom to the top $g = 13^\circ$ (solid line), $g = 30^\circ$ (short dashed line), $g = 60^\circ$ (long dashed line), $g = 90^\circ$ (dot-short dashed line) and $g = 120^\circ$ (dot-long dashed line). All the spectra are normalized to unity at $0.55 \mu\text{m}$.

behavior was observed for the other two samples. For phase angles between 13° and 30° a slight reddening is observed in the LL6 spectra, while a slight blueing (i.e. decreasing of the spectral slope with increasing phase angle) is seen in the L6 and H6 spectra. Variations in the strengths of the absorption bands are also seen for the three samples.

In Fig. 6 we plotted the spectral slopes (panel a), the BAR values (panel b), the Band I depths (panel c), the Band II depths (panel d) and the band centers (panels e and f) as functions of the phase angle for the LL6 ordinary chondrite. The dashed lines are polynomial fits.

From the “a” panel we can see that the measured spectral slopes remain more or less constant for phase angles between 13° and 30° , and then they increase as the phase angle increases up to 120° . A similar trend was observed for the L6 and H6 ordinary chondrites. The largest difference in spectral slope between the lowest (13°) and the highest (120°) phase angle was found for the LL6 ordinary chondrite, which increased $0.34\% \mu^{-1}$, followed by the L6 ordinary chondrite with an increase of $0.29\% \mu^{-1}$ and the H6 ordinary chondrite with an increase of $0.16\% \mu^{-1}$.

The Band I depth of the three samples has its maximum spectral contrast near $g = 60^\circ$. The LL6 spectra show a progressive increase of Band I depth from $g = 13^\circ$ to 60° (Fig. 6 panel c), however the L6 and H6 spectra show almost no change in Band I depth for phase angles between 13° and 30° , and then an increase in Band I depth

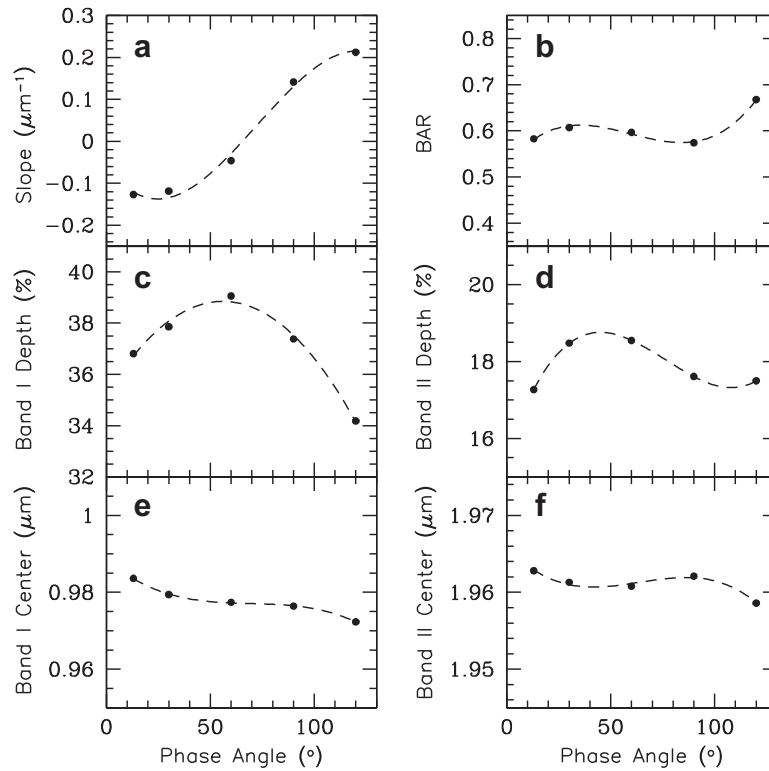


Fig. 6. LL6 ordinary chondrite: Measured spectral slopes (a), BAR values (b), Band I depths (c), Band II depths (d) Band I centers (e) and Band II centers (f) as a function of the phase angle. The error bars are smaller than the symbols. The dashed lines represent polynomial fits.

from $g = 30^\circ$ to 60° . The spectra of the three samples show a decrease in Band I depth between 60° and 120° phase angle. The largest increase in Band I depth between the lowest phase angle (13°) and the phase angle at which the Band I reaches its maximum spectral contrast ($\sim 60^\circ$) corresponds to the LL6 sample, with an increase of 2.25%, followed by the L6 and H6 with an increase of 1.36 and 0.53% respectively. Of the three samples, the LL6 also shows the most significant decrease of Band I depth between the phase angle corresponding to the maximum spectral contrast and the highest phase angle (120°), with a decrease of 4.88%, followed by the H6 with a decrease of 4.21% and the L6 with a decrease of 3.89%.

The behavior of the Band II depths seems to be more complex. The LL6 spectra show a progressive increase of Band II depths from $g = 13^\circ$ to $\sim 45^\circ$ (where the band reaches its maximum spectral contrast) and then it drops between 45° and 90° , becoming more or less constant from 90° to 120° phase angle (Fig. 6 panel d). The Band II depths of the L6 spectra show almost no change between 13° and 30° . From 30° to 60° Band II depths increase and beyond 60° gradually decrease with phase angle increasing to 120° . The Band II depths of the H6 spectra show a slight increase from 13° to 30° and then drop from 30° to 120° . The most significant increase in Band II depths between the lowest phase angle and the phase angle at which the Band II reaches its maximum spectral contrast was observed for the LL6 sample, which shows an increase of 1.56%, followed by the L6 with an increase in Band II depth of 0.56% and the H6 with the lowest increase of 0.16%. The largest difference in Band II depth between the phase angle corresponding to the maximum spectral contrast and the largest phase angle (120°) was observed for the L6 sample that shows a decrease of 3.11%, followed by the H6 with a decrease of 3.02% and the L6 with a decrease of 1.33%.

Variations in the BAR values are observed among the three samples, being the maximum difference between the lowest and

highest phase angle ~ 0.1 , however no systematic trends were found. A similar situation occur with the band centers, where the maximum shift (to shorter wavelengths) between the lowest and highest phase angle is $\sim 0.01 \mu\text{m}$ for the Band I center of the LL6 sample (Fig. 6 panel e).

4. Phase reddening and mineralogical analysis

The analysis of the laboratory samples indicate that the (olivine-rich) LL6 ordinary chondrite is the most affected by phase reddening. This sample shows the largest variation in spectral slopes and band depths with increasing phase angles. This material-dependence of the phase reddening confirm the results reported by previous studies (e.g., Adams and Filice, 1967; Gradie et al., 1980). A comparison between the measurements obtained from the laboratory samples with those from the NEAs spectra, reveal that the rate of change in band depths for the ordinary chondrites is lower than that found for the asteroids. Differences in grain size, composition and packing between the NEAs studied and the meteorite samples could explain this discrepancy. Of the three samples, the spectral behavior of the LL6 is the closest to the NEAs. This resemblance could be attributed to the fact that half of the asteroids studied are located in the same region as the LL ordinary chondrites in the Band I center versus BAR diagram (see Figs. 10 and 11).

Because band centers and composition of mafic minerals are related, these band parameters are used to derive information about the pyroxene and olivine composition of asteroids surfaces. For that purpose, and from the analysis of laboratory samples, different empirical equations have been derived (e.g., Gaffey et al., 2002; Burbine et al., 2007; Dunn et al., 2010). Our results show that there is no significant change in band centers with increasing phase angle for both asteroid and meteorite spectra, being the largest shift

of $\sim 0.01 \mu\text{m}$ (for the meteorite spectra), which is on the order of the uncertainty associated with this parameter for the asteroid spectra. Based on this, it seems to be unlikely that phase reddening could lead to a misinterpretation of the minerals composition in asteroids.

In addition to the band centers, we used the BAR values and Eq. (1) to estimate olivine and pyroxene abundances for both NEAs and the laboratory samples. The results obtained (Tables 3 and 4) show that the largest variation in the $ol/(ol + px)$ ratio with increasing phase angles for NEAs is ~ 0.02 (not taken into account the values obtained from the noisy spectra), and for the ordinary chondrites between 0.03 and 0.05. Since these variations are on the order of the errors, effects of phase reddening on the estimation of the olivine–pyroxene abundance ratio seems to be negligible.

5. Phase reddening and space weathering

Space weathering is the term commonly used to refer to any process that modifies the surfaces of airless bodies. The effects of space weathering on the spectra can be seen as reddening of the spectral slopes and suppression of the absorption bands, (Pieters et al., 2000; Hapke, 2001; Gaffey, 2010). The analysis of returned samples from the Moon and Asteroid (25143) Itokawa have shown that the cause of the spectral changes is the presence of submicroscopic metallic iron (SMFe) incorporated into the soil grains (Pieters et al., 2000; Taylor et al., 2001; Noguchi et al., 2011). This SMFe is produced by condensation of vapors created by micrometeorite impacts and/or deposition of atoms sputtered off from silicates by solar wind ions (Taylor et al., 2001; Hapke, 2001; Clark et al., 2002a). Ion irradiation experiments conducted by Brunetto and Strazzulla (2005) showed that solar wind irradiation can also redden reflectance spectra by creation of displacements (the sum of the vacancies and the replacements) caused by elastic collisions between ions and target nuclei.

Brunetto et al. (2006) determined that the effects of space weathering due to ion irradiation can be described by an exponential continuum. They computed the ratio between the reflectance spectra of irradiated and unirradiated samples and then modeled it with an exponential curve given by

$$\text{Ratio} = W(\lambda) = K \exp(C_S/\lambda) \quad (12)$$

where λ is the wavelength, K is a scale factor and the parameter C_S is a measure of the effects of space weathering. They called $W(\lambda)$ the weathering function. Since both effects, phase reddening and space weathering, are manifested in a similar way, we investigated whether the red slopes exhibited by spectra obtained at high phase angles could be misinterpreted as space weathering. In order to do this we carried out two different experiments.

For the first experiment we followed the same procedure used by Brunetto et al. (2006), with the difference that instead of dividing the reflectance spectra of an irradiated by an unirradiated sample, we computed the ratio between the spectra obtained at high phase angles and those obtained at low phase angles. Since there is no significant change in spectral slope between $g = 13^\circ$ and 30° we used the spectrum obtained at a phase angle of 30° as reference point. Fig. 7 shows the ratio plots (solid lines) between the spectra of the LL6 obtained at $g = 60^\circ$ and $g = 30^\circ$ (bottom), at $g = 90^\circ$ and $g = 30^\circ$ (middle) and at $g = 120^\circ$ and $g = 30^\circ$ (top panel). The ratio plots were modeled by fitting the same exponential curve used by Brunetto et al. (2006)

$$\text{Ratio} = P_R(\lambda) = A \exp(C_P/\lambda) \quad (13)$$

where we have just changed the name of the function, we call it the phase reddening function (P_R) and the parameters A and C_P are equivalents to the parameters K and C_S respectively, with the

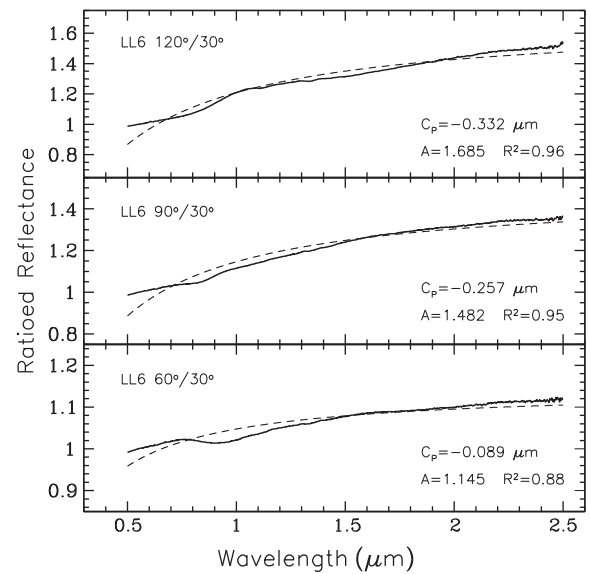


Fig. 7. Ratio plots (solid lines) between the spectra of the LL6 obtained at $g = 60^\circ$ and $g = 30^\circ$ (bottom), at $g = 90^\circ$ and $g = 30^\circ$ (middle) and at $g = 120^\circ$ and $g = 30^\circ$ (top panel). Dashed curves are the best fit curves obtained using Eq. (13). For each ratio plot the resultant A , C_P and R^2 values are given.

difference that C_P would be a measure of the effect of the phase reddening. The best fit curves obtained using Eq. (13) are represented with dashed lines in Fig. 7. Here we have used the LL6 spectra as an example, but the same procedure can be used with the other samples. In Fig. 7 we have also included the resultant A and C_P values and the coefficient of determination (R^2) of the fitted curves for each ratio plot. Similarly to the results obtained by Brunetto et al. (2006) the ratio of the spectra show some traces of Bands I and II, which can affect the fitting in those spectral regions. Nevertheless, the R^2 for the fitted curves ranges between 0.88 and 0.96 and, in general, the results are comparable to those of Brunetto et al. (2006). After comparing the C_P values with the C_S obtained by Brunetto et al. (2006) for different samples, we found that the C_P values are similar to the C_S obtained for the H5 ordinary chondrite Epinal, which was irradiated with Ar^{++} (60 keV) at three different ion fluences.

Brunetto et al. (2006) found that there is a strong correlation between the C_S parameter and the number of displacements per cm^2 (damage parameter). From their experimental data they were able to create a damage curve that was fitted by

$$C_S = \alpha \ln(\beta d + 1) \quad (14)$$

where d is the damage parameter, $\alpha = -0.33 \pm 0.06 \mu\text{m}$ and $\beta = (1.1 \pm 0.5) \times 10^{-19} \text{cm}^2$. Using this equation we calculated the number of displacements per cm^2 that would correspond to our C_P values. It is important to point out that in this case the d values calculated using the C_P have no real physical meaning, since the C_P parameter quantifies the effect of the phase reddening and not the space weathering, however their calculation is useful to illustrate how the phase reddening can resemble different degrees of space weathering. This can be seen in Fig. 8 where we have plotted the C_P (LL6 ordinary chondrite) and C_S (Epinal ordinary chondrite) values versus the calculated damage parameter for each sample. The LL6 data are represented with filled symbols while the Epinal values are plotted as open symbols. These results indicate that an increase in phase angle in the range of 30° – 120° would be equivalent to irradiate the sample with high mass ions (Ar^{++} 60 keV) with an ion fluence in the range of $\sim 1.3 \times 10^{15}$ – 1.7×10^{16} ions cm^{-2} . These ion fluences are equivalent to exposure times of $\sim 0.1 \times 10^6$ – 1.3×10^6 years at about 1 AU from the Sun (calculated as in

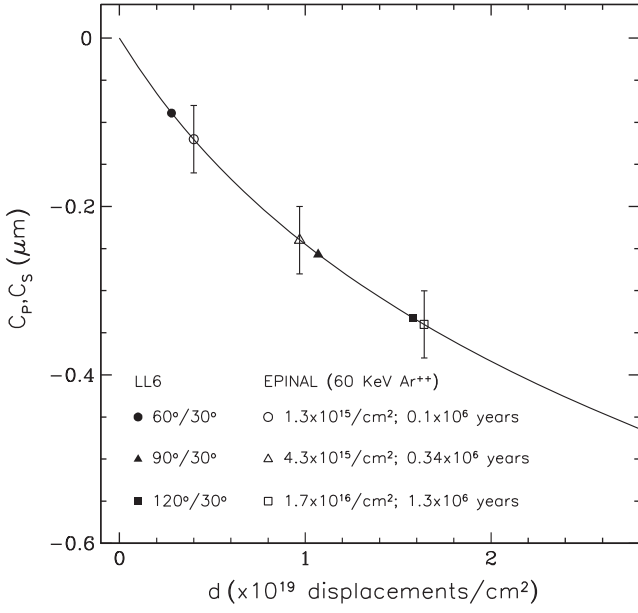


Fig. 8. The C_p (LL6 ordinary chondrite) and C_s (Epinal ordinary chondrite) parameters as a function of the number of displacements per cm^2 (damage parameter). The data corresponding to the Epinal meteorite were obtained from Brunetto et al. (2006). The LL6 and the Epinal data are plotted as filled and open symbols respectively. For the LL6 each symbol represents the value obtained from the ratioed spectra of different phase angles. The symbols corresponding to the Epinal meteorite represent different ions fluences. Approximate exposure times (at 1 AU) corresponding to each ion fluence are also shown. The solid line represents the experimental damage curve from Brunetto et al. (2006). The error bars of the LL6 data are on the order of the size of symbols.

Strazzulla et al. (2005)). Laboratory experiments (e.g., Strazzulla et al., 2005) have shown that the timescale for the weathering of NEAs surfaces due to ion irradiation is on the order of 10^4 – 10^6 years. Thus, observing NEAs at high phase angles could produce spectral slopes that resemble those exhibited by weathered surfaces.

For the second experiment we modeled the optical effects of the SMFe on the laboratory spectra by using Hapke's radiative transfer model (Hapke, 1981, 1993, 2001), and then we compared these spectra with those obtained at different phase angles.

From Hapke (2001) the bidirectional reflectance of a medium of isotropic scatterers ignoring the opposition effect is given by

$$r(i, e, g) = \frac{w}{4\pi} \frac{\mu_0}{\mu_0 + \mu} H(\gamma, \mu_0) H(\gamma, \mu) \quad (15)$$

where i , e and g are the incidence, emission and phase angle respectively, $\mu_0 = \cos(i)$, $\mu = \cos(e)$, w is the single scattering albedo, $\gamma = (1 - w)^{1/2}$, and $H(\gamma, \mu)$ is an analytic approximation to the Ambartsumian–Chandrasekhar H functions. Since most reflectances are relative to a standard, Hapke (2001) represented this relative reflectance as

$$F(\gamma) = \frac{1 - \gamma^2}{(1 + 2\gamma\mu_0)(1 + 2\gamma\mu)} \quad (16)$$

from which γ can be determined, and the single scattering albedo of the sample can be calculated as

$$w = 1 - \gamma^2 \quad (17)$$

The single scattering albedo can be also written as a function of the properties of the particles of the medium by

$$w = S_e + (1 - S_e) \frac{1 - S_i}{1 - S_i \Theta} \quad (18)$$

where S_e is the Fresnel reflection coefficient for externally incident light, S_i is the Fresnel reflection coefficient for internally scattered light (see Hapke, 2001), and Θ is the single-pass transmission of the particle. If there is no internal scattering, then

$$\Theta = e^{-\alpha(D)} \quad (19)$$

where (D) is the mean ray path length (Hapke, 1993) and α is the absorption coefficient given by

$$\alpha = \frac{4\pi nk}{\lambda} \quad (20)$$

where n and k are the real and imaginary part of the refractive index respectively and λ is the wavelength. From Eqs. (18) and (19) the absorption coefficient can be also calculated as

$$\alpha = \frac{1}{(D)} \ln \left[S_i + \frac{(1 - S_e)(1 - S_i)}{w - S_e} \right] \quad (21)$$

To model the effects of the SMFe, the absorption coefficient of the host material (α_h) is increased by adding to it the absorption coefficient of the SMFe (α_{Fe}). Using the Maxwell–Garnett effective medium theory, Hapke (2001) derived an expression to calculate α_{Fe} ,

$$\alpha_{\text{Fe}} = \frac{36\pi z f \rho_h}{\lambda \rho_{\text{Fe}}} \quad (22)$$

where f is the mass fraction of the Fe particles, ρ_h is the density of the host material, ρ_{Fe} is the density of iron and z is given by

$$z = \frac{n_h^3 n_{\text{Fe}} k_{\text{Fe}}}{(n_{\text{Fe}}^2 - k_{\text{Fe}}^2 + 2n_h^2)^2 + (2n_{\text{Fe}} k_{\text{Fe}})^2} \quad (23)$$

where n_h and n_{Fe} are the real part of the refractive indices of the host material and iron respectively, and k_{Fe} is the imaginary part of the refractive index of iron. Thus, if we use Eq. (21) to calculate the absorption coefficient of the host material (α_h), then the absorption coefficient of the material containing SMFe is given by

$$\alpha_w = \alpha_h + \alpha_{\text{Fe}} \quad (24)$$

Looking at Eqs. (15) and (18)–(20) we can understand why phase reddening and space weathering are manifested in similar ways. Reflectance spectra are controlled by the single scattering albedo (w), which is a function of the absorption coefficient (α). The absorption coefficient is a parameter that characterizes how deep into a material light of a particular wavelength can penetrate before being absorbed. As the phase angle increases, light is less able to escape from the medium, meaning that photons are more absorbed, resulting in a decrease of reflectance throughout the entire spectrum. However, because the absorption coefficient is inversely proportional to the wavelength (the shorter the wavelength the higher the absorption coefficient) the reflectance in the blue part of the spectrum will decrease faster than in the red part, producing the increase in spectral slope (reddening). Similarly, the addition of the SMFe (Eq. (24)) will decrease the blue part of the spectrum more than the red part due to the stronger absorption at short wavelengths, increasing the spectral slope (Hapke, 2001).

For our experiment we used the spectrum of the LL6 ordinary chondrite obtained at a phase angle of 13° as reference point. Using these data we first calculated α_h with Eqs. (16)–(21), where we have assumed $n_h = 1.7$, which is a typical value for mafic minerals (Hapke, 2001). Then using Eqs. (22) and (23) we estimated α_{Fe} . For this calculation we have assumed $\rho_h = 3.48$, which is the average grain density for LL chondrites (Britt and Consolmagno, 2003) and $\rho_{\text{Fe}} = 7.87$. The optical constants of iron, n_{Fe} and k_{Fe} , were taken from Johnson and Christy (1974). Since these values were measured only for $\lambda \sim 1.9 \mu\text{m}$, we did a polynomial fit to the data in order to extrapolate them to $2.5 \mu\text{m}$. The α_{Fe} was calculated for different mass fractions of Fe and then the resulting values were

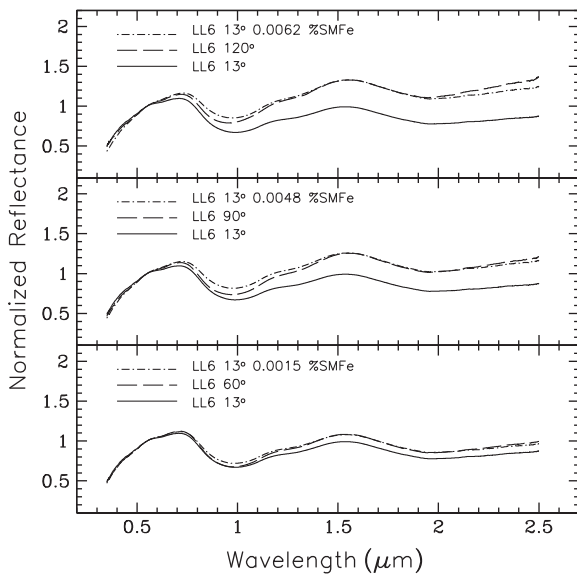


Fig. 9. Reflectance spectra of the LL6 chondrite Dhurmsala after adding different amounts of SMFe (dot-short dashed lines) to the spectrum obtained at $g = 13^\circ$. For comparison the spectra of the LL6 obtained at $g = 13^\circ$ (solid lines) and $g = 60^\circ$, 90° and 120° (long dashed lines from the bottom to the top) have been included. All the spectra are normalized to unity at $0.55 \mu\text{m}$.

added to the calculated α_h in order to obtain α_w . These α_w values were then inserted into Eq. (19), which combined with Eq. (18) allowed us to determine the new single scattering albedos. Finally, we calculated γ from Eq. (17) and using Eq. (16) we obtained the “weathered spectra” for the different % of SMFe. In Fig. 9 we plot the reflectance spectra of the LL6 after adding different amounts of SMFe. We found that the spectrum obtained at $g = 60^\circ$ shows a spectral slope comparable to the spectrum obtained at $g = 13^\circ$ after adding 0.0015% SMFe. For phase angles of 90° and 120° the spectral slopes are equivalent to adding 0.0048 and 0.0062% SMFe respectively, to the spectrum obtained at $g = 13^\circ$. If we consider that an amount of $\sim 0.02\%$ of SMFe is required to explain the red slopes of some S-complex asteroids (e.g., Hapke, 2001; Rivkin et al., 2004), this means that the spectral slope for the highest phase angle ($g = 120^\circ$) would be equivalent to $\sim 30\%$ of that SMFe.

6. Phase reddening and taxonomic classification

The taxonomic classification of asteroids is based on shared observational parameters like spectral slope, color, albedo and band depth. Most of the current classification systems are based on visible data (e.g., Tholen, 1984; Bus and Binzel, 2002b,a), in part because only during the last decade sufficient high-quality NIR spectral data became available to extend the classification to the near-infrared wavelengths. Two of the most common systems used to classify asteroids using VIS–NIR data are those introduced by Gaffey et al. (1993) and more recently by DeMeo et al. (2009). Gaffey et al. (1993) developed their classification system from the analysis of 39 asteroids classified as S-type by Tholen (1984). They divided the S-population into seven main compositional subgroups designated S(I)–S(VII). These subgroups range from pure olivine through olivine–pyroxene mixtures to pure pyroxene mixtures, and were derived on the basis of two band parameters, the Band I center and the BAR. The Bus–DeMeo taxonomy, on the other hand, is based on Principal Component Analysis and is comprised of 24 classes that include three major complexes (S-, C- and X-complex) and the end members O, Q, R, V, D, K, L, T. The S-complex is subdivided into S, Sa, Sq, Sr and Sv. Since both taxonomic

systems use band depths as one of the primary criteria to classify the objects, multiple observations of the same asteroid obtained at different phase angles could lead to ambiguous classifications. In order to test the influence of phase reddening on the taxonomic classification, we have applied the two classification systems described above to each of the observed asteroids.

Fig. 10 shows the measured Band I center versus BAR for the NEAs. Within the uncertainties all the NEAs studied are classified either as S(III) or S(IV). There are four cases (1620 Geographos, 1627 Ivar, 1980 Tezcatlipoca and 1036 Ganymed) that show large variations of the BAR from one phase angle to another, but this is likely attributed to noisy spectra rather than phase reddening. The rest of the asteroids show variations in Band I centers and BAR that are on the order of the error bars. The results obtained from the laboratory samples (Fig. 11) indicate that the largest variation in the BAR (~ 0.1) is larger than the typical uncertainty associated with the BAR values measured from asteroids (represented by the $1 - \sigma$ error bars in the upper corner of this figure). This means that in certain cases phase reddening could contribute to an ambiguous classification, particularly if the measured band parameters of the object are located close to the boundaries that define each class.

The classification into the Bus–DeMeo system was done using the online taxonomy calculator (<http://smass.mit.edu/busedmeo-class.html>). The class assigned to each spectrum and the calculated principal components PC1' and PC2' are given in Table 3. Only in three cases asteroids were ambiguously classified. Asteroid (1036) Ganymed was classified as S and Sr, (1620) Geographos was classified as S and Sq and (4954) Eric was classified as Sw and Sr. The letter “w” was introduced by DeMeo et al. (2009) to indicate an object exhibiting a high slope, but does not represent a different class, thus an object designated as “Sw” is an asteroid

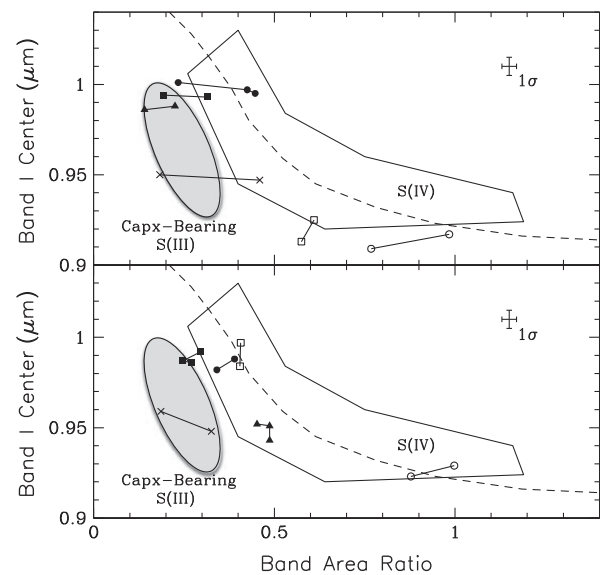


Fig. 10. Plot of the Band I center versus BAR for the NEAs. The polygonal region represents the mafic silicate components of ordinary chondrites and S(IV) asteroids (Gaffey et al., 1993). The gray oval region represents the mineralogical zone corresponding to the calcic pyroxene-bearing where the S(III) subtypes are located (Gaffey et al., 1993). The dashed curve indicates the location of the olivine–orthopyroxene mixing line (Cloutis et al., 1986). The top panel shows the measured values for Asteroids 1620 Geographos (filled circles), 1036 Ganymed (open circles), 1862 Apollo (filled triangles), 1980 Tezcatlipoca (crosses), 11398 (open squares) and 6239 Minos (filled squares). The bottom panel shows the measured values for Asteroids 4954 Eric (open circles), 66146 (filled squares), 1627 Ivar (crosses), 35107 (open squares), 25143 Itokawa (filled circles) and 4179 Toutatis (filled triangles). Measured values from multiple observations of individual asteroids are connected by lines. The average $1 - \sigma$ error bars are shown in the upper right corner.

classified as S-type that exhibit a higher slope than the typical S-types. This distinction is based on an arbitrary cutoff at slope = 0.25 (DeMeo et al., 2009). Table 3 shows that the notation of “w” was added to many asteroids from one phase angle to another. Certainly the phase reddening most play a role on this variation in spectral slope, however as it was stated earlier this is a

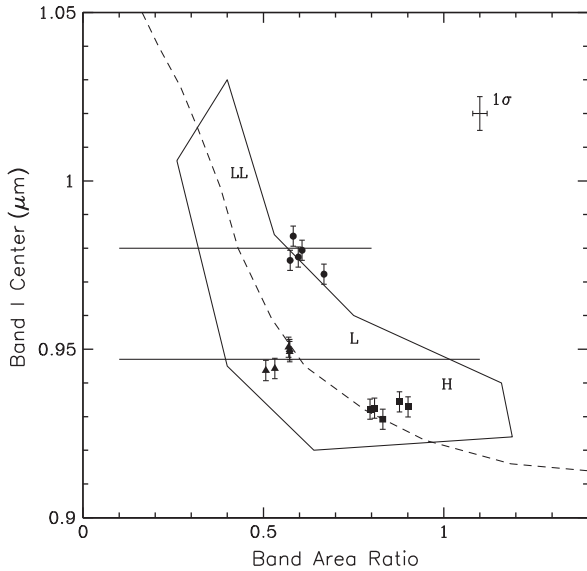


Fig. 11. Plot of the Band I center versus BAR for the LL6 (circles), L6 (triangles) and H6 (squares) ordinary chondrites. The polygonal region represents the mafic silicate components of ordinary chondrites and S(IV) asteroids (Gaffey et al., 1993). The dashed curve indicates the location of the olivine-orthopyroxene mixing line (Cloutis et al., 1986). The horizontal lines represent the approximate boundaries that separate the three types of ordinary chondrites found by Dunn et al. (2010). The error bar in the x-axis is of the order of the size of symbols. For comparison purpose we have included the average $1 - \sigma$ error bars (upper right corner) associated with the Band I center and BAR value measured for asteroids.

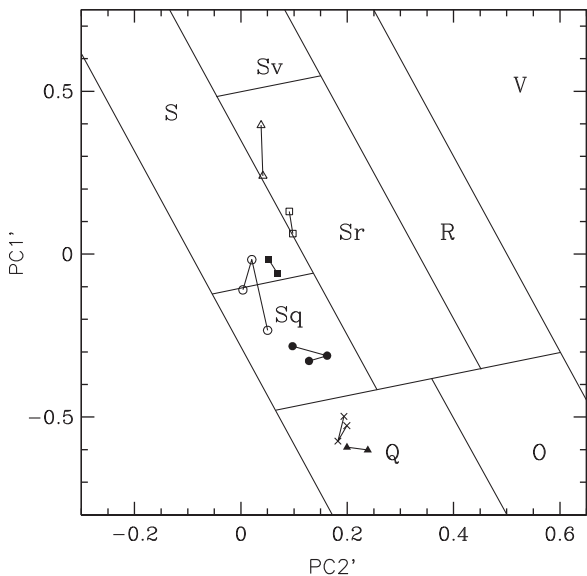


Fig. 12. Calculated PC values for some of the NEAs studied represented in a PC1' versus PC2' diagram from DeMeo et al. (2009). The letters indicate the different classes within the S-complex plus Q-, O-, R- and V-types. The asteroids whose calculated PC values have been plotted are: (1036) Ganymed (open triangles), (1620) Geographos (open circles), (1627) Ivar (filled squares), (4179) Toutatis (filled circles), (1862) Apollo (filled triangles), 11398 (open squares) and 66146 (crosses).

very sensitive parameter that can be affected by other factors. What is important to point out is that in the Bus–DeMeo system the spectral slope is removed prior to the classification. For those objects which were given two classifications it is likely that the phase reddening was not the only contribution, since some of the spectra show more scatter than others. However from our analysis we estimate an average variation of about 0.04 and 0.03 for the PC1' and PC2' respectively, that could be attributed to phase reddening. These results suggest that phase reddening could lead to an ambiguous classification but only if the calculated PC values are close to the lines that separate each class. This can be seen in Fig. 12 where we have plotted the PC values in a PC1' versus PC2' diagram from DeMeo et al. (2009). For clarity only the calculated PC values for some of the asteroids have been plotted. These values are represented by different symbols, which are connected by lines to indicate multiple values for individual asteroids.

7. Conclusions

The analysis of VIS–NIR spectra of 12 NEAs observed at different phase angles has revealed an increase of band depths with increasing phase angles in the range of $2^\circ < g < 70^\circ$ for Band I and $2^\circ < g < 55^\circ$ for Band II. Our analysis showed that, on average, Band I and Band II depths will increase 0.66% and 0.93% respectively, for every 10° increase in phase angle. From the available data we have derived equations that can be used to correct the effects of phase reddening in the band depths. Small variations in band centers and BAR values with increasing phase angle were also found. Similar trends were observed in the laboratory spectra of three different types of ordinary chondrites. In addition, an increase in the spectral slope with increasing phase angles was found for the ordinary chondrites. This increase in spectral slope is more significant for phase angles higher than 30° . Of the three types of ordinary chondrites the (olivine-rich) LL6 is the most affected by phase reddening, showing the largest variations in spectral slopes and band depths with increasing phase angles. These variations in spectral band parameters seems to have no significant impact on the mineralogical analysis though. We have also found that the increase in spectral slope caused by phase reddening can mimic the effect of space weathering. In particular, an increase in phase angle in the range of $30\text{--}120^\circ$ will produce a reddening of the reflectance spectra equivalent to exposure times of $\sim 0.1 \times 10^6\text{--}1.3 \times 10^6$ years at about 1 AU from the Sun. Furthermore, the increase in spectral slope due to phase reddening is comparable to the effects caused by the addition of various amounts of SMFe. These results imply that phase reddening should be considered when studying space weathering effects on spectral data. Regarding to the taxonomic classification, we found that phase reddening can lead to an ambiguous classification, but only if the measured spectral band parameters and/or principal components (depending on the taxonomic system) are located close to the boundaries that define each class.

Acknowledgments

The authors thank, Francesca DeMeo, John Hinrichs and Paul Lucey for providing us with data for this research. We also thank to Michael Gaffey for the meteorite samples and Stefan Schröder and Silvia Protopapa for the fruitful discussions related to this work. We would also like to thank Tasha Dunn and Jian-Yang Li for their reviews, which helped to improve the manuscript. J.A. Sanchez acknowledges a PhD fellowship of the International Max Planck Research School on Physical Processes in the Solar System and Beyond. Vishnu Reddy's research is supported by NASA NEOO Program Grant NNX07AL29G, and NASA Planetary Geology and Geophysics Grant NNX07AP73G. E.A.C. thanks the Canada

Foundation for Innovation, the Manitoba Research Innovations Fund, and the Canadian Space Agency for their support of the establishment of the University of Winnipeg Planetary Spectrophotometer Facility, and NSERC for a Discovery grant, and the University of Winnipeg for various internal grants, to support this project.

Appendix A. Asteroid spectra

This appendix contains the spectra of all NEAs analyzed in this study. The numerical designation and the date of the observation (YYMMDD) for each asteroid are given (see Figs. A.13–A.15).

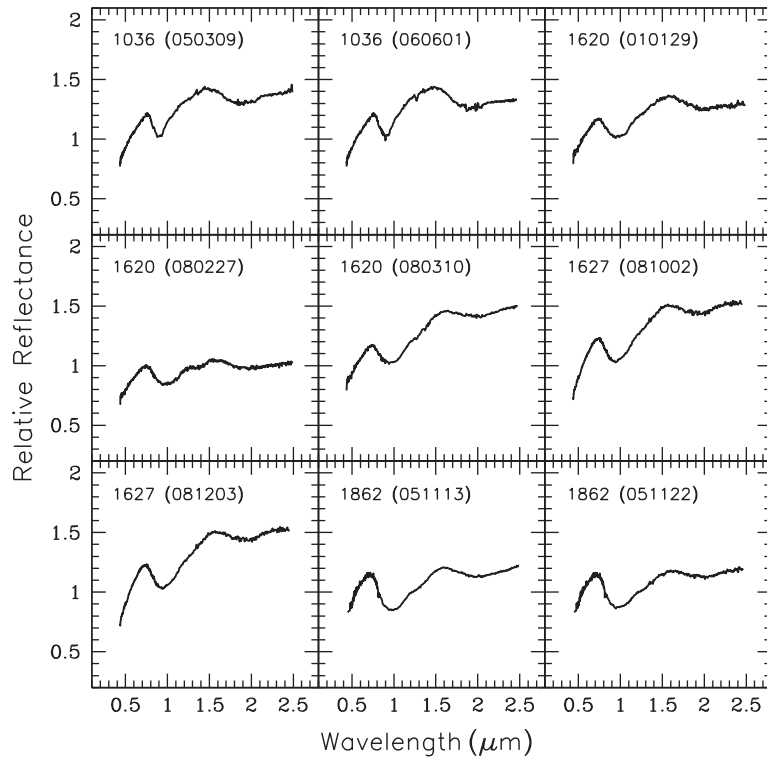


Fig. A.13. Reflectance spectra of NEAs analyzed in this study.

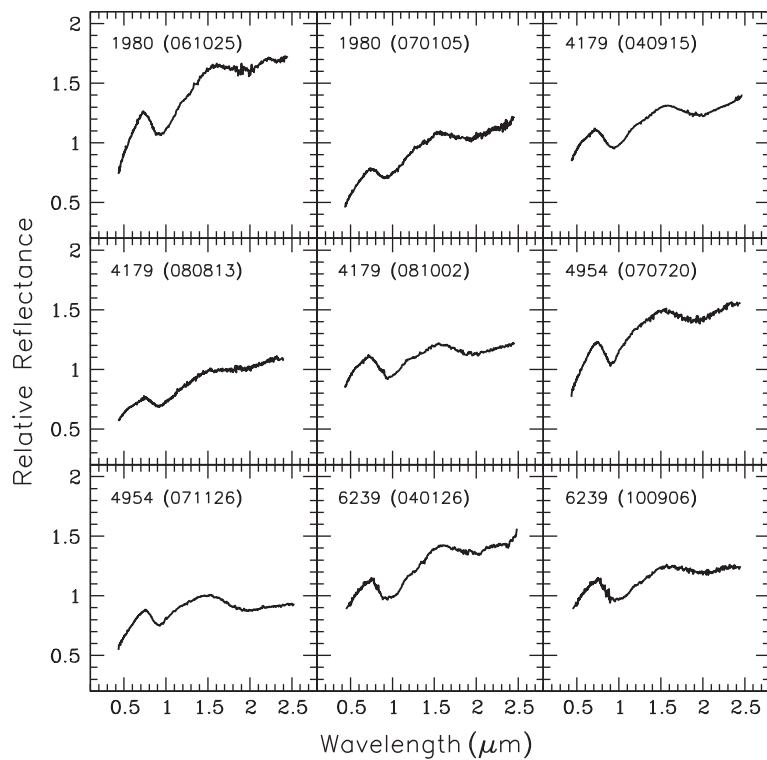


Fig. A.14. Reflectance spectra of NEAs analyzed in this study.

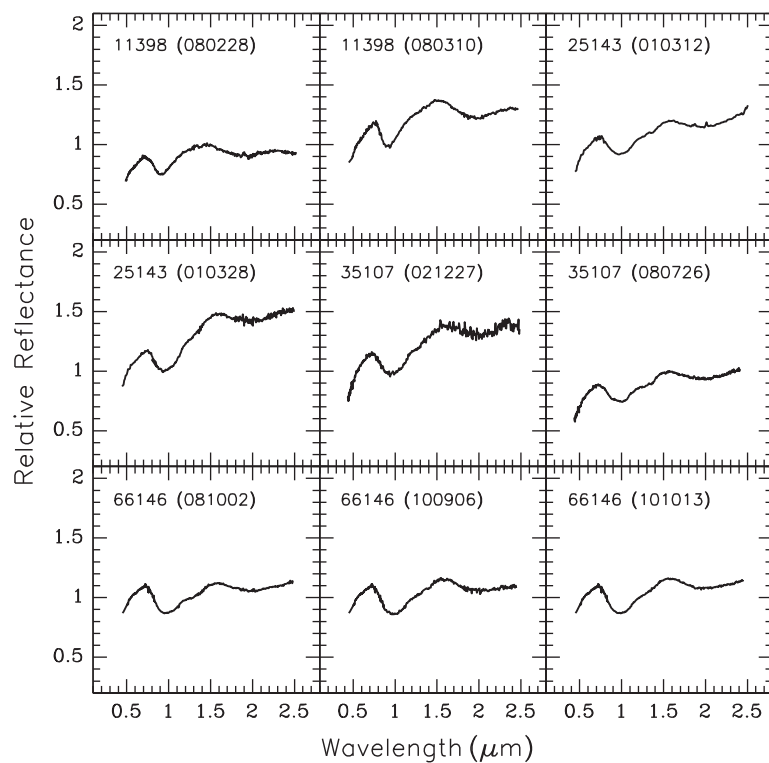


Fig. A.15. Reflectance spectra of NEAs analyzed in this study.

References

- Abell, P.A., Vilas, F., Jarvis, K.S., Gaffey, M.J., Kelley, M.S., 2007. Mineralogical composition of (25143) Itokawa 1998 SF36 from visible and near-infrared reflectance spectroscopy: Evidence for partial melting. *Meteorit. Planet. Sci.* 42, 2165–2177.
- Adams, J.B., 1974. Visible and near-infrared diffuse reflectance spectra of pyroxenes as applied to remote sensing of solid objects in the Solar System. *J. Geophys. Res.* 79, 4829–4836.
- Adams, J.B., 1975. Interpretation of visible and near-infrared diffuse reflectance spectra of pyroxenes and other rock-forming minerals. In: Karr, C.I. (Ed.), *Infrared and Raman Spectroscopy of Lunar and Terrestrial Minerals*. Academic, New York, pp. 91–116.
- Adams, J.B., Filice, A.L., 1967. Spectral reflectance 0.4 to 2.0 microns of silicate rock powders. *J. Geophys. Res.* 72, 5705–5715.
- Bell, J.F., Izenberg, N.I., Lucey, P.G., Clark, B.E., Peterson, C., Gaffey, M.J., Joseph, J., Carcich, B., Harch, A., Bell, M.E., Warren, J., Martin, P.D., McFadden, L.A., Wellnitz, D., Murchie, S., Winter, M., Veverka, J., Thomas, P., Robinson, M.S., Malin, M., Cheng, A., 2002. Near-IR reflectance spectroscopy of 433 Eros from the NIS instrument on the NEAR mission: I – Low phase angle observations. *Icarus* 155, 119–144.
- Binzel, R.P., Rivkin, A.S., Bus, S.J., Sunshine, J.M., Burbine, T.H., 2001. MUSES-C target Asteroid (25143) 1998 SF36: A reddened ordinary chondrite. *Meteorit. Planet. Sci.* 36, 1167–1172.
- Binzel, R.P., Rivkin, A.S., Stuart, J.S., Harris, A.W., Bus, S.J., Burbine, T.H., 2004. Observed spectral properties of near-Earth objects: Results for population distribution, source regions, and space weathering processes. *Icarus* 170, 259–294.
- Britt, D.T., Consolmagno, G.J., 2003. Stony meteorite porosities and densities: A review of the data through 2001. *Meteorit. Planet. Sci.* 38, 1161–1180.
- Brunetto, R., Strazzulla, G., 2005. Elastic collisions in ion irradiation experiments: A mechanism for space weathering of silicates. *Icarus* 179, 265–273.
- Brunetto, R., Vernazza, P., Marchi, S., Birlan, M., Fulchignoni, M., Orfino, V., Strazzulla, G., 2006. Modeling asteroid surfaces from observations and irradiation experiments: The case of 832 Karin. *Icarus* 184, 327–337.
- Burbine, T.H., McCoy, T.J., Jaresowich, E., Sunshine, J.M., 2003. Deriving asteroid mineralogies from reflectance spectra: Implications for the MUSES-C target asteroid. *Antarct. Meteorite Res.* 16, 185–195.
- Burbine, T.H., Buchanan, P.C., Binzel, R.P., 2007. Deriving formulas from HED spectra for determining the pyroxene mineralogy of Vesta and Vestoids. *Lunar Planet. Sci.* 2117 (abstract).
- Burbine, T.H., Buchanan, P.C., Dolkar, T., Binzel, R.P., 2009. Pyroxene mineralogies of near-Earth Vestoids. *Meteorit. Planet. Sci.* 44, 1331–1341.
- Burns, R.G., 1993. *Mineralogical Applications of Crystal Field Theory*. Cambridge University Press, Cambridge, UK, 575pp.
- Bus, S.J., Binzel, R.P., 2002a. Phase II of the small main-belt asteroid spectroscopic survey a feature-based taxonomy. *Icarus* 158, 146–177.
- Bus, S.J., Binzel, R.P., 2002b. Phase II of the small main-belt asteroid spectroscopic survey the observations. *Icarus* 158, 106–145.
- Bus, S.J., Vilas, F., Barucci, M.A., 2002. Visible-wavelength spectroscopy of asteroids. In: Bottke, W., Cellino, A., Paolicchi, P., Binzel, R. (Eds.), *Asteroids III*. University of Arizona Press, pp. 169–182.
- Clark, B.E., Hapke, B., Pieters, C., Britt, D., 2002a. Asteroid space weathering and regolith evolution. In: Bottke, W., Cellino, A., Paolicchi, P., Binzel, R. (Eds.), *Asteroids III*. University of Arizona Press, pp. 585–599.
- Clark, B.E., Helfenstein, P., Bell, J.F., Peterson, C., Veverka, J., Izenberg, N.I., Domingue, D., Wellnitz, D., McFadden, L., 2002b. NEAR infrared spectrometer photometry of Asteroid 433 Eros. *Icarus* 155, 189–204.
- Cloutis, E.A., Gaffey, M.J., Jackowski, T.L., Reed, K.L., 1986. Calibrations of phase abundance, composition, and particle size distribution for olivine-orthopyroxene mixtures from reflectance spectra. *J. Geophys. Res.* 91, 11641–11653.
- Cushing, M.C., Vacca, W.D., Rayner, J.T., 2004. Spextool: A spectral extraction package for SpeX, a 0.8–5.5 micron cross-dispersed spectrograph. *Publ. Astron. Soc. Pacific* 116, 362–376.
- DeMeo, F.E., Binzel, R.P., Slivan, S.M., Bus, S.J., 2009. An extension of the Bus asteroid taxonomy into the near-infrared. *Icarus* 202, 160–180.
- DeMeo, F.E., Carry, B., Marchis, F., Birlan, M., Binzel, R.P., Bus, S.J., Descamps, P., Nedelcu, A., Busch, M., Bouy, H., 2011. A spectral comparison of (379) Huenna and its satellite. *Icarus* 212, 677–681.
- Dunn, T.L., McCoy, T.J., Sunshine, J.M., McSween, H.Y., 2010. A coordinated spectral, mineralogical, and compositional study of ordinary chondrites. *Icarus* 208, 789–797.
- Filippenko, A.V., 1982. The importance of atmospheric differential refraction in spectrophotometry. *Publ. Astron. Soc. Pacific* 94, 715–721.
- Gaffey, M.J., 2003. Observational and data reduction techniques to optimize mineralogical characterizations of asteroid surface materials. In: Mackwell, S., Stansbery, E. (Eds.), *Lunar and Planetary Institute Science Conference*, p. 1602 (abstract).
- Gaffey, M.J., 2010. Space weathering and the interpretation of asteroid reflectance spectra. *Icarus* 209, 564–574.
- Gaffey, M.J., Burbine, T.H., Piatek, J.L., Reed, K.L., Chaky, D.A., Bell, J.F., Brown, R.H., 1993. Mineralogical variations within the S-type asteroid class. *Icarus* 106, 573–602.
- Gaffey, M.J., Cloutis, E.A., Kelley, M.S., Reed, K.L., 2002. Mineralogy of asteroids. In: Bottke, W., Cellino, A., Paolicchi, P., Binzel, R. (Eds.), *Asteroids III*. University of Arizona Press, pp. 183–204.
- Gehrels, T., 1970. Photometry of asteroids. In: Dollfus, A. (Ed.), *Surfaces and Interiors of Planets and Satellites*. Academic Press, London, pp. 317–375.
- Gradie, J., Veverka, J., 1986. The wavelength dependence of phase coefficients. *Icarus* 66, 455–467.

- Gradie, J., Veveřka, J., Buratti, B., 1980. The effects of scattering geometry on the spectrophotometric properties of powdered material. In: Bedini, S.A. (Ed.), *Lunar and Planetary Science Conference Proceedings*. Pergamon Press, New York, pp. 799–815.
- Hapke, B., 1981. Bidirectional reflectance spectroscopy: I – Theory. *J. Geophys. Res.* 86, 3039–3054.
- Hapke, B., 1993. *Theory of Reflectance and Emittance Spectroscopy*. Cambridge University Press, Cambridge, UK.
- Hapke, B., 2001. Space weathering from Mercury to the asteroid belt. *J. Geophys. Res.* 106, 10039–10074.
- Hardersen, P.S., Gaffey, M.J., Cloutis, E.A., Abell, P.A., Reddy, V., 2006. Near-infrared spectral observations and interpretations for S-asteroids 138 Tolosa, 306 Unitas, 346 Hermentaria, and 480 Hansa. *Icarus* 181, 94–106.
- Hinrichs, J.L., Lucey, P.G., 2002. Temperature-dependent near-infrared spectral properties of minerals, meteorites, and lunar soil. *Icarus* 155, 169–180.
- Johnson, P.B., Christy, R.W., 1974. Optical constants of transition metals: Ti, V, Cr, Mn, Fe, Co, Ni, and Pd. *Phys. Rev. B* 9, 5056–5070.
- Kitazato, K., Clark, B.E., Abe, M., Abe, S., Takagi, Y., Hiroi, T., Barnouin-Jha, O.S., Abell, P.A., Lederer, S.M., Vilas, F., 2008. Near-infrared spectrophotometry of Asteroid 25143 Itokawa from NIRS on the Hayabusa spacecraft. *Icarus* 194, 137–145.
- Lumme, K., Bowell, E., 1981. Radiative transfer in the surfaces of atmosphereless bodies: I – Theory. II – Interpretation of phase curves. *Astron. J.* 86, 1694–1721.
- Luu, J.X., Jewitt, D.C., 1990. Charge-coupled device spectra of asteroids: I – Near-Earth and 3:1 resonance asteroids. *Astron. J.* 99, 1985–2011.
- Mann, P., Cloutis, E.A., Reddy, V., 2011. The effect of changing viewing geometry on pyroxene and eucrite reflectance spectra. *Lunar Planet. Sci.* 2268 (abstract).
- Millis, R.L., Bowell, E., Thompson, D.T., 1976. UVB photometry of Asteroid 433 Eros. *Icarus* 28, 53–67.
- Moroz, L., Schade, U., Wäsch, R., 2000. Reflectance spectra of olivine-orthopyroxene-bearing assemblages at decreased temperatures: Implications for remote sensing of asteroids. *Icarus* 147, 79–93.
- Moskovitz, N.A., Willman, M., Burbine, T.H., Binzel, R.P., Bus, S.J., 2010. A spectroscopic comparison of HED meteorites and V-type asteroids in the inner main belt. *Icarus* 208, 773–788.
- Nakamura, T. et al., 2011. Itokawa dust particles: A direct link between S-type asteroids and ordinary chondrites. *Science* 333, 1113–1116.
- Nathues, A., 2000. *Spectroscopic Study of Eunomia Asteroid Family*. Ph.D. Dissertation, University of Berlin, Germany.
- Nathues, A., 2010. Spectral study of the Eunomia asteroid family. Part II: The small bodies. *Icarus* 208, 252–275.
- Noguchi, T. et al., 2011. Incipient space weathering observed on the surface of Itokawa dust particles. *Science* 333, 1121–1125.
- Pieters, C.M. et al., 2000. Space weathering on airless bodies: Resolving a mystery with lunar samples. *Meteorit. Planet. Sci.* 35, 1101–1107.
- Rayner, J.T. et al., 2003. SpeX: A medium-resolution 0.8–5.5 micron spectrograph and imager for the NASA Infrared Telescope Facility. *Publ. Astron. Soc. Pacific* 115, 362–382.
- Reddy, V., 2009. *Mineralogical Survey of Near-Earth Asteroid Population: Implications for Impact Hazard Assessment and Sustainability of Life on Earth*. Ph.D. Dissertation, University of North Dakota, Grand Forks.
- Reddy, V., Sanchez, J.A., Nathues, A., Moskovitz, N.A., Li, J.Y., Cloutis, E.A., Archer, K., Tucker, R.A., Gaffey, M.J., Paul Mann, J., Sierks, H., Schade, U., 2012. Photometric, spectral phase and temperature effects on 4 Vesta and HED meteorites: Implications for the Dawn mission. *Icarus* 217, 153–168.
- Rivkin, A.S., Binzel, R.P., Sunshine, J., Bus, S.J., Burbine, T.H., Saxena, A., 2004. Infrared spectroscopic observations of 69230 Hermes (1937 UB): Possible unweathered endmember among ordinary chondrite analogs. *Icarus* 172, 408–414.
- Schade, U., Wäsch, R., 1999. NIR reflectance spectroscopy of mafic minerals in the temperature range between 80 and 473 K. *Adv. Space Res.* 23, 1253–1256.
- Shepard, M.K., Cloutis, E., 2011. Laboratory measurements of band depth variation with observation geometry. *Lunar Planet. Sci.* 1043 (abstract).
- Shestopalov, D.I., Golubeva, L.F., 2000. Influence of temperature on reflectance spectra of asteroids. *Lunar Planet. Sci.* 1003 (abstract).
- Singer, R.B., Roush, T.L., 1985. Effects of temperature on remotely sensed mineral absorption features. *J. Geophys. Res.* 90, 12434–12444.
- Strazzulla, G., Dotto, E., Binzel, R., Brunetto, R., Barucci, M.A., Blanco, A., Orfino, V., 2005. Spectral alteration of the Meteorite Epinal (H5) induced by heavy ion irradiation: A simulation of space weathering effects on near-Earth asteroids. *Icarus* 174, 31–35.
- Sunshine, J.M., Bus, S.J., McCoy, T.J., Burbine, T.H., Corrigan, C.M., Binzel, R.P., 2004. High-calcium pyroxene as an indicator of igneous differentiation in asteroids and meteorites. *Meteorit. Planet. Sci.* 39, 1343–1357.
- Taylor, L.A. et al., 2001. The effects of space weathering on Apollo 17 mare soils: Petrographic and chemical characterization. *Meteorit. Planet. Sci.* 36, 285–299.
- Tholen, D.J., 1984. *Asteroid Taxonomy from Cluster Analysis of Photometry*. Ph.D. Thesis, Arizona Univ., Tucson.
- Vernazza, P. et al., 2008. Compositional differences between meteorites and near-Earth asteroids. *Nature* 454, 858–860.



Photometric, spectral phase and temperature effects on 4 Vesta and HED meteorites: Implications for the Dawn mission

Vishnu Reddy^{a,b,*,1}, Juan A. Sanchez^{b,c}, Andreas Nathues^{b,1}, Nicholas A. Moskovitz^{d,1}, Jian-Yang Li^e, Edward A. Cloutis^f, Ken Archer^g, Roy A. Tucker^h, Michael J. Gaffey^{i,1}, J. Paul Mann^f, Holger Sierks^b, Ulrich Schade^j

^a Department of Space Studies, Room 520, Box 9008, University of North Dakota, Grand Forks, ND 58202, USA

^b Max Planck Institut für Sonnensystemforschung, 37191 Katlenburg-Lindau, Germany

^c Institut für Planetologie, 48149 Münster, Germany

^d Carnegie Institution of Washington, Department of Terrestrial Magnetism, 5241, Broad Branch Road, Washington, DC 20008, USA

^e Department of Astronomy, University of Maryland, College Park, MD 20742, USA

^f Department of Geography, University of Winnipeg, Winnipeg, Manitoba, Canada

^g Ironwood Remote Observatory, 59-495 Hoalike Road, Haleiwa, HI 96712, USA

^h Goodricke-Pigott Observatory, 5500 West Nebraska Street, Tucson, AZ 85757, USA

ⁱ Department of Space Studies, Room 518, Box 9008, University of North Dakota, Grand Forks, ND 58202, USA

^j Berliner Elektronenspeicherring-Gesellschaft für Synchrotronstrahlung m.b.H., Albert-Einstein-Strasse 15, 12489 Berlin, Germany

ARTICLE INFO

Article history:

Received 20 June 2011

Revised 18 October 2011

Accepted 18 October 2011

Available online 31 October 2011

Keywords:

Asteroid Vesta

Asteroids, Composition

Spectroscopy

Photometry

Infrared observations

ABSTRACT

Phase angle and temperature are two important parameters that affect the photometric and spectral behavior of planetary surfaces in telescopic and spacecraft data. We have derived photometric and spectral phase functions for the Asteroid 4 Vesta, the first target of the Dawn mission, using ground-based telescopes operating at visible and near-infrared wavelengths (0.4–2.5 μm). Photometric lightcurve observations of Vesta were conducted on 15 nights at a phase angle range of 3.8–25.7° using duplicates of the seven narrowband Dawn Framing Camera filters (0.4–1.0 μm). Rotationally resolved visible (0.4–0.7 μm) and near-IR spectral observations (0.7–2.5 μm) were obtained on four nights over a similar phase angle range. Our Vesta photometric observations suggest the phase slope is between 0.019 and 0.029 mag/deg. The G parameter ranges from 0.22 to 0.37 consistent with previous results (e.g., Lagerkvist, C.-I., Magnusson, P., Williams, I.P., Buontempo, M.E., Argyle, R.W., Morrison, L.V. [1992]. *Astron. Astrophys. Suppl. Ser.* 94, 43–71; Piironen, J., Magnusson, P., Lagerkvist, C.-I., Williams, I.P., Buontempo, M.E., Morrison, L.V. [1997]. *Astron. Astrophys. Suppl. Ser.* 121, 489–497; Hasegawa, S. et al. [2009]. *Lunar Planet. Sci.* 40. ID 1503) within the uncertainty. We found that in the phase angle range of $0^\circ < \alpha \leq 25^\circ$ for every 10° increase in phase angle Vesta's visible slope (0.5–0.7 μm) increases 20%, Band I and Band II depths increase 2.35% and 1.5% respectively, and the BAR value increase 0.30. Phase angle spectral measurements of the eucrite Moama in the lab show a decrease in Band I and Band II depths and BAR from the lowest phase angle 13° to 30°, followed by possible small increases up to 90°, and then a dramatic drop between 90° and 120° phase angle. Temperature-induced spectral effects shift the Band I and II centers of the pyroxene bands to longer wavelengths with increasing temperature. We have derived new correction equations using a temperature series (80–400 K) of HED meteorite spectra that will enable interpretation of telescopic and spacecraft spectral data using laboratory calibrations at room temperature (300 K).

© 2011 Elsevier Inc. All rights reserved.

1. Introduction

Asteroid 4 Vesta is the first target of NASA's Dawn mission, which began its yearlong orbital mission in July 2011. Vesta has been extensively studied (e.g., McCord et al., 1970; Chapman et al., 1971; McFadden et al., 1977; Binzel et al., 1997; Thomas et al., 1996; Zellner et al., 1996; Gaffey, 1997; Li et al., 2010; Reddy et al., 2010) by ground-based telescopes and the Hubble Space Telescope since its discovery by Heinrich Wilhelm Olbers in

* Corresponding author at: Department of Space Studies, Room 520, Box 9008, University of North Dakota, Grand Forks, ND 58202, USA. Fax: +1 701 777 3711.

E-mail address: reddy@space.edu (V. Reddy).

¹ Visiting Astronomer at the Infrared Telescope Facility, which is operated by the University of Hawaii under Cooperative Agreement No. NCC 5-538 with the National Aeronautics and Space Administration, Science Mission Directorate, Planetary Astronomy Program.

1807. Unlike most main belt asteroids, Vesta's rotational brightness variation (lightcurve) is mainly caused by surface albedo variations. Vesta's surface composition also changes with rotation phase (e.g. Gaffey, 1997) as seen in changing spectral band parameters in its reflectance spectrum.

The Framing Cameras (FC) on NASA's Dawn mission will map the surface of Vesta in seven color filters and one clear filter with up to 20-m spatial resolution in an effort to examine its geology and cratering history. Precise photometric correction of these data is vital for producing higher-level products that are useful for revealing Vesta's geologic and compositional history as well as its topography by using the photoclinometry method. A major correction to be applied to optical spacecraft data is the correction for the observation geometry, which is compositionally dependent (Gradie et al., 1980). This correction is required in order to extract the physical properties (e.g. compaction state, particle albedo, particle size, etc.) of the surface.

One significant parameter controlling the apparent brightness of a surface element is the phase angle, which is defined as the angle between the Sun and the observer as seen from the target object. Spectral phase effects on Vesta have been detected and approximately quantified by Gaffey (1997). He noted an increase in the intensity of Vesta's 1- μm band with increasing phase angle. Hence there is a wavelength dependent phase effect, which will alter the reflectance values of FC data depending on the band pass of the filter and viewing geometry (mainly phase angle). A further parameter that affects FC data as well as spectral data from the Visual and Infrared Spectrometer (VIR) is temperature. Temperature uncertainties arise when spacecraft spectral data, obtained at low (80–250 K) temperatures, are interpreted using laboratory calibrations obtained at room (~ 300 K) temperatures.

In order to quantify phase angle- and temperature-induced spectral effects prior to the arrival of Dawn, we conducted a series of laboratory and telescopic studies of Vesta and howardite, eucrite and diogenite (HED) meteorites. Telescopic studies included photometric observations of Vesta with Dawn's FC filters, visible wavelength spectra, and near-IR spectra obtained at a range of phase angles. This is the first time that original flight filters are being used to conduct ground-based observations of the target prior to arrival of the spacecraft. This will not only help in wavelength-dependent phase calibration but also in cross comparison of ground-based and spacecraft data through the same filters if Dawn captures the whole disk of Vesta in a single image frame during approach.

1.1. Photometric studies of Vesta

Several authors have investigated Vesta's photometric phase functions (e.g., Lagerkvist and Williams, 1987; Hasegawa et al., 2009, and references therein). Rotational color variations on Vesta have been known for nearly a century (Bobrovnikoff, 1929) and have been well characterized by several authors (e.g., Gaffey, 1997). The rotational period of Vesta is $5.342129760 \pm 0.00000096$ h (Drummond et al., 1998) and unlike other asteroids, its lightcurve shows a single maximum and minimum per rotation. This is because rotational albedo variations across Vesta's surface contribute more to the lightcurve than its shape (Thomas et al., 1997). Gaffey (1997) presented a comprehensive review of the physical characterization of Vesta up to that time.

Due to its orbital motion around the Sun, Vesta's phase angle as viewed from the Earth ranges typically from 2° to 25° . Hasegawa et al. (2009) observed Vesta at a phase angle of 0.12° and estimated a slope parameter G (B filter 0.24 ± 0.01 , R filter 0.21 ± 0.01), this parameter describes the shape of the phase curve (Bowell et al., 1989) and was found to be much lower than the previously reported values (e.g., Lagerkvist and Williams, 1987) ranging from 0.32 to 0.47. They suggested that this difference was probably due

to the fact that they had photometric data at extremely low phase angles ($<1^\circ$) compared to other authors.

1.2. Photometric and spectral phase effects on Vesta

Effects of phase angle on broadband photometry and spectral reflectance have been well documented from laboratory, telescopic and spacecraft observations of the Moon, asteroids, and planetary satellites (e.g., Lane and Irvine, 1973; Millis et al., 1976; Gradie et al., 1980; Bell et al., 2002). Photometric phase functions of asteroids are derived by observing the change in brightness (typically in V magnitude) as a function of phase angle from ground-based observations and have been modeled using Hapke (1981, 1984, 1986) and Lumme and Bowell (1981a,b) scattering theories. The phase function contains important information about the physical properties of the surface (e.g., single-scattering albedo, particle size, packing, large scale roughness, transparency, etc.).

An important photometric effect is the steep increase in brightness for phase angles less than $\sim 7^\circ$ (Opposition Effect) which has been explained as being a consequence of disappearing shadows at extremely low phase angle or coherent backscattering (e.g., Shkuratov, 1988; Hapke, 1990; Rosenbush et al., 2006; Hapke et al., 2009). The intensity of the opposition effect depends on the object's albedo where low and medium albedo objects ($<25\%$) show no dependence of opposition effect with albedo and high albedo objects (E-type asteroids and Vesta) show a steeper opposition effect.

Spectral phase effects are manifested primarily as phase reddening and spectral band changes. Phase reddening is an effect where the spectral slope of the reflectance spectrum reddens with increasing phase angle. This effect on pyroxene reflectance spectra has not been extensively examined (Adams and Filice, 1967; Pieters, 1983; Yon and Pieters, 1988). The effects caused by viewing geometry are known to be wavelength dependent (e.g., French and Veverka, 1983). This suggests that spectral variations seen on asteroid surfaces (e.g., Clark et al., 2002) may be attributable, at least in part, to viewing geometry variations (e.g., Nathues, 2000, 2010; Cord et al., 2003; Piatek et al., 2004).

Gradie et al. (1980) studied spectral phase effects on laboratory spectra of meteorites and minerals and found an increase in spectral slope and absorption band depth with increasing phase angle. Ground based observations of main belt asteroids (4) Vesta by Gaffey (1997) and (306) Unitas by Reddy et al. (2005) have confirmed these spectral phase effects. NEAR Shoemaker spacecraft observations of near-Earth Asteroid (433) Eros conducted by the Near-Infrared Spectrometer (NIS) showed the most intense phase angle effects in the 1- μm absorption band. Clark et al. (2002) concluded that correcting for photometric and phase angle effect is important for accurate mineralogical interpretation of spacecraft spectral observations.

Band depth of an absorption feature is related to the abundance of the absorbing species in the surface material (Burns, 1993), but is also influenced by particle size (Gaffey et al., 1993). Gaffey (1997) noted a 7% variation in band depth of the 1- μm pyroxene absorption feature as Vesta rotates. This change in band depth could be attributed to an increase in abundance of mafic mineral (like pyroxene) or particle size effects on Vesta's surface. The phase angle effect leads (often) to a change in band depth, which results in an overestimation of the pyroxene content and an increase in spectral slope which can be misinterpreted as being caused by the space weathering process or the presence of metal on the surface. Both issues are expected to be critical for mineralogical analysis of Vesta data especially for the Dawn mission.

In an effort to constrain photometric and spectral phase effects, we launched an observing campaign in 2010 with three main objectives, to obtain (1) photometric lightcurves of Vesta at a broad phase angle range to derive photometric phase functions that are

valid for FC filters, (2) rotationally-resolved visible wavelength (0.4–0.7 μm) spectra to constrain spectral slope variations by phase angle and, (3) rotationally-resolved near-infrared wavelength (0.7–2.5 μm) spectra to constrain possible band depth effects. Here we present our results from this study that will be used for analyzing the data from the Framing Camera and the VIR spectrometer on Dawn.

1.3. Temperature-induced spectral effects

Temperature effects on spectral shape are twofold: broadening or narrowing of absorption features, and shifting of band centers (Singer and Roush, 1985; Hinrichs and Lucey, 2002; Hinrichs et al., 1999; Moroz et al., 2000; Schade and Wäsch, 1999). The thermally-induced variations of absorption features are explained by Crystal Field Theory (CFT) (Burns, 1993). The works of Singer and Roush (1985), Hinrichs and Lucey (2002), Hinrichs et al. (1999), Moroz et al. (2000) and Schade and Wäsch (1999) summarize the found effects on spectral parameters of olivine and pyroxene.

The primary absorption feature in olivine is centered near 1.04 μm and is composite of three bands, which are all caused by the presence of Fe^{2+} cations (Burns, 1993). With increasing temperature, this feature broadens and the resolution of the ~ 0.45 and 0.64 μm Fe^{2+} spin-forbidden transitions is reduced. The 1.04 μm band broadens significantly with increased temperature (80–400 K) on the longer wavelength side of the composite absorption feature (Singer and Roush, 1985; Hinrichs and Lucey, 2002; Hinrichs et al., 1999; Moroz et al., 2000; Schade and Wäsch, 1999). Based on high temperature X-ray crystallographic data, olivines and pyroxenes are known to show two trends where the expansion of the coordination sites is not identical (Burns, 1993).

The average surface temperature (T) of an asteroid can be determined using the equation

$$T = [(1 - A)L_o/16\eta\epsilon\sigma\pi r^2]^{1/4} \quad (1)$$

where A is the albedo of the asteroid, L_o is the solar luminosity (3.827×10^{26} W), η is the beaming factor (assumed to be unity) (from Cohen et al. (1998)), ϵ is the asteroid's infrared emissivity (assumed to be 0.9), σ is the Stefan–Boltzman constant ($5.67 \times 10^{-8} \text{ J s}^{-1} \text{ m}^{-2} \text{ K}^{-4}$), and r is the asteroid's distance from the Sun (meters). The Band I center of olivine essentially remains unchanged with change in temperature (Burns, 1970; Singer and Roush, 1985; Hinrichs and Lucey, 2002.) However, the band centers of both Bands I and II absorption features in pyroxene shift to longer wavelength with increasing temperature (Lucey et al., 2002).

Moroz et al. (2000) measured the change in band centers of two pyroxenes (bronzite and enstatite) at different temperatures (293, 173 and 80 K). Based on this Burbine et al. (2009) developed a set of equations for band center correction for temperature.

Bronzite

$$\text{Band I center correction } (\mu\text{m}) = 0.0047 - 0.000015 * T \text{ (K)} \quad (2)$$

$$\text{Band II center correction } (\mu\text{m}) = 0.044 - 0.00015 * T \text{ (K)} \quad (3)$$

Enstatite

$$\text{Band I center correction } (\mu\text{m}) = 0.0054 - 0.000019 * T \text{ (K)} \quad (4)$$

$$\text{Band II center correction } (\mu\text{m}) = 0.0649 - 0.00022 * T \text{ (K)} \quad (5)$$

Typically, Band I center corrections are small (~ 0.0005 μm) while Band II corrections are slightly larger (~ 0.01 μm), but this may vary depending on the mineral and the temperature difference. Unfortunately, no calibrations exist for temperature corrections that are based on HED meteorite spectra. Part of the problem is the difficulty in obtaining high-quality spectra of samples at different temperatures. In this work we have reanalyzed spectra of HED meteorites taken between 80 and 400 K to constrain the effects on

spectral band parameters and spectral colors. Our goal is to develop a new temperature correction calibration based on HED meteorite spectra that will correct near-IR spectra obtained using the VIR spectrometer on Dawn and color ratios from the Dawn Framing Camera data.

2. Photometric observations

2.1. Observations and data reduction

Photometric observations of Vesta were obtained with an 8-in. F/4 Newtonian telescope and SBIG ST-10 CCD Camera at the Ironwood Remote Observatory, a private observatory on Oahu, Hawai'i. All observations were obtained in automated scripted mode. Lightcurves were obtained using the spare Dawn Framing Camera filter set, which was on loan from the Max-Planck Institute for Solar System Research, Germany. The Dawn filter set consists of a clear filter plus seven narrowband interference filters with FWHM of ~ 40 nm. The filter's band passes and transmission curves are shown in Fig. 1 and listed in Table 1. Observations were taken in sequence starting with clear and cycling through the seven filters and this process repeated till full rotational coverage was achieved. Observational circumstances for the photometry data are listed in Table 2. Note that the sub-Earth latitude given is planetographic calculated using the Thomas et al. (1997) pole position.

The data reduction has been accomplished using the MPO Canopus Software (Brian D. Warner, Publishing, 2009a). MPO Canopus is a full-featured astrometry and photometry program capable of providing high accuracy results. This software includes many different applications to process and measure astronomical images, do photometric transforms, generate lightcurves, analyze periods and times of minimum, etc. (Warner, 2006).

Lightcurves in each filter for 15 different nights have been obtained using the derived magnitudes method. With this procedure

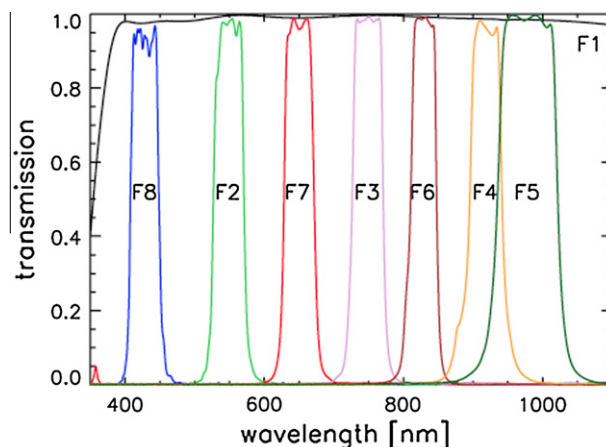


Fig. 1. Transmission profiles of the Dawn Framing Camera filters.

Table 1

Dawn Framing Camera filter names, band passes and FWHM used in our photometric study (Sierks et al., 2011).

Dawn FC designation	λ_{eff} (μm)	FWHM (μm)
F8	$0.438^{+0.010/-0.030}$	0.040
F2	$0.555^{+0.015/-0.028}$	0.043
F7	$0.653^{+0.018/-0.024}$	0.042
F3	$0.749^{+0.022/-0.022}$	0.044
F6	$0.829^{+0.018/-0.018}$	0.036
F4	$0.917^{+0.024/-0.021}$	0.045
F5	$0.965^{+0.056/-0.029}$	0.086

Table 2
Observing circumstances for photometry data.

Dates of observations	Visual magnitude	Sub-Earth latitude (°)	Phase angle (°)
February-21, 2010	6.13	32.29	3.8
February-24, 2010	6.16	32.24	4.7
February-25, 2010	6.18	32.22	5.0
March-7, 2010	6.36	32.17	9.3
March-12, 2010	6.43	32.20	11.2
March-13, 2010	6.47	32.21	11.9
March-21, 2010	6.62	32.33	15.2
March-24, 2010	6.68	32.40	16.3
March-27, 2010	6.74	32.47	17.3
April-11, 2010	7.01	32.96	21.6
April-12, 2010	7.03	32.99	21.9
April-25, 2010	7.24	33.47	24.2
April-26, 2010	7.26	33.51	24.4
April-27, 2010	7.27	33.54	24.5
May-11, 2010	7.46	33.95	25.7

it is possible to obtain a catalog-based magnitude for the asteroid by finding the instrumental magnitude difference between the asteroid and a set of comparison stars, and then adding the mean catalog magnitude of the comparisons. It is important to point out that catalogs of comparisons stars do not include the magnitudes in the dawn FC filters (see discussion below). When using several comparison stars, a separate derived magnitude is computed for each target-comparison pair and the mean of those derived values becomes the derived magnitude for the comparison. The error is given by the standard deviation, in magnitudes of the mean of the derived magnitude value. For additional details about this procedure refer to the MPO Canopus User Guide (<http://bdwpublishing.com/about-us.aspx>).

Different problems that arose during the observations made the data processing a very challenging task. Due to the thickness of the filters, specially the F4, F5 and F6 (~5 mm), an internal reflection from one layer to the other was produced causing a “ghost image” that can be seen as a halo around the stars and the target. The brightness of Vesta was also an inconvenience. Due to the brightness of the asteroid (V. Mag ~6.0) it was challenging to keep the detector from saturating. Due to this limitation the exposure times had to be kept short (~0.001 s) which resulted in very low signal from the comparison stars and subsequently higher noise. A related problem to the short exposure time is the ‘shutter effect,’ where the S/N was higher for the stars closer to the middle of the frame than at the edge.

An additional problem during the data reduction was related to the limitations of the catalog magnitudes of the comparison stars, which were only available in standard filters. Since we have customized filters, the magnitudes of the asteroid that we have obtained correspond to the Johnson filters. This means that the best we could do was to find the closest in response to the Dawn filters (see Table 1). We caution that any use of this data should account for uncertainties introduced by this assumption. For the F8 we found that the closest in response was the Johnson B filter (center of the photometric band 0.43 μm), for the F2 the Johnson V (0.55 μm), for the F7 and F3 the Johnson R (0.70 μm), and for the F6, F4 and F5 the Johnson I (0.90 μm). Due to the broad nature of the Johnson filters, Dawn FC filters lie within their passbands (relatively close to the peak of the spectral response), however since these are different filters the derived magnitudes that we have obtained only provide us with an approximation for the apparent magnitude of the asteroid. The situation for the filters F4, F5 and F6 was the most difficult, on one hand due to the problem of the ghost image mentioned before, and the other because the closest in response was the Johnson I filter, which is about 0.07 μm off with respect to the F5 and F6. As a result, it was not possible to

generate the lightcurves for all the nights and their error bars are larger than those obtained with the other filters.

A correction to unity distances at a fixed phase angle was applied to the entire data set by using the standard correction of $-5 * \log(rR)$, where “ r ” is the Earth–asteroid distance and “ R ” is the Sun–asteroid distance (both values in AU), in this way the magnitudes obtained are those that the object would have if it were at 1 AU from the Sun and 1 AU from the Earth at the given phase angle.

2.2. Analysis

We fit the phase functions of Vesta through all FC filters except for F8, which has an effective wavelength of 440 nm and suffers additional difficulties in the calibration due to the characteristics of the filter. The lightcurve of Vesta is single-peaked with an amplitude of about 0.15–0.2 magnitude over all wavelengths we observed, and is dominated by its surface albedo variations rather than shape (Binzel et al., 1997; Li et al., 2010). Therefore we took the mid-point between the minimum and the maximum of each lightcurve to represent the average surface and construct the phase function of Vesta through each filter. The modeling is based on the mid-point lightcurve phase function. The nominal measurement errors of the photometric data are much smaller than the lightcurve amplitude. For some cases the measured brightness variations of Vesta at similar phase angle varies from night to night, caused by telescope systematics and/or observing conditions. Fig. 2 shows an example of the phase function and the modeling for filter F4.

Two empirical phase function models were used, including a linear model and the IAU HG phase function model (Bowell et al., 1989). For linear fit, we only used data points with phase angles higher than 7° in order to avoid including the opposition effect, which cannot be characterized from our data due to the limited coverage at low phase angles. The fit returns phase slopes ranging from 0.019 through F5 to 0.029 mag/deg through F6 (Fig. 3 top panel). The uncertainties are typically 10–15%. With the large uncertainties of fitted parameters, there is no systematic trend for the phase slope with respect to wavelength visible outside of the 1- μm band. Within the band, it appears to be a decreasing trend of phase slope with wavelength, but not statistically significant. The

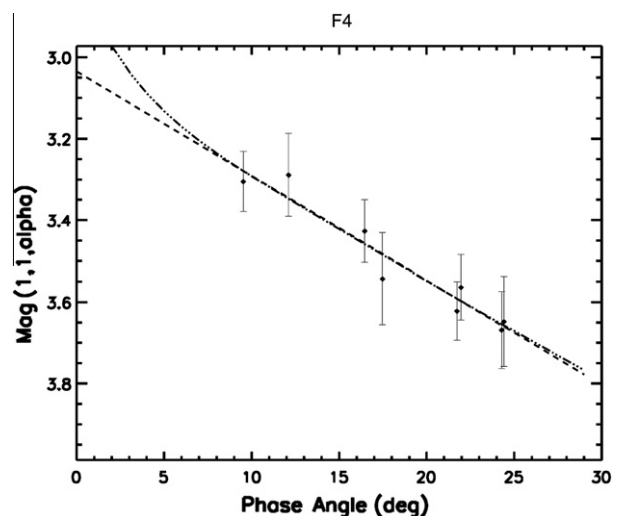


Fig. 2. The observed phase function of Vesta through F4 (symbols) at 920 nm wavelength, and the fit with two models. The values $\text{mag}(1,1,\alpha)$ refer to the magnitude corrected to observer range and target heliocentric distance both at 1 AU. Each symbol represents the mid-point between the maximum and minimum of a single lightcurve obtained in one night. The error bars show the observed lightcurve amplitude. The dashed line is a linear model with data at phase angle higher than 7°. The dash-dot line is the best-fit IAU HG phase function.

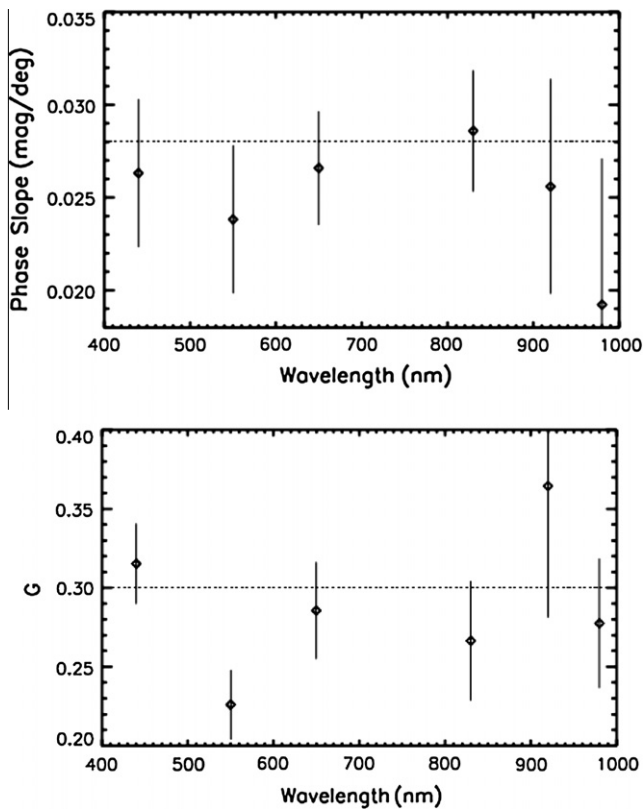


Fig. 3. The best-fit phase slope parameters as a function of wavelength through FC filters (top panel). Bottom panel shows the best-fit IAU G parameter. The fit for F3 is not shown here because of the bad quality of photometric data.

shallowest phase slope is inside the 1- μm mafic band (filter F5) with a value of 0.019 mag/deg.

IAU HG phase function model is a purely empirical model based on main belt asteroids and then extended to all asteroids. Two parameters are used: H is the absolute magnitude at zero phase angle, and G is a parameter to characterize phase slope with higher value corresponding to shallower phase slope (Bowell et al., 1989). For IAU HG phase function model fit, we used data points at all phase angles. The range of fitted G parameter is from 0.22 to 0.37, with model uncertainties of 10–15% (Fig. 3 bottom panel). These values are consistent with those reported by other authors (e.g., Lagerkvist et al., 1992; Piironen et al., 1997; Hasegawa et al., 2009) within the uncertainty. Similar with linear fit, no systematic trend for the slope parameter G is evident with the large scatter and fitted uncertainties.

2.3. Summary

We found that the phase slopes, and the H and G values are in general consistent with previous results. However, no trend for the phase slope and G parameter with respect to wavelength is observed. These inconclusive results are probably due to the large uncertainty in the photometric data resulted from the difficulty of obtaining high quality photometric data from the FC filters, and the limitations we had during the data reduction process.

3. Visible spectroscopic observations

3.1. Observations and data reduction

The visible spectral data (0.4–0.70 μm) were acquired by using a C14 telescope (14" aperture, f/11 optics) equipped with a Santa

Barbara Instrument Group (SBIG) SGS spectrograph and a SBIG ST-7ME thermoelectrically-cooled CCD camera. The observations were made from Goodricke–Pigott Observatory, a small private observatory in Tucson, Arizona. The CCD and pixel size are 6.9×4.3 mm and 9×9 μm respectively. The spectrograph is equipped with two gratings. We used the 150 lines/mm grating providing a dispersion of $4.3 \text{ \AA}/\text{pixel}$ across the 765 active pixels of the CCD. The narrow entrance slit with an effective width of 18 μm lead to an effective width of 0.95 arcsec and had a total covered spectral range of 3290 \AA (4.3×765).

The procedure for each observation was to acquire four individual 300-s integrations allowing us to compute an average image (median) free of cosmic rays. Eight dark images were median-combined and subtracted from the observations to remove the pixel-to-pixel thermal dark current pattern. Image processing involving the dark-subtraction and median-combining was done with Maxim DL. Spectral data processing was done with VSpec. VSpec permitted wavelength calibration using mercury and neon lamps, sky subtraction, and flux calibration using G2 V reference star Rho Corona Borealis. Observational circumstances for the visible data are provided in Table 3.

3.2. Analysis

Visible spectral observations from each night were averaged to create a full rotationally averaged spectrum for each phase angle. Spectral slope was calculated by normalizing the data to unity at 0.55 μm and then fitting a straight-line continuum to the data between 0.55 and 0.70 μm . This procedure was repeated for all observed nights, the measured values are presented in Table 4. A comparison of the spectral slopes values provides an empirical estimate of the error. After correcting for the phase reddening (see Eq. (8)) we found that the $1 - \sigma$ error associated to the corrected spectral slopes is $0.043\%/\mu\text{m}$. A similar approach has been used in the past by other authors (e.g., Luu and Jewitt, 1990). Fig. 4 shows the full rotationally averaged visible spectra of Vesta on three nights at phase angles of 3.7° , 10.7° and 25.1° (from bottom to top). In this plot the spectra obtained at phase angles 17.4° and 25.0° were omitted and the data was normalized to unity at 0.4 μm for clarity. Extracted slope values have been used to calculate the rate of change in slope (reddening coefficient) with phase angle. Fig. 5 plots spectral slope as a function of phase angle. From this figure is possible to see how the spectral slope (filled black diamonds) increase with increasing phase angle. The black line is a

Table 3
Observing circumstances for visible spectral data.

Dates of observations	Visual magnitude	Sub-Earth latitude ($^\circ$)	Phase angle ($^\circ$)
February-20, 2010	6.12	32.31	3.7
March-10, 2010	6.41	32.18	10.7
March-27, 2010	6.74	32.47	17.4
May-01, 2010	7.33	33.67	25.0
May-02, 2010	7.34	33.67	25.1

Table 4
Visible spectral slopes. The $1 - \sigma$ error associated to the spectral slopes is $0.043\%/\mu\text{m}$.

Phase angle ($^\circ$)	Spectral slope ($\%/\mu\text{m}$)
3.7	0.867
10.7	0.907
17.4	1.098
25.1	1.271

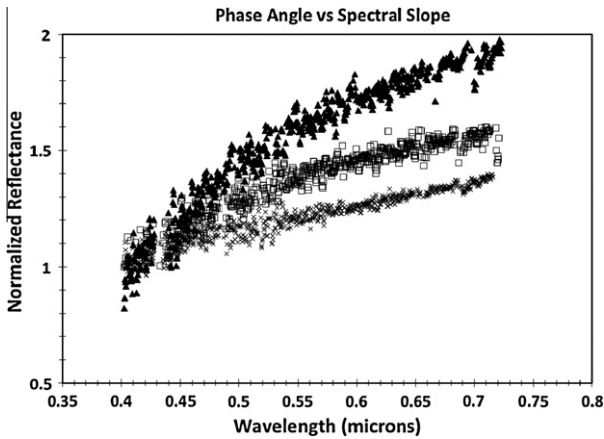


Fig. 4. Full rotation average visible spectra of Vesta taken at 3.7° (crosses), 10.7° (squares) and 25.1° (triangles) phase angle.

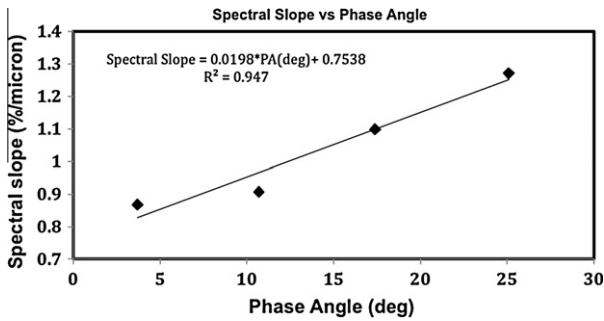


Fig. 5. Spectral slope of Vesta in VIS (0.55–0.70 μm) as a function of phase angle. The slopes were determined from full rotation average spectra shown in Fig. 4. The estimated error associated to the measured spectral slopes is 0.043%/ μm .

linear fit ($R^2 = 0.94$) through this data set. This gives us an equation to calculate the effect of phase angle on spectral slope,

$$\text{Spectral Slope} = 0.0198 * (\alpha) + 0.7538 \quad 0^\circ < \alpha \leq 25^\circ \quad (6)$$

where α is the phase angle. Based on this equation, the spectral slope of Vesta increases 20% for every 10° increase in phase angle. This phase angle influence needs consideration before any interpretation can be made regarding the degree of space weathering based on visible wavelength slope. From Eq. (6) the reddening coefficient is given by

$$\gamma = 0.0198\%/ \mu\text{m}/\text{deg} \quad (7)$$

Thus, the corrected spectral slope S_c is

$$S_c = S - \gamma\alpha \quad 0^\circ < \alpha \leq 25^\circ \quad (8)$$

where S is the measured spectral slope.

3.3. Results

Spectral slope especially in the visible has been traditionally used as a measure for the degree of space weathering (Gaffey, 2010). From our analysis of visible spectral slope it is confirmed that one has to decouple the effect on spectral slope due to phase angle before any analysis can be made to quantify the effects of space weathering. If one assumes lunar-style space weathering to be prevalent on Vesta then a corresponding decrease in albedo will be noted with increasing spectral slope and decreasing band depth in spectra of terrains where space weathering is active. Hence assuming spectral slope to be the sole indicator of space weathering

on Vesta would lead to inaccurate interpretation of both Dawn FC and VIR data.

4. NIR spectroscopic observations

4.1. Observations and data reduction

Near-IR (0.64–2.5 μm) spectral observations of asteroid (4) Vesta were conducted using the low-resolution SpeX instrument in prism mode (Rayner et al., 2003) on the NASA Infrared Telescope Facility (IRTF). Apart from Vesta, local standard star and solar analog star observations were also performed to correct for telluric absorption and solar continuum, respectively. Nearly 4000 spectra of the asteroid were obtained during each night that covered a full rotation of Vesta. Detailed description of the observing protocol is presented in Reddy et al. (2009). Observational circumstances for SpeX data are presented in Table 5.

SpeX prism data were processed using the IDL-based Spextool provided by the NASA IRTF (Cushing et al., 2004). Analysis of the data to determine spectral band parameters like band centers, band depths and Band Area Ratio (BAR) was done using SpecPR based on the protocols discussed by Cloutis et al. (1986), Gaffey et al. (2002), and Gaffey (2003, 2005). All-night average spectra were used to extract spectral band parameters. Band centers were calculated by dividing out the linear continuum and fitting an n -order polynomial over the bottom third of each band. Band areas and band depths were calculated from continuum removed absorption features in SpecPR. While asteroid continua are probably not straight lines, applying straight line continua systematically for lab and asteroid data gives us the ability to interpret asteroid spectra using lab-based spectral calibrations and eliminate the effects of spectral slope. After ratioing the absorption feature to a straight-line continuum, a subroutine in SpecPR was used to calculate the area under the curve. The ratio of Band II area to Band I area gives the BAR. The errors of the band centers were estimated from 10 measurements of each one of them using different order polynomial fits (typically third and fourth order), and then calculating the $1 - \sigma$ (standard deviation of the mean) error from the multiple measurements of the band centers. This procedure was repeated for each all-night average spectrum and then the average $1 - \sigma$ was taken as the error. We estimated $1 - \sigma$ errors of 0.001 and 0.002 μm for the Band I center and Band II center respectively. A similar procedure was used to determine the uncertainties of the band depths and band areas. Ten measurements of each parameter were taken by sampling different ranges of points within the corresponding intervals. The errors are given by the average $1 - \sigma$ calculated from the multiple measurements of each band parameter. The $1 - \sigma$ error associated to Band I and Band II depths is 0.1%. For the BAR value we obtained an average error of 0.01. Spectral band parameters for Near-IR data of Vesta are presented in Table 6.

4.2. Vesta phase angle data: spectral band analysis

Near-infrared spectra of Vesta for full rotational coverage were similarly averaged to obtain an all-night average spectrum. For the

Table 5
Observing circumstances for Near-IR data.

Dates of observations	Visual magnitude	Sub-Earth latitude (°)	Phase angle (°)
February-23, 2010	6.15	32.25	4.87
March-7, 2010	6.36	32.17	9.5
March-26, 2010	6.72	32.45	17.0
May-02, 2010	7.34	33.67	24.0

Table 6

Spectral band parameters for Near-IR data of Vesta. The $1 - \sigma$ errors of Band I and Band II centers are 0.001 and 0.002 μm respectively. The $1 - \sigma$ error associated to Band I and Band II depths is 0.1%. For the BAR value the average error is 0.01.

Phase angle ($^\circ$)	Band I center (μm)	Band I depth (%)	Band II center (μm)	Band II depth (%)	BAR
4.87	0.928	30.08	1.932	23.27	2.28
9.50	0.932	31.29	1.931	24.09	1.74
17.00	0.928	33.37	1.910	25.60	2.22
24.00	0.929	34.60	1.948	26.08	2.27

four nights an average of approximately 16,000 spectra were used to create the final spectra for our analysis. Fig. 6 shows the all-night average spectra of Vesta for two of the four nights at phase angles of 4.4° (top dotted) and 17.0° (bottom line). The other two nights have been omitted for clarity and the data is normalized at $0.75 \mu\text{m}$. Spectral band parameters, primarily Bands I and II depths, were measured for all four nights and plotted as a function of phase angle in Fig. 7.

Fig. 7 (top panel) shows an increase of Band I depth with increasing phase angle, the black diamonds are actual measured Band I depths and the black line is a linear fit ($R^2 = 0.99$) through the measured values. This gives us an equation to estimate the correction factor for Band I depth assuming that the phase angle is the only factor affecting the band depth,

$$\gamma_1 = 0.2402\%/deg \tag{9}$$

Then the corrected Band I depth BI_{depc} is

$$BI_{depc} = BI_{dep} - \gamma_1 \alpha \quad 0^\circ < \alpha \leq 25^\circ \tag{10}$$

where BI_{dep} is the measured Band I depth. Based on the linear fit shown in Fig. 7 (top panel) the band depth increases 2.35% for every 10° increase in phase angle. Fig. 7 (bottom panel) shows a similar relationship between Band II depth and phase angle giving us the equations,

$$\gamma_2 = 0.1525\%/deg \tag{11}$$

$$BII_{depc} = BII_{dep} - \gamma_2 \alpha \quad 0^\circ < \alpha \leq 25^\circ \tag{12}$$

where BII_{depc} and BII_{dep} are the corrected and measured Band II depth respectively. The rate of change for Band II depth is 1.5% for every 10° increase in phase angle, which is much lower than the Band I depth change.

From our analysis of near-IR spectra of Vesta it is clear that the depth of the absorption bands change with phase angle, with the rate of change being higher for Band I than for Band II. A similar trend was found from spacecraft observations of Asteroid (433)

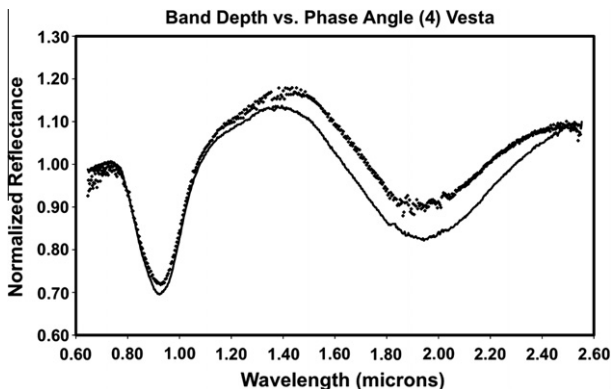


Fig. 6. Full rotation average near-IR spectra of Vesta taken at 4.4° (top dotted) and 17.0° (bottom line) phase angle. The data is normalized to unity at $0.75 \mu\text{m}$.

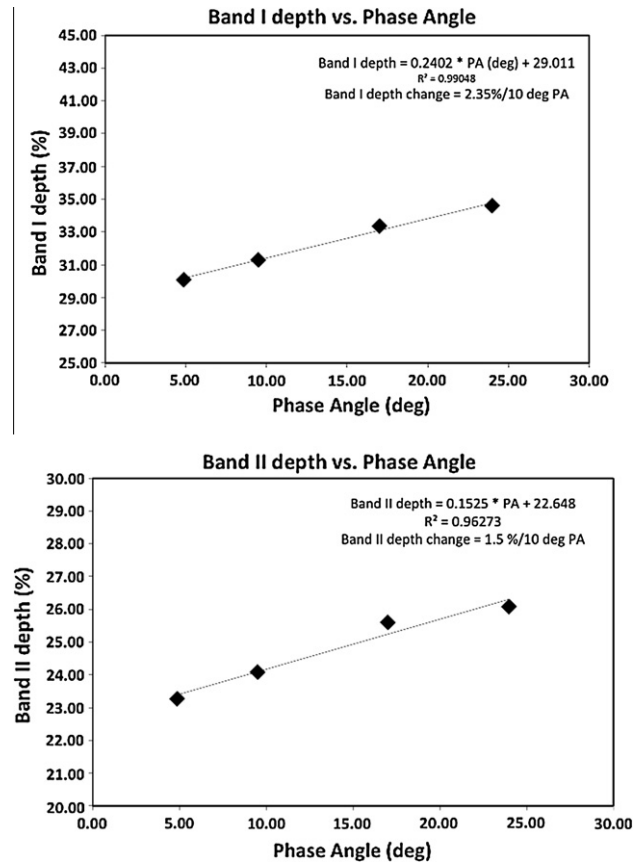


Fig. 7. Change in Vesta's Band I and Band II depths as a function of phase angle. The $1 - \sigma$ error of Band I and Band II depths (0.1%) is smaller than the data points. The black lines are linear fits through the measured values.

Eros (Bell et al., 2002) and can be explained as the result of the wavelength dependence of the single-scattering albedo and the phase function (Gradie et al., 1980; Gradie and Veverka, 1986; Clark et al., 2002). Small variations on Band centers with increasing phase angle were observed, but no systematic trends were found within the data.

While we have observed and quantified phase angle-induced spectral effects on Vesta, it is useful to test and see how much they will affect the mineralogical interpretation of spectral data from the Dawn mission. Band depth alone provides little quantitative information about the mineralogy of the surface because it is affected by both mineral chemistry and grain size (as well as phase angle). A more relevant parameter is the BAR value. In olivine-orthopyroxene mixtures, the BAR increases with increasing pyroxene content and a decrease in BAR (coupled with increase Band I center) is typically an indication of increasing olivine content. Gaffey (1997) used this calibration and suggested the presence of olivine-rich regions on the surface of Vesta based on ground-based observations. Disk-resolved spectra of Vesta's surface from the VIR spectrometer should be able to detect olivine-rich regions similar to those suggested by Gaffey (1997) or in the $\sim 20 \text{ km}$ deep South Pole Impact crater.

Fig. 8 shows the "all night" average BAR values for Vesta at four different phase angles (black diamonds). The plot also shows BAR ranges for Vesta's northern hemisphere as measured by Gaffey (1997), Vesta's southern hemisphere as measured by Reddy et al. (2010), 21 HED samples from the RELAB database, and inner main belt Vestoids from Moskovitz et al. (2010). Phase angles of these BAR ranges have been arbitrarily given offset values of 3° , 6° , 9° , and 12° for clarity. A linear fit ($R^2 = 0.98$) to the BAR values of Vesta

for the four different phase angles gives us an equation to calculate the effect of phase angle on BAR,

$$BAR = 0.0292 * (\alpha) + 1.5823 \quad 0^\circ < \alpha \leq 25^\circ \quad (13)$$

Based on this fit, Vesta's BAR increases 0.30° for a 10° increase in phase angle. Then the reddening coefficient and the corrected BAR are given by

$$\gamma_3 = 0.0292/\text{deg} \quad (14)$$

$$BAR_c = BAR - \gamma_3\alpha \quad 0^\circ < \alpha \leq 25^\circ \quad (15)$$

Looking at this plot it is evident that the BAR for Vesta changes significantly just due to composition than due to any phase angle effects. While this might be true, mineralogical interpretation of observations of the same surface feature at two different phase angles would produce different olivine/pyroxene ratios if the data were not corrected for spectral phase effects. So it is important to decouple effects of phase angle on BAR from real BAR change due to composition. For example, if the BAR of an olivine-rich surface unit observed at 20° phase angle is 1.1, the same unit will have a BAR of 1.4 when observed at 30° phase angle. This would translate to olivine content of $51 \pm 1\%$ at 20° phase angle and $44 \pm 1\%$ at 30° phase angle for the same surface unit based on calibrations by Burbine et al. (2003). The other issue one cannot ignore is that the application of any of these corrections to spectral band parameters is only for comparing relative BAR values of the same surface unit. Comparison of absolute values could be made if all the data was normalized to a common phase angle.

5. Laboratory spectra

5.1. Phase angle and temperature series

In order to determine the effects of phase angle variations on pyroxene reflectance spectra, we utilized two samples in this study. One is the <45 μm fraction of a terrestrial low-calcium pyroxene (LCP; PYX032: $Fs_{41.5}En_{54.9}Wo_{3.6}$). The second is a sample of the eucrite Moama sieved to 74–250 μm. The eucrite sample was selected for this study because eucrites are believed to have derived from Vesta (the main focus of this study). The eucrite Moama consists of 49 vol.% plagioclase feldspar ($An_{\sim 94}$) and 48.9 vol.% pyroxene ($Fs_{39.4}En_{53.0}Wo_{7.6}$ for the primary pigeonite) (Lovering, 1975).

Reflectance spectra in the 0.35–2.50 μm wavelength range were measured at the University of Winnipeg's HOSERLab with an ASD FieldSpec Pro HR spectrometer, equipped with a fiber optic cable to direct reflected light to the spectrometer's three internal detectors (Cloutis et al., 2010). The fiber cable consists of 75 randomly arranged 200 μm diameter optical fibers. This helps to minimize any viewing differences for the three detectors. Each fiber has an acceptance angle of ~25°. Sample illumination was provided by a 150 W quartz-tungsten-halogen in-house collimated light source. A total of 200 spectra were averaged to improve signal to noise.

A calibrated Spectralon® disk was used as a reflectance standard. It was measured at an incident angle $i = 13^\circ$ and emission angle $e = 0^\circ$ (13° phase angle). The powdered samples were placed in aluminum sample cups that were wide and deep enough to ensure that the powdered sample completely filled the field of view of the spectrometer. The sample was not moved during the entire set of

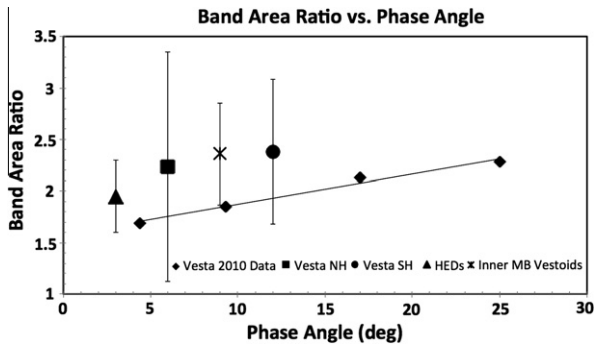


Fig. 8. Full rotation average BAR values of Vesta (black diamonds) at four different phase angles. The $1 - \sigma$ error of BAR (0.01) is smaller than the data points. Also plotted are BAR ranges for Vesta's northern hemisphere (square) as measured by Gaffey (1997), Vesta's southern hemisphere (circle) as measured by Reddy et al. (2010), 21 HED samples (triangle) from RELAB database, and inner main belt Vestoids (cross) from Moskovitz et al. (2010). Phase angles of these BAR ranges have been arbitrarily given offset values of 3°, 6°, 9°, and 12° for clarity. The linear fit was done only to the full rotation average BAR values of Vesta. The vertical lines shown for Gaffey (1997), Reddy et al. (2010), RELAB database and Vestoids depict the observed spread in BAR due to composition variations.

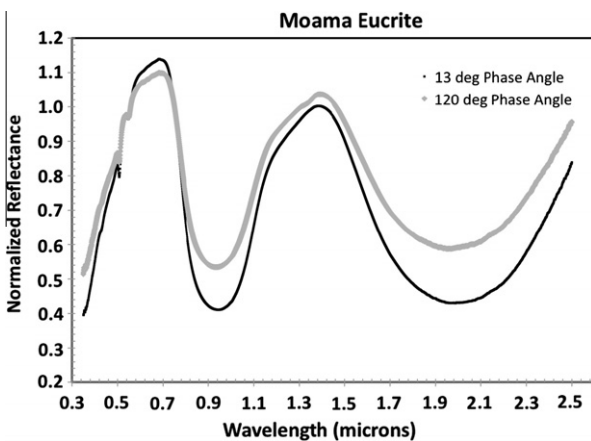


Fig. 9. Spectra of the eucrite Moama taken at 13° and 120° phase angle. Both spectra have been normalized to unity at 0.55 μm.

Table 7
Spectral band parameters for the eucrite Moama, particle size <45 μm. The average $1 - \sigma$ errors of Band I and Band II centers are 0.001 and 0.002 μm respectively. The average $1 - \sigma$ errors associated to Band I and Band II depths are 0.2% and 0.15% respectively, while the average error of the BAR value is 0.01.

Incidence angle (°)	Emission angle (°)	Phase angle (°)	Band I center (μm)	Band I depth (%)	Band II center (μm)	Band II depth (%)	BAR
13.00	0.00	13	0.940	62.00	1.963	52.00	1.68
30.00	0.00	30	0.937	61.05	1.958	51.90	1.71
0.00	30.00	30	0.937	59.88	1.952	49.95	1.62
-30.00	60.00	30	0.937	59.90	1.953	49.96	1.70
60.00	0.00	60	0.942	62.21	1.946	53.00	1.72
30.00	30.00	60	0.940	62.46	1.957	52.00	1.65
0.00	60.00	60	0.932	58.77	1.955	48.50	1.66
60.00	30.00	90	0.935	60.17	1.950	52.42	1.79
30.00	60.00	90	0.926	59.41	1.965	49.58	1.69
60.00	60.00	120	0.931	50.30	1.953	40.30	1.57

spectral measurements. The spectra were measured in the phase angle range between 13° and 120° with an in-house goniometer that allowed i and e to be varied independently. The measured data were corrected for dark current, detector offsets at 1.00 and 1.83 μm , as well as small irregularities in Spectralon's reflectance in the 2.0–2.5 μm region. All the spectra were calibrated against the $i = 13^\circ$ and $e = 0^\circ$ Spectralon standard. The ASD spectrometer has a spectral resolution of between 2 nm (in the visible region) and 7 nm (in the near infrared), with a sampling interval of 1.4 nm. The data are internally interpolated to provide an output at 1 nm intervals.

Reflectance spectra over the 2–5 μm range were measured with a Bruker Vertex 70 FTIR spectrometer equipped with a KBr beamsplitter, a glowbar light source, an MCT broadband detector, and a Specac Monolayer Grazing Angle goniometer, which allows i and e to be varied independently. Reflectance spectra over the 2–5 μm range were measured relative to a Labsphere diffuse gold (Infragold) standard. The reflectance standard was measured at $i = 18^\circ$ and $e = 0^\circ$ (note that the lowest phase angle possible for this spectrometer is 18°). For this wavelength range the spectra were obtained at phase angles between 18° and 120°. The resultant data were corrected for dark current and calibrated against the gold standard measured at $i = 18^\circ$ and $e = 0^\circ$. Spectra were measured with a spectral resolution of 15 cm^{-1} . A total of 2500 scans were acquired and averaged to improve signal to noise. The sample chamber was sealed and flushed with dry nitrogen passed through Drierite. In the configuration used for these measurements, the sample chamber had to be opened to adjust the goniometer. The chamber was flushed for at least 5 min prior to each new spectral measurement.

Data of temperature spectral series were obtained from two published sources, Hinrichs and Lucey (2002) and Schade and Wäsch (1999), and reanalyzed after resampling to the Dawn FC and VIR wavelength ranges.

5.2. Eucrite and LCP phase angle series: (0.35–2.5 μm)

Moama is a pyroxene–plagioclase cumulate eucrite similar to Serra de Mage consisting of 49.1 vol.% plagioclase and 48.9% pyroxene (Lovering, 1975) with a mean pyroxene chemistry of approximately $\text{Fs}_{43}\text{Wo}_8$. Fig. 9 shows spectra from two extreme ends of the phase angle range (13° and 120°), clearly showing the differences in band depths.

Spectral band parameters of Moama and the terrestrial LCP and their uncertainties were measured following the same procedure described in Section 4.1. For these samples we found that the average $1 - \sigma$ errors of Band I and Band II depths are 0.2% and 0.15% respectively, while the average error of the BAR value is 0.01. Spectral band parameters for the eucrite Moama and the LCP are presented in Tables 7 and 8 respectively. Fig. 10 shows the Band depths, and Band Area Ratio of Moama as a function of phase angle.

All three plots indicate a general decrease in band depths and BAR from the lowest phase angle 13° to 30°, followed by relatively unchanging values between 30° and 90°, and a dramatic drop from

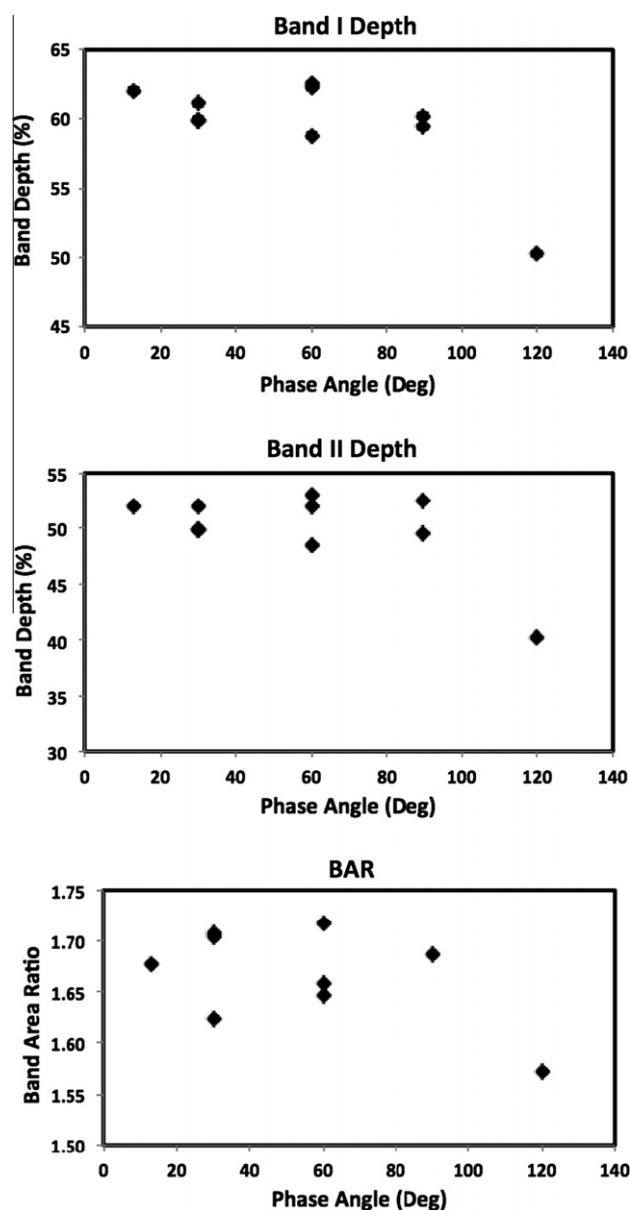


Fig. 10. Plot showing the change in Band I, Band II depths and Band Area Ratio of the eucrite Moama as a function of phase angle. The $1 - \sigma$ errors of Band I depth (0.2%), Band II depths (0.15%) and BAR (0.01) are smaller than the data points.

Table 8

Spectral band parameters for orthopyroxene (PYX032), particle size <45 μm . The average $1 - \sigma$ errors of Band I and Band II centers are 0.001 and 0.002 μm respectively. The average $1 - \sigma$ errors associated to Band I and Band II depths are 0.2% and 0.15% respectively, while the average error of the BAR value is 0.01.

Incidence angle (°)	Emission angle (°)	Phase angle (°)	Band I center (μm)	Band I depth (%)	Band II center (μm)	Band II depth (%)	BAR
13.00	0.00	13.00	0.935	43.52	1.962	32.81	2.11
30.00	0.00	30.00	0.936	44.99	1.966	33.61	2.08
0.00	30.00	30.00	0.935	46.26	1.972	35.12	2.09
-30.00	60.00	30.00	0.935	45.28	1.964	34.91	2.18
60.00	0.00	60.00	0.936	43.54	1.960	31.78	1.98
30.00	30.00	60.00	0.935	45.90	1.967	35.38	2.18
0.00	60.00	60.00	0.934	45.40	1.970	33.68	2.06
60.00	30.00	90.00	0.935	43.57	1.964	33.04	2.09
30.00	60.00	90.00	0.932	41.01	1.961	29.93	2.10
60.00	60.00	120.00	0.933	36.88	1.956	26.14	1.96

90° to 120° phase angle. A similar trend is observed for the terrestrial LCP (Fig. 11) for phase angles higher than 30°, however for the lowest phase angle the trend is the opposite to the eucrite Moama. Due to the physical limitations of the instrument used for the measurements it is not possible to acquire spectra at phase angles lower than 13°, and therefore we cannot know whether the value observed for Moama at a phase angle of 13° will continue increasing for lower phase angles or not. It is worth mentioning that different configuration of the same phase angle will produce different values and hence variations in the trend of the curve. This behavior was noticed by Gradie et al. (1980) and can be seen in Figs. 10 and 11, where the multiple data points of the same phase angles correspond to different combination of the incident and emission angles. These variations and the difference in particle size could explain the observed discrepancy between Moama and the terrestrial LCP. As in the case of the NIR spectra of Vesta small variations

on Band centers with increasing phase angle were observed, but no systematic trends were found within the data.

5.3. Eucrite phase angle series: (2.5–5.0 μm)

Fig. 12 shows 2.5–5.0 μm spectra of Moama at three different phase angles (top panel). At longer wavelengths, eucrites exhibit an absorption band near 3 μm that is due to OH/H₂O, which may be present in a number of forms, such as adsorbed water, OH/H₂O-bearing alteration products, and fluid inclusions, and is not diagnostic of pyroxene. Moama also exhibits absorption bands near 3.3–3.5 and 4.2–4.3 μm that are, respectively, attributable to organic C–H stretching bands (likely due to residues of solvents used to wet sieve the samples), and CO₂ which was incompletely purged from the sample chamber. None of these features are diagnostic of pyroxene. Weak absorption bands at 4.7–4.9 μm (Fig. 12 bottom panel) are Si–O overtones whose Si–O stretching fundamental bands lie between 8.7 and 12.0 μm (Saksena, 1961; Hamilton, 2000).

5.4. Eucrite phase angle series: effects on spectral band parameters

Sunshine et al. (2004) used the Modified Gaussian Model (MGM) technique to deconvolve spectra of several S-type asteroids (including members of the Agnia and Merxia families) and suggested them to be mixtures of high (HCP) and low-Ca (LCP) pyroxenes. Using MGM they obtained the ratio of HCP/(HCP + LCP) and suggested that this method could be used for identifying various degrees of asteroid differentiation. This method could be applied

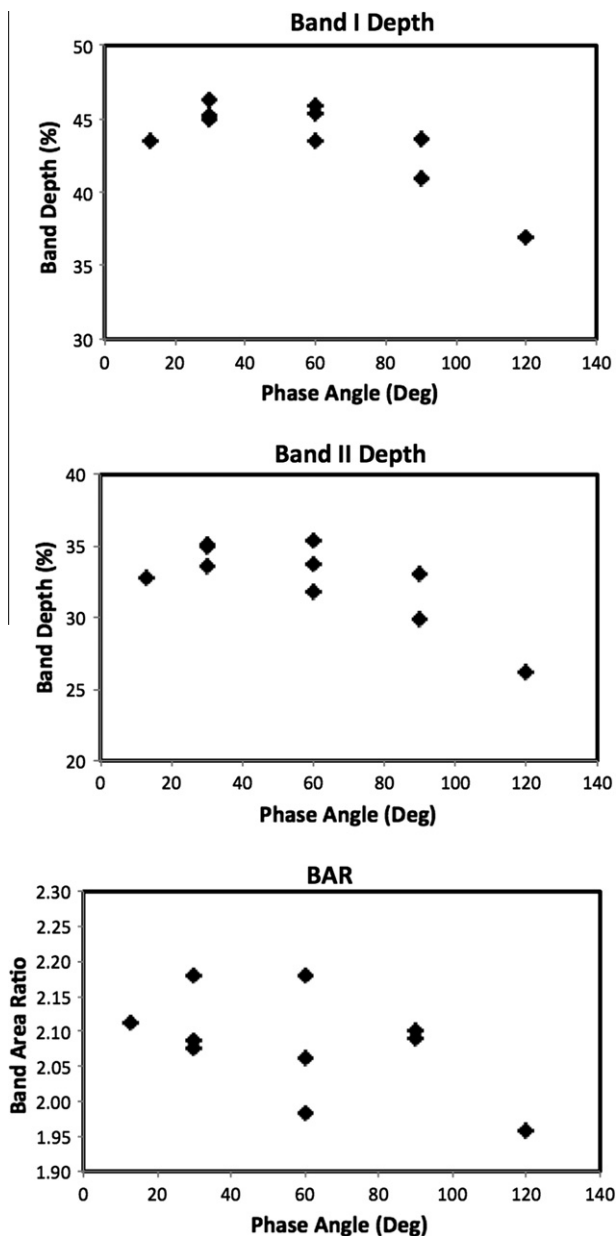


Fig. 11. Plot showing the change in Band I, Band II depths and Band Area Ratio of the terrestrial LCP; PYX032: $\text{Fs}_{41.5}\text{En}_{54.9}\text{Wo}_{3.6}$. The $1 - \sigma$ errors of Band I depth (0.2%), Band II depths (0.15%) and BAR (0.01) are smaller than the data points.

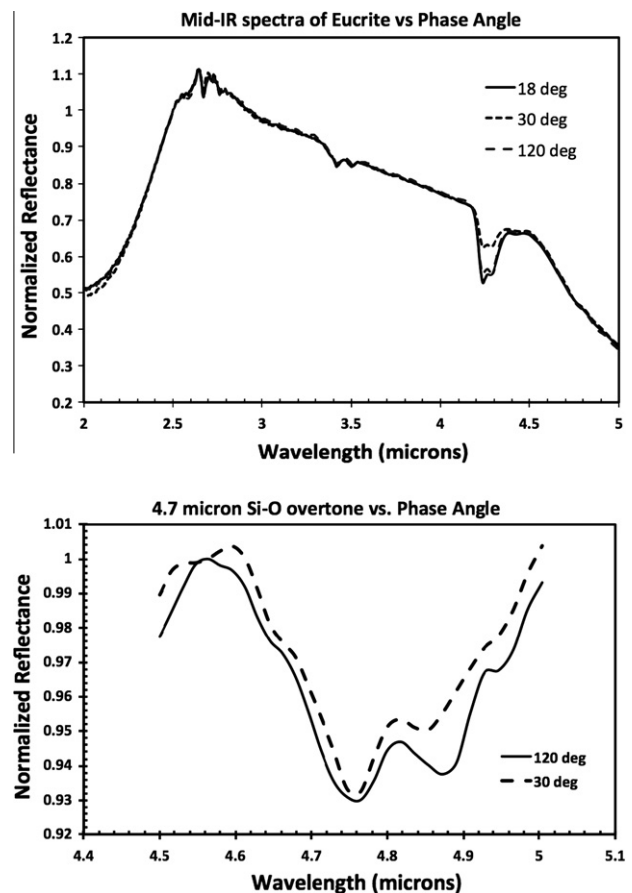


Fig. 12. Mid-IR (2.5–5.0 μm) spectra of the eucrite Moama at three different phase angles (top panel) and the 4.7–4.9 μm Si–O overtone at two different phase angles (bottom panel).

to VIR data from Dawn to extract the ratio of HCP in a mixture of HCP and LCP, which are the primary absorbing species in eucrites. We wanted to quantify how much the HCP/(HCP + LCP) ratio is affected by increasing band depth due to phase angle. Therefore, we applied MGM analysis to laboratory spectra of Moama obtained at various phase angles, however this attempt was largely unsuccessful. The inability to produce reasonable MGM fits for complex lithologies like Moama is a well-known challenge for the MGM technique and is in part due to a lack of suitable calibration studies of pyroxenes with iron compositions analogous to the eucrites (Mayne et al., 2010). Nevertheless, detailing this unsuccessful MGM analysis does provide useful insight into the spectral changes that result from variable phase angle.

Spectra of Moama were obtained at phase angles of 13° and 120°. Table 9 summarizes our best fits from the MGM analysis. A two-pyroxene model with 10 absorption bands was required to produce a fit with residuals under 1%. The 10 MGM bands are as follows: two charge transfer bands around 0.3 and 0.4 μm, a Cr³⁺ band around 0.6 μm, LCP bands near 0.9 and 1.8 μm, HCP bands near 1.0 and 2.2 μm, an additional band shortwards of 0.9 μm due to Fe²⁺ in the M1 site of pyroxene, one band around 1.2 μm due to Fe²⁺ in the M1 site of LCP or HCP or plagioclase feldspar, and an atmospheric water band longwards of 2.5 μm. MGM-derived fits to the spectra of other cumulate eucrites also employ these 10 bands (Mayne et al., 2010). Attempts to fit the spectra of Moama with fewer bands produced markedly higher residuals.

Several features of these best-fit MGM models suggest they are unreasonable. First, the band parameters, though within the ranges measured for eucrites (Mayne et al., 2010; Sunshine et al., 2004), are in many cases at the limits of those ranges. For example, the central wavelengths of the 1 μm LCP and HCP bands, 2 μm LCP band and M1 band are all more than one standard deviation away from the mean band centers for eucrites (Mayne et al., 2010). Second, and perhaps more importantly, the pyroxene chemistry

implied by this best-fit MGM model is inconsistent with Moama's known composition. The ratio of LCP to HCP band strengths for the 1 and 2 μm bands (Table 9) predict an average HCP/(HCP + LCP) value of ~66% (Fig. 7 in Sunshine and Pieters (1993)). This is very different from X-ray diffraction data which show HCP/(HCP + LCP) of ~15% for Moama (Lovering, 1975). The spectra of Moama cannot reasonably be fit with a model corresponding to 15% HCP content. This may be due to differences in the inversion behavior of pigeonite between Moama and samples used by Sunshine and Pieters (1993).

Though compositionally incorrect, the fitted MGM bands for the two spectra have nearly identical central wavelengths, widths and relative strengths (Table 9). The spectrum measured at higher phase angle exhibits lower spectral contrast, resulting in MGM bands that are all consistently shallower by ~20%. This general decrease in spectral contrast for large phase angles can be explained by diffusive reflectance. Hapke (1993) derived an expression for the diffusive reflectance (r_0) as a power series of the single scattering albedo (w)

$$r_0(w) = (1/4)w + (1/8)w^2 + (5/64)w^3 + \dots \quad (16)$$

Table 10

Temperature series data for the eucrite EET8325 (particle size 45–90 μm) from Hinrichs and Lucey (2002) acquired in the temperature range between 80 and 400 K. The average 1 – σ errors of Band I and Band II centers are 0.001 and 0.002 μm respectively. The average uncertainty of the BAR value is 0.01.

Temp. (K)	Band I center (μm)	Band II center (μm)	BAR
80	0.927	1.936	1.38
100	0.928	1.936	1.73
120	0.928	1.933	1.68
140	0.930	1.935	1.80
160	0.931	1.937	1.70
180	0.932	1.948	1.74
200	0.932	1.947	1.67
220	0.932	1.952	1.75
240	0.933	1.963	1.99
260	0.935	1.959	1.70
280	0.937	1.953	1.46
300	0.939	1.952	1.49
320	0.938	1.969	1.56
340	0.941	1.975	1.58
360	0.941	1.973	1.48
380	0.943	2.000	1.61
400	0.946	1.985	1.55

Table 11

Temperature series data for the howardite EET87503 (particle size 45–90 μm) from Hinrichs and Lucey (2002) acquired in the temperature range between 80 and 400 K. The average 1 – σ errors of Band I and Band II centers are 0.001 and 0.002 μm respectively. The average uncertainty of the BAR value is 0.01.

Temp. (K)	Band I center (μm)	Band II center (μm)	BAR
80	0.928	1.934	1.71
100	0.930	1.937	1.75
120	0.928	1.935	1.66
140	0.929	1.938	1.80
160	0.932	1.945	1.75
180	0.932	1.947	1.75
200	0.932	1.949	1.67
220	0.931	1.951	1.80
240	0.934	1.968	2.02
260	0.935	1.958	1.70
280	0.937	1.958	1.52
300	0.939	1.953	1.50
320	0.938	1.970	1.59
340	0.942	1.968	1.62
360	0.941	1.971	1.52
380	0.944	2.003	1.64
400	0.946	1.976	1.54

Table 9

MGM analysis of the eucrite Moama phase angle spectra.

Bands	Band center (μm)	Band width (μm)	Strength (log reflectance)
<i>Phase angle 13°</i>			
Band 1	0.337	0.101	–0.65
Band 2	0.415	0.249	–0.61
Band 3	0.663	0.118	–0.12
Band 4	0.817	0.118	–0.31
Band 5	0.894	0.181	–0.86
Band 6	1.022	0.182	–0.76
Band 7	1.202	0.294	–0.36
Band 8	1.806	0.584	–0.89
Band 9	2.226	0.585	–0.81
Band 10	2.711	0.413	–0.16
Continuum intercept = 0.945, slope = –0.005 μm ^{–1}			
RMS error = 0.70%			
1 μm LCP/HCP = 1.14			
2 μm LCP/HCP = 1.09			
<i>Phase angle 120°</i>			
Band 1	0.335	0.108	–0.50
Band 2	0.426	0.249	–0.48
Band 3	0.664	0.122	–0.12
Band 4	0.811	0.118	–0.24
Band 5	0.892	0.181	–0.66
Band 6	1.022	0.186	–0.55
Band 7	1.203	0.297	–0.28
Band 8	1.801	0.582	–0.66
Band 9	2.227	0.564	–0.55
Band 10	2.714	0.412	–0.11
Continuum intercept = 0.787, slope = –0.003 μm ^{–1}			
RMS error = 0.57%			
1 μm LCP/HCP = 1.20			
2 μm LCP/HCP = 1.20			

where the term w^j is the contribution of the j th order of multiple scattering to r_0 . When the bidirectional reflectance of a material is measured at low phase angles, with the incident and emission angles close to the normal, the multiple scattering will be important in the wings of the absorption band, where w is high, therefore the higher-order terms in the expression above becomes significant and r_0 will increase nonlinearly. However, the multiple scattering will be less important within the band, where w is low and single scattering is the primary contributor to the brightness, resulting in a linear increase of r_0 near the band center. As a consequence the absorption bands become deeper. As the phase angle increases, the multiply scattered light is less able to escape from a surface element to the mean surface, therefore only single scattering contributes throughout the whole band and r_0 increase linearly in both the wings and near the band center. As a consequence the absorption bands become weaker. It is interesting that such a large shift in observed phase angle only affects band strength. If compositional

information could be extracted from this MGM fit, then it seems that changes in phase angle would not obscure this interpretation.

For the 2.5–5.0 μm spectrum of Moama, measurement of spectral band parameters (band depth and center) of the 4.7–4.9 μm Si–O overtone revealed no significant changes due to phase angle. A weak increase (<1.5%) in band depth was noted with increase in phase angle (Fig. 12 bottom panel) and the band center essentially remained the same with changing phase angle.

5.5. Temperature spectral series of HEDs

Laboratory spectral measurements of HED meteorites obtained at various temperatures (80–400 K) from Schade and Wäsch (1999) and Hinrichs and Lucey (2002) were resampled to the Dawn FC filter band passes prior to analysis. The eucrite and howardite data from Hinrichs and Lucey (2002) were obtained at 17 different temperatures (80–400 K) and the diogenite spectra from Schade and Wäsch (1999) were obtained at four temperatures (80, 173, 288, 373 K). Spectral band parameters (band centers and BAR) and their corresponding errors were also measured for full resolution spectra using methods similar to those applied to the telescopic data. The average $1 - \sigma$ errors of Band I and Band II centers for the HED are 0.001 and 0.002 μm respectively. The average uncertainty in the calculated BAR was estimated to be 0.01. The measured Band centers and BAR values for the eucrite, howardite and diogenite are presented in Tables 10–12 respectively. Changes in spectral band parameters will be used to calibrate the impact of surface temperature on spectral data from the VIR instrument. Although the VIR spectrometer wavelength range

Table 12

Temperature series data for the diogenite Ellemeet (particle size 60–200 μm) from Schade and Wäsch (1999) acquired in the temperature range between 80 and 373 K. The average $1 - \sigma$ errors of Band I and Band II centers are 0.001 and 0.002 μm respectively. The average uncertainty of the BAR value is 0.01.

Temp. (K)	Band I center (μm)	Band II center (μm)	BAR
80	0.922	1.890	2.48
173	0.919	1.903	2.27
288	0.924	1.915	2.19
373	0.925	1.929	2.13

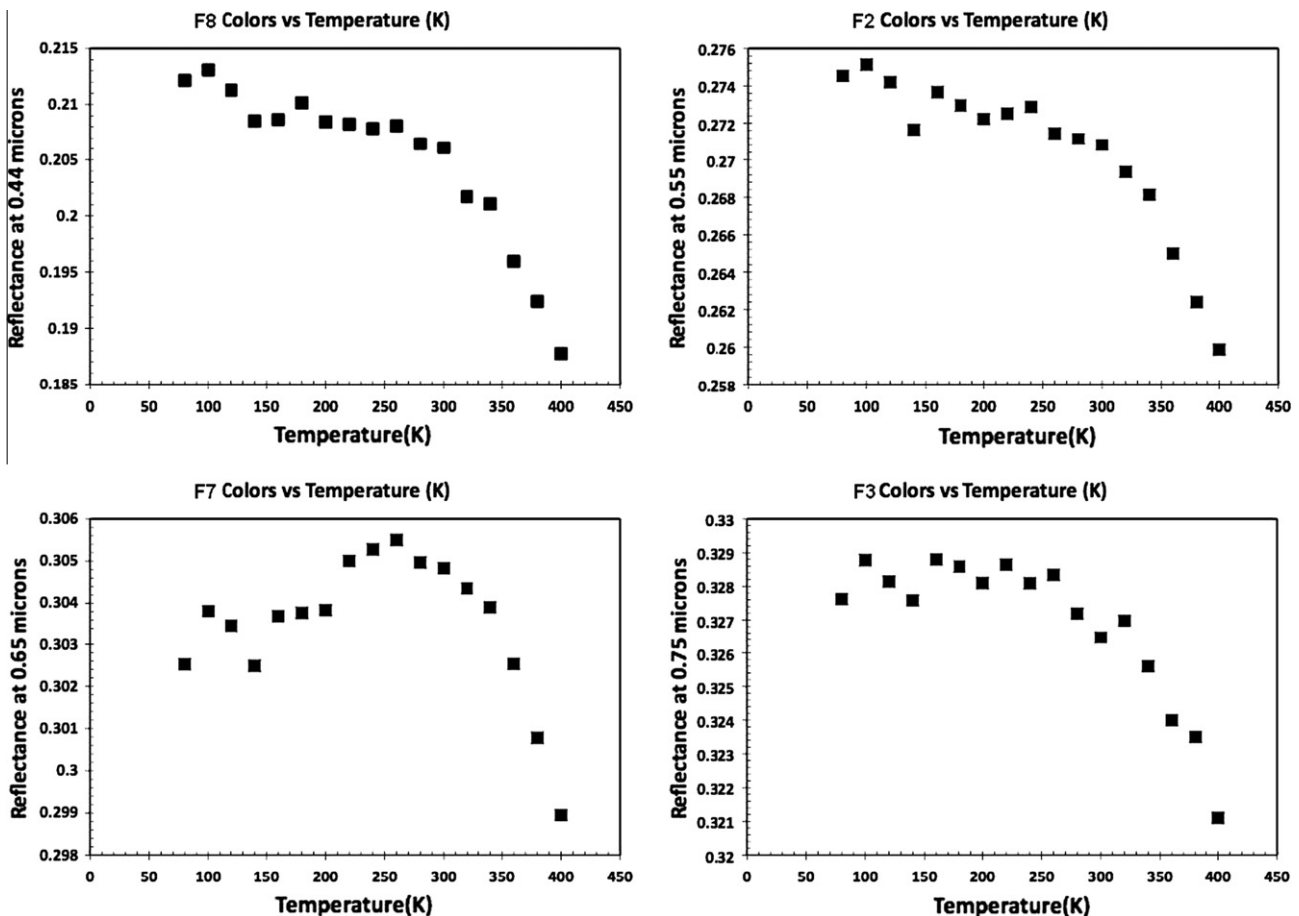


Fig. 13A. Plots showing the temperature influence (80–400 K) on the spectral appearance of the eucrite EET83251 in Dawn F8, F2, F7 and F3 bands.

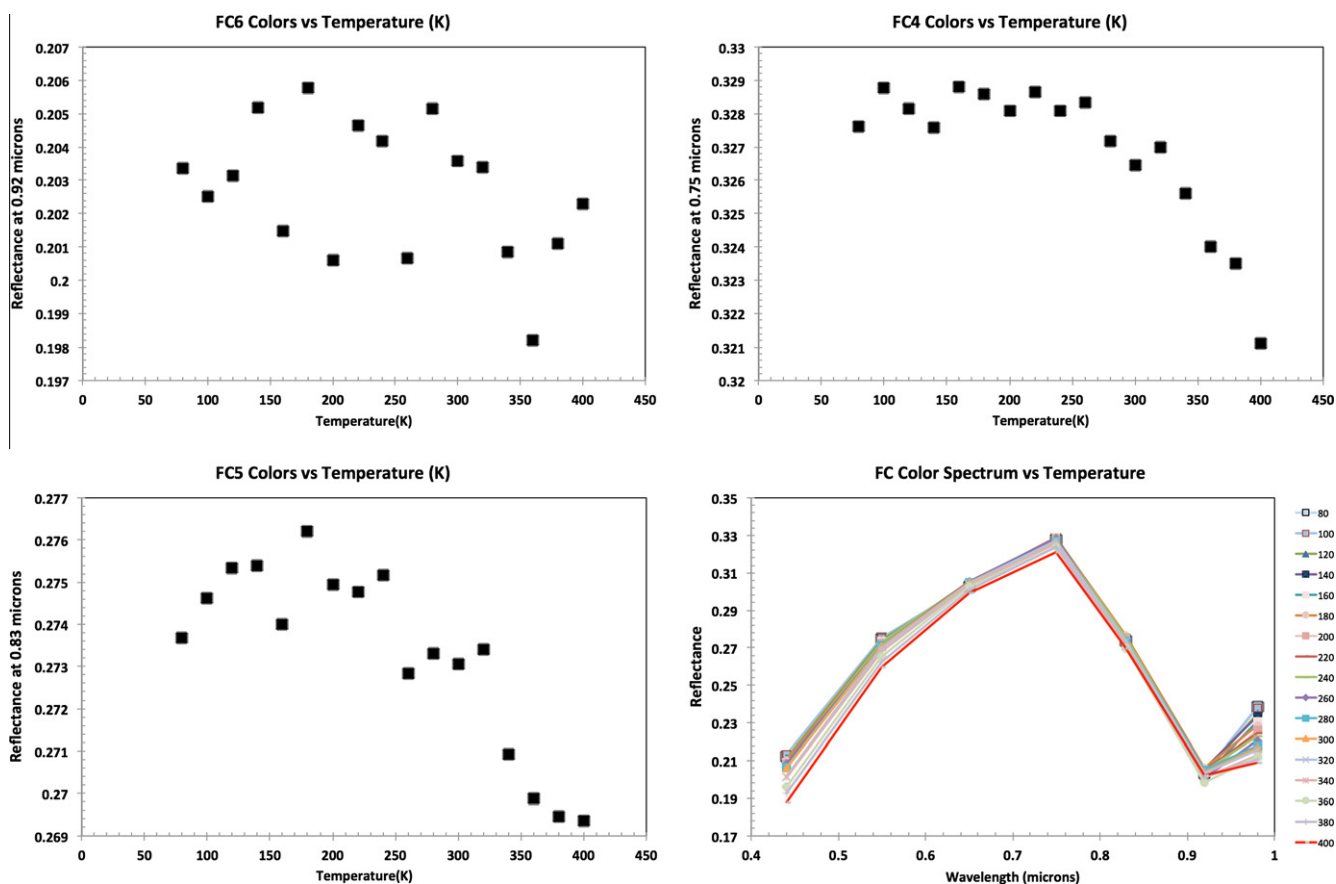


Fig. 13B. Plots showing the temperature influence (80–400 K) on the spectral appearance of the eucrite EET83251 in Dawn F6, F4, F5 bands. The last panel shows the color spectra of EET83251 as a function of temperature (400 K at the bottom and 80 K at the top). (For interpretation of the references to color in this figure legend, the reader is referred to the web version of this article.)

spans 0.25–5.0 μm , our analysis here is restricted to wavelengths between 0.30 and 2.5 μm due to the lack of temperature series data between 2.5 and 5.0 μm .

Figs. 13A and 13B show a series of plots depicting the effects of temperature on the spectra of the eucrite EET83251 resampled for the seven Dawn FC filters. Fig. 13B (bottom right panel) shows the Dawn FC seven color ‘spectrum’ of eucrite EET83251 at different temperatures ranging from 80 to 400 K. Note that the series goes from the warmest temperature (400 K) spectrum that has the lowest reflectance value at 0.98 μm at the bottom, to the coldest spectrum (80 K) with the highest value at the top. Figs. 13A and 13B show that the reflectance values of filters 0.44-, 0.55-, 0.65-, 0.75- and 0.83- μm are relatively unaffected for temperatures ranging between 80 and 250 K but reveal a steep drop in reflectance for higher temperatures. Even this drop off does seem to be significant (0.001–0.006) for the 0.65-, 0.75- and 0.83- μm filters. For the 0.92- μm filter no trend is visible. The only filter for which a clear trend can be seen is the 0.98- μm filter, which shows a 0.14 drop between 80 K and 400 K. Similar effects were noted for FC color spectra of howardite EET87503 and diogenite Elmeemet.

Figs. 14 and 15 show the change in Bands I and II centers of eucrite EET83251 and howardite EET87503. The solid lines represent a linear fit to all the data. As can be seen in these figures the trend for the two samples is very similar and in both cases the band centers move to longer wavelength with increasing temperature. For the diogenite Elmeemet from Schade and Wäsch (1999) the Band I center shows a weak increasing trend, but Band II center shows a much steeper trend with increasing temperature. In this case we found that the Band I centers are better fitted with a third order

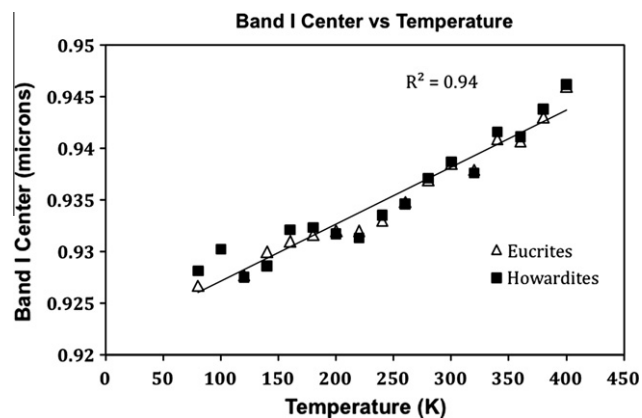


Fig. 14. Band I center change in eucrite EET83251 (triangles) and howardite EET87503 (squares) as a function of temperature. The average 1 - σ error of Band I center is 0.001 μm . The solid line represents a linear fit to all the data.

polynomial, while the Band II centers can be fitted with a straight line (Figs. 16 and 17). Band I centers for all three meteorites show a plateau between 150 and 225 K where the parameters remain constant. Eucrite, howardite, and diogenite temperature spectra show a weak overall decreasing trend in BAR with increasing temperature.

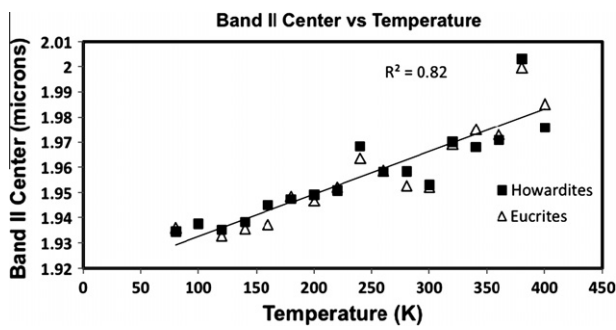


Fig. 15. Band II center change in eucrite EET83251 (triangles) and howardite EET87503 (squares) as a function of temperature. The average $1 - \sigma$ error of Band II center is $0.002 \mu\text{m}$. The solid line represents a linear fit to all the data.

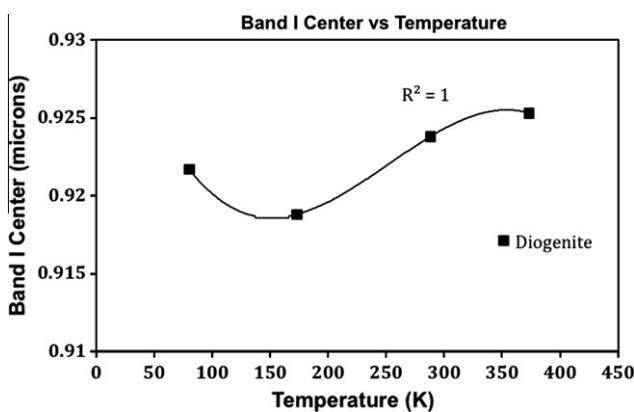


Fig. 16. Band I center change in diogenite Ellemeet as a function of temperature. The average $1 - \sigma$ error of Band I center is $0.001 \mu\text{m}$. The solid line represents a linear fit to the data.

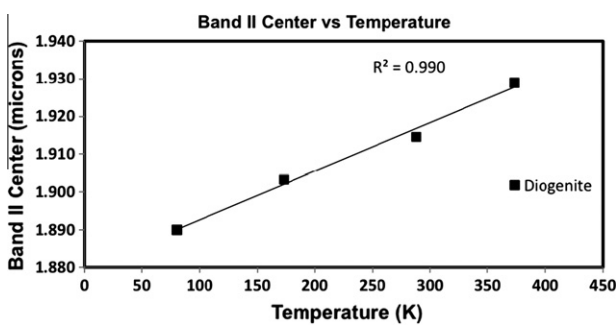


Fig. 17. Band II center change in diogenite Ellemeet as a function of temperature. The average $1 - \sigma$ error of Band II center is $0.002 \mu\text{m}$. The solid line represents a linear fit to the data.

5.6. HED temperature series: effects on spectral band parameters

Spectral band parameters of the HED spectra from Schade and Wäsch (1999) and Hinrichs and Lucey (2002) show their clear dependence on changing temperature (Figs. 14–17). Burbine et al. (2009) developed a set of temperature correction equations (see Section 1.3) based on data of bronzite and enstatite from Moroz et al. (2000); here we have attempted to develop similar equations to correct Band I and II centers for temperature using the HED spectra. The Band I and II corrections will enable the VIR data of Vesta obtained between 100 and 220 K to be interpreted using laboratory spectra taken at room temperature (300 K). From

the polynomial fits the formulae derived for howardites and eucrites are

$$\text{Band I center correction } (\mu\text{m}) = 0.01656 - 0.0000552 * T \text{ (K)} \quad (17)$$

$$\text{Band II center correction } (\mu\text{m}) = 0.05067 - 0.00017 * T \text{ (K)} \quad (18)$$

Similarly, the formulae derived for diogenites are given by

$$\begin{aligned} \text{Band I center correction } (\mu\text{m}) \\ = 0.000000017 * T^3 \text{ (K)} - 0.0000012602 * T^2 \text{ (K)} \\ + 0.0002664351 * T \text{ (K)} - 0.0124 \end{aligned} \quad (19)$$

$$\text{Band II center correction } (\mu\text{m}) = 0.038544 - 0.000128 * T \text{ (K)} \quad (20)$$

As with the eucrite and howardite formulae, the diogenite wavelength corrections need to be added to the Band I and II centers to obtain values at 300 K. While cross checking these equations with Burbine et al. (2009), we noticed that the errors in correcting howardite and eucrite Band I center using their bronzite calibration is better ($0.0003 \mu\text{m}$) than our method here ($0.00096 \mu\text{m}$), but their enstatite calibration yields a much higher error ($0.003 \mu\text{m}$) compared to ours. Since Burbine et al. (2009) suggest using both enstatite and bronzite formulae and averaging the corrections, the average error from their correction is a bit higher ($0.0011 \mu\text{m}$) than our errors. A similar trend is noted for Band II center correction for howardites and eucrites. For diogenites errors from our formulae yield smaller errors compared to Burbine et al. (2009) calibration.

6. Summary and conclusions

Our analysis of phase angle and temperature effects on spectral Vesta and HED meteorites data has revealed a wealth of new information. This information will be important for the analysis of the Dawn FC and VIR data. Ground-based telescopic observations of Vesta using Dawn FC filters revealed no trend for the phase slope and G parameter with respect to wavelength. Spectral observations in the visible showed an increase of the spectral slope with increasing phase angle. The NIR spectra of Vesta, on the other hand, showed an increase of band depths and BAR as the phase angle increase.

These results have been used to derive equations to correct for effects of changing phase angle on spectral slope and absorption band depth as well as Band Area Ratio. This set of equations is the first ever derived from telescopic data to correct for these effects prior to interpretation of spacecraft data. We have also updated existing equations (Burbine et al., 2009) to correct for temperature-induced spectral effects by developing specific corrections for HED meteorites. These corrections are applied to Bands I and II centers and normalize them to room temperature (300 K), which will enable interpretation of spacecraft data using laboratory calibrations at room temperature.

Acknowledgments

V.R. and M.J.G. were supported by NASA Dawn Participating Scientist Program Grant NNNH09ZDA001N-DAVPS, NASA NEOO Program Grant NNX07AL29G, and NASA Planetary Geology and Geophysics Grant NNX07AP73G. The authors would like to thank, Reid Archer, Paul Lucey, and Brian Warner for their support in this research and Mike Hicks and Cristina Thomas for their helpful reviews. We thank the IRTF TAC for awarding time to this project, and to the IRTF TOs and MKSS staff for their support. J.A. Sanchez acknowledges a PhD fellowship of the International Max Planck

Research School on Physical Processes in the Solar System and Beyond. E.A.C. thanks the Canada Foundation for Innovation, the Manitoba Research Innovation Fund, the Canadian Space Agency, and NSERC for funding to establish and operate HOSERLab.

References

- Adams, J.B., Filice, A.L., 1967. Spectral reflectance 0.4 to 2.0 microns of silicate rock powders. *J. Geophys. Res.* 72, 5705–5715.
- Bell III, J.F., Izenberg, N.I., Lucey, P.G., Clark, B.E., Peterson, C., Gaffey, M.J., Joseph, J., Carcich, B., Harch, A., Bell, M.E., Warren, J., Martin, P.D., McFadden, L.A., Wellnitz, D., Murchie, S., Winter, M., Veverka, J., Thomas, P., Robinson, M.S., Malin, M., Cheng, A., 2002. Near-IR reflectance spectroscopy of 433 Eros from the NIS instrument on the NEAR mission. 1. Low phase angle observations. *Icarus* 155, 119–144.
- Binzel, R.P., Gaffey, M.J., Thomas, P.C., Zellner, B., Storrs, A.D., Wells, E.N., 1997. Geologic mapping of Vesta from 1994 Hubble Space Telescope images. *Icarus* 128, 95–103.
- Bobrovnikoff, N.T., 1929. The spectra of minor planets. *Lick Obs. Bull.* 14, 18–27 (No. 407, U. Cal. Pub.).
- Bowell, E., Hapke, B., Domingue, D., Lumme, K., Peltoniemi, J., Harris, A.W., 1989. Application of photometric models to asteroids. In: Binzel, R.P., Gehrels, T., Matthews, M.S. (Eds.), *Asteroids II*. Univ. Arizona Press, pp. 524–556.
- Burbine, T.H., McCoy, T.J., Jaresowich, E., Sunshine, J.M., 2003. Deriving asteroid mineralogies from reflectance spectra: Implications for the MUSES-C target asteroid. *Antarc. Meteorite Res.* 16, 185–195.
- Burbine, T.H., Buchanan, P.C., Dolkar, T., Binzel, R.P., 2009. Pyroxene mineralogies of near-Earth Vestoids. *Meteorit. Planet. Sci.* 44, 1331–1341.
- Burns, R.G., 1970. *Mineralogical Applications of Crystal Field Theory*. Cambridge Univ. Press, 224pp.
- Burns, R.G., 1993. *Mineralogical Applications of Crystal Field Theory*, second ed. Cambridge Univ. Press, 551pp.
- Chapman C.R., Johnson, T.V., McCord, T.B., 1971. A review of spectrophotometric studies of asteroids. In: Gehrels, T. (Ed.), *Physical Studies of Minor Planets*. NASA SP-267, pp. 51–65.
- Clark, Beth.E., Helfenstein, P., Bell, J.F., Peterson, C., Veverka, J., Izenberg, N.I., Domingue, D., Wellnitz, D., McFadden, Lucy., 2002. Near infrared spectrometer photometry of Asteroid 433 Eros. *Icarus* 155, 189–204.
- Cloutis, E.A., Gaffey, M.J., Jackowski, T.L., Reed, K.L., 1986. Calibration of phase abundance, composition, and particle size distribution for olivine-orthopyroxene mixtures from reflectance spectra. *J. Geophys. Res.* 91, 11641–11653.
- Cloutis, E.A. et al., 2010. Spectral reflectance properties of ureilites. *Meteorit. Planet. Sci.* 45, 1668–1694.
- Cohen, M., Witteborn, F.C., Roush, T., Bregman, J., Wooden, D., 1998. Spectral irradiance calibration in the infrared. VIII. 5–14 micron spectroscopy of the Asteroids Ceres, Vesta, and Pallas. *Astron. J.* 115, 1671–1679.
- Cord, A.M., Pinet, P.C., Daydou, Y., Chevrel, S., 2003. Experimental investigation of the potential wavelength dependence of Hapke parameters in the visible and near infrared range. *Lunar Planet. Sci.* 28, Abstract 1548.
- Cushing, M.C., Vacca, W.D., Rayner, J.T., 2004. Spextool: A spectral extraction package for SpeX, a 0.8–5.5 micron cross-dispersed spectrograph. *Publ. Astron. Soc. Pacific* 116 (818), 362–376.
- Drummond, J.D., Fugate, R.Q., Christou, J.C., Hege, E.K., 1998. Full adaptive optics images of Asteroids Ceres and Vesta; rotational poles and triaxial ellipsoid dimensions. *Icarus* 132 (1), 80–99.
- French, L.M., Veverka, J., 1983. Limb darkening of meteorites and asteroids. *Icarus* 54 (April), 38–47.
- Gaffey, M.J., 1997. Surface lithologic heterogeneity of Asteroid 4 Vesta. *Icarus* 127, 130–157.
- Gaffey, M.J., 2003. Observational and data reduction techniques to optimize mineralogical characterizations of asteroid surface materials. *Lunar Planet. Sci.* XXXIV, Abstract #1602.
- Gaffey, M.J., 2005. The critical importance of data reduction calibration in the interpretability of S-type asteroid spectra. *Lunar Planet. Sci.* XXXIV, Abstract #1916.
- Gaffey, M.J., 2010. Space weathering and the interpretation of asteroid reflectance spectra. *Icarus* 209, 564–574.
- Gaffey, M.J., Bell, J.F., Brown, R.H., Burbine, T.H., Piatek, J.L., Reed, K.L., Chaky, D.A., 1993. Mineralogical variations within the S-type asteroid class. *Icarus* 106, 573–602.
- Gaffey, M.J., Cloutis, E.A., Kelley, M.S., Reed, K.L., 2002. Mineralogy of asteroids. In: Bottke, W.F., Cellino, A., Paolicchi, P., Binzel, R.P. (Eds.), *Asteroids III*. Univ. of Arizona Press, pp. 183–204.
- Gradie, J., Veverka, J., 1986. The wavelength dependence of phase coefficients. *Icarus* 66, 455–467.
- Gradie, J., Veverka, J., Buratti, B., 1980. The effects of scattering geometry on the spectrophotometric properties of powdered material. *Lunar Planet. Sci.* 11, 799–815.
- Hamilton, V.E., 2000. Thermal infrared emission spectroscopy of the pyroxene mineral series. *J. Geophys. Res.* 105, 9701–9716.
- Hapke, B., 1981. Bidirectional reflectance spectroscopy. 1. Theory. *J. Geophys. Res.* 86, 4571–4586.
- Hapke, B., 1984. Bidirectional reflectance spectroscopy. III – Correction for macroscopic roughness. *Icarus* 59, 41–59.
- Hapke, B., 1986. Bidirectional reflectance spectroscopy. IV – The extinction coefficient and the opposition effect. *Icarus* 67, 264–280.
- Hapke, B., 1990. Coherent backscatter and the radar characteristics of outer planet satellites. *Icarus* 88, 407–417.
- Hapke, B., 1993. *Theory of Reflectance and Emittance Spectroscopy*. Cambridge Univ. Press, Cambridge, UK.
- Hapke, Bruce W., Shepard, Michael K., Nelson, Robert M., Smythe, William D., Piatek, Jennifer L., 2009. A quantitative test of the ability of models based on the equation of radiative transfer to predict the bidirectional reflectance of a well-characterized medium. *Icarus* 199, 210–218.
- Hasegawa, S. et al., 2009. BRz' phase function of Asteroid 4 Vesta during the 2006 opposition. *Lunar Planet. Sci.* 40. ID. 1503.
- Hinrichs, J.L., Lucey, P.G., 2002. Temperature-dependent near-infrared spectral properties of minerals, meteorites, and lunar soil. *Icarus* 155, 169–180.
- Hinrichs, J.L., Lucey, P.G., Meibom, A., Krot, A.N., 1999. Temperature dependent near-infrared spectra of olivine and H5 ordinary chondrites. *Lunar Planet. Sci.* 30, Abstract 1505.
- Lagerkvist, C.I., Williams, I.P., 1987. Physical studies of asteroids. XV – Determination of slope parameters and absolute magnitudes for 51 asteroids. *Astron. Astrophys. Suppl. Ser.* 68, 295–315.
- Lagerkvist, C.-I., Magnusson, P., Williams, I.P., Buontempo, M.E., Argyle, R.W., Morrison, L.V., 1992. Physical studies of asteroids. XXIV – Phase relations for 48 asteroids obtained with the Carlsberg Meridian Circle. *Astron. Astrophys. Suppl. Ser.* 94, 43–71.
- Lane, Adair P., Irvine, William M., 1973. Monochromatic phase curves and albedos for the lunar disk. *Astron. J.* 78, 267–277.
- Li, J.-Y., McFadden, L.A., Thomas, P.C., Mutchler, M.J., Parker, J.Wm., Young, E.F., Russell, C.T., Sykes, M.V., Schmidt, B.E., 2010. Photometric mapping of Asteroid (4) Vesta's southern hemisphere with Hubble Space Telescope. *Icarus* 208, 238–251.
- Lovering, J.F., 1975. The Moama eucrite – A pyroxene-plagioclase adcumulate. *Meteoritics* 10, 101–114.
- Lucey, P.G., Hinrichs, J., Urquhart, M.L., Wellnitz, D., Izenberg, N., Murchie, S., Robinson, M., Clark, B.E., Bell, J.F., 2002. Detection of temperature-dependent spectral variation on the asteroid Eros and new evidence for the presence of an olivine-rich silicate assemblage. *Icarus* 155, 181–188.
- Lumme, K., Bowell, E., 1981a. Radiative transfer in the surfaces of atmosphereless bodies. I – Theory. II – Interpretation of phase curves. *Astron. J.* 86, 1694–1721.
- Lumme, K., Bowell, E., 1981b. Radiative transfer in the surfaces of atmosphereless bodies. II. Interpretation. *Astron. J.* 86, 1705–1721.
- Luu, J.X., Jewitt, D.C., 1990. Charge-coupled device spectra of asteroids. I. Near-Earth and 3:1 resonance asteroids. *Astron. J.* 99, 1985–2011.
- Mayne, Rhiannon G., Sunshine, Jessica M., McSween, Harry Y., McCoy, Timothy J., Corrigan, Catherine M., Gale, Allison, 2010. Petrologic insights from the spectra of the unbrecciated eucrites: Implications for Vesta and basaltic asteroids. *Meteorit. Planet. Sci.* 45, 1074–1092.
- McCord, T.B., Adams, J.B., Johnson, T.V., 1970. Asteroid Vesta: Spectral reflectivity and compositional implications. *Science* 168, 1445–1447.
- McFadden, L.A., McCord, T.B., Pieters, C., 1977. Vesta: The first pyroxene band from new spectroscopic measurements. *Icarus* 31, 439–446.
- Millis, R.L., Bowell, E., Thompson, D.T., 1976. UVB photometry of Asteroid 433 Eros. *Icarus* 28, 53–67.
- Moroz, L., Schade, U., Wäsch, R., 2000. Reflectance spectra of olivine-orthopyroxene bearing assemblages at decreased temperatures: Implications for remote sensing of asteroids. *Icarus* 147, 79–93.
- Moskovitz, N.A., Willman, M., Burbine, T.H., Binzel, R.P., Bus, S.J., 2010. A spectroscopic comparison of HED meteorites and V-type asteroids in the inner main belt. *Icarus* 208, 773–788.
- Nathues, A.N., 2000. *Spectroscopic Study of Eunomia Asteroid Family*, Ph.D. Dissertation, University of Berlin, Germany. 224pp.
- Nathues, A.N., 2010. Spectral study of the Eunomia asteroid family. Part II: The small bodies. *Icarus* 208, 252–275.
- Piatek, Jennifer L., Hapke, Bruce W., Nelson, Robert M., Smythe, William D., Hale, Amy Snyder, 2004. Scattering properties of planetary regolith analogs. *Icarus* 171, 531–545.
- Pieters, C.M., 1983. Strength of mineral absorption features in the transmitted component of near-infrared reflected light: First results from RELAB. *J. Geophys. Res.* 88, 9534–9544.
- Piironen, J., Magnusson, P., Lagerkvist, C.-I., Williams, I.P., Buontempo, M.E., Morrison, L.V., 1997. Physical studies of asteroids. XXXI. Asteroid photometric observations with the Carlsberg Automatic Meridian Circle. *Astron. Astrophys. Suppl. Ser.* 121, 489–497.
- Rayner, J.T. et al., 2003. SpeX: A medium-resolution 0.8–5.5 micron spectrograph and imager for the NASA Infrared Telescope Facility. *Publ. Astron. Soc. Pacific* 115, 362–382.
- Reddy, V., 2009. *Mineralogical Survey of Near-Earth Asteroid Population: Implications for Impact Hazard Assessment and Sustainability of Life on Earth*, Ph.D. Dissertation. University of North Dakota, Grand Forks. 355pp.
- Reddy, V., Hardersen, P.S., Gaffey, M.J., Abell, P.A., 2005. Temperature and Phase Angle-induced Spectral Effects on A- and S-type Asteroids. Asteroids, Comets, Meteors Conference, IAU Symposium No. 229. Brazil.
- Reddy, V., Gaffey, M.J., Kelley, M.S., Nathues, A., Li, J.-Y., Yarbrough, R., 2010. Compositional heterogeneity of Asteroid 4 Vesta's Southern Hemisphere: Implications for the Dawn mission. *Lunar Planet. Sci.* 41 (LPI Contribution No. 1373).

- Rosenbush, Vera., Kiselev, Nikolai., Avramchuk, Viktor., 2006. Similarity and diversity in photometric and polarimetric opposition effects of small Solar System bodies. *J. Quant. Spectrosc. Radiat. Transfer* 100, 325–339.
- Saksena, B.D., 1961. Infra-red absorption studies of some silicate structures. *Trans. Faraday Soc.* 57, 242–258.
- Schade, U., Wäsch, R., 1999. Near-infrared reflectance spectra from bulk samples of the two SNC meteorites Zagami and Nakhla. *Meteorit. Planet. Sci.* 34, 417–424.
- Shkuratov, Iu.G., 1988. A diffraction mechanism for the formation of the opposition effect of the brightness of surfaces having a complex structure. *Kinematika i Fizika Nebesnykh Tel* 4, 33–39.
- Sierks, H. et al., 2011. The Dawn Framing Camera. *Space Sci. Rev.* doi:10.1007/s11214-011-9745-4.
- Singer, R.B., Roush, T.L., 1985. Effects of temperature on remotely sensed mineral absorption features. *J. Geophys. Res.* 90, 12434–12444.
- Sunshine, J.M., Pieters, C.M., 1993. Estimating modal abundances from the spectra of natural and laboratory pyroxene mixtures using the Modified Gaussian Model. *J. Geophys. Res.* 98, 9075–9087.
- Sunshine, J.M., Bus, S.J., McCoy, T.J., Burbine, T.H., Corrigan, C.M., Binzel, R.P., 2004. High-calcium pyroxene as an indicator of igneous differentiation in asteroids and meteorites. *Meteorit. Planet. Sci.* 39, 1343–1357.
- Thomas, P.C. et al., 1996. Vesta: Spin Pole, Size and Shape from HST Images. *Workshop on Evolution of Igneous Asteroids: Focus on Vesta and the HED Meteorites*, p. 32.
- Thomas, P.C., Binzel, R.P., Gaffey, M.J., Zellner, B.H., Storrs, A.W., Wells, E., 1997. Vesta: Spin pole, size, and shape from HST images. *Icarus* 128, 88–94.
- Warner, B., 2006. *A Practical Guide to Lightcurve Photometry and Analysis*, second ed. Springer Science + Business Media.
- Yon, S.A., Pieters, C.M., 1988. Interactions of light with rough dielectric surfaces: Spectral reflectance and polarimetric properties. *Proc. Lunar Sci. Conf.* 18, 581–592.
- Zellner, B., Binzel, R., Gaffey, M., Thomas, P., Storrs, A., Wells, E.N., 1996. HST Images of Vesta near Perihelion. *American Astronomical Society, DPS Meeting #28*, vol. 28, p. 1100.



Note

Composition of near-Earth Asteroid (4179) Toutatis

Vishnu Reddy^{a,b,*,1}, Juan A. Sanchez^c, Michael J. Gaffey^{a,1}, Paul A. Abell^{d,1}, Lucille Le Corre^{b,1}, Paul S. Hardersen^{a,1}

^a Department of Space Studies, University of North Dakota, Grand Forks, ND 58202, USA

^b Max Planck Institute for Solar System Research, Katlenburg-Lindau 37191, Germany

^c Institut für Planetologie, University of Münster, 48149 Münster, Germany

^d Astromaterials Research & Exploration Science Directorate, NASA Johnson Space Center, Mail Code KR, 2101 NASA Parkway, Houston, TX 77058-3696, USA

ARTICLE INFO

Article history:

Received 24 September 2012

Revised 9 October 2012

Accepted 9 October 2012

Available online 23 October 2012

Keywords:

Asteroids

Asteroids, Composition

Spectroscopy

Meteorites

Infrared observations

ABSTRACT

Surface composition of near-Earth Asteroid (4179) Toutatis is consistent with an undifferentiated L-chondrite composition. This is inconsistent with early observations that suggested high pyroxene iron content and a differentiated body.

© 2012 Elsevier Inc. All rights reserved.

1. Introduction

Near-Earth Asteroid (NEA) (4179) Toutatis is an Apollo asteroid that has been the focus of several ground-based observational campaigns using different remote sensing techniques (photometry, spectroscopy and radar). One of the first studies of Toutatis was conducted by Spencer et al. (1995), who generated phase curves using the IAU H, G system developed by Bowell et al. (1989). From these photometric data, they obtained a mean H of 15.3 and a slope parameter G of 0.10 for the asteroid. From Toutatis' lightcurve, Spencer et al. (1995) determined that the asteroid has a complex rotation with a period between 3 and 7.3 days. Hudson and Ostro (1995), used radar observations to reconstruct Toutatis' shape and spin state. They found that Toutatis has an irregular two-lobes shape, whose dimensions along the principal axes are 1.92, 2.40 and 4.60 km. This study showed that Toutatis has a non-principal axis rotation. The rotation period around its long axis ($P\psi$) was found to be 5.41 days, with an average of 7.35 days for the long-axis precession period ($P\phi$). These numbers were slightly refined by Ostro et al. (1999), who found values of $P\psi = 5.37$ and $P\phi = 7.42$. These results were later confirmed by the findings of Mueller et al. (2002).

Hudson and Ostro (1998) combined the data from Spencer et al. (1995), and Hudson and Ostro (1995) to estimate the Hapke parameters (see e.g., Hapke, 1981, 1993) of Toutatis. They found a particle single-scattering albedo $w = 0.261 \pm 0.019$, opposition surge width $h = 0.036 \pm 0.023$, a particle phase function asymmetry factor $g = -0.29 \pm 0.06$, an amplitude $B_0 = 1.20 \pm 0.32$, and macro-

scopic roughness parameter $\theta = 32 \pm 8^\circ$. The analysis of Hudson and Ostro (1998) indicated that a fine regolith layer covers a large part of the surface of Toutatis. Howell et al. (1994), obtained spectroscopic and spectrophotometric data (0.5–3.35 μm) of Toutatis during its opposition on January 1993. They found that the spectrum of Toutatis exhibits a pyroxene absorption band centered at 1.966 μm . The VIS spectrum of Toutatis indicated that the Band I center is located at wavelengths longer than 0.96 μm , suggesting the presence of some olivine. Based on the work of Adams (1974), and from the measured band centers of Toutatis, Howell et al. (1994) determined that its average pyroxene composition was $\text{Fs}_{45-55}\text{En}_{50-35}\text{Wo}_{5-10}$. After applying the thermophysical model to the 3- μm spectral region of Toutatis, Howell et al. (1994) found a thermal inertia of $3-8 \times 10^5 \text{ erg cm}^{-2} \text{ K}^{-1} \text{ s}^{-1/2}$, a geometrical albedo ≥ 0.20 , a beaming parameter ≥ 0.9 , an emissivity ≥ 0.9 , and a phase coefficient in the range of 0.005–0.01.

Additional spectral data of Toutatis were obtained by Davies et al. (2007), who acquired NIR spectra (1.0–2.5 μm) with the UKIRT telescope over a wide range of phase angles (0.7–81°). These observations were intended to seek evidence for phase reddening and to search for possible surface variations with rotational phase. However, within the uncertainties of their data neither phase reddening nor surface heterogeneities were detected. In this work we present detailed compositional analysis of Toutatis and constrain its surface mineralogy. Our interest in this object is heightened by the possibility of a flyby by the Chinese lunar spacecraft Chang'e 2 on December 13, 2012 (Li et al., 2012). Although no official confirmation of this event is available, optical astrometry of the Chang'e 2 spacecraft strongly support such an event.

2. Observations and data reduction

Observations of (4179) Toutatis were obtained remotely with the SpeX instrument (Rayner et al., 2003) on the NASA IRTF, Mauna Kea, Hawai'i. The NIR spectra (~0.7–2.5 μm) were acquired using SpeX in low-resolution ($R \sim 150$) prism mode with a 0.8" slit width. The asteroid was observed on August 13, 2008 when its V-mag was 14.8. To correct for telluric water vapor features, and to obtain the relative

* Corresponding author at: Max-Planck Institute for Solar System Research, Katlenburg-Lindau 37191, Germany.

E-mail address: reddy@space.edu (V. Reddy).

¹ Visiting Astronomer at the Infrared Telescope Facility, which is operated by the University of Hawaii under Cooperative Agreement No. NNX-08AE38A with the National Aeronautics and Space Administration, Science Mission Directorate, Planetary Astronomy Program.

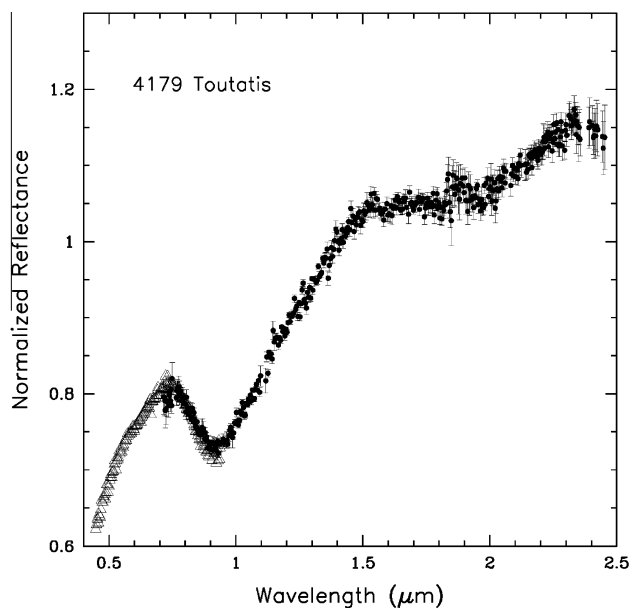


Fig. 1. NIR spectrum of 4179 Toutatis (solid circles) obtained with the SpeX instrument on NASA IRTF. The spectrum exhibits the two absorption bands characteristic of olivine–pyroxene assemblages. The visible spectrum of Toutatis (open triangles) was taken from the SMASS survey (Bus and Binzel, 2002a,b).

reflectance, standard and solar analog stars were observed at similar air masses as the asteroid. Flat fields and lamp spectra were also acquired. SpeX prism data were processed using the IDL-based Sxtool provided by the NASA IRTF (Cushing et al., 2004). Detailed description of data reduction procedure is available in Reddy et al. (2012).

3. Analysis

The near-IR spectrum of Toutatis is shown in Fig. 1 (solid circles). This spectrum exhibits two absorption bands characteristics of olivine–orthopyroxene assemblages, and it is consistent with previous observations of this asteroid (e.g., Davies et al., 2007; Dunn and Burbine, 2012). In order to extend the wavelength range we combined our NIR spectrum of Toutatis with its visible spectrum (Fig. 1, open triangles) obtained by the SMASS survey (Bus and Binzel, 2002a,b). Spectral band parameters, band centers, band depths, and band area ratio (BAR) were measured in the same way as in Sanchez et al. (2012). BAR is the ratio of area of Band II to that of Band I. Temperature corrections to Band II center; Band II depth and BAR were applied using the equations from Sanchez et al. (2012). No corrections were applied for Band I center. Olivine and pyroxene chemistries were determined using the spectral calibrations derived by Dunn et al. (2010a). Toutatis has a Band I center of $0.94 \pm 0.01 \mu\text{m}$, a Band II center of $1.98 \pm 0.03 \mu\text{m}$ and a BAR of 0.5 ± 0.05 . The absorption bands themselves have band depths of $15 \pm 0.3\%$ (Band I) and $4 \pm 0.5\%$ (Band II). The Band I center of Toutatis is longer than what is normally expected for pure low calcium pyroxene ($0.90\text{--}0.93 \mu\text{m}$). This would suggest the presence of a second pyroxene phase like high calcium pyroxene (Band I center range $0.91\text{--}1.06 \mu\text{m}$). The Band II center of Toutatis ($1.98 \pm 0.03 \mu\text{m}$) is consistent with those of low calcium ($1.8\text{--}2.1 \mu\text{m}$) and high calcium pyroxenes ($1.97\text{--}2.35 \mu\text{m}$). Spectral band parameters and mineral chemistry values are presented in Table 1. A side lobe at $1.3 \mu\text{m}$ suggests the possible presence of olivine, which can also affect the Band I center and cause it to shift to longer wavelengths.

Fig. 2A shows a close up of the S(IV) region of the Gaffey S-asteroid subtypes. The measured Band I center and BAR of Toutatis are depicted as a filled triangle. Based on these band parameters, Toutatis is classified as S(IV) in the system of Gaffey et al. (1993), which is consistent with an ordinary chondrite-like composition for this asteroid. The dotted line shows the olivine–orthopyroxene (low calcium pyroxene) mixing line and Toutatis band parameters are offset from it to the left, which is an indication for the presence of high calcium pyroxene in the surface.

The asteroid plots at the boundary between H and L chondrites within the S(IV) region.

Pyroxene and olivine abundance and chemistry can be used to constrain the surface composition and identify meteorite analogs. Using equations from Dunn et al. (2010a) we calculate the olivine and pyroxene chemistry to be $\text{Fa}_{20 \pm 1.3}$ ($\text{Fo}_{80 \pm 1.3}$) and $\text{Fs}_{17 \pm 1.4}$, respectively. The ratio of olivine in a mixture of olivine and pyroxene is 0.61 ± 0.03 . These values are within the olivine and pyroxene chemistry ranges derived by Dunn et al. (2010a,b) for H ($\text{Fa}_{15\text{--}21}$ and $\text{Fs}_{13\text{--}19}$) and L ($\text{Fa}_{21\text{--}27}$ and $\text{Fs}_{17\text{--}23}$) chondrites. Independent olivine chemistry ($\text{Fa}_{22\text{--}26}$) and abundance ($0.53\text{--}0.66$) estimates by Dunn and Burbine (2012) using a different set of observations are also consistent with our values ($\text{Fa}_{20 \pm 1.3}$ and 0.61 ± 0.03). However, their values are more consistent with an L/LL chondrite type assemblage compared to H/L type from our data. This discrepancy could be attributed to the use of a different technique when calculating the band parameters. Combining Dunn and Burbine (2012) with our olivine and pyroxene chemistry and abundance values we get mean values of $\text{Fa}_{23 \pm 1.3}$, $\text{Fs}_{19.5 \pm 1.4}$ and 0.60 ± 0.03 , respectively. These values are consistent with an L chondrite type surface assemblage, which we think is the best analog for Toutatis' surface.

However, pyroxene chemistry values ($\text{Fs}_{45\text{--}55}$) estimated by Howell et al. (1994) are inconsistent with our values ($\text{Fs}_{19.5 \pm 1.4}$). Based on this high ferrosilite content ($\text{Fs}_{45\text{--}55}$), Howell et al. (1994) suggested Toutatis parent body “had considerable differentiation of the silicates.” We believe these differences are primarily due to incomplete spectral coverage of the Band I and II features in their data, unavailability of thermal correction equations of band parameters (Sanchez et al., 2012), and the lack of robust laboratory calibration for determining mineral chemistry (Dunn et al., 2010a) at that time. Fig. 2B shows the molar contents of Fa vs. Fs for Toutatis (filled square), along with the values for LL (open triangles), L (open circles) and H (\times symbols) ordinary chondrites from Nakamura et al. (2011). As with Fig. 2A, Toutatis plots in the boundary region between H and L chondrites consistent with olivine and pyroxene chemistries and abundance calculated from our observations.

4. Discussion

Surface composition of Toutatis is consistent with an L chondrite type assemblage based on the mean olivine and pyroxene chemistry and the abundance of olivine. Toutatis' olivine and pyroxene chemistries are similar to those of (433) Eros (Fa_{20} and Fs_{24}), the target of the NEAR mission (Izenberg et al., 2003). However, the olivine abundance is higher on Eros ($0.65\text{--}0.69$) compared to Toutatis (0.60). Typically increasing olivine abundance is a sign of increasing oxidation where L and LL chondrites (which are more oxidized) have higher olivine abundance ($0.52\text{--}0.72$) than H chondrites ($0.44\text{--}0.62$) (Dunn et al., 2010b). Oxygen isotope analysis also shows that H, L and LL chondrites formed on different parent bodies (Clayton, 1993).

Nesvorný et al. (2009) suggested the Gefion family is the source of L chondrites based on dynamical modeling. The formation of this family is also linked to the influx of L chondrite meteorites to the Earth as evident from fossil meteorites discovered in limestone quarry in southern Sweden that all date ~ 467 myr. A majority of the L chondrites in our terrestrial meteorite collection are heavily shocked and have $^{39}\text{Ar}\text{--}^{40}\text{Ar}$ age near 470 myr (Korochantseva et al., 2007). This suggests a major impact event on the L chondrite parent body ~ 470 myr ago that led to the formation of the Gefion family (Nesvorný et al., 2009). If Toutatis was formed as part of the Gefion family, it was transported to the 5:2 resonance with Jupiter (Nesvorný et al., 2009) via Yarkovsky effect and then to near-Earth space more recently (few million years). This is because the collisional lifetime of the NEA is much shorter (few tens of millions of years) than the age of the Gefion family (470 myr) (Bottke et al., 2005). Cosmic ray exposure (CRE) ages of L chondrites suggest that they were spalled off their parent body (in the main belt or near-Earth asteroid population) on two occasions (~ 28 and ~ 40 myr). It is possible that some L chondrites in our terrestrial collection were spalled off Toutatis as meter-sized objects during those events, although these events are at the limits of NEA lifetimes in the inner Solar System.

Ostro et al. (1999) suggested that 1/3rd of Toutatis' surface was covered by a ‘smooth component’ or regolith with porosity of lunar soils. They argued that if the surface composition of Toutatis was like an ordinary chondrite, then this smooth component is a solid layer with no “more than a centimeter of overlying regolith” (Ostro et al., 1999). The shape derived from radar observations, along with its surface regolith properties and mineralogy suggests that Toutatis' surface would be similar to that of (25143) Itokawa, which was studied by the Hayabusa spacecraft. Our observations and predictions about Toutatis' surface properties would be confirmed if the Chang'e-2 spacecraft makes a successful flyby of Toutatis.

Table 1
Spectral band parameters, ol/(ol + px) ratio, and olivine and pyroxene chemistry for 4179 Toutatis.

Band I center (μm)	Band II center (μm)	Band I depth (%)	Band II depth (%)	Band area ratio	Olivine (olv + pyx)	Fayalite (mol%)	Ferrosilite (mol%)
0.94 ± 0.01	1.98 ± 0.03	15 ± 0.3	4 ± 0.5	0.5 ± 0.05	0.61 ± 0.03	20.2 ± 1.3	17.4 ± 1.4

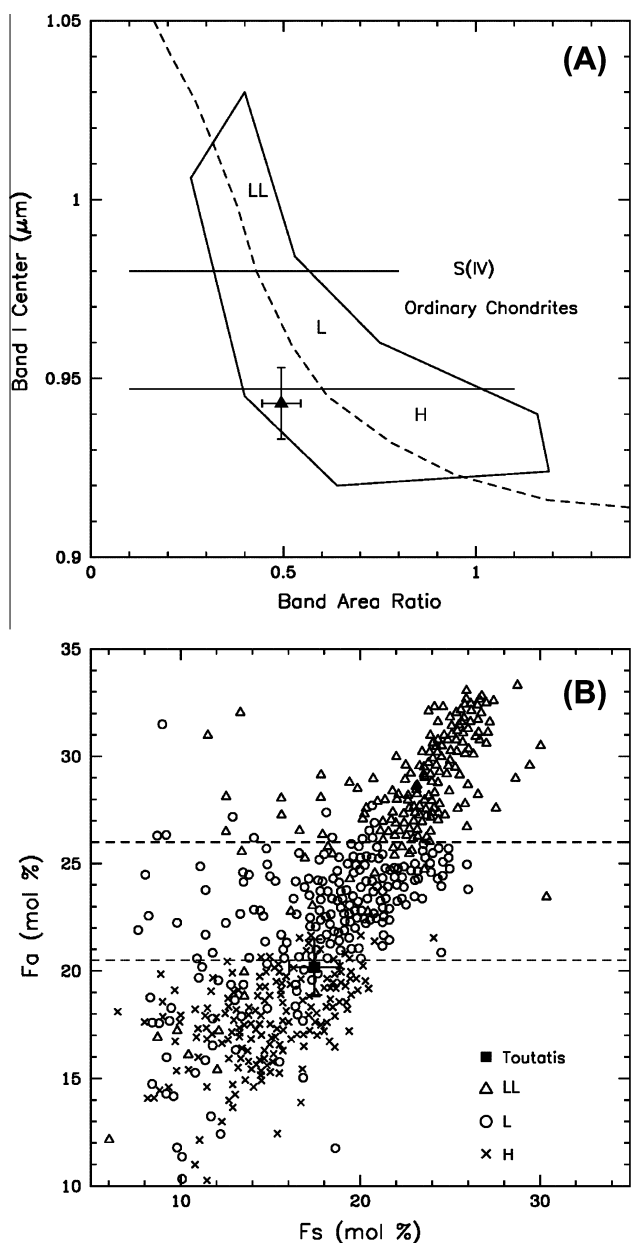


Fig. 2. (A) Plot of the Band I center vs. BAR for 4179 Toutatis (filled triangle). The polygonal region corresponding to the S(IV) subgroup represents the mafic silicate components of ordinary chondrites (Gaffey et al., 1993). The dashed curve indicates the location of the olivine–orthopyroxene mixing line (Cloutis et al., 1986). The horizontal lines represent the approximate boundaries for LL, L, and H ordinary chondrites found by Dunn et al. (2010a). (B) Molar contents of Fa vs. Fs for 4179 Toutatis (filled square) calculated using the spectral calibrations of Dunn et al. (2010a). For comparison, values for LL (open triangles), L (open circles) and H (×) ordinary chondrites from Nakamura et al. (2011) are also shown. The horizontal dashed-lines represent the approximate boundaries for LL, L, and H ordinary chondrites.

Acknowledgments

This research was supported by NASA NEOO Program Grant NNX12AG12G, and NASA Planetary Geology and Geophysics Grant NNX11AN84G. We thank the IRTF TAC for awarding time to this project, and to the IRTF TOs and MKSS staff for their support. The authors would like to thank Tasha Dunn and an anonymous reviewer for their helpful reviews to improve the manuscript.

References

Adams, J.B., 1974. Visible and near infrared diffuse reflectance spectra of pyroxenes as applied to remote sensing of solid objects in the solar system. *J. Geophys. Res.* 79, 4829–4836.

Bottke, W.F., Durda, D., Nesvorný, D., Jedicke, R., Morbidelli, A., Vokrouhlický, D., Levison, H.F., 2005. Linking the collisional history of the main asteroid belt to its dynamical excitation and depletion. *Icarus* 179, 63–94.

Bowell, E., Hapke, B., Domingue, D., Lumme, K., Peltoniemi, J., Harris, A.W., 1989. Application of photometric models to asteroids. In: Binzel, R.P., Gehrels, T., Matthews, M.S. (Eds.), *Asteroids II*. Univ. Arizona Press, pp. 524–556.

Bus, S.J., Binzel, R.P., 2002a. Phase II of the small main-belt asteroid spectroscopic survey a feature-based taxonomy. *Icarus* 158, 146–177.

Bus, S.J., Binzel, R.P., 2002b. Phase II of the small main-belt asteroid spectroscopic survey the observations. *Icarus* 158, 106–145.

Clayton, R.N., 1993. Oxygen isotopes in meteorites. *Annu. Rev. Earth Planet. Sci.* 21, 115–149.

Cloutis, E.A., Gaffey, M.J., Jackowski, T.L., Reed, K.L., 1986. Calibrations of phase abundance, composition, and particle size distribution for olivine–orthopyroxene mixtures from reflectance spectra. *J. Geophys. Res.* 91, 11641–11653.

Cushing, M.C., Vacca, W.D., Rayner, J.T., 2004. Spextool: A spectral extraction package for SpeX, a 0.8–5.5 micron cross-dispersed spectrograph. *Publ. Astron. Soc. Pacific* 116 (818), 362–376.

Davies, John K., Harris, Alan W., Rivkin, Andrew S., Wolters, Stephen D., Green, Simon F., McBride, Neil, Mann, Rita K., Kerr, Tom H., 2007. Near-infrared spectra of 12 near-Earth objects. *Icarus* 186, 111–125.

Dunn, T.L., Burbine, T.H., 2012. Mineralogies of near Earth asteroids. *Lunar Planet. Sci.* 43, March 19–23, 2012, The Woodlands, Texas. LPI Contribution No. 1659, ID 2305.

Dunn, T.L., McCoy, T.J., Sunshine, J.M., McSween, H.Y., 2010a. A coordinated spectral, mineralogical, and compositional study of ordinary chondrites. *Icarus* 208, 789–797.

Dunn, T.L., McSween Jr., H.Y., McCoy, T.J., Cressy, G., 2010b. Analysis of ordinary chondrites using powder X-ray diffraction: 2. Applications to ordinary chondrite parent-body processes. *Meteorit. Planet. Sci.* 45, 135–156.

Gaffey, M.J., Burbine, T.H., Piatek, J.L., Reed, K.L., Chaky, D.A., Bell, J.F., Brown, R.H., 1993. Mineralogical variations within the S-type asteroid class. *Icarus* 106, 573–602.

Hapke, B., 1981. Bidirectional reflectance spectroscopy: I – Theory. *J. Geophys. Res.* 86, 3039–3054.

Hapke, B., 1993. *Theory of Reflectance and Emittance Spectroscopy*. Cambridge University Press, Cambridge, UK.

Howell, E.S., Britt, D.T., Bell, J.F., Binzel, R.P., Lebofsky, L.A., 1994. Visible and near-infrared spectral observations of 4179 Toutatis. *Icarus* 111, 468–474.

Hudson, R.S., Ostro, S.J., 1995. Shape and non-principal-axis spin state of Asteroid 4179 Toutatis. *Science* 270, 84–86.

Hudson, R.S., Ostro, S.J., 1998. Photometric properties of Asteroid 4179 Toutatis from lightcurves and a radar-derived physical model. *Icarus* 135, 451–457.

Izenberg, N.R. et al., 2003. Spectral properties and geologic processes on Eros from combined NEAR NIS and MSI data sets. *Meteorit. Planet. Sci.* 38, 1053–1077.

Korochantseva, E.V. et al., 2007. L-chondrite asteroid breakup tied to Ordovician meteorite shower by multiple isochron 40Ar–39Ar dating. *Meteorit. Planet. Sci.* 42, 113–130.

Li, M., Zheng, J., Liu, X., 2012. Low energy trajectory optimization for CE-2’s extended mission after 2012. *International Astronautical Congress*, Abstract IAC-12,C1,5,12,x15724.

Mueller, Béatrice E.A., Samarasinha, Nalin H., Belton, Michael J.S., 2002. The diagnosis of complex rotation in the lightcurve of 4179 Toutatis and potential applications to other asteroids and bare cometary nuclei. *Icarus* 158, 305–311.

Nakamura, T. et al., 2011. Itokawa dust particles: A direct link between S-type asteroids and ordinary chondrites. *Science* 333, 1113–1116.

Nesvorný, D., Vokrouhlický, D., Morbidelli, A., Bottke, W.F., 2009. Asteroidal source of L chondrite meteorites. *Icarus* 200 (2), 698–701.

Ostro, S.J., Hudson, R.S., Rosema, K.D., Giorgini, J.D., Jurgens, R.F., Yeomans, D.K., Chodas, P.W., Winkler, R., Rose, R., Choate, D., Cormier, R.A., Kelley, D., Littlefair, R., Benner, L.A.M., Thomas, M.L., Slade, M.A., 1999. Asteroid 4179 Toutatis: 1996 radar observations. *Icarus* 137, 122–139.

Rayner, J.T. et al., 2003. SpeX: A medium-resolution 0.8–5.5 micron spectrograph and imager for the NASA Infrared Telescope Facility. *Publ. Astron. Soc. Pacific* 115, 362–382.

Reddy, V., Sanchez, J.A., Nathues, A., Moskovitz, N.A., Li, J.-Y., Cloutis, E.A., Archer, K., Tucker, R.A., Gaffey, M.J., Mann, P.J., Sierks, H., Schade, U., 2012. Photometric, spectral phase and temperature effects on 4 Vesta and HED meteorites: Implications for the Dawn mission. *Icarus* 217, 153–168.

Sanchez, J.A., Reddy, V., Nathues, A., Cloutis, E.A., Mann, P., Hiesinger, H., 2012. Phase reddening on near-Earth asteroids: Implications for mineralogical analysis, space weathering and taxonomic classification. *Icarus* 220, 36–50.

Spencer, J.R. et al., 1995. The lightcurve of 4179 Toutatis: Evidence for complex rotation. *Icarus* 117, 71–89.



Surface composition and taxonomic classification of a group of near-Earth and Mars-crossing asteroids

Juan A. Sanchez^{a,*}, René Michelsen^c, Vishnu Reddy^{b,1}, Andreas Nathues^c

^a Institut für Planetologie, Westfälische Wilhelms-Universität Münster, Germany

^b Department of Space Studies, University of North Dakota, Grand Forks, ND 58202, USA

^c Max Planck Institut für Sonnensystemforschung, Max Planck Str. 2, 37191 Katlenburg-Lindau, Germany

ARTICLE INFO

Article history:

Received 2 November 2012

Revised 3 February 2013

Accepted 15 February 2013

Available online 1 April 2013

Keywords:

Asteroids

Near-Earth objects

Spectroscopy

Infrared observations

Meteorites

ABSTRACT

In the past, constraining the surface composition of near-Earth asteroids (NEAs) has been difficult due to the lack of high quality near-IR spectral data (0.7–2.5 μm) that contain mineralogically diagnostic absorption bands. Here we present visible (~ 0.43 – $0.95 \mu\text{m}$) and near-infrared (~ 0.7 – $2.5 \mu\text{m}$) spectra of nine NEAs and five Mars-crossing asteroids (MCs). The studied NEAs are: 4055 Magellan, 19764 (2000 NF5), 89830 (2002 CE), 138404 (2000 HA24), 143381 (2003 BC21), 159609 (2002 AQ3), 164121 (2003 YT1), 241662 (2000 KO44) and 2007 ML13. The studied MCs are: 1656 Suomi, 2577 Litva, 5407 (1992 AX), 22449 Ottijeff and 47035 (1998 WS). The observations were conducted with the NTT at La Silla, Chile, the 2.2 m telescope at Calar Alto, Spain, and the IRTF on Mauna Kea, Hawai'i. The taxonomic classification (Bus system) of asteroids showed that all observed MC asteroids belong to the S-complex, including the S, Sr and Sl classes. Seven of the NEAs belong to the S-complex, including the S, Sa, Sk and Sl classes, and two NEAs were classified as V-types. The classification of the NEA 164121 (2003 YT1) as a V-type was made on the basis of its near-infrared spectrum since no visible spectrum is available for this asteroid. A mineralogical analysis was performed on six of the asteroids (those for which near-IR spectra were obtained or previously available). We found that three asteroids (241662 (2000 KO44), 19764 (2000 NF5), 138404 (2000 HA24)) have mafic silicate compositions consistent with ordinary chondrites, while three others (4055 Magellan, 164121 (2003 YT1), 5407 (1992 AX)) are pyroxene-dominated basaltic achondrite assemblages. In the case of 5407 (1992 AX) we found that its basaltic surface composition contrasts its taxonomic classification as a S-type.

© 2013 Elsevier Inc. All rights reserved.

1. Introduction

Among the small body population, near-Earth asteroids (NEAs) are defined as asteroids having perihelion distances of ≤ 1.3 AU. The NEA population shows a great diversity in terms of taxonomic classification, including almost all classes of asteroids found in the main belt (Binzel et al., 2002). However, of all taxonomic types, S-complex asteroids are the dominant class among NEAs. This high proportion of S-complex is caused in part by a selection effect, due to the fact that S-complex asteroids have higher albedos than C-types (the dominant class among all main-belt asteroids),

making them easier to discover. In addition, there are some regions in the main belt that contribute more than others to the delivery of objects into the inner Solar System. According to some dynamical models (e.g., Morbidelli and Nesvorný, 1999; Bottke et al., 2000, 2002; Morbidelli et al., 2002), the 3:1 mean-motion resonance with Jupiter (occurring at ~ 2.5 AU), and the ν_6 secular resonance at the inner asteroid belt (where S-complex are most common) provide the most significant fraction of objects to the near-Earth population.

Based on their orbital parameters NEAs are divided into three subgroups called Amor, Apollo, and Aten asteroids (Shoemaker et al., 1979). Some of these objects are also classified as potentially hazardous asteroids (PHAs), which are defined as objects whose minimal orbital intersection distance (MOID) with Earth is ≤ 0.05 AU. In addition to this dynamical classification, there is another group of objects called Mars-crossing asteroids (MCs), whose orbits cross or approach that of Mars, and are characterized by perihelion distances $1.30 < q < 1.66$ AU. Similarly to NEAs, the MC population is dominated by S-complex asteroids (Angeli and Lazzaro, 2002; Binzel et al., 2004). With time, MCs can eventually

* Corresponding author. Address: Max Planck Institut für Sonnensystemforschung, Max Planck Str. 2, 37191 Katlenburg-Lindau, Germany.

E-mail address: sanchez@mps.mpg.de (J.A. Sanchez).

¹ Visiting Astronomer at the Infrared Telescope Facility, which is operated by the University of Hawaii under Cooperative Agreement No. NNX-08AE38A with the National Aeronautics and Space Administration, Science Mission Directorate, Planetary Astronomy Program.

become NEAs as a result of close approaches with Mars, that move them into a resonance, and from there, to the near-Earth space (Michel et al., 2000).

NEAs are of great interest for study, and due to their proximity they could be the source of some of the meteorites found on Earth. Thus, establishing links between the spectral properties of NEAs and those measured in the laboratory for meteorite samples is fundamental to determine their possible parent bodies (Burbine et al., 2002; Binzel et al., 2002). Recent studies show that about 2/3 of the observed NEAs have surface compositions consistent with LL chondrites, which represent only about 10% of the ordinary chondrites falls (Vernazza et al., 2008; de León et al., 2010; Dunn et al., 2013). These results contradict the general assumption that the spectral characteristics of the most common type of NEAs should be consistent with those of the most common meteorites to fall on Earth. The reason for this discrepancy still remains unclear.

NEAs are also interesting for study because they are relatively easy to reach compared to their counterparts in the main belt. Some NEAs have low velocities with respect to Earth (ΔV), which make them especially accessible for sample-return and manned missions (e.g., Sears et al., 2000; Abell et al., 2009; Reddy et al., 2012a). Furthermore, it is now recognized the threat that some NEAs could represent for civilization in the eventuality of collision (e.g., Chapman and Morrison, 1994; Morrison et al., 2002). Hence, having a better understanding of their physical properties could help us to develop mitigation strategies in the future.

In this work we report visible (VIS) and near-infrared (NIR) spectroscopic observations of five MCs and nine NEAs. Although limited, our sample is diverse and comprises both basaltic an ordinary chondrite-like asteroids. Furthermore, three objects are classified as PHAs and one object is considered as a possible target for robotic and manned missions. Thus, the present work seeks to obtain new compositional information that could help tracing the origin of some meteorites, contribute in planning future robotic and manned missions, and contribute in the development of mitigation strategies. In addition, one of the goals of this paper is to study the compositional trend in the MC population and compare it with the NEA population. This will help us understand the source regions from which the NEAs are derived, and if the same compositional types dominate both populations. This is a preliminary study since our current sample is small. The selection of these particular asteroids for study was influenced by different factors that limit the number of objects that can be observed for a certain period of time. Magnitude limitations imposed by the telescope size,

the zenith distance of the asteroids at the time of the observations (i.e., in order to minimize distortion from atmospheric extinction the asteroid must be observed at rather small airmass <1.5), and the proximity of the targets to the galactic plane, are among the factors that normally reduce an initial list of several tens of targets to only a few of them. In Section 2 we describe the observations and data reduction procedure. In Section 3 we present the results, including the taxonomic classification and mineralogical analysis of the asteroids. In Section 4, we present and summarize our conclusions.

2. Observations and data reduction

2.1. Visible spectra

The VIS spectroscopic observations were conducted with the New Technology Telescope (NTT) at La Silla, Chile on August 2010, and with the 2.2 m telescope at Calar Alto, Spain, on October 2010.

The VIS spectra obtained with the NTT were acquired using the EFOSC2 spectrograph, equipped with a 2048×2048 pixels Loral/Lesser CCD (detector # 40), with a pixel size of $15 \mu\text{m}$, corresponding to $0.12''/\text{pixel}$. The disperser element used was the Grism #1 with a $5''$ slit width, providing an effective wavelength range of $\sim 0.43\text{--}0.95 \mu\text{m}$. The spectrograph used with the 2.2 m telescope was CAFOS. Due to a technical problem two different detectors were used during the observing run at Calar Alto. The first two nights (October 05 and 06) the Lor#11i $2 \text{ k} \times 2 \text{ k}$ chip (pixel size of $15 \mu\text{m}$) was used. During the last night (October 07), data were acquired with the SITE-1d $2 \text{ k} \times 2 \text{ k}$ chip ($24 \mu\text{m}$ pixel, i.e., $0.53''/\text{pixel}$). This is the standard CCD for CAFOS. The disperser element was the Grism R-400 with a $5''$ slit width. The covered wavelength range is $\sim 0.5\text{--}0.92 \mu\text{m}$.

Asteroid spectra were acquired using a nodding technique in which the object is alternated between two different slit positions (A and B) following the sequence ABBA. During the observations the slit was oriented along the parallactic angle in order to minimize the effects of differential atmospheric refraction. To obtain the relative reflectance, solar analog stars were observed at similar air masses as the asteroids. For each night, flat fields, bias and arc line spectra were acquired. Observational circumstances for the studied objects are presented in Table 1.

The NTT is capable of differential tracking, however previous studies found that for exposure times longer than ~ 10 min, NEAs

Table 1
Observational circumstances. The columns in this table are: object number and designation, orbit, UT date, telescope and instrument used, number of exposures, phase angle (α), V-magnitude at the time of observation, air mass and solar analog used. Asteroids with the (*) symbol have a MOID ≤ 0.05 AU and therefore are also classified as PHAs. The integration time with NTT/EFOSC2 was 600 s, with CA 2.2 m/CAFOS was 900 s, and with IRTF/SpeX was 120 s.

Object	Orbit	UT date	Telescope and instrument	Exp.	α ($^\circ$)	Mag. (V)	Air mass	Solar analog
1656 Suomi	MC	07-October-2010	CA 2.2 m/CAFOS	4	10.4	14.5	1.52	16 Cyg B
2577 Litva	MC	17-August-2010	NTT/EFOSC2	3	12.5	15.8	1.36	Land 115–271
5407 (1992 AX)	MC	12-August-2010	NTT/EFOSC2	4	22.8	16.6	1.06	Land 112–1333
5407 (1992 AX)	MC	07-January-2007	IRTF/SpeX	20	16.2	15.8	1.25	Hyades 64
22449 Ottijeff	MC	12-August-2010	NTT/EFOSC2	4	10.5	17.1	1.24	Land 112–1333
47035 (1998 WS)	MC	13-August-2010	NTT/EFOSC2	6	8.7	17.7	1.22	HD 1835
4055 Magellan	Amor	12-August-2010	NTT/EFOSC2	2	52.8	15.7	1.49	Land 112–1333
4055 Magellan	Amor	21-July-2010	IRTF/SpeX	10	49.4	15.9	1.02	16 Cyg B
19764 (2000 NF5)	Amor	12-August-2010	NTT/EFOSC2	3	36.8	16.5	1.38	Land 112–1333
89830 (2002 CE)	Amor ^(*)	07-October-2010	CA 2.2 m/CAFOS	2	68.1	16.3	1.41	Hyades 64
138404 (2000 HA24)	Apollo ^(*)	17-August-2010	NTT/EFOSC2	5	2.7	16.9	1.08	Land 112–1333
143381 (2003 BC21)	Amor	17-August-2010	NTT/EFOSC2	4	12.7	17.2	1.51	Land 115–271
143381 (2003 BC21)	Amor	07-October-2010	CA 2.2 m/CAFOS	4	27.4	16.6	1.20	Hyades 64
159609 (2002 AQ3)	Amor	16-August-2010	NTT/EFOSC2	4	38.8	16.7	1.25	Land 112–1333
164121 (2003 YT1)	Apollo ^(*)	20-October-2009	IRTF/SpeX	20	70.4	14.8	1.24	Hyades 64
241662 (2000 KO44)	Amor	13-August-2010	NTT/EFOSC2	2	54.7	17.1	1.35	HD 1835
2007 ML13	Amor	17-August-2010	NTT/EFOSC2	6	14.7	18.0	1.12	Land 112–1333

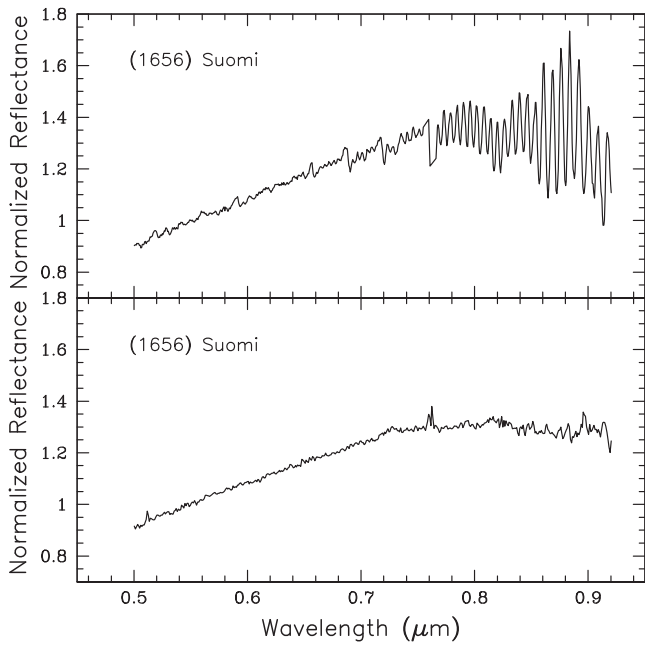


Fig. 1. The spectrum of Asteroid (1656) Suomi obtained with the 2.2 m telescope using two different detectors, the Lor#11i (top panel) and the SiTe-1d (bottom panel). The spectrum obtained with the Lor#11i CCD exhibits strong fringing longwards of 0.7 μm . In the present work we only report the data obtained with the SiTe-1d CCD.

tend to move out of the slit (Michelsen et al., 2006). Therefore, exposures were limited to 600 s. In the case of the 2.2 m telescope,

due to its excellent tracking capability the exposure time for the asteroids was 900 s.

The data reduction was performed using ESO-MIDAS following the same procedure described in (e.g., Michelsen et al., 2006; Nathues, 2010). The steps involved in the reduction process are: (1) sky background removal by subtracting A from B and B from A, (2) flat-field correction, (3) median filtering for removal of cosmic hits, (4) extraction of the one-dimensional spectra, (5) wavelength calibration using Helium and Argon arc spectra (for the NTT data) and HgHeRb arc spectra (for the Calar Alto data), (6) extinction correction (for the NTT data), using La Silla's mean extinction curve (Tüg, 1977), (7) co-adding of individual spectra to increase the S/N, (8) division of the asteroids spectrum by the spectrum of a solar analog star, and (9) normalization of the spectra to unity at 0.55 μm .

After reducing the data we noticed that the spectra obtained with the 2.2 m telescope and the Lor#11i CCD exhibit strong fringing longwards of 0.7 μm . This can be seen in Fig. 1 that shows the spectrum of Asteroid (1656) Suomi obtained with the two detectors used during the observations, the Lor#11i (top panel) and the SiTe-1d (bottom panel). Since the fringing pattern could not be removed during the reduction process, in the present work we only report the data obtained with the SiTe-1d CCD.

2.2. Near-infrared spectra

The NIR observations were conducted remotely with the NASA Infrared Telescope Facility (IRTF) on Mauna Kea, Hawai'i, on January 2007, October 2009 and July 2010. NIR spectra were obtained with the SpeX instrument (Rayner et al., 2003), equipped with a Raytheon Aladdin 3 1024 \times 1024 InSb array.

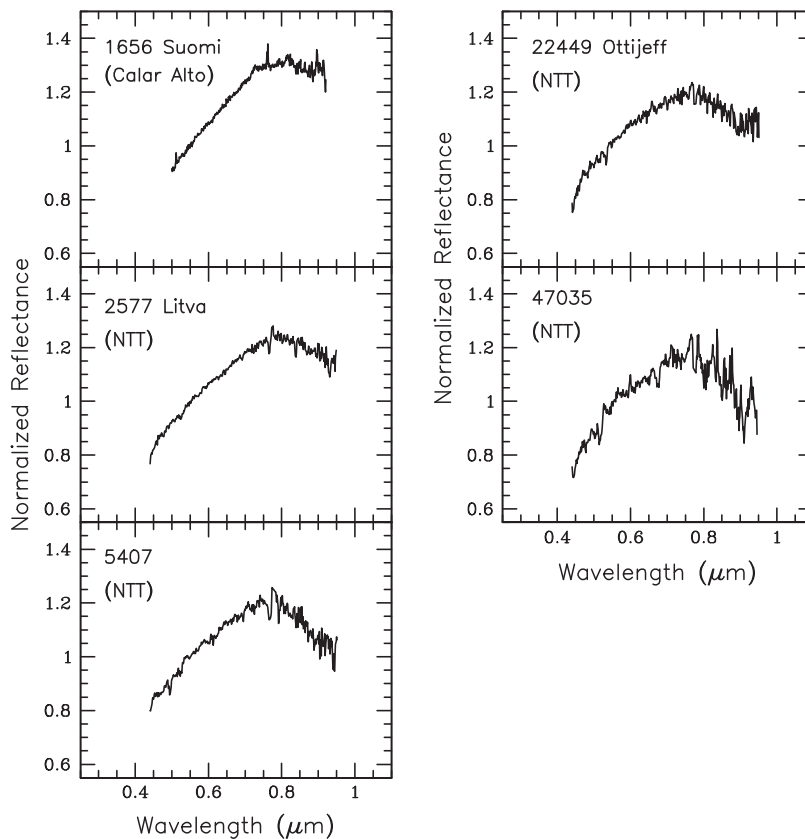


Fig. 2. Spectra of MC asteroids obtained with the NTT and the 2.2 m telescope. The numerical designation for each asteroid is given. All spectra are normalized to unity at 0.55 μm .

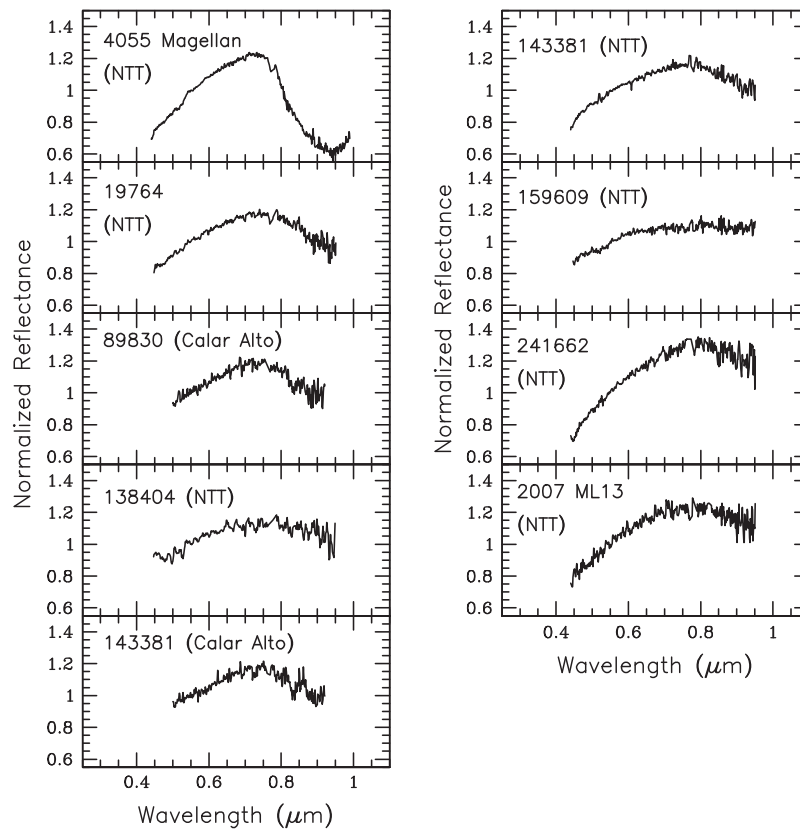


Fig. 3. Spectra of NEAs obtained with the NTT and the 2.2 m telescope. The numerical designation for each asteroid is given. All spectra are normalized to unity at 0.55 μm . Asteroid 143381 (2003 BC21) was observed with both telescopes, due to bad weather conditions the spectrum obtained with the 2.2 m telescope at Calar Alto looks noisier than the one obtained with the NTT.

Table 2

Taxonomic classification (Bus) of the observed asteroids. The measured spectral slope for each asteroid is given. If the asteroid has been classified by previous work the reference is indicated by (a) Bus and Binzel (2002a,b), (b) Lazzaro et al. (2004) and (c) Binzel et al. (2004). Asteroid 143381 (2003 BC21) was observed with two telescopes, the (*) symbol was assigned to the spectrum obtained with the 2.2 m telescope at Calar Alto. In the case of Asteroid 164121 (2003 YT1) there is no VIS spectrum, therefore it is not possible to classify it in the Bus system. However, based on its NIR spectral characteristics we concluded that this NEA is a V-type.

Object	Slope (μm^{-1})	Tax (previous work)	Tax (present work)
1656 Suomi	1.080	Ld ^(b)	S-complex
2577 Litva	0.819	SJ ^(b)	SI
5407 (1992 AX)	0.575	SK ^(a)	S
22449 Ottijeff	0.567	S ^(a)	S
47035 (1998 WS)	0.462	Sr ^(a)	Sr
4055 Magellan	-0.153	V ^(b,c)	V
19764 (2000 NF5)	0.441	-	S
89830 (2002 CE)	0.382	-	S
138404 (2000 HA24)	0.449	-	S
143381 (2003 BC21)	0.528	-	S
143381 (2003 BC21) ^(*)	0.354	-	S
159609 (2002 AQ3)	0.419	-	Sk
164121 (2003 YT1)	-	-	V
241662 (2000 KO44)	1.066	-	Sa
2007 ML13	0.797	-	SI

Spectral data were acquired using Spex in its low resolution ($R \sim 150$) prism mode with a 0.8" slit width. The covered wavelength range is ~ 0.7 – $2.5 \mu\text{m}$. The procedure to acquire NIR spectra is essentially the same to that followed to acquire VIS spectra. The main difference is that in addition to the solar analogs, and in order to correct for telluric water vapor features, local standard stars are also observed. Due to a higher and more variable background at NIR wavelengths exposures were limited to 120 s. Spex data were reduced with Spextool (Cushing et al., 2004). NIR spectra are normalized to unity at 1.4 μm . Observational circumstances for the studied asteroids are presented in Table 1.

3. Results

3.1. Taxonomic classification

The taxonomic classification of the asteroids was made following the system developed by Bus (1999), which is comprised of 26 classes that include three major complexes (S-, C- and X-complex). The classification was obtained using a computer program that includes the steps described in Bus (1999). Asteroid VIS spectra are shown in Figs. 2 and 3. The taxonomic classification of the observed asteroids is presented in Table 2. If the asteroid was previously classified the taxonomic class and reference are indicated.

Five of the observed objects are MC asteroids, and according to our analysis all belong to the S-complex (see Tables 1 and 2). These objects have been observed and classified by previous studies (Bus and Binzel, 2002a,b; Lazzaro et al., 2004; Binzel et al., 2004). Discrepancies between the taxonomic classification assigned by us and that by previous work were found for two of the asteroids (1656 Suomi and 5407). According to our results Asteroid (1656) Suomi belongs to the S-complex, however due to the scattering in the data beyond $0.8\ \mu\text{m}$ we were not able to establish its subtype within the S-complex. Lazzaro et al. (2004) classified this asteroid as Ld. In the case of Asteroid 5407 it was classified by us as S-type, while Bus and Binzel (2002a,b) classified it as Sk (same complex, different subtype). Fig. 4 shows the spectra of Asteroid (1656) Suomi and 5407 compared with those obtained by Lazzaro et al. (2004) and Bus and Binzel (2002a,b), respectively. As noted by Bus et al. (2002), these kind of discrepancies are often reported when the spectra of asteroids observed by different surveys are compared. These differences could be attributed to several factors like instrumental effects and viewing geometry effects (Bus et al., 2002). The latter can manifest themselves as phase reddening, which produces an increase of the spectral slope and variations in the intensity of the absorption bands (Sanchez et al., 2012). The poor weather conditions during our observing run at Calar Alto could also contribute to explain the difference between the taxonomic classification assigned by us and that by previous studies.

Of the nine NEAs observed, only two, 4055 Magellan and 164121 (2003 YT1), do not belong to the S-complex. The VIS spectrum of 4055 Magellan exhibits a very deep $1\text{-}\mu\text{m}$ absorption band characteristic of pyroxene assemblages (e.g., Cloutis and Gaffey, 1991; Gaffey et al., 2002; Moskovitz et al., 2010). Our classification of this asteroid as a V-type is consistent with previous studies (Lazzaro et al., 2004; Binzel et al., 2004). For 164121 (2003 YT1) we only have a NIR spectrum, therefore we could not classify it under the Bus system. However, based on its mineralogical analysis (see below) we found that this NEA is a V-type asteroid as well (see Fig. 5). NEAs 19764 (2000 NF5), 138404 (2000 HA24), 143381 (2003 BC21) and 89830 (2002 CE) were classified as S-types, while 241662 (2000 KO44), 159609 (2002 AQ3) and 2007 ML13 were classified as Sa, Sk and Sl, respectively.

3.2. Mineralogical analysis

Our observations with the IRTF include NIR spectra of Asteroids 4055 Magellan, 164121 (2003 YT1), and 5407 (1992 AX). For three of the NEAs that we obtained visible spectra, 241662 (2000 KO44), 19764 (2000 NF5) and 138404 (2000 HA24), there is also available NIR spectra ($0.8\text{--}2.5\ \mu\text{m}$) from the MIT-UH-IRTF Joint Campaign for NEO Spectral Reconnaissance (NEOSR). These spectra were acquired with the IRTF and SpeX. All the data (with the exception of 164121 (2003 YT1)) were combined with the VIS spectra to increase the wavelength coverage, allowing the mineralogical characterization of these asteroids. For that purpose, spectral band parameters, band centers and Band Area Ratios (BARs) for each VIS–NIR spectrum were measured in the same way as in Sanchez et al. (2012). In the case of NEA 164121 (2003 YT1), the wavelength range covered ($\sim 0.7\text{--}2.5\ \mu\text{m}$) was sufficient to allow us to measure these band parameters.

The VIS–NIR spectra of Asteroids 4055 Magellan and 5407 (1992 AX), and the NIR spectrum of 164121 (2003 YT1) are shown in Fig. 5. The spectra of these objects show absorption bands characteristics of pyroxene assemblages, one centered near $0.9\text{--}1\ \mu\text{m}$ (Band I) and the other at $\sim 1.9\text{--}2\ \mu\text{m}$ (Band II). These absorption bands are caused by the presence of Fe^{2+} cations located in the M2 crystallographic site (Adams, 1974, 1975; Burns, 1993). The

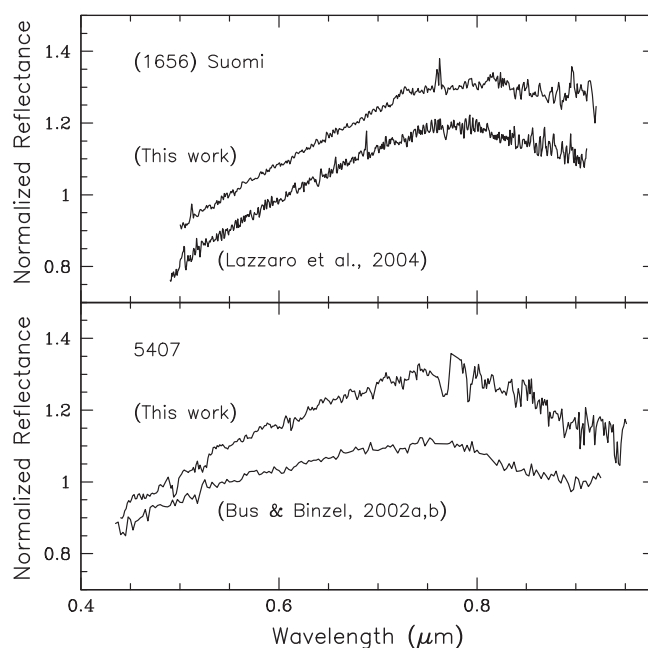


Fig. 4. Spectra of Asteroids (1656) Suomi (top panel) and 5407 (bottom panel) compared with those obtained by Lazzaro et al. (2004) and Bus and Binzel (2002a,b), respectively. Spectra are normalized to unity at $0.55\ \mu\text{m}$, and are offset for clarity.

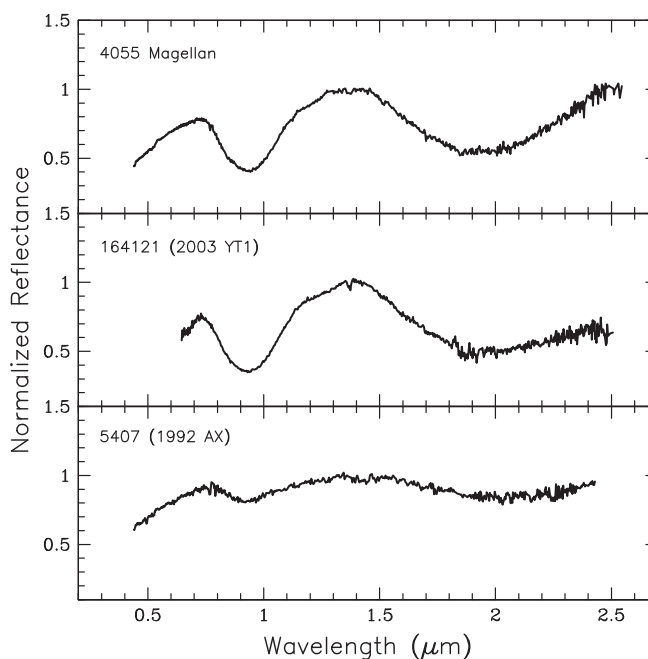


Fig. 5. VIS–NIR spectra of Asteroids 4055 Magellan (top panel) and 5407 (1992 AX) (bottom panel), and NIR spectrum of 164121 (2003 YT1) (middle panel). All spectra are normalized to unity at $1.4\ \mu\text{m}$.

VIS–NIR spectra of Asteroids 241662 (2000 KO44), 19764 (2000 NF5) and 138404 (2000 HA24) (shown in Fig. 6) exhibit the two absorption bands characteristics of olivine–orthopyroxene assemblages.

As stated earlier, the VIS–NIR spectra of 4055 Magellan and 5407 (1992 AX), and the NIR spectrum of 164121 (2003 YT1) show spectral characteristics of basaltic asteroids. Therefore, to the band parameters, we applied the temperature corrections derived by Reddy et al. (2012c). In addition, the pyroxene compositions of

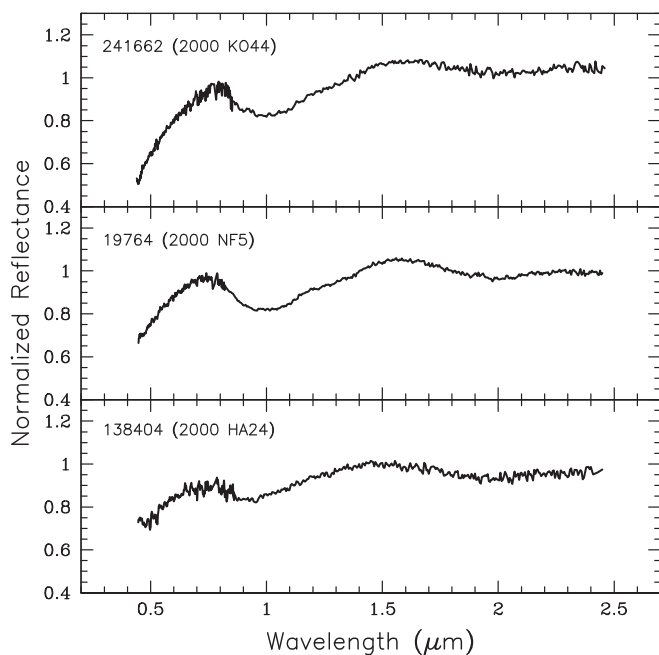


Fig. 6. VIS–NIR spectra of Asteroids 241662 (2000 KO44) (top panel), 19764 (2000 NF5) (middle panel) and 138404 (2000 HA24) (bottom panel). NIR asteroid spectra were obtained from the NEOSR survey (<http://smass.mit.edu/minus.html>). All spectra are normalized to unity at 1.4 μm .

these objects were determined using the equations derived by Burbine et al. (2007). With these equations we can determine the molar contents of ferrosilite (Fs) and wollastonite (Wo) for basaltic asteroids.

For Asteroids 241662 (2000 KO44), 19764 (2000 NF5) and 138404 (2000 HA24), which exhibit spectral characteristics of olivine–orthopyroxene assemblages, temperature corrections to band parameters were applied using the equations obtained by Sanchez et al. (2012). The mafic silicate compositions of these objects were determined using the equations derived by Dunn et al. (2010). With these equations it is possible to determine the molar contents of fayalite (Fa) in olivine and ferrosilite (Fs) in pyroxene in olivine–orthopyroxene assemblages. In addition, the mineral abundances ($ol/(ol + px)$) were calculated from the BAR values using the relationship found by Dunn et al. (2010). This relationship was obtained from the analysis of ordinary chondrites and therefore can be applied to asteroids with similar mineralogies. Spectral band parameters and mineral chemistry values for the studied asteroids are presented in Table 3.

Apart from the mineralogical analysis, the spectral band parameters (Band I center and BAR) were also used to classify these asteroids in the system introduced by Gaffey et al. (1993), which divides the S-population into seven main compositional subgroups designated S(I)–S(VII). Fig. 7 shows the measured Band I center versus

BAR for 4055 Magellan (open square), 5407 (1992 AX) (open circle) and 164121 (2003 YT1) (open triangle). These three asteroids are located in the rectangular zone (BA), which includes the pyroxene-dominated basaltic achondrite assemblages (Gaffey et al., 1993). Within the uncertainties, Asteroids 241662 (2000 KO44), 19764 (2000 NF5) and 138404 (2000 HA24) are classified as S(IV) under the system of Gaffey et al. (1993). In Fig. 7 are also depicted the measured Band I center versus BAR for 241662 (2000 KO44) (filled triangle), 19764 (2000 NF5) (filled circle) and 138404 (2000 HA24) (filled square).

For NEA 4055 Magellan, the Band I center is located at $0.93 \pm 0.01 \mu\text{m}$ and the Band II center is at $1.92 \pm 0.02 \mu\text{m}$ with a BAR of 1.95 ± 0.06 . After plotting the band centers of this asteroid on the Band I vs. Band II center plot (Fig. 8, filled circle), we found that this object has a surface assemblage dominated by orthopyroxene. For comparison we also plotted the band centers of Asteroid (4) Vesta (star symbol) measured by Reddy et al. (2012c). The spectrum of this asteroid shows an inflection at $\sim 1.3 \mu\text{m}$, which is visible in Type A clinopyroxene, olivine–orthopyroxene mixtures and plagioclase (Burns, 1993). From our calculation we determined that the pyroxene chemistry of 4055 Magellan is $\text{Fs}_{35}\text{En}_{58}\text{Wo}_7$. These values are consistent with those measured for howardites ($\text{Fs}_{24-42}\text{Wo}_{2-8}$), and cumulate eucrites ($\text{Fs}_{30-44}\text{Wo}_{6-10}$) (Mittlefehldt et al., 1998). Our results are in agreement with those found by Burbine et al. (2009), which gave a pyroxene chemistry of $\text{Fs}_{36}\text{En}_{57}\text{Wo}_7$ for Magellan. In Fig. 9 we plot the molar content of Wo versus Fs for 4055 Magellan, depicted as a filled circle. The approximated range of pyroxene chemistries found for howardites, eucrites and diogenites are shown as dashed-line boxes.

For the PHA 164121 (2003 YT1), the Band I and Band II centers are located at $0.93 \pm 0.01 \mu\text{m}$ and $1.90 \pm 0.02 \mu\text{m}$, respectively. The calculated BAR is 1.64 ± 0.06 . Similarly to 4055 Magellan, this asteroid exhibits a surface assemblage dominated by orthopyroxene (filled triangle in Fig. 8). Like Magellan, the spectrum of 164121 (2003 YT1) shows an inflection at $\sim 1.3 \mu\text{m}$. For this NEA the pyroxene chemistry was determined to be $\text{Fs}_{32}\text{En}_{62}\text{Wo}_6$. These values are consistent with the measured ranges for both howardites and cumulate eucrites, and are similar to the values reported by Abell et al. (2004), who estimated a pyroxene chemistry of $\text{Fs}_{32}\text{En}_{60}\text{Wo}_8$ for this asteroid. The molar contents of Wo and Fs for 164121 (2003 YT1) are shown in Fig. 9 (filled triangle).

The measured Band I and Band II centers of the MC 5407 (1992 AX) are located at $0.93 \pm 0.01 \mu\text{m}$ and $2.01 \pm 0.02 \mu\text{m}$, respectively, with a BAR of 2.31 ± 0.06 . The position of the band centers, which are represented in Fig. 8 as a filled square, indicates that this asteroid has a surface assemblage possibly dominated by clinopyroxenes. As in the previous cases, the pyroxene chemistry of the asteroid was calculated, given the value of $\text{Fs}_{45}\text{En}_{45}\text{Wo}_{10}$. This pyroxene chemistry is consistent with the range estimated for non-cumulate eucrites ($\text{Fs}_{43-55}\text{Wo}_{9-15}$) (Mittlefehldt et al., 1998). The molar contents of Wo and Fs calculated for 5407 (1992 AX) are indicated in Fig. 9 with a filled square. The surface composition of this asteroid contrast with its taxonomic classification derived from the VIS spectrum, which classify it as a S-type. However,

Table 3
Spectral band parameters for the asteroids studied. Molar contents of fayalite (Fa), ferrosilite (Fs), wollastonite (Wo), and $ol/(ol + px)$ ratio for each asteroid (where applicable) are presented.

Object	Band I center (μm)	Band II center (μm)	BAR	Fa (mol%)	Fs (mol%)	Wo (mol%)	$ol/(ol + px)$
5407 (1992 AX)	0.93 ± 0.01	2.01 ± 0.02	2.31 ± 0.06	–	$44.5 \pm 3.3\%$	$10.4 \pm 1.1\%$	–
4055 Magellan	0.93 ± 0.01	1.92 ± 0.02	1.95 ± 0.06	–	$34.9 \pm 3.3\%$	$6.7 \pm 1.1\%$	–
19764 (2000 NF5)	1.01 ± 0.01	1.99 ± 0.02	0.26 ± 0.06	$29.9 \pm 1.3\%$	$24.6 \pm 1.4\%$	–	0.66 ± 0.03
138404 (2000 HA24)	0.95 ± 0.01	1.98 ± 0.02	0.84 ± 0.06	$21.6 \pm 1.3\%$	$18.4 \pm 1.4\%$	–	0.52 ± 0.03
164121 (2003 YT1)	0.93 ± 0.01	1.90 ± 0.02	1.64 ± 0.06	–	$31.9 \pm 3.3\%$	$5.5 \pm 1.1\%$	–
241662 (2000 KO44)	1.02 ± 0.01	1.99 ± 0.02	0.28 ± 0.06	$30.7 \pm 1.3\%$	$25.2 \pm 1.4\%$	–	0.66 ± 0.03

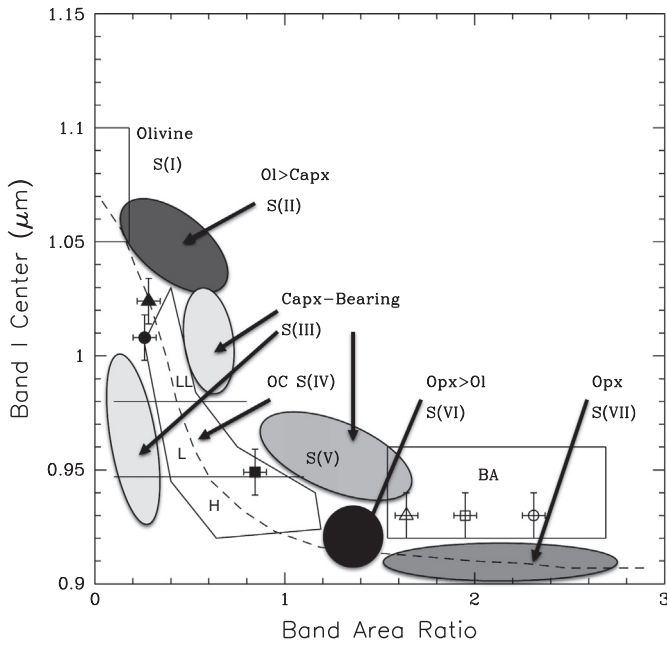


Fig. 7. Plot of the Band I center versus BAR for 241662 (2000 KO44) (filled triangle), 19764 (2000 NF5) (filled circle), 138404 (2000 HA24) (filled square), 4055 Magellan (open square), 5407 (1992 AX) (open circle), and 164121 (2003 YT1) (open triangle). The average 1- σ error bars were calculated as in Sanchez et al. (2012). The rectangular zone (BA) includes the pyroxene-dominated basaltic achondrite assemblages (Gaffey et al., 1993). The polygonal region, corresponding to the S(IV) subgroup, represents the mafic silicate components of ordinary chondrites (OC). The dashed curve indicates the location of the olivine-orthopyroxene mixing line (Cloutis et al., 1986). The horizontal lines represent the approximate boundaries for ordinary chondrites found by Dunn et al. (2010).

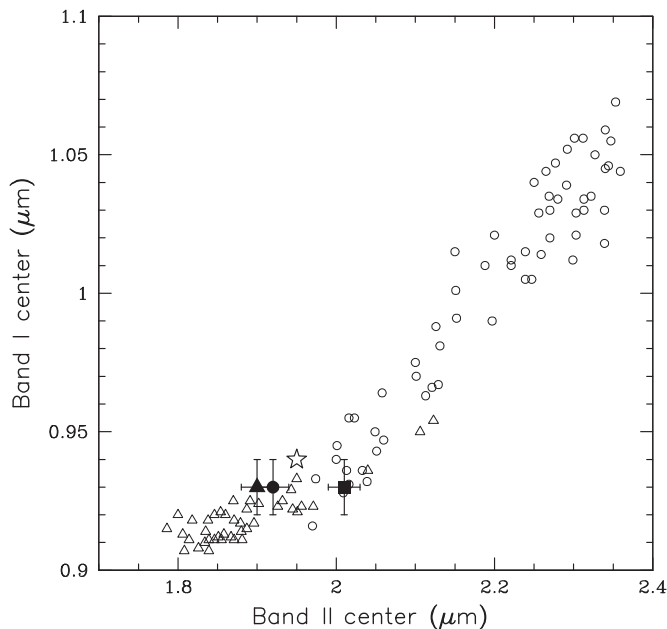


Fig. 8. Plot of Band I center vs. Band II center for 4055 Magellan (filled circle), 164121 (2003 YT1) (filled triangle), and 5407 (1992 AX) (filled square). The average 1- σ error bars were calculated as in Sanchez et al. (2012). Open triangles represent measured band centers for orthopyroxenes from Adams (1974), open circles correspond to measured band centers for clinopyroxenes from Cloutis and Gaffey (1991). For comparison we plotted the band centers of (4) Vesta (star symbol) measured by Reddy et al. (2012c). The error bars are smaller than the symbol.

the analysis of NIR spectra of individual S-type asteroids has proved that this class can include both differentiated and primitive

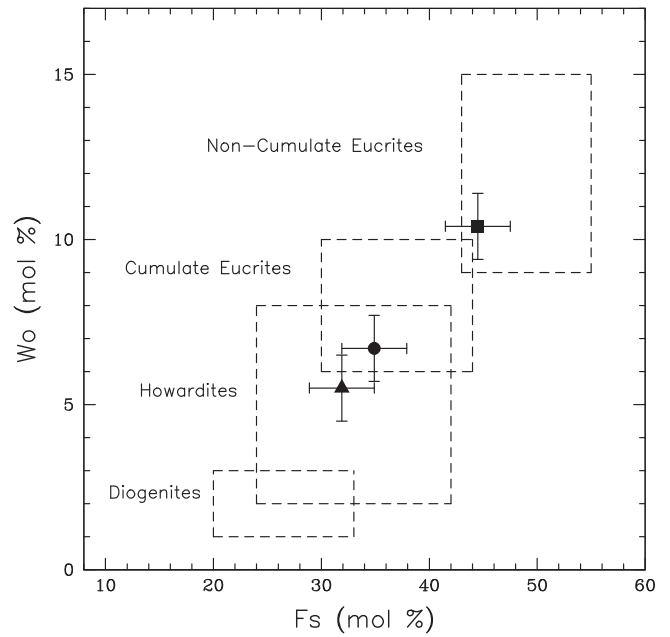


Fig. 9. Molar contents of Wo vs. Fs for NEAs 4055 Magellan (filled circle), 164121 (2003 YT1) (filled triangle), and 5407 (1992 AX) (filled square). The error bars correspond to the values determined by Burbine et al. (2007), 3 mol% for Fs and 1 mol% for Wo. The approximated range of pyroxene chemistries for howardites, non-cumulate eucrites, cumulate eucrites, and diogenites from Mittlefehldt et al. (1998) are indicated as dashed-line boxes.

objects (Gaffey et al., 1993). Asteroid 5407 represents one of those cases in which a S-type exhibits signs of differentiation. This object is also a good example of the limitations of taxonomic classification, and shows how the assumption that objects belonging to the same class share similar mineralogies can lead to a misinterpretation about the real nature of the asteroid.

For NEA 241662 (2000 KO44), the Band I center is located at $1.02 \pm 0.01 \mu\text{m}$ and the Band II center is at $1.99 \pm 0.02 \mu\text{m}$ with a BAR of 0.28 ± 0.06 . The Band I center and BAR values of this object place it in the upper limit of the polygonal region defined by Gaffey et al. (1993), and just on the olivine-orthopyroxene mixing line of Cloutis et al. (1986) (Fig. 7). Within the error bars this asteroid is classified as a S(IV) in the system of Gaffey et al. (1993). Using the equations derived by Dunn et al. (2010) we determined that the olivine and pyroxene chemistries are $\text{Fa}_{31}(\text{Fo}_{69})$ and Fs_{25} , respectively. These values are consistent with those derived for LL ordinary chondrites by Dunn et al. (2010), which give a range of $\text{Fa}_{(25-33)}$ for fayalite and $\text{Fs}_{(21-27)}$ for ferrosilite. The molar contents of Fa vs. Fs for 241662 (2000 KO44) are shown in Fig. 10 as a filled triangle. For comparison we also plotted the values for LL (open triangles), L (open circles) and H (x symbols) ordinary chondrites from Nakamura et al. (2011). From the BAR value we estimated that the olivine and pyroxene percentages for this asteroid are 0.66 and 0.34, respectively. These values are also in agreement with X-ray diffraction (XRD) measurements reported by Dunn et al. (2010) for LL ordinary chondrites, that give $ol/(ol + px)$ values in the range of 0.58–0.69.

The Band I center of NEA 19764 (2000 NF5) is located at $1.01 \pm 0.01 \mu\text{m}$ and the Band II center is at $1.99 \pm 0.02 \mu\text{m}$ with a BAR of 0.26 ± 0.06 . The Band II center of this asteroid is consistent with those of low calcium ($\sim 1.8\text{--}2.1 \mu\text{m}$) and high calcium pyroxenes ($\sim 1.97\text{--}2.35 \mu\text{m}$). The band parameters of 19764 (2000 NF5) are slightly offset to the left of the olivine-orthopyroxene mixing line (see Fig. 7). This shift could be due to the presence of small amounts of high calcium pyroxene along with olivine and orthopyroxene in the assemblage. Within the error bars, 19764 (2000 NF5)

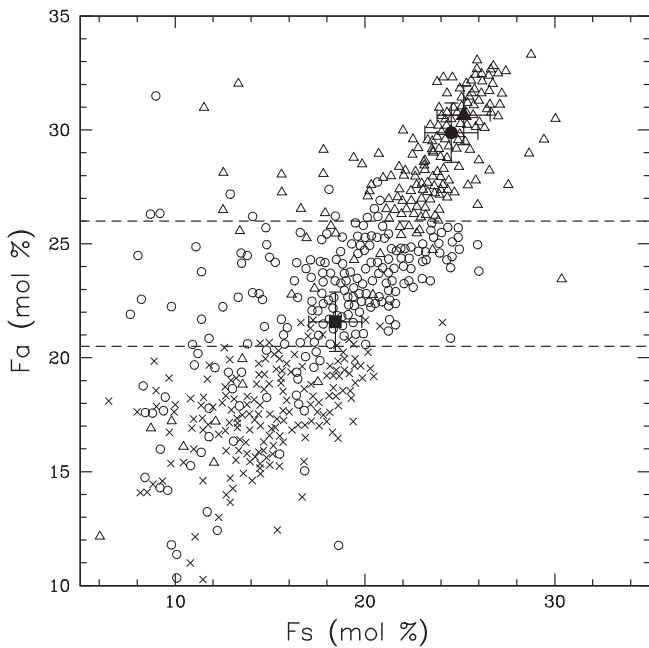


Fig. 10. Molar contents of Fa vs. Fs for NEAs 241662 (2000 KO44) (filled triangle), 19764 (2000 NF5) (filled circle), 138404 (2000 HA24) (filled square), along with the values for LL (open triangles), L (open circles) and H (\times) ordinary chondrites from Nakamura et al. (2011). The error bars correspond to the values determined by Dunn et al. (2010), 1.4 mol% for Fs and 1.3 mol% for Fa. The horizontal dashed-lines represent the approximate boundaries for LL, L, and H ordinary chondrites.

belongs to the S(IV) compositional subgroup. For this asteroid the calculated Fa and Fs content (Fa₃₀ and Fs₂₅), as well as the $ol/(ol + px)$ ratio of 0.66, fall into the range of LL ordinary chondrites. Fig. 10 shows the molar contents of Fa and Fs for 19764 (2000 NF5) (filled circle).

In the case of the PHA 138404 (2000 HA24), the Band I and Band II centers are located at $0.95 \pm 0.01 \mu\text{m}$ and $1.98 \pm 0.02 \mu\text{m}$, respectively, with a BAR of 0.84 ± 0.06 . This asteroid plots in the S(IV) region (Fig. 7) at the boundary between H and L chondrites. As can be seen in Fig. 7 the band parameters of this object are offset to the right of the olivine–orthopyroxene mixing line, which is an indication for the presence of high calcium pyroxene on the surface of the asteroid (Gaffey et al., 1993). According to our calculations, the olivine and pyroxene chemistries for this asteroid are Fa₂₂(Fo₇₈) and Fs₁₈, respectively. These values are in the borderline of those derived by Dunn et al. (2010) for L (Fa_{21–27} and Fs_{17–23}) and H (Fa_{15–21} and Fs_{13–19}) ordinary chondrites. The $ol/(ol + px)$ ratio of 0.52 calculated for 138404 (2000 HA24) falls into the range of H ordinary chondrites (0.46–0.60) measured by Dunn et al. (2010). The derived olivine and pyroxene chemistries of 138404 (2000 HA24) are shown in Fig. 10 as a filled square.

4. Conclusions

We have found that all observed MC asteroids, five in total, belong to the S-complex, including the S, Sr and Sl classes. The classifications assigned by us are consistent with previous work with the exception of two cases. This discrepancy could be attributed to atmospheric conditions or phase angle effects. Among the NEAs observed, seven belong to the S-complex, including the S, Sa, Sk and Sl classes. All of them have been classified for the first time in the present work. Two NEAs were classified as V-type asteroids.

The mineralogical analysis of NEAs 4055 Magellan and 164121 (2003 YT1), showed that their pyroxene chemistries are consistent with both, howardites and cumulate eucrites. Howardites are

polymict breccia composed by a mixture of eucrite and diogenite fragments. Cumulate eucrites, on the other hand, are achondritic meteorites, which are thought to have formed in shallow magma chambers within the crust of their parent body, where they slowly crystallized. Howardites and eucrites along with diogenites (HED meteorites) have been linked to Asteroid (4) Vesta, on the basis of their spectral and mineralogical similarities derived from ground-based observations (e.g., McCord et al., 1970; Consolmagno and Drake, 1977; Gaffey, 1997; Keil, 2002). This idea has been supported by recent spacecraft spectroscopic observations obtained by Dawn (e.g., Reddy et al., 2012b; De Sanctis et al., 2012), that shows Vesta as the most likely parent body of these meteorites. The Vesta asteroid family extends from the ν_6 secular resonance to the 3:1 mean motion resonance with Jupiter, providing a viable route for the delivery of these objects to the near-Earth space (Wisdom, 1985; Bottke et al., 2002). Our results suggest that 4055 Magellan and 164121 (2003 YT1) are formed by regolith breccia originated in a larger asteroid that experienced extensive igneous processing. The pyroxene chemistries derived for these asteroids are similar to those found by Burbine et al. (2009) for a group of V-type NEAs. Although we cannot rule out a different parent body for these NEAs, these results are consistent with the aforementioned scenario, which would link Vesta with these asteroids via secular or mean motion resonances.

The mineralogical analysis of MC 5407 (1992 AX) revealed a pyroxene chemistry consistent with the range estimated for non-cumulate eucrites. These results suggest that the parent body of this asteroid experienced temperatures high enough to cause at least partial melting, making basaltic achondrites the most plausible meteorite analogs (Gaffey et al., 1993).

For NEAs, 241662 (2000 KO44), 19764 (2000 NF5) and 138404 (2000 HA24), the mineralogical analysis revealed ordinary chondrite-like compositions. In particular, 241662 (2000 KO44) and 19764 (2000 NF5) showed mineral compositions consistent with olivine-rich LL ordinary chondrites. Within the error bars the olivine and pyroxene chemistries of these two asteroids, as well as the olivine abundances, are consistent with the values measured from the returned samples of Asteroid 25143 Itokawa. The mean compositions of olivine and low-Ca pyroxene for these samples gave values of Fa₂₉ and Fs₂₄, respectively (Nakamura et al., 2011), with an olivine abundance of 64% (Tsuchiyama et al., 2011). The analysis of Itokawa samples also revealed that this asteroid is a breccia, consisting of poorly equilibrated LL4 and highly equilibrated LL5 and LL6 materials (Nakamura et al., 2011). This degree of thermal metamorphism indicates that the parent body where Itokawa originated must have had a diameter larger than 20 km, necessary to reach temperatures of $\sim 800^\circ\text{C}$ that can explain the range of petrologic types observed among the Itokawa particles (Nakamura et al., 2011). LL ordinary chondrites have been linked to the Flora family (Vernazza et al., 2008), which is located in the inner part of the main belt near the ν_6 secular resonance. Although the derived silicate compositions of 241662 (2000 KO44) and 19764 (2000 NF5) are consistent with that of LL ordinary chondrites, we noticed that their olivine abundances (66%) are lower than the ranges found by Vernazza et al. (2008) for LL chondrites (70–85%), and members of the Flora family (76–82%). However, this discrepancy could be explained by the fact that Vernazza et al. (2008) used a radiative transfer model (Shkuratov et al., 1999) to calculate the $ol/(ol + px)$ ratios, while we used empirical spectral calibrations derived from the analysis of ordinary chondrites.

NEA 138404 (2000 HA24) is considered as a possible target for robotic and manned missions due to its low ΔV (Landau and Strange, 2011). This asteroid showed a composition similar to L and H ordinary chondrites. If this NEA formed in a L ordinary chondrite parent body, then its origin could be related to the formation of the Gefion family. Nesvorný et al. (2009) found a possible link

between this family (located at 2.7–2.82 AU) and L ordinary chondrites. Asteroids in the Gefion family are thought to have originated after an impact event that disrupted its parent body ~470 myr ago (Haack et al., 1996; Korochantseva et al., 2007). This group of objects exhibit spectral characteristics compatible with S-complex asteroids (Cellino et al., 2002). According to Nesvorný et al. (2009) the location of the Gefion family, near the 5:2 mean motion resonance with Jupiter, provides a viable source for the delivery of this material to Earth. Thus, objects in the Gefion family could eventually escape from the main belt and evolve to Earth-crossing orbits.

Another possible scenario for the origin of 138404 (2000 HA24) is that this object is a fragment of a H ordinary chondrite parent body. The main belt Asteroid 6 Hebe, which is located at 2.426 AU between the ν_6 secular resonance and the 3:1 mean motion resonance, shows spectral characteristics and mafic silicate compositions consistent with those of H chondrites (Gaffey, 1996; Gaffey and Gilbert, 1998), making of this asteroid its probably parent body. Cosmic ray exposure ages (CREs) of H chondrites indicate that their parent body, or a fragment of it, experienced multiple collisional events, occurred ~60, ~33 and ~8 myr ago (Graf and Marti, 1995). Numerical experiments have shown that fragments ejected from Hebe at velocities of a few hundreds m/s can be transported into the resonance zones and from there into Earth-crossing orbits within a time span of ~1 myr (Farinella et al., 1993). Thus, a possible scenario for the origin of 138404 (2000 HA24) is that this object was ejected during one of the collisional events and later transported to the near-Earth space. If 138404 (2000 HA24) is indeed a fragment of Hebe, then it could be also linked to some of the H ordinary chondrites found on Earth. It is believed that the latest collisional event occurred ~8 myr ago is the source of ~45% of H chondrites that reach the Earth (Graf and Marti, 1995). Since this collisional event took place within the typical lifetimes (10^6 – 10^7 years) associated with NEAs (Morbidelli et al., 2002), it is possible that some H chondrite meteorites were ejected from the surface of 138404 (2000 HA24).

The compositional information derived in this work from the analysis of VIS–NIR spectral data, along with dynamical considerations allowed us to discuss possible scenarios for the origin of the studied asteroids, as well as their connection with meteorites found on Earth. Since our sample included PHAs an a possible target for robotic and manned missions, the information gathered here could eventually help in planning future missions, and contribute in the development of mitigation strategies.

Acknowledgments

This paper is based on data obtained with the New Technology Telescope at La Silla, Chile, observations collected at the Centro Astronómico Hispano Alemán (CAHA), operated jointly by the Max-Planck Institut für Astronomie and the Instituto de Astrofísica de Andalucía (CSIC), and observations acquired with the Infrared Telescope Facility on Mauna Kea, Hawai'i. Part of the data used in this work were obtained from the MIT-UH-IRTF Joint Campaign for NEO Reconnaissance. The authors would like to thank Olivier Hainaut for his help during the observations at the NTT. JAS research was supported by a PhD fellowship of the International Max Planck Research School on Physical Processes in the Solar System and Beyond, and the Deutsche Forschungsgemeinschaft. V.R. research was supported by NASA 182 NEOO Program Grant NNX12AG12G, and NASA Planetary Geology and Geophysics Grant NNX11AN84G. We thank the IRTF TAC for awarding time to this project, and to the IRTF TOs and MKSS staff for their support. The authors thank Paul Abell and an anonymous reviewer for their reviews, which helped to improve the manuscript.

References

- Abell, P.A., Gaffey, M.J., Hardersen, P.S., 2004. Compositional results of binary near-Earth Asteroid 2003 YT1: A basaltic achondrite. In: AAS/Division for Planetary Sciences Meeting, p. 1132. Abstracts #36.
- Abell, P.A. et al., 2009. Scientific exploration of near-Earth objects via the Orion Crew Exploration Vehicle. *Meteorit. Planet. Sci.* 44, 1825–1836.
- Adams, J.B., 1974. Visible and near-infrared diffuse reflectance spectra of pyroxenes as applied to remote sensing of solid objects in the Solar System. *J. Geophys. Res.* 79, 4829–4836.
- Adams, J.B., 1975. Interpretation of visible and near-infrared diffuse reflectance spectra of pyroxenes and other rock-forming minerals. In: Karr, C.I. (Ed.), *Infrared and Raman Spectroscopy of Lunar and Terrestrial Minerals*. Academic, New York, pp. 91–116.
- Angeli, C.A., Lazzaro, D., 2002. Spectral properties of Mars-crossers and near-Earth objects. Results of the S³OS² survey. *Astron. Astrophys.* 391, 757–765.
- Binzel, R.P., Lupishko, D., di Martino, M., Whiteley, R.J., Hahn, G.J., 2002. Physical properties of near-Earth objects. In: Bottke, W., Cellino, A., Paolicchi, P., Binzel, R. (Eds.), *Asteroids III*. University of Arizona Press, pp. 255–271.
- Binzel, R.P., Rivkin, A.S., Stuart, J.S., Harris, A.W., Bus, S.J., Burbine, T.H., 2004. Observed spectral properties of near-Earth objects: Results for population distribution, source regions, and space weathering processes. *Icarus* 170, 259–294.
- Bottke, W.F., Jedicke, R., Morbidelli, A., Petit, J.M., Gladman, B., 2000. Understanding the distribution of near-Earth asteroids. *Science* 288, 2190–2194.
- Bottke Jr., W.F., Vokrouhlický, D., Rubincam, D.P., Broz, M., 2002. The effect of Yarkovsky thermal forces on the dynamical evolution of asteroids and meteoroids. In: Bottke, W., Cellino, A., Paolicchi, P., Binzel, R. (Eds.), *Asteroids III*. University of Arizona Press, pp. 395–408.
- Burbine, T.H., McCoy, T.J., Meibom, A., Gladman, B., Keil, K., 2002. Meteoritic parent bodies: Their number and identification. In: Bottke, W., Cellino, A., Paolicchi, P., Binzel, R. (Eds.), *Asteroids III*. University of Arizona Press, pp. 653–667.
- Burbine, T.H., Buchanan, P.C., Binzel, R.P., 2007. Deriving formulas from HED spectra for determining the pyroxene mineralogy of Vesta and Vestoids. *Lunar Planet. Sci. Conf.* 2117 (abstracts).
- Burbine, T.H., Buchanan, P.C., Dolkar, T., Binzel, R.P., 2009. Pyroxene mineralogies of near-Earth Vestoids. *Meteorit. Planet. Sci.* 44, 1331–1341.
- Burns, R.G., 1993. *Mineralogical Applications of Crystal Field Theory*. Cambridge University Press, Cambridge, UK, 575pp.
- Bus, S.J., 1999. Compositional Structure in the Asteroid Belt: Results of a Spectroscopic Survey. Ph.D. Thesis. Massachusetts Institute of Technology.
- Bus, S.J., Binzel, R.P., 2002a. Phase I of the small main-belt asteroid spectroscopic survey a feature-based taxonomy. *Icarus* 158, 146–177.
- Bus, S.J., Binzel, R.P., 2002b. Phase II of the small main-belt asteroid spectroscopic survey the observations. *Icarus* 158, 106–145.
- Bus, S.J., Vilas, F., Barucci, M.A., 2002. Visible-wavelength spectroscopy of asteroids. In: Bottke, W., Cellino, A., Paolicchi, P., Binzel, R. (Eds.), *Asteroids III*. University of Arizona Press, pp. 169–182.
- Cellino, A., Bus, S.J., Doressoundiram, A., Lazzaro, D., 2002. Spectroscopic properties of asteroid families. In: Bottke, W., Cellino, A., Paolicchi, P., Binzel, R. (Eds.), *Asteroids III*. University of Arizona Press, pp. 633–643.
- Chapman, C.R., Morrison, D., 1994. Impacts on the Earth by asteroids and comets: Assessing the hazard. *Nature* 367, 33–40.
- Cloutis, E.A., Gaffey, M.J., 1991. Pyroxene spectroscopy revisited – Spectral-compositional correlations and relationship to geothermometry. *J. Geophys. Res.* 96, 22809–22826.
- Cloutis, E.A., Gaffey, M.J., Jackowski, T.L., Reed, K.L., 1986. Calibrations of phase abundance, composition, and particle size distribution for olivine-orthopyroxene mixtures from reflectance spectra. *J. Geophys. Res.* 91, 11641–11653.
- Consolmagno, G.J., Drake, M.J., 1977. Composition and evolution of the eucrite parent body – Evidence from rare Earth elements. *Geochim. Cosmochim. Acta* 41, 1271–1282.
- Cushing, M.C., Vacca, W.D., Rayner, J.T., 2004. Spextool: A spectral extraction package for SpeX, a 0.8–5.5 micron cross-dispersed spectrograph. *Publ. Astron. Soc. Pacific* 116, 362–376.
- de León, J., Licandro, J., Serra-Ricart, M., Pinilla-Alonso, N., Campins, H., 2010. Observations, compositional, and physical characterization of near-Earth and Mars-crosser asteroids from a spectroscopic survey. *Astron. Astrophys.* 517, A23, 25pp.
- De Sanctis, M.C. et al., 2012. Spectroscopic characterization of mineralogy and its diversity across Vesta. *Science* 336, 697–700.
- Dunn, T.L., McCoy, T.J., Sunshine, J.M., McSween, H.Y., 2010. A coordinated spectral, mineralogical, and compositional study of ordinary chondrites. *Icarus* 208, 789–797.
- Dunn, T.L., Burbine, T.H., Bottke, W.F., Clark, J.P., 2013. Mineralogies and source regions of near-Earth asteroids. *Icarus* 222, 273–282.
- Farinella, P., Froeschle, C., Gonczi, R., 1993. Meteorites from the Asteroid 6 Hebe. *Celest. Mech. Dynam. Astron.* 56, 287–305.
- Gaffey, M.J., 1996. Spectral Identification of Asteroid 6 Hebe as the mainbelt parent body of the H-type ordinary chondrites. *Meteorit. Planet. Sci. Suppl.* 31, 47.
- Gaffey, M.J., 1997. Surface lithologic heterogeneity of Asteroid 4 Vesta. *Icarus* 127, 130–157.
- Gaffey, M.J., Gilbert, S.L., 1998. Asteroid 6 Hebe: The probable parent body of the H-type ordinary chondrites and the IIE iron meteorites. *Meteorit. Planet. Sci.* 33, 1281–1295.

- Gaffey, M.J., Burbine, T.H., Piatek, J.L., Reed, K.L., Chaky, D.A., Bell, J.F., Brown, R.H., 1993. Mineralogical variations within the S-type asteroid class. *Icarus* 106, 573–602.
- Gaffey, M.J., Cloutis, E.A., Kelley, M.S., Reed, K.L., 2002. Mineralogy of asteroids. In: Bottke, W., Cellino, A., Paolicchi, P., Binzel, R. (Eds.), *Asteroids III*. University of Arizona Press, pp. 183–204.
- Graf, T., Marti, K., 1995. Collisional history of H chondrites. *J. Geophys. Res.* 100, 21247–21264.
- Haack, H., Farinella, P., Scott, E.R.D., Keil, K., 1996. Meteoritic, asteroidal, and theoretical constraints on the 500 MA disruption of the L chondrite parent body. *Icarus* 119, 182–191.
- Keil, K., 2002. Geological history of Asteroid 4 Vesta: “The smallest terrestrial planet”. In: Bottke, W., Cellino, A., Paolicchi, P., Binzel, R. (Eds.), *Asteroids III*. University of Arizona Press, pp. 573–584.
- Korochantseva, E.V. et al., 2007. L-chondrite asteroid breakup tied to Ordovician meteorite shower by multiple isochron ^{40}Ar – ^{39}Ar dating. *Meteorit. Planet. Sci.* 42, 113–130.
- Landau, D., Strange, N., 2011. Near-Earth asteroids accessible to human exploration with high-power electric propulsion. *Am. Astronaut. Soc.*, 11–46.
- Lazzaro, D., Angeli, C.A., Carvano, J.M., Mothé-Diniz, T., Duffard, R., Florczak, M., 2004. $S^3\text{OS}^2$: The visible spectroscopic survey of 820 asteroids. *Icarus* 172, 179–220.
- McCord, T.B., Adams, J.B., Johnson, T.V., 1970. Asteroid Vesta: Spectral reflectivity and compositional implications. *Science* 168, 1445–1447.
- Michel, P., Migliorini, F., Morbidelli, A., Zappalà, V., 2000. The population of Mars-crossers: Classification and dynamical evolution. *Icarus* 145, 332–347.
- Michelsen, R., Nathues, A., Lagerkvist, C.I., 2006. Spectroscopy of near-Earth asteroids. *Astron. Astrophys.* 451, 331–337.
- Mittlefehldt, D.W., McCoy, T.J., Goodrich, C.A., Kracher, A., 1998. Non-chondritic meteorites from asteroidal bodies. In: Papike, J. (Ed.), *Reviews in Mineralogy, Planetary Materials*, vol. 36. Mineralogical Society of America, pp. 4-001–4-196.
- Morbidelli, A., Nesvorný, D., 1999. Numerous weak resonances drive asteroids toward terrestrial planets orbits. *Icarus* 139, 295–308.
- Morbidelli, A., Bottke Jr., W.F., Froeschlé, C., Michel, P., 2002. Origin and evolution of near-Earth objects. In: Bottke, W., Cellino, A., Paolicchi, P., Binzel, R. (Eds.), *Asteroids III*. University of Arizona Press, pp. 409–422.
- Morrison, D., Harris, A.W., Sommer, G., Chapman, C.R., Carusi, A., 2002. Dealing with the impact hazard. In: Bottke, W., Cellino, A., Paolicchi, P., Binzel, R. (Eds.), *Asteroids III*. University of Arizona Press, pp. 739–754.
- Moskovitz, N.A., Willman, M., Burbine, T.H., Binzel, R.P., Bus, S.J., 2010. A spectroscopic comparison of HED meteorites and V-type asteroids in the inner Main Belt. *Icarus* 208, 773–788.
- Nakamura, T. et al., 2011. Itokawa dust particles: A direct link between S-type asteroids and ordinary chondrites. *Science* 333, 1113–1116.
- Nathues, A., 2010. Spectral study of the Eunomia asteroid family Part II: The small bodies. *Icarus* 208, 252–275.
- Nesvorný, D., Vokrouhlický, D., Morbidelli, A., Bottke, W.F., 2009. Asteroidal source of L chondrite meteorites. *Icarus* 200, 698–701.
- Rayner, J.T. et al., 2003. SpeX: A medium-resolution 0.8–5.5 micron spectrograph and imager for the NASA infrared telescope facility. *Publ. Astron. Soc. Pacific* 115, 362–382.
- Reddy, V., Corre, L.L., Hicks, M., Lawrence, K., Buratti, B.J., Abell, P.A., Gaffey, M.J., Hardersen, P.S., 2012a. Composition of near-Earth Asteroid 2008 EV5: Potential target for robotic and human exploration. *Icarus* 221, 678–681.
- Reddy, V. et al., 2012b. Color and albedo heterogeneity of Vesta from Dawn. *Science* 336, 700–704.
- Reddy, V., Sanchez, J.A., Nathues, A., Moskovitz, N.A., Li, J.Y., Cloutis, E.A., Archer, K., Tucker, R.A., Gaffey, M.J., Paul Mann, J., Sierks, H., Schade, U., 2012c. Photometric, spectral phase and temperature effects on 4 Vesta and HED meteorites: Implications for the Dawn mission. *Icarus* 217, 153–168.
- Sanchez, J.A., Reddy, V., Nathues, A., Cloutis, E.A., Mann, P., Hiesinger, H., 2012. Phase reddening on near-Earth asteroids: Implications for mineralogical analysis, space weathering and taxonomic classification. *Icarus* 220, 36–50.
- Sears, D.W.G. et al., 2000. A multiple near-Earth asteroid sample return mission called Hera. *Meteorit. Planet. Sci. Suppl.* 35, 145.
- Shkuratov, Y., Starukhina, L., Hoffmann, H., Arnold, G., 1999. A model of spectral albedo of particulate surfaces: Implications for optical properties of the Moon. *Icarus* 137, 235–246.
- Shoemaker, E.M., Williams, J.G., Helin, E.F., Wolfe, R.F., 1979. Earth-crossing asteroids – Orbital classes, collision rates with Earth, and origin. In: Gehrels, T. (Ed.), *Asteroids*. University of Arizona Press, pp. 253–282.
- Tsuchiyama, A. et al., 2011. Three-dimensional structure of Hayabusa samples: Origin and evolution of Itokawa regolith. *Science* 333, 1125–1128.
- Tüg, H., 1977. Vertical extinction on La Silla. *The Messenger* 11, 7–8.
- Vernazza, P. et al., 2008. Compositional differences between meteorites and near-Earth asteroids. *Nature* 454, 858–860.
- Wisdom, J., 1985. Meteorites may follow a chaotic route to Earth. *Nature* 315, 731–733.

Bibliography

- Abell, P. A., Vilas, F., Jarvis, K. S., Gaffey, M. J., Kelley, M. S., 2007, Mineralogical composition of (25143) Itokawa 1998 SF36 from visible and near-infrared reflectance spectroscopy: Evidence for partial melting, *Meteoritics and Planetary Science*, 42, 2165–2177
- Adams, J. B., 1974, Visible and near-infrared diffuse reflectance spectra of pyroxenes as applied to remote sensing of solid objects in the solar system, *Journal of Geophysical Research*, 79, 4829–4836
- Adams, J. B., 1975, Interpretation of visible and near-infrared diffuse reflectance spectra of pyroxenes and other rock-forming minerals, in *Infrared and Raman Spectroscopy of Lunar and Terrestrial Minerals*, (Ed.) I. Karr, C., pp. 91–116, Academic, New York
- Adams, J. B., Filice, A. L., 1967, Spectral Reflectance 0.4 to 2.0 Microns of Silicate Rock Powders, *Journal of Geophysical Research*, 72, 5705–5715
- Alvarez, L. W., Alvarez, W., Asaro, F., Michel, H. V., 1980, Extraterrestrial Cause for the Cretaceous-Tertiary Extinction, *Science*, 208, 1095–1108
- Bell, J. F., Owensby, P. D., Hawke, B. R., Gaffey, M. J., 1988, The 52-Color Asteroid Survey: Final Results and Interpretation, in *Lunar and Planetary Institute Science Conference Abstracts*, vol. 19 of Lunar and Planetary Inst. Technical Report, p. 57
- Bell, J. F., Izenberg, N. I., Lucey, P. G., Clark, B. E., Peterson, C., Gaffey, M. J., Joseph, J., Carcich, B., Harch, A., Bell, M. E., Warren, J., Martin, P. D., McFadden, L. A., Wellnitz, D., Murchie, S., Winter, M., Veverka, J., Thomas, P., Robinson, M. S., Malin, M., Cheng, A., 2002, Near-IR Reflectance Spectroscopy of 433 Eros from the NIS Instrument on the NEAR Mission. I. Low Phase Angle Observations, *Icarus*, 155, 119–144
- Binzel, R. P., Xu, S., 1993, Chips off of asteroid 4 Vesta - Evidence for the parent body of basaltic achondrite meteorites, *Science*, 260, 186–191
- Binzel, R. P., Rivkin, A. S., Bus, S. J., Sunshine, J. M., Burbine, T. H., 2001, MUSES-C target asteroid (25143) 1998 SF36: A reddened ordinary chondrite, *Meteoritics and Planetary Science*, 36, 1167–1172
- Binzel, R. P., Lupishko, D., di Martino, M., Whiteley, R. J., Hahn, G. J., 2002, Physical Properties of Near-Earth Objects, *Asteroids III*, pp. 255–271
- Binzel, R. P., Rivkin, A. S., Stuart, J. S., Harris, A. W., Bus, S. J., Burbine, T. H., 2004, Observed spectral properties of near-Earth objects: results for population distribution, source regions, and space weathering processes, *Icarus*, 170, 259–294

- Botta, O., Bada, J. L., 2002, Extraterrestrial Organic Compounds in Meteorites, *Surveys in Geophysics*, 23, 411–467
- Bottke, W. F., Jedicke, R., Morbidelli, A., Petit, J.-M., Gladman, B., 2000, Understanding the Distribution of Near-Earth Asteroids, *Science*, 288, 2190–2194
- Bottke, W. F., Morbidelli, A., Jedicke, R., Petit, J.-M., Levison, H. F., Michel, P., Metcalfe, T. S., 2002a, Debaised Orbital and Absolute Magnitude Distribution of the Near-Earth Objects, *Icarus*, 156, 399–433
- Bottke, Jr., W. F., Cellino, A., Paolicchi, P., Binzel, R. P., 2002b, An Overview of the Asteroids: The Asteroids III Perspective, *Asteroids III*, pp. 3–15
- Bottke, Jr., W. F., Vokrouhlický, D., Rubincam, D. P., Broz, M., 2002c, The Effect of Yarkovsky Thermal Forces on the Dynamical Evolution of Asteroids and Meteoroids, *Asteroids III*, pp. 395–408
- Britt, D. T., Consolmagno, G. J., 2003, Stony meteorite porosities and densities: A review of the data through 2001, *Meteoritics and Planetary Science*, 38, 1161–1180
- Brunetto, R., Strazzulla, G., 2005, Elastic collisions in ion irradiation experiments: A mechanism for space weathering of silicates, *Icarus*, 179, 265–273
- Brunetto, R., Vernazza, P., Marchi, S., Birlan, M., Fulchignoni, M., Orofino, V., Strazzulla, G., 2006, Modeling asteroid surfaces from observations and irradiation experiments: The case of 832 Karin, *Icarus*, 184, 327–337
- Burbine, T. H., 1998, Could G-class asteroids be the parent bodies of the CM chondrites?, *Meteoritics and Planetary Science*, 33, 253–258
- Burbine, T. H., McCoy, T. J., Meibom, A., Gladman, B., Keil, K., 2002, Meteoritic Parent Bodies: Their Number and Identification, in *Asteroids III*, (Eds.) W. Bottke, A. Cellino, P. Paolicchi, R. Binzel, pp. 653–667, University of Arizona Press
- Burbine, T. H., Buchanan, P. C., Binzel, R. P., 2007, Deriving Formulas from HED Spectra for Determining the Pyroxene Mineralogy of Vesta and Vestoids, in *Lunar and Planetary Institute Science Conference Abstracts*, vol. 38 of *Lunar and Planetary Institute Science Conference Abstracts*, p. 2117
- Burbine, T. H., Buchanan, P. C., Dolkar, T., Binzel, R. P., 2009, Pyroxene mineralogies of near-Earth vestoids., *Meteoritics and Planetary Science*, 44, 1331–1341
- Burns, R. G., 1993, *Mineralogical Applications of Crystal Field Theory*, Cambridge, UK: Cambridge University Press, 575pp
- Bus, S. J., Binzel, R. P., 2002a, Phase II of the Small Main-Belt Asteroid Spectroscopic Survey The Observations, *Icarus*, 158, 106–145
- Bus, S. J., Binzel, R. P., 2002b, Phase II of the Small Main-Belt Asteroid Spectroscopic Survey A Feature-Based Taxonomy, *Icarus*, 158, 146–177

- Bus, S. J., Vilas, F., Barucci, M. A., 2002, Visible-Wavelength Spectroscopy of Asteroids, in Asteroids III, (Eds.) W. Bottke, A. Cellino, P. Paolicchi, R. Binzel, pp. 169–182, University of Arizona Press
- Chapman, C. R., Salisbury, J. W., 1973, Comparisons of meteorite and asteroid spectral reflectivities, *Icarus*, 19, 507–522
- Chapman, C. R., Johnson, T. V., McCord, T. B., 1971, A Review of Spectrophotometric Studies of Asteroids, in NASA Special Publication, vol. 267, p. 51
- Christensen, P. R., Bandfield, J. L., Hamilton, V. E., Howard, D. A., Lane, M. D., Piatek, J. L., Ruff, S. W., Stefanov, W. L., 2000, A thermal emission spectral library of rock-forming minerals, *Journal of Geophysical Research*, 105, 9735–9740
- Chyba, C., Sagan, C., 1992, Endogenous production, exogenous delivery and impact-shock synthesis of organic molecules: an inventory for the origins of life, *Nature*, 355, 125–132
- Clark, B. E., Hapke, B., Pieters, C., Britt, D., 2002a, Asteroid Space Weathering and Regolith Evolution, in Asteroids III, (Eds.) W. Bottke, A. Cellino, P. Paolicchi, R. Binzel, pp. 585–599, University of Arizona Press
- Clark, B. E., Helfenstein, P., Bell, J. F., Peterson, C., Veverka, J., Izenberg, N. I., Domingue, D., Wellnitz, D., McFadden, L., 2002b, NEAR Infrared Spectrometer Photometry of Asteroid 433 Eros, *Icarus*, 155, 189–204
- Clark, R. N., 1999, Spectroscopy of Rocks and Minerals, and Principles of Spectroscopy, in *Manual of Remote Sensing, Volume 3, Remote Sensing for the Earth Sciences*, (Ed.) A. Rencz, pp. 3–58, John Wiley and Sons, New York
- Cloutis, E. A., Gaffey, M. J., 1991, Pyroxene spectroscopy revisited - Spectral-compositional correlations and relationship to geothermometry, *Journal of Geophysical Research*, 96, 22 809
- Cloutis, E. A., Gaffey, M. J., Jackowski, T. L., Reed, K. L., 1986, Calibrations of phase abundance, composition, and particle size distribution for olivine-orthopyroxene mixtures from reflectance spectra, *Journal of Geophysical Research*, 91, 11 641–11 653
- Cloutis, E. A., Gaffey, M. J., Smith, D. G. W., Lambert, R. S. J., 1990, Reflectance spectra of 'featureless' materials and the surface mineralogies of M- and E-class asteroids, *Journal of Geophysical Research*, 95, 281–293
- Cohen, M., Witteborn, F. C., Roush, T., Bregman, J., Wooden, D., 1998, Spectral Irradiance Calibration in the Infrared. VIII. 5-14 Micron Spectroscopy of the Asteroids Ceres, Vesta, and Pallas, *The Astronomical Journal*, 115, 1671–1679
- Consolmagno, G. J., Drake, M. J., 1977, Composition and evolution of the eucrite parent body - Evidence from rare earth elements, *Geochimica et Cosmochimica Acta*, 41, 1271–1282
- Cushing, M. C., Vacca, W. D., Rayner, J. T., 2004, Spextool: A Spectral Extraction Package for SpeX, a 0.8-5.5 Micron Cross-Dispersed Spectrograph, *Publications of the Astronomical Society of the Pacific*, 116, 362–376

- Davis, D. R., Durda, D. D., Marzari, F., Campo Bagatin, A., Gil-Hutton, R., 2002, Collisional Evolution of Small-Body Populations, *Asteroids III*, pp. 545–558
- De Sanctis, M. C., Ammannito, E., Capria, M. T., Tosi, F., Capaccioni, F., Zambon, F., Carraro, F., Fonte, S., Frigeri, A., Jaumann, R., Magni, G., Marchi, S., McCord, T. B., McFadden, L. A., McSween, H. Y., Mittlefehldt, D. W., Nathues, A., Palomba, E., Pieters, C. M., Raymond, C. A., Russell, C. T., Toplis, M. J., Turrini, D., 2012, Spectroscopic Characterization of Mineralogy and Its Diversity Across Vesta, *Science*, 336, 697–700
- Delaney, J. S., Prinz, M., Takeda, H., 1984, The polymict eucrites, in *Lunar and Planetary Science Conference Proceedings*, vol. 15 of *Lunar and Planetary Science Conference Proceedings*, pp. 251–288
- Delbó, M., Harris, A. W., 2002, Physical properties of near-Earth asteroids from thermal infrared observations and thermal modeling, *Meteoritics and Planetary Science*, 37, 1929–1936
- DeMeo, F. E., Binzel, R. P., Slivan, S. M., Bus, S. J., 2009, An extension of the Bus asteroid taxonomy into the near-infrared, *Icarus*, 202, 160–180
- DeMeo, F. E., Carry, B., Marchis, F., Birlan, M., Binzel, R. P., Bus, S. J., Descamps, P., Nedelcu, A., Busch, M., Bouy, H., 2011, A spectral comparison of (379) Huenna and its satellite, *Icarus*, 212, 677–681
- Dunn, T. L., McCoy, T. J., Sunshine, J. M., McSween, H. Y., 2010, A coordinated spectral, mineralogical, and compositional study of ordinary chondrites, *Icarus*, 208, 789–797
- Filippenko, A. V., 1982, The importance of atmospheric differential refraction in spectrophotometry, *Publications of the Astronomical Society of the Pacific*, 94, 715–721
- Foderà Serio, G., Manara, A., Sicoli, P., 2002, Giuseppe Piazzi and the Discovery of Ceres, *Asteroids III*, pp. 17–24
- Gaffey, M. J., 1976, Spectral reflectance characteristics of the meteorite classes, *Journal of Geophysical Research*, 81, 905–920
- Gaffey, M. J., 1997, Surface Lithologic Heterogeneity of Asteroid 4 Vesta, *Icarus*, 127, 130–157
- Gaffey, M. J., 2003, Observational and Data Reduction Techniques to Optimize Mineralogical Characterizations of Asteroid Surface Materials, in *Lunar and Planetary Institute Science Conference Abstracts*, (Ed.) S. Mackwell & E. Stansbery, vol. 34 of *Lunar and Planetary Institute Science Conference Abstracts*, p. 1602
- Gaffey, M. J., 2010, Space weathering and the interpretation of asteroid reflectance spectra, *Icarus*, 209, 564–574
- Gaffey, M. J., McCord, T. B., 1978, Asteroid surface materials - Mineralogical characterizations from reflectance spectra, *Space Science Reviews*, 21, 555–628

- Gaffey, M. J., Bell, J. F., Cruikshank, D. P., 1989, Reflectance spectroscopy and asteroid surface mineralogy, in *Asteroids II*, (Eds.) R. P. Binzel, T. Gehrels, M. S. Matthews, pp. 98–127, University of Arizona Press
- Gaffey, M. J., Burbine, T. H., Piatek, J. L., Reed, K. L., Chaky, D. A., Bell, J. F., Brown, R. H., 1993, Mineralogical variations within the S-type asteroid class, *Icarus*, 106, 573–602
- Gaffey, M. J., Cloutis, E. A., Kelley, M. S., Reed, K. L., 2002, Mineralogy of Asteroids, in *Asteroids III*, (Eds.) W. Bottke, A. Cellino, P. Paolicchi, R. Binzel, pp. 183–204, University of Arizona Press
- Gastineau-Lyons, H. K., McSween, Jr., H. Y., Gaffey, M. J., 2002, A critical evaluation of oxidation versus reduction during metamorphism of L and LL group chondrites, and implications for asteroid spectroscopy, *Meteoritics and Planetary Science*, 37, 75–89
- Gehrels, T., 1970, Photometry of asteroids., in *Surfaces and Interiors of Planets and Satellites*, (Ed.) A. Dollfus, pp. 317–375
- Gehrels, T., Coffeen, T., Owings, D., 1964, Wavelength dependence of polarization. III. The lunar surface., *The Astronomical Journal*, 69, 826–852
- Geiger, C. A., 2004, An introduction to spectroscopic methods in the mineral sciences and geochemistry, in *Spectroscopic Methods in Mineralogy*, (Eds.) A. Beran, E. Libowitzky, pp. 1–42, Eötvös University Press
- Gradie, J., Veverka, J., 1986, The wavelength dependence of phase coefficients, *Icarus*, 66, 455–467
- Gradie, J., Veverka, J., Buratti, B., 1980, The effects of scattering geometry on the spectrophotometric properties of powdered material, in *Lunar and Planetary Science Conference Proceedings*, (Ed.) S. A. Bedini, vol. 11 of *Lunar and Planetary Science Conference Proceedings*, pp. 799–815
- Hapke, B., 1981, Bidirectional reflectance spectroscopy. I - Theory, *Journal of Geophysical Research*, 86, 3039–3054
- Hapke, B., 1993, *Theory of reflectance and emittance spectroscopy*, Cambridge, UK: Cambridge University Press
- Hapke, B., 2001, Space weathering from Mercury to the asteroid belt, *Journal of Geophysical Research*, 106, 10 039–10 074
- Hardersen, P. S., Gaffey, M. J., Cloutis, E. A., Abell, P. A., Reddy, V., 2006, Near-infrared spectral observations and interpretations for S-asteroids 138 Tolosa, 306 Unitas, 346 Hermentaria, and 480 Hansa, *Icarus*, 181, 94–106
- Harris, A. W., Lagerros, J. S. V., 2002, Asteroids in the Thermal Infrared, *Asteroids III*, pp. 205–218
- Hayakawa, S., Matsumoto, T., Mizuno, T., Nishimura, T., Okuda, H., Sugimoto, D., 1968, Infrared Observations of the Moon, *Icarus*, 9, 357–359

- Hinrichs, J. L., Lucey, P. G., 2002, Temperature-Dependent Near-Infrared Spectral Properties of Minerals, Meteorites, and Lunar Soil, *Icarus*, 155, 169–180
- Hinrichs, J. L., Lucey, P. G., Robinson, M. S., Meibom, A., Krot, A. N., 1999, Implications of temperature-dependent near-IR spectral properties of common minerals and meteorites for remote sensing of asteroids, *Geophysical Research Letters*, 26, 1661–1664
- Johnson, P. B., Christy, R. W., 1974, Optical constants of transition metals: Ti, V, Cr, Mn, Fe, Co, Ni, and Pd, *Physical Review B*, 9, 5056–5070
- Kargel, J. S., 1994, Metalliferous asteroids as potential sources of precious metals, *Journal of Geophysical Research*, 99, 21 129–21 141
- Keil, K., 2002, Geological History of Asteroid 4 Vesta: The "Smallest Terrestrial Planet", in *Asteroids III*, (Eds.) W. Bottke, A. Cellino, P. Paolicchi, R. Binzel, pp. 573–584, University of Arizona Press
- King, T. V. V., Ridley, W. I., 1987, Relation of the spectroscopic reflectance of olivine to mineral chemistry and some remote sensing implications, *Journal of Geophysical Research*, 92, 11 457–11 469
- Kitazato, K., Clark, B. E., Abe, M., Abe, S., Takagi, Y., Hiroi, T., Barnouin-Jha, O. S., Abell, P. A., Lederer, S. M., Vilas, F., 2008, Near-infrared spectrophotometry of Asteroid 25143 Itokawa from NIRS on the Hayabusa spacecraft, *Icarus*, 194, 137–145
- Lane, A. P., Irvine, W. M., 1973, Monochromatic phase curves and albedos for the lunar disk, *The Astronomical Journal*, 78, 267–277
- Lebofsky, L. A., Spencer, J. R., 1989, Radiometry and a thermal modeling of asteroids, in *Asteroids II*, (Ed.) . M. S. M. R. P. Binzel, T. Gehrels, pp. 128–147
- Lewis, J. S., Hutson, M. L., 1993, Asteroidal resource opportunities suggested by meteorite data., in *Resources of near-earth space*, (Ed.) Lewis, J. S., Matthews, M. S., & Guerrieri, M. L., pp. 523–542, Univ. of Arizona, Tucson
- Lim, L. F., McConnochie, T. H., Bell, J. F., Hayward, T. L., 2005, Thermal infrared (8-13 μm) spectra of 29 asteroids: the Cornell Mid-Infrared Asteroid Spectroscopy (MIDAS) Survey, *Icarus*, 173, 385–408
- Lumme, K., Bowell, E., 1981, Radiative transfer in the surfaces of atmosphereless bodies. I - Theory. II - Interpretation of phase curves, *The Astronomical Journal*, 86, 1694–1721
- Luu, J. X., Jewitt, D. C., 1990, Charge-coupled device spectra of asteroids. I - Near-earth and 3:1 resonance asteroids, *The Astronomical Journal*, 99, 1985–2011
- Mann, P., Cloutis, E. A., Reddy, V., 2011, The Effect of Changing Viewing Geometry on Pyroxene and Eucrite Reflectance Spectra, in *Lunar and Planetary Institute Science Conference Abstracts*, vol. 42 of *Lunar and Planetary Institute Science Conference Abstracts*, p. 2268

- Martins, Z., Botta, O., Fogel, M. L., Sephton, M. A., Glavin, D. P., Watson, J. S., Dworkin, J. P., Schwartz, A. W., Ehrenfreund, P., 2008, Extraterrestrial nucleobases in the Murchison meteorite, *Earth and Planetary Science Letters*, 270, 130–136
- McCord, T. B., Adams, J. B., Johnson, T. V., 1970, Asteroid Vesta: Spectral Reflectivity and Compositional Implications, *Science*, 168, 1445–1447
- McCoy, T. J., Nittler, L. R., Burbine, T. H., Trombka, J. I., Clark, P. E., Murphy, M. E., 2000, Anatomy of a Partially Differentiated Asteroid: A “NEAR”-Sighted View of Acapulcoites and Lodranites, *Icarus*, 148, 29–36
- McCoy, T. J., Mittlefehldt, D. W., Wilson, L., 2006, Asteroid Differentiation, in *Meteorites and the Early Solar System II*, (Eds.) D. S. Lauretta, H. Y. McSween, pp. 733–745, University of Arizona Press
- McSween, H., Huss, G., 2010, *Cosmochemistry*, Cambridge, UK: Cambridge University Press
- McSween, Jr., H. Y., Ghosh, A., Grimm, R. E., Wilson, L., Young, E. D., 2002, Thermal Evolution Models of Asteroids, *Asteroids III*, pp. 559–571
- Menichella, M., Paolicchi, P., Farinella, P., 1996, The Main Belt as a Source of Near-Earth Asteroids, *Earth Moon and Planets*, 72, 133–149
- Michel, P., Froeschlé, C., Farinella, P., 1996, Dynamical Evolution of NEAs: Close Encounters, Secular Perturbations and Resonances, *Earth Moon and Planets*, 72, 151–164
- Millis, R. L., Bowell, E., Thompson, D. T., 1976, UVB photometry of asteroid 433 Eros, *Icarus*, 28, 53–67
- Mittlefehldt, D. W., McCoy, T. J., Goodrich, C. A., Kracher, A., 1998, Non-Chondritic Meteorites from Asteroidal Bodies, in *Reviews in Mineralogy Vol. 36, Planetary Materials*, (Ed.) J. Papike, pp. 4–001–4–196, Mineralogical Society of America
- Morbidelli, A., Nesvorný, D., 1999, Numerous Weak Resonances Drive Asteroids toward Terrestrial Planets Orbits, *Icarus*, 139, 295–308
- Morbidelli, A., Bottke, Jr., W. F., Froeschlé, C., Michel, P., 2002, Origin and Evolution of Near-Earth Objects, *Asteroids III*, pp. 409–422
- Moroz, L., Schade, U., Wäsch, R., 2000, Reflectance Spectra of Olivine-Orthopyroxene-Bearing Assemblages at Decreased Temperatures: Implications for Remote Sensing of Asteroids, *Icarus*, 147, 79–93
- Moskovitz, N. A., Willman, M., Burbine, T. H., Binzel, R. P., Bus, S. J., 2010, A spectroscopic comparison of HED meteorites and V-type asteroids in the inner Main Belt, *Icarus*, 208, 773–788
- Nakamura, T., Noguchi, T., Tanaka, M., Zolensky, M. E., Kimura, M., Tsuchiyama, A., Nakato, A., Ogami, T., Ishida, H., Uesugi, M., Yada, T., Shirai, K., Fujimura, A., Okazaki, R., Sandford, S. A., Ishibashi, Y., Abe, M., Okada, T., Ueno, M., Mukai, T., Yoshikawa, M., Kawaguchi, J., 2011, Itokawa Dust Particles: A Direct Link Between S-Type Asteroids and Ordinary Chondrites, *Science*, 333, 1113–1116

- Nathues, A., 2000, Spectroscopic Study of Eunomia Asteroid Family, Ph.d. dissertation, University of Berlin, Germany
- Nathues, A., 2010, Spectral study of the Eunomia asteroid family Part II: The small bodies, *Icarus*, 208, 252–275
- Nesvorný, D., Ferraz-Mello, S., Holman, M., Morbidelli, A., 2002, Regular and Chaotic Dynamics in the Mean-Motion Resonances: Implications for the Structure and Evolution of the Asteroid Belt, *Asteroids III*, pp. 379–394
- Noguchi, T., Nakamura, T., Kimura, M., Zolensky, M. E., Tanaka, M., Hashimoto, T., Konno, M., Nakato, A., Ogami, T., Fujimura, A., Abe, M., Yada, T., Mukai, T., Ueno, M., Okada, T., Shirai, K., Ishibashi, Y., Okazaki, R., 2011, Incipient Space Weathering Observed on the Surface of Itokawa Dust Particles, *Science*, 333, 1121–1125
- Pieters, C. M., Taylor, L. A., Noble, S. K., Keller, L. P., Hapke, B., Morris, R. V., Allen, C. C., McKay, D. S., Wentworth, S., 2000, Space weathering on airless bodies: Resolving a mystery with lunar samples, *Meteoritics and Planetary Science*, 35, 1101–1107
- Rabinowitz, D. L., 1997, Are Main-Belt Asteroids a Sufficient Source for the Earth-Approaching Asteroids?, *Icarus*, 130, 287–295
- Rayner, J. T., Toomey, D. W., Onaka, P. M., Denault, A. J., Stahlberger, W. E., Vacca, W. D., Cushing, M. C., Wang, S., 2003, SpeX: A Medium-Resolution 0.8-5.5 Micron Spectrograph and Imager for the NASA Infrared Telescope Facility, *Publications of the Astronomical Society of the Pacific*, 115, 362–382
- Reddy, V., 2009, Mineralogical Survey of near-Earth asteroid population: Implications for impact hazard assessment and sustainability of life on Earth, Ph.d. dissertation, University of North Dakota, Grand Forks
- Reddy, V., Corre, L. L., Hicks, M., Lawrence, K., Buratti, B. J., Abell, P. A., Gaffey, M. J., Hardersen, P. S., 2012a, Composition of near-Earth Asteroid 2008 EV5: Potential target for robotic and human exploration, *Icarus*, 221, 678–681
- Reddy, V., Nathues, A., Le Corre, L., Sierks, H., Li, J.-Y., Gaskell, R., McCoy, T., Beck, A. W., Schröder, S. E., Pieters, C. M., Becker, K. J., Buratti, B. J., Denevi, B., Blewett, D. T., Christensen, U., Gaffey, M. J., Gutierrez-Marques, P., Hicks, M., Keller, H. U., Maue, T., Mottola, S., McFadden, L. A., McSween, H. Y., Mittlefehldt, D., O'Brien, D. P., Raymond, C., Russell, C., 2012b, Color and Albedo Heterogeneity of Vesta from Dawn, *Science*, 336, 700–704
- Reddy, V., Sanchez, J. A., Gaffey, M. J., Abell, P. A., Corre, L. L., Hardersen, P. S., 2012c, Composition of near-Earth Asteroid (4179) Toutatis, *Icarus*, 221, 1177–1179
- Reddy, V., Sanchez, J. A., Nathues, A., Moskovitz, N. A., Li, J.-Y., Cloutis, E. A., Archer, K., Tucker, R. A., Gaffey, M. J., Paul Mann, J., Sierks, H., Schade, U., 2012d, Photometric, spectral phase and temperature effects on 4 Vesta and HED meteorites: Implications for the Dawn mission, *Icarus*, 217, 153–168

- Rivkin, A. S., Binzel, R. P., Sunshine, J., Bus, S. J., Burbine, T. H., Saxena, A., 2004, Infrared spectroscopic observations of 69230 Hermes (1937 UB): possible unweathered endmember among ordinary chondrite analogs, *Icarus*, 172, 408–414
- Roush, T. L., Singer, R. B., 1985, The Effects of Temperature on the Spectral Reflectance of Asteroid Surfaces: a Model, in *Lunar and Planetary Institute Science Conference Abstracts*, vol. 16, pp. 714–715
- Roush, T. L., Singer, R. B., 1986, Gaussian analysis of temperature effects on the reflectance spectra of mafic minerals in the 1- μ m region, *Journal of Geophysical Research*, 91, 10 301–10 308
- Safronov, V. S., 1979, On the origin of asteroids, in *Asteroids*, (Ed.) T. Gehrels, pp. 975–991, University of Arizona Press
- Sanchez, J. A., Reddy, V., Nathues, A., Cloutis, E. A., Mann, P., Hiesinger, H., 2012, Phase reddening on near-Earth asteroids: Implications for mineralogical analysis, space weathering and taxonomic classification, *Icarus*, 220, 36–50
- Sanchez, J. A., Michelsen, R., Reddy, V., Nathues, A., 2013, Surface composition and taxonomic classification of a group of near-Earth and Mars-crossing asteroids, *Icarus*, 225, 131–140
- Schade, U., Wäsch, R., 1999, NIR reflectance spectroscopy of mafic minerals in the temperature range between 80 and 473 K, *Advances in Space Research*, 23, 1253–1256
- Shepard, M. K., Cloutis, E., 2011, Laboratory Measurements of Band Depth Variation with Observation Geometry, in *Lunar and Planetary Institute Science Conference Abstracts*, vol. 42 of *Lunar and Planetary Institute Science Conference Abstracts*, p. 1043
- Shestopalov, D. I., Golubeva, L. F., 2000, Influence of Temperature on Reflectance Spectra of Asteroids, in *Lunar and Planetary Institute Science Conference Abstracts*, vol. 31 of *Lunar and Planetary Institute Science Conference Abstracts*, p. 1003
- Shkuratov, Y., Starukhina, L., Hoffmann, H., Arnold, G., 1999, A Model of Spectral Albedo of Particulate Surfaces: Implications for Optical Properties of the Moon, *Icarus*, 137, 235–246
- Shoemaker, E. M., Williams, J. G., Helin, E. F., Wolfe, R. F., 1979, Earth-crossing asteroids - Orbital classes, collision rates with earth, and origin, in *Asteroids*, (Ed.) T. Gehrels, pp. 253–282, University of Arizona Press
- Shukolyukov, A., Lugmair, G. W., 2002, Chronology of Asteroid Accretion and Differentiation, *Asteroids III*, pp. 687–695
- Singer, R. B., Roush, T. L., 1985, Effects of temperature on remotely sensed mineral absorption features, *Journal of Geophysical Research*, 90, 12 434–12 444
- Smith, M. O., Johnson, P. E., Adams, J. B., 1985, Quantitative determination of mineral types and abundances from reflectance spectra using principal components analysis, in *Lunar and Planetary Science Conference Proceedings*, (Eds.) G. Ryder, G. Schubert, vol. 15 of *Lunar and Planetary Science Conference Proceedings*, pp. 797–804

- Strazzulla, G., Dotto, E., Binzel, R., Brunetto, R., Barucci, M. A., Blanco, A., Orofino, V., 2005, Spectral alteration of the Meteorite Epinal (H5) induced by heavy ion irradiation: a simulation of space weathering effects on near-Earth asteroids, *Icarus*, 174, 31–35
- Sunshine, J. M., Bus, S. J., McCoy, T. J., Burbine, T. H., Corrigan, C. M., Binzel, R. P., 2004, High-calcium pyroxene as an indicator of igneous differentiation in asteroids and meteorites, *Meteoritics and Planetary Science*, 39, 1343–1357
- Taylor, L. A., Pieters, C., Keller, L. P., Morris, R. V., McKay, D. S., Patchen, A., Wentworth, S., 2001, The effects of space weathering on Apollo 17 mare soils: Petrographic and chemical characterization, *Meteoritics and Planetary Science*, 36, 285–299
- Tholen, D. J., 1984, Asteroid taxonomy from cluster analysis of Photometry, Ph.D. thesis, Arizona Univ., Tucson
- Vernazza, P., Binzel, R. P., Thomas, C. A., DeMeo, F. E., Bus, S. J., Rivkin, A. S., Tokunaga, A. T., 2008, Compositional differences between meteorites and near-Earth asteroids, *Nature*, 454, 858–860
- Watson, F. G., 1941, *Between the planets*, Philadelphia, The Blakiston company, p. 222
- Weisberg, M. K., McCoy, T. J., Krot, A. N., 2006, Systematics and Evaluation of Meteorite Classification, in *Meteorites and the Early Solar System II*, (Ed.) Lauretta, D. S. & McSween, H. Y., pp. 19–52, University of Arizona Press
- Weissman, P. R., Bottke, Jr., W. F., Levison, H. F., 2002, Evolution of Comets into Asteroids, *Asteroids III*, pp. 669–686
- Wetherill, G. W., 1989, Origin of the asteroid belt, in *Asteroids II*, (Eds.) R. P. Binzel, T. Gehrels, M. S. Matthews, pp. 661–680
- Wiechert, U. H., Halliday, A. N., Palme, H., Rumble, D., 2004, Oxygen isotope evidence for rapid mixing of the HED meteorite parent body, *Earth and Planetary Science Letters*, 221, 373–382
- Yamaguchi, A., Clayton, R. N., Mayeda, T. K., Ebihara, M., Oura, Y., Miura, Y. N., Haramura, H., Misawa, K., Kojima, H., Nagao, K., 2002, A New Source of Basaltic Meteorites Inferred from Northwest Africa 011, *Science*, 296, 334–36
- Zappalà, V., Cellino, A., dell’Oro, A., Paolicchi, P., 2002, Physical and Dynamical Properties of Asteroid Families, *Asteroids III*, pp. 619–631
- Zellner, B., Tholen, D. J., Tedesco, E. F., 1985, The eight-color asteroid survey - Results for 589 minor planets, *Icarus*, 61, 355–416

Talks and Posters

- **Sanchez, Juan A.**; Reddy, Vishnu; Nathues, Andreas; Cloutis, Edward A.; Mann, Paul; Hiesinger, Harald, Phase reddening on near-Earth asteroids: Implications for mineralogical analysis, taxonomic classification and space weathering, EGU General Assembly, Vienna, Austria, 22-27 April 2012
- **Sanchez, Juan A.**, Reddy, V., Nathues, A., Surface mineralogy of two V-type near-Earth asteroids, EPSC-DPS Joint Meeting, Nantes, France, 2-7 October 2011
- Reddy, Vishnu; Nathues, A.; Archer, K. A.; **Sanchez, J. A.**; Gaffey, M. J.; Sierks, H.; Archer, R. A., Phase Angle-induced Photometric And Spectral Effects On Vesta: Implications For The Dawn Mission, DPS meeting, Pasadena, CA, 3-8 October 2010
- Reddy, V.; Cloutis, E. A.; Gaffey, M. J.; GalČd, A.; Pravec, P.; Harris, A. W.; Nathues, A.; **Sanchez, J. A.**, Compositional Investigation of (5404) Uemura: The Largest Fast-Rotating Monolith, Lunar and Planetary Science Conference, Texas, 1-5 March 2010
- Nathues, A.; Reddy, V.; Schaeff, S.; Wiegand, A.; Michelsen, R.; **Sanchez, J. A.**; Boehnhardt, H., Ground-based Mineralogical Characterization of low Δv ASTEX Mission Targets, Lunar and Planetary Science Conference, Texas, 1-5 March 2010

Acknowledgements

I would like to thank my supervisors Dr. Andreas Nathues, Dr. Vishnu Reddy and Prof. Dr. Harald Hiesinger for their useful comments and fruitful discussions related to this work. A special acknowledgement to Dr. Vishnu Reddy from whom I learned many of the techniques and tools used in the present work. I really appreciate his help. I would also like to thank Dr. Dieter Schmitt for giving me the opportunity to develop my thesis in the framework of the International Max Planck Research School (IMPRS). I want to thank Dr. René Michelsen who worked with me during my observing runs at Calar Alto, and Dr. Olivier Hainaut for his help during the observations at the NTT. I am thankful to Dr. Ed Cloutis, Dr. John Hinrichs, Dr. Paul Lucey and Dr. Francesca DeMeo for providing me with data for this research.

I am grateful to Prof. Dr. Ulrich Christensen, Prof. Dr. Addi Bischoff, and Prof. Dr. Hans Kerp for taking part as committee members of my thesis. I want to thank Dr. Miriam Rengel for all her help and good advices during my time at MPS. I am also thankful to Dr. José Antonio López for helping with all the paper work required during the submission process of my thesis.

I want to express my gratitude to Karsten Schindler for helping me with critical issues during the final stage of my thesis. Special thanks to Dr. Thibault Cavalié and Dr. Daniel Verscharen my former flatmate and office mate, respectively, whose presence created a nice and quiet working environment for me. Thanks also to Armando, Juanjo, Chemedá, Lúcia, Yeon Joo, Nafiseh, and the rest of the students and colleagues for the time we shared. Finally, I would like to thank to my family for all their support during these years.

This thesis is based on data obtained with the New Technology Telescope at La Silla, Chile, observations collected at the Centro Astronómico Hispano Alemán (CAHA), operated jointly by the Max-Planck Institut für Astronomie and the Instituto de Astrofísica de Andalucía (CSIC), and observations acquired with the Infrared Telescope Facility on Mauna Kea, Hawai'i. Part of the data utilized in this thesis were obtained and made available by the MIT-UH-IRTF Joint Campaign for NEO Reconnaissance. The IRTF is operated by the University of Hawaii under Cooperative Agreement no. NCC 5-538 with the National Aeronautics and Space Administration, Office of Space Science, Planetary Astronomy Program. The MIT component of this work is supported by NASA grant 09-NEOO009-0001, and by the National Science Foundation under Grants Nos. 0506716 and 0907766. Any opinions, findings, and conclusions or recommendations expressed in this material are those of the author(s) and do not necessarily reflect the views of NASA or the National Science Foundation. Part of this research was supported by the Deutsche Forschungsgemeinschaft.

Curriculum Vitae

Name: Juan Andrés Sánchez

Geburtsdatum: 10. October 1979

Geburtsort: Caracas, Venezuela

Staatsangehörigkeit: Venezuelan

Studium

2006 Bachelor in physics
Universidad Central de Venezuela

2009 Magister Scientiarum in physics
Universidad Central de Venezuela

2013 Dr. rer. nat
Westfälischen Wilhelms-Universität Münster, Germany
Max Planck Institut für Sonnensystemforschung
Katlenburg-Lindau, Germany